Optical Information Processing for Aerospace Applications II

NASA

Optical Information Processing for Aerospace Applications II

Compiled by Robert L. Stermer
Langley Research Center

NASA

National Aeronautics
and Space Administration

Scientific and Technical
Information Branch

1984

PREFACE

The Optical Information Processing Conference II was held on August 30-31, 1983, at Langley Research Center, Hampton, Virginia. The purpose of this conference was to review current research in optical processing and to determine its role in future aerospace systems. It is clear from these proceedings that optical processing offers significant potential in the fields of aircraft and spacecraft control, pattern recognition, and robotics. The development of optical devices and components has demonstrated that system concepts can be implemented in practical aerospace configurations.

This conference was sponsored by the Office of Aeronautics and Space Technology (OAST) of NASA Headquarters and managed by Langley Research Center. Special thanks are offered to Dr. Martin Sokoloski of OAST for his excellent summary comments, which were presented at the close of the conference, and to the many others who gave their time and talents to make the conference possible.

Use of trade names or names of manufacturers in this report does not constitute an official endorsement of such products or manufacturers, either expressed or implied, by the National Aeronautics and Space Administration.

Robert L. Stermer
Chairman

CONTENTS

SESSION IV - OPTICAL DATA PROCESSING FUNCTIONS AND PROCESSORS - I

Chairman: S. Eng

SESSION V - OPTICAL DATA PROCESSING FUNCTIONS AND PROCESSORS - II

Chairman: G. Chin

FUTURE DIRECTIONS IN OPTICAL PROCESSING

John A. Neff
Defense Sciences Office
Defense Advanced Research Projects Agency
Arlington, VA 22209

SUMMARY

Three aspects of the field of optical processing will be discussed. First, a brief sampling will be presented of the potential of this emerging technology. Second, I will discuss what I believe are the major limitations preventing wide-scale implementation of optical processors. The importance of future research in these areas will be emphasized. Third, I will discuss the importance of nonlinear optics in developing optoelectronic interconnects for VLSI, an area of optics that I perceive will receive increased emphasis over the next several years.

PRESENT CAPABILITIES

Figure 1 is a listing of representative application areas for optical processing – areas in which speed and information throughput take precedence over accuracy and precision. The signal processing systems are the furthest advanced, especially in spectrum analysis and excision, because of the maturity of acousto-optic devices. However, the advantages to be gained by using optics in these areas rather than digital processors are not as great as for most image processing or two-dimensional processing applications due to the inherent two-dimensionality of bulk optics. The appeal of optics in image processing is greatest for the global operations; i.e., those operations involving identical action with respect to each image pixel such as in frame differencing, image enhancement, feature extraction, data compression, image restoration, smoothing, and spectral estimation.

Computing with optics received very little attention until the mid-1970s when the residue arithmetic and optical matrix-vector work emerged at Stanford. A very significant research area has now evolved in using optics to realize lower cost, smaller size, reduced power, and higher speed processors for matrix-vector and matrix-matrix products, polynomial evaluation, partial differential and integral equation solutions, and solutions of sets of linear equations. As continued improvements in electronic speed and power begin to slow, optics will assume a role of increasing importance in our quest to maintain computational superiority over our rivals in both the economic and national security realms.

The final area of hybrid systems was given separate billing because of the importance of not losing sight of the fact that the vast majority of the optical processors of the future will actually involve the systematic integration of both electronic and optical processing. For example, an image understanding system will likely employ optical processing to perform the low-level or global operations required to prepare the data for the high-level processing involving feature evaluation, interpretation, and knowledge synthesis. Ideally, the optical processor will have eliminated the irrelevant image content and reduced the data to a level at which digital computers could bring their increased flexibility and programmability into play while still satisfying requirements for real-time processing. Another example is in statistical analysis where it has been shown that optics could be used to perform the computationally intensive operation of moment generation, the results of which would then be fed to a digital computer.

Figures 2-6 illustrate some of the capabilities of optical processing. Frame differencing, as shown in figure 2, is a relatively straightforward process for optics, yet highly relevant to DoD and NASA missions. In such operations as reconnaissance, target tracking, surveillance, robotics and weather forecasting, the decision to act or not act is based on whether or not any change has occurred between one image frame and another. Therefore, an image subtraction operation is required, and this can be done with optics by using a spatial light modulator (SLM) with a contrast reversal capability. The first frame is contrast reversed and stored by the SLM. As shown in the figure, the second frame, which differs from the first by the presence of a man, is superimposed by the SLM onto the first frame, thus producing no modulation field except at the location of the change.

Figure 3 illustrates image subtraction being used as an edge detector in an optical image compression scheme[1]. The technique shown is somewhat the optical analog to differential pulse code modulation. The low frequency information is derived from applying a sampling mask to the original image and the high frequency supplement derives from blurring (optically interpolating) the sampled image and subtracting the result from the original. This yields a two-dimensional signal composed of the high frequency content in the original image or, in essence, it comprises an edge detector. The bandwidth required to transmit, individually, the low frequency and the high frequency information is about an order of magnitude less than that required to transmit the original image using 8 bits per pixel. The output is reconstructed merely by adding the two transmitted signals, and is shown to be a good reproduction of the original.

The data flow concept of systolic processing has recently found its way into a number of optical processing architectures. This is not surprising since analog processing schemes are much more closely allied with continuously flowing data than are the conventional von Neumann digital architectures. The term systolic was borrowed from the biological sciences due to the similarity of the data flow in these systems to the systolic action of the heart. In systolic processors, data flows from memory in a rhythmic manner, passing through many processing elements before returning. The optical implementations of two such processors designed for computing the product of two matrices are shown in figure 4. The RUBIC Cube[2] is a systolic architecture whose major components are a pulsed noncoherent light source, a spatial light modulator for each of the two input matrices, a 2-dimensional photodetector array for reading out the input matrix, and a polarizing beam splitter. The two light modulators synchronously march the matrix information across the optical aperture where the proper terms superimpose to produce each element of the output matrix. The frequency multiplexed matrix-vector processor[3] is a systolic architecture using a linear LED array, acousto-optic cell, a Fourier transform lens, and a linear photodetector array. Input matrix B is fed in the space and time multiplexed fashion shown (rows of B spatially multiplexed and columns time multiplexed) while the matrix A is multiplexed in frequency and space using the acousto-optic cell. Each row element of matrix A is placed on a separate frequency carrier such that after multiplication with the appropriate B elements via acousto-optic modulation, the resulting output term is refracted by the transform lens to a particular photodetector element depending on the carrier frequency. This architecture may be viewed as a matrix-vector multiplier in which frequency multiplexing is used to expand the vector to a matrix.

Figure 5 illustrates the use of optics in solving partial differential equations. The processor consists of two confocal mirrors which form a Fabry-Perot interferometer within which the light beams are modulated by filter functions. This modulation, which occurs in the Fourier plane of the processor, corresponds to

differentiation in the spatial domain. The resulting system has a complex-valued feedback transfer function and performs analog solutions of partial differential equations. The original processor, constructed at the University of California, San Diego, solved only two-dimensional partial differential equations by employing the two spatial dimensions of optics. The processor has now been expanded using the time dimension to represent the third variable by pulsing the system and observing the output in time[4]. The evolution of a particular solution is shown by the series of optical intensity patterns shown at the bottom of the illustration.

Figure 6 illustrates the potential of hybrid optical/digital processing. The processor shown was designed as an optimal nonlinear phase estimator[5]. In a high noise environment, the phase locked loop and the extended Kalman filter are suboptimal phase demodulators; therefore, one must go to a recursive nonlinear filter. The speed of the filter is critical since the cycle time determines the bandwidth of the signals which can be accommodated. Unfortunately, the nonlinear filter must perform a time consuming two-dimensional convolution of the state variable probability density function with the probability density function of the noise. Instead of performing the two-dimensional convolution digitally, the state variable probability density function was converted to an optical representation via an LED array, convolved with the noise function, and the result reconverted via a CCD array. As one may surmise, a considerable degree of effort was expended in addressing interface problems during development of this processor, not the least of which was the problem of data synchronization around the loop. Such hybrid systems will see considerable improvement as better source and detector arrays become available.

CRITICAL NEEDS FOR FUTURE TECHNOLOGY ADVANCES

The major developments that are needed to advance the utility of optical processing fall into the four categories of: architectures and algorithms; materials; spatial light modulators; and sources and detectors. Over the years algorithm development has been severely constrained by hardware limitations. For example, image processing operators are local rather than global, two dimensional signals are computer segmented into a series of one dimensional signals, and computer architectures are still von Neumann based. Even the expanding capabilities of VLSI are not being fully exploited because in the past 25 years processing algorithms and architectures have not changed significantly. The digital community has recently been showing interest in parallel processing with advances being made in data flow architectures and functional level programming; however, a great deal of research and development remains to be accomplished in parallel algorithm formulation if we are to realize a significant improvement in throughput rates. Those researchers having experience with optical architectures may be more visionary toward parallel algorithm concepts than their digital counterparts because of the hands-on experience with parallel devices. I challenge the optical processing community to lead the way in conceiving these new algorithms which will be a building block for both optical and digital processors of the future.

Materials research is the foundation of device research and current device research is very materials limited. Fundamental studies of the interaction of light with materials should be pursued along with the search for new materials and better ways of growing existing materials. Promising new polymerization processes should be applied to the growth of new polymeric and organic crystals with unique or improved electro-optical characteristics. Ion exchange processes should be investigated with regard to existing electro-optical materials in an attempt to induce larger

changes in the index of refraction. Table 1 lists the more important characteristics to be sought in pursuing improved materials.

TABLE 1

DESIRED PARAMETERS OF ELECTRO-OPTIC/PHOTOCONDUCTIVE MATERIALS

Crystallographic space/point group at high symmetry
    Affects dynamic range/contrast ratio on SLMs
Large electro-optic coefficient
    Influences optical transfer function/device operating voltage
High dark resistivity
    Controls image retention time
High mobility lifetime product
    Controls device sensitivity/response times
Ease of crystal growth and impurity control
Controlled residual birefringence
    Influences phase uniformity
Optical quality and flatness

The full advantage of optical processing cannot be realized until a device exists for inputting the data to the processors at rates commensurate with the speed of optics itself. These devices are the spatial light modulators (SLMs), and the lack of an adequate SLM is probably the most serious handicap in the advancement of optical processing. For this reason, DARPA has initiated a program for SLM development with the goal of achieving a viable modulator with the operating parameters shown in the right-most column of figure 7. Also included in the figure are characteristic parameters for some other modulators that are either available on the market or are under development. Table 2 lists those devices in the figure along with their respective developers. The numbers in parentheses represent parameters that have not been demonstrated experimentally but which have been shown theoretically to be attainable.

TABLE 2

SPATIAL LIGHT MODULATORS AND THEIR DEVELOPERS

Microchannel Spatial Light Modulator	MIT
Deformable Membrane Device	Texas Instruments
PROM	ITEK
Silicon on PLZT	UC-San Diego
Magneto-optic Light Mod	Litton
Ruticon	Xerox
Liquid Crystal Light Valve	Hughes

Much of the device work in sources and detectors has been driven by communications requirements rather than by optical processing needs; consequently, the area is dominated by one-dimensional hardware. The parallel computing goal is to achieve one million parallel channels; therefore, one would ideally like 1000x1000 element source and detector arrays that are compatible with one another and with the SLMs. Source properties requiring improvement are: greater linearity and larger dynamic range in the current/light-intensity transfer characteristics, on-chip temperature control and drive circuitry, increased uniformity, enhanced modal stability, and longer lifetime. Detector advances should focus on: increased linear dynamic range, reduced cross-talk, better sensitivity, parallel readout capability,

increased speed, and better uniformity. In addition, improved post detection electronics will be needed to handle the high throughput rates, amounting to as much as a billion bits per second on a million parallel channels. This will likely require the capabilities of the silicon VHSIC devices or GaAs microcircuits.

OPTICS AND SUPERCOMPUTATION

Pursuit of intelligence-based supercomputers has become a national goal, motivated to a large extent by the Japanese plan to build a fifth generation supercomputer. The U.S. efforts will be spearheaded in the private domain by The Microelectronics and Computer Technology Corp. and by the Semiconductor Research Corp. and in the public domain by DARPA. The major goal of the DARPA program is to enable a wide range of new military capabilities and commercial spinoffs by developing a new class of super intelligent computers for Defense and by developing the underlying technology base in a strong and competitive industrial setting. As shown in figure 8, DARPA proposes to exceed the goals of the Japanese in processing speed by several orders of magnitude.

Besides the increased processing speeds, a major difference between this new generation of computing capability and the existing state of the art is the plan to incorporate intelligence into these new supercomputers. The new systems are known as symbolic computers as opposed to the label of numeric computer applied to the existing machines.

How does symbolic computing differ from numeric computing? The data in numeric processing is explicit whereas for a symbolic processor only a small fraction of the knowledge needed to solve any specific problem is explicitly represented--the remaining is implicit and therefore must be deduced. Thus the symbolic compuer encompasses thousands of rules and logical inferences which form the foundation for deductive reasoning. Table 3 lists some defining characteristics for the numeric and symbolic computers which help to differentiate between the operational characteristics of the two types of machines. Besides the use of logical inferences instead of arithmetic operations, the symbolic processor will focus on the use of English in order to facilitate operator interfacing, will have a distributed as opposed to pipelined architecture, will possess a rapid retrieval capability for affording ready access to all needed rules, will have the capability to learn from its environment, and will be capable of integrating various functions such as speech, vision, natural language processing, and graphics.

TABLE 3

SYMBOLIC VS. NUMERIC COMPUTATION

SYMBOLIC	NUMERIC
Logical inferences	Floating point operations.
English	Numbers
Array processing	Array processing
Distributed	Pipelined
Rapid retrieval	
Semantic memory	
Heuristic	
Function integration	

If one accepts the increasingly popular contention that current techniques for intracomputer communications are a major factor limiting further scale-downs of computer circuits for numeric computers, then one can easily see that the communications problem is compounded for symbolic computers. The above listed attributes of distributed architecture, rapid retrieval, and function integration together with the need for massive parallelness will escalate the requirements for inter- and intrachip communications. This is where I feel that optics can take a major step forward--not only in offering potentially superior techniques for computer interconnects, but also in getting a so-called "foot in the door" in the mainstream of computer development in this country.

What are these advantages that optics can potentially offer in improving computer interconnects? Besides the potential for gigabit propagation rates, the conversion from electronics to optics conveniently provides a decoupling of the various circuits from one another. In the case of intrachip interconnects, significant gains should be realized in reducing cross talk between the metallic routings, and the interconnects need no longer be constrained to the plane of a thin film on the VLSI chip. In addition, optics can offer an increased programming flexibility. These advantages will become more evident in the ensuing discussion.

The optoelectronic interconnect goals may be divided into optoelectronic conversion and switching mechanisms and into interconnect topology. For the former, the first goal is to integrate the optical components onto the VLSI chips. These components would be detectors and either sources or modulators. Modulation would be the conversion process used if one were to consider using a central laser source whose light is distributed among all the VLSI chips rather than using separate sources at each conversion point. The second goal would be to attain the required conversions at submilliwatt power levels. The final goal in the area of conversion and switching would be to realize two-dimensional arrays of optical switches operating at subnanosecond switching speeds. Such switching arrays would enable one to restructure the interconnects. The three goals under interconnect topology are generalized networks, non-contentual communications, and programmable systems. Ideally an interchip or inter-microprocessor interconnect scheme would enable direct communications between any communicator and any receiver without contention, permitting simultaneous communications throughout the system. The complexity of such generalized interconnects escalates rapidly as the size of the overall system grows.

Let us take a look at how optics might be used. Figure 9 illustrates four possible concepts--the top two using guided channels while the bottom two are unguided schemes; i.e., they do not involve waveguides. The planar waveguide configuration could be realized by incorporating a waveguide layer in the VLSI chip, but we would still be faced with the planar constraints, and waveguide scattering might generate some cross talk. The optical fiber scheme overcomes these disadvantages, but does not allow us to take advantage of the spatial multiplexing capability of optics. This leads us to look to unguided techniques, which take advantage of the fact that any number of optical beams may independently exist in the same spatial location in a linear medium. The scheme shown on the left employs a mask which determines which sources "see" which detectors. Even if the masking structure were to employ imaging elements which could refract the light to the appropriate detectors, the overall system is not light efficient due to the absorption by the mask. The final concept employs holographic optical elements to diffract the light to the correct location, and affords a great deal of architectural flexibility. An intermixed arrangement of VLSI chips and hologram arrays could someday eliminate the need for the massive bundles of wires currently used to move information inside computers.

Architectural concepts need not involve detectors. As shown in figure 10, an optical beam may be used to directly influence an electronic circuit, either by changing the conduction in an electronic interconnect so as to perform switching, or by altering the transfer characteristics of electronic components. For example, picosecond light pulses may be used to rapidly sample electronic signals or to trigger electronic flip-flops.

The interconnect methods considered so far have been fixed in the system design, but optoelectronic interconnects have considerable potential for programmability. This extended capability may be considered for each of the unguided schemes shown in figure 9. In the masking technique, consider replacing the mask with a two-dimensional array of bistable switches. Such a system is best understood by analyzing the interconnect problem via matrix algebra. The highest level of interconnection entails a generalized crossbar network involving N^2 interconnects available for N processors (N units communicating with N units) as shown in figure 11. Such a network becomes very expensive when implemented electronically for large N, but the inherent parallelism of optics holds great potential for inexpensive and high-speed crossbar switching. If one labels the unit inputs as x's as shown and the outputs as y's, then $y = Ax$, where A represents the interconnect switch settings. This suggests pursuing a reinvestigation of the existing techniques in optical algebra to determine their applicability to interconnection networks.

The matrix A suggests the need for a two-dimensional array of bistable switches. The optical realization of such an array requires a nonlinear optical material in conjunction with feedback, either in an external configuration similar to figure 12[6] or within a Fabry-Perot resonator. One may also consider hybrid structures employing electronic feedback in order to produce effective nonlinearities much greater than currently possible using intrinsic nonlinearities.

Referring back to figure 9 once again, the grating scheme could be made programmable by employing four-wave mixing to do real-time holography. The array of holographic optical elements could then be written at speeds limited principally by the response times of the nonlinear materials used as the interaction medium. The similarity between degenerate four-wave mixing and conventional holography is illustrated in figure 13[7]. If one uses the grating point of view, four-wave mixing can be viewed as the simultaneous recording and reading of two sets of gratings. The object wave interferes with each of the two counter-propagating input waves (E_1 and E_2) producing the two sets of gratings. For each set, the non-interfering wave is Bragg diffracted by the respective grating to produce a phase conjugated component wave. These two components then coherently superimpose with one another to produce the phase-conjugate return wave.

The field of research underlying most of these desired capabilities in optoelectronic interconnection is nonlinear optics. Both optical bistability and four-wave mixing are dependent on optical nonlinearities, principally the third order optical susceptibility of the nonlinear medium. Two promising areas of nonlinear optical materials research are superlattices and organic films. In creating superlattices one constructs periodic variations of two compound semiconductor thin films (e.g., HgTe and CdTe or GaAs and GaAlAs) to generate quantum well effects[8]. For very high switching speeds (picoseconds, even down to femtoseconds) one is interested in nonresonant nonlinear phenomena. A major contributing factor to nonresonant nonlinearities is the nonlinear motion of charge carriers due to the nonparabolic nature of the conduction band, and this normally becomes more prominent the narrower the bandgap. In superlattices the conduction band is broken up

into a series of minibands, increasing this nonparabolic nature of the band. Shown in figure 14 is a reduced zone representation of the energy dispersion where the band structure is folded into the first zone illustrating this nonparabolic effect.

Another potential for higher speed is in the use of organics[9] because the electronic effects dominate the electro-optic switching times in the organics whereas crystal vibrations limit the switching times in the inorganic crystals (about two orders of magnitude slower). Figure 15 illustrates the technique for depositing these films, known as Langmuir-Blodgett (or LB) film deposition. The films must be ones that lay on the surface of the water; i.e., they must consist of molecules which are polar on one end causing that end to be hydrophilic (having an affinity for water) and nonpolar on the other end (hydrophobic). The uniformity of the films will be governed solely by van der Waals forces along the length of the molecular chains; thus, the films are very fragile during deposition. The film is prepared by first dissolving the organic material in a suitable volatile solvent and then applying this solution to the surface of the water. The volatility of the solvent causes it to evaporate, leaving the organic molecules dispersed over the surface of the water. The surface is then compressed to form a uniform homogeneous film on the water surface. This film is then transferred onto the substrate by drawing the substrate up through the film in a very controlled manner. As shown, a second layer may be deposited by drawing the substrate down through the film. Repetitions of this process will yield organic superlattices which have the potential for combining the nonlinear effects of the organic materials (large nonlinear polarizabilities due to the distribution of electron clouds in the pi bonds) and those of the superlattices.

Bistable switching and four-wave mixing are not the only techniques available for reconfiguring optical channels. For example, figure 16 shows how a device might be constructed which would permit an optical beam to change the index of refraction in an integrated optical circuit. Besides changing the diffraction grating via the optically induced changes in the index of refraction, one could control the activation of the various channels by selective addressing of the source array elements. For large source and detector arrays, the number of possible circuit configurations would be extensive.

The next step in thinking about reconfigurable optical circuits is to envision this flexibility in the context of an optical computer. Figure 17 is one such architecture employing one source array, two detector arrays (one acting as the computer output and the other as a direct memory access), two SLMs (one as the CPU and the other as a RAM), and a switching array. The switching array structures the communication paths between the CPU and memory or between the CPU and the output detector. If one thinks in terms of one million parallel channels of data continuously flowing in a bidirectional sense between the CPU and memory, the processing potential is staggering. In the face of this massive parallel capability, research must address the impact from the algorithmic viewpoint. The algorithms based on Von Neumann architectures must be abandoned in favor of new concepts which will take advantage of the parallel processing capability. The reconfigurable character of optics should be incorporated into these new algorithms and architectures in order to fully benefit from this flexibility. In the end it may be such an edge that would influence system designers to incorporate optics into information processing systems.

REFERENCES

1. B. R. Hunt and S. D. Cabrera, "Optical Computations for a Spatially Adaptive Image Data Compression System," Optical Engineering 20, 616 (1981).
2. R. P. Bocker, H. J. Caulfield, and K. Bromley, "Rapid Unbiased Bipolar Incoherent Calculator Cube," Applied Optics 22,804 (1983).
3. D. Casasent, J. Jackson, and C. Neuman, "Frequency-Multiplexed and Pipelined Iterative Optical Systolic Array Processors," Applied Optics 22, 115 (1983).
4. R. Akins and S. H. Lee, "Transient Response and Time Evolution of 2-D Solutions in a Coherent Optical Processor with Feedback," Applied Optics 22, 4515 (1982).
5. W. E. Stephens and W. H. Steier, "Hybrid Optical-Digital Signal Processing Applied to an Optimal Nonlinear Phase Estimator," Applied Optics 22, 787 (1983).
6. P. W. Smith and W. J. Tomlinson, "Bistable Optical Devices Promise Subpicosecond Switching," IEEE Spectrum, June 1981.
7. D. M. Pepper, "Nonlinear Optical Phase Conjugation," Optical Engineering 21, 156 (1982).
8. H. M. Gibbs, S. S. Tarng, J. L. Jewell, D. A. Weinberger, and K. Tai, "Room Temperature Excitonic Optical Bistability in a GaAs-GaAlAs Superlattice Etalon," Applied Physics Letters 41, 221 (1982).
9. A. F. Garito and K. D. Singer, "Organic Crystals and Polymers – A New Class of Nonlinear Optical Materials," Laser Focus 80, 59 (1982).

- SIGNAL PROCESSING

  - SPECTRUM ANALYSIS & EXCISION
  - CODING/DECODING
  - CORRELATION/CONVOLUTION
  - A/D CONVERSION

- COMPUTING

  - TENSOR ALGEBRA
  - PARTIAL DIFFERENTIAL EQUATIONS
  - INTEGRAL EQUATIONS
  - ARCHIVAL STORAGE
  - INTERCONNECT

- IMAGE PROCESSING

  - FRAME DIFFERENCING
  - MULTISENSOR IMAGING
  - BANDWIDTH COMPRESSION
  - ADAPTIVE PHASED ARRAYS

- HYBRID SYSTEMS

  - PRE/POST PROCESSORS
  - TARGET IDENTIFICATION
  - MULTISENSOR CORRELATION
  - STATISTICAL ANALYSIS

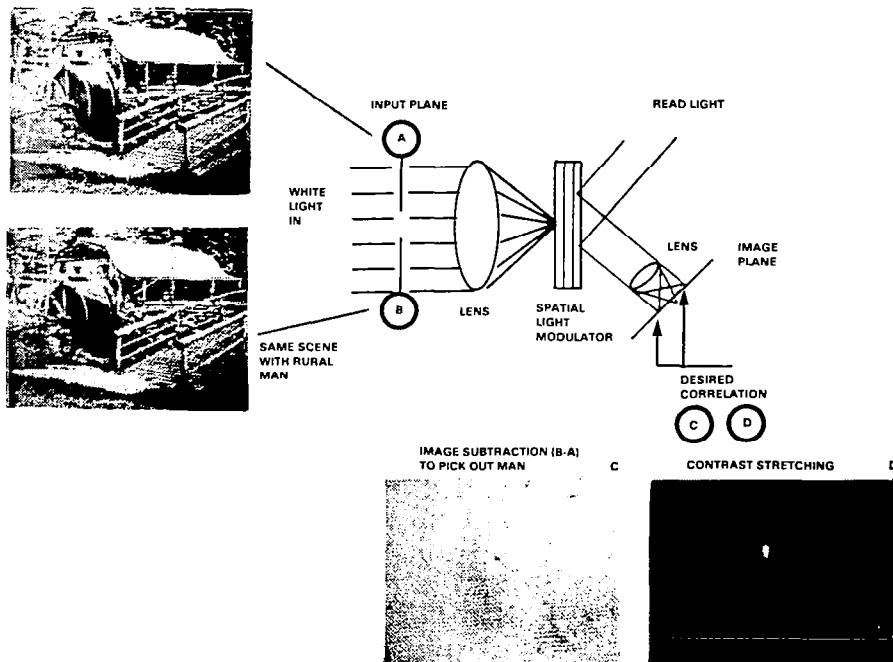Figure 1.- Representative applications of optical processing.
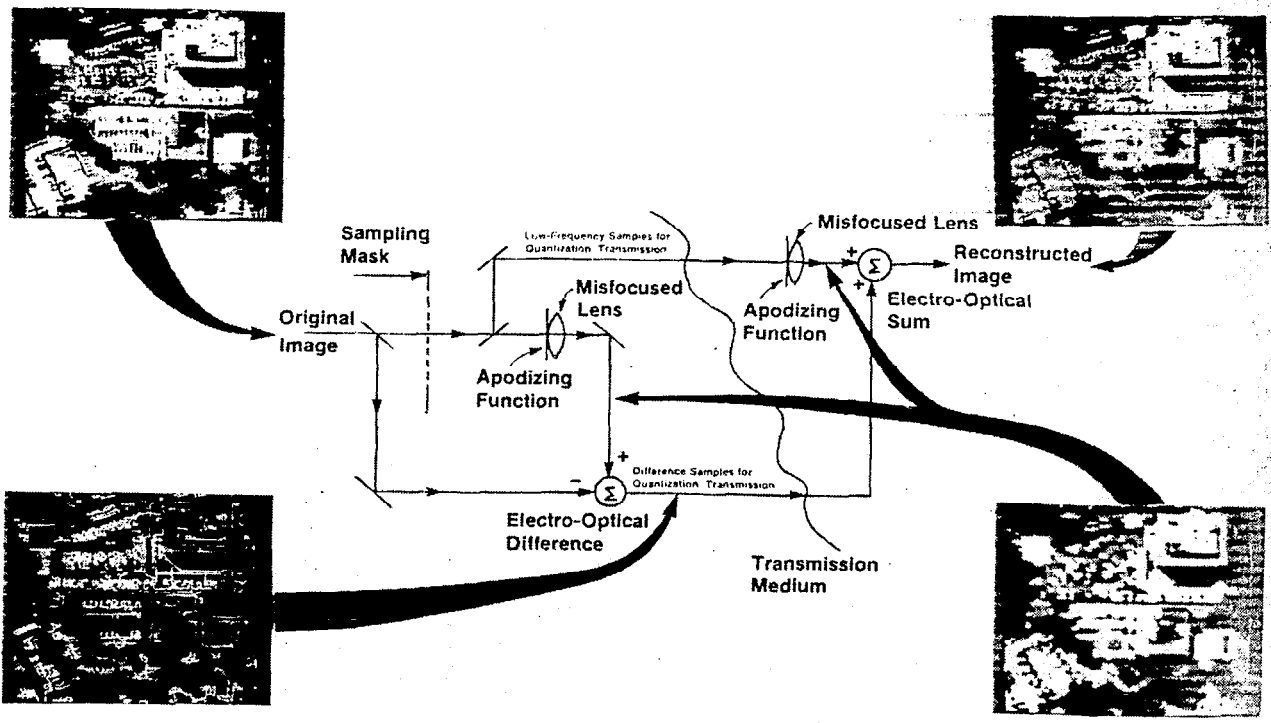

Figure 2.- Frame differencing.

Figure 3.

Sampling Mask

Original Image

Misfocused Lens

Apodizing Function

Low-Frequency Samples for Quantization Transmission

Misfocused Lens

Reconstructed Image

Apodizing Function

Electro-Optical Sum

Difference Samples for Quantization Transmission

Electro-Optical Difference

Transmission Medium

Figure 3.- Image compression.

Figure 4.

OPTICALLY REFLECTING LIGHT VALVE

c_{13} c_{23} c_{33}
c_{12} c_{22} c_{32}
c_{11} c_{21} c_{31}

PHOTODETECTOR ARRAY

a_{11}
a_{12} a_{21}
a_{13} a_{22} a_{31}
a_{23} a_{32}
a_{33}

b_{33}
b_{32} b_{23}
b_{31} b_{22} b_{13}
b_{21} b_{12}
b_{11}

OPTICALLY REFLECTING LIGHT VALVE

SOURCE

RUBIC CUBE

c_{1n} c_{2n} c_{3n}

PHOTODETECTORS

FOURIER TRANSFORM LENS

ACOUSTO-OPTIC CELL

$A_{1n} f(w_1)$, $A_{2n} f(w_2)$, $A_{3n} f(w_3)$

LED ARRAY

b_{11} b_{21} b_{31}
b_{12} b_{22} b_{32}
b_{13} b_{23} b_{33}

FREQUENCY MULTIPLEXED MATRIX-VECTOR

Figure 4.- Matrix product systolic processors.

PROCESSOR:

Filters and/or Active Cell

Real-Time 2-D Input

Mirror

Mirror

Output
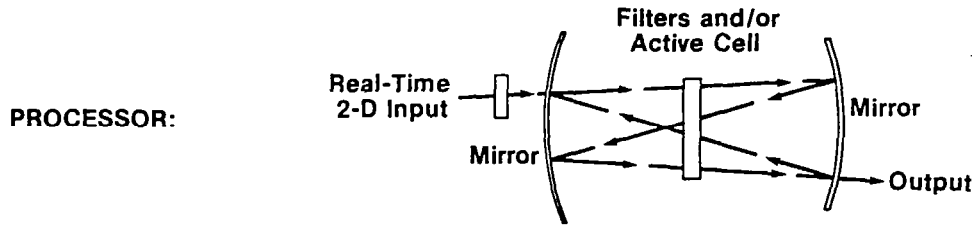
PERFORMANCE: Solution cycle time = (4 x mirror separation)/speed of light

Mirror separation = 1.06 m ⇒ solution cycle time = 14 nanoseconds

EXAMPLE:

$$\frac{\sigma\theta}{\sigma t} + \theta = \frac{\sigma^2\theta}{\sigma x \sigma y}$$

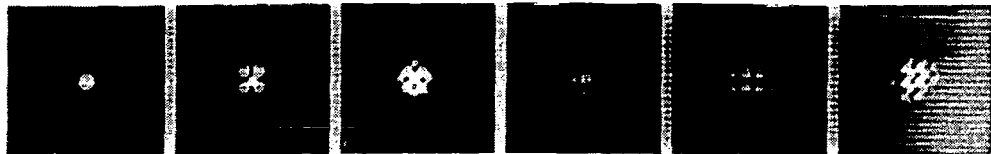$\theta (x, y, o) = $ sinc (x) sinc (y)

Figure 5.- Solutions to three-dimensional partial differential equations.

TIME-DOMAIN RECURSIVE NONLINEAR FILTER FOR 2-D PROBABILITY STATE

VIDEO

A/D

BUFFER MINICOMPUTER
INPUT TO
ELECTROPTICAL PROCESSOR

MINICOMPUTER

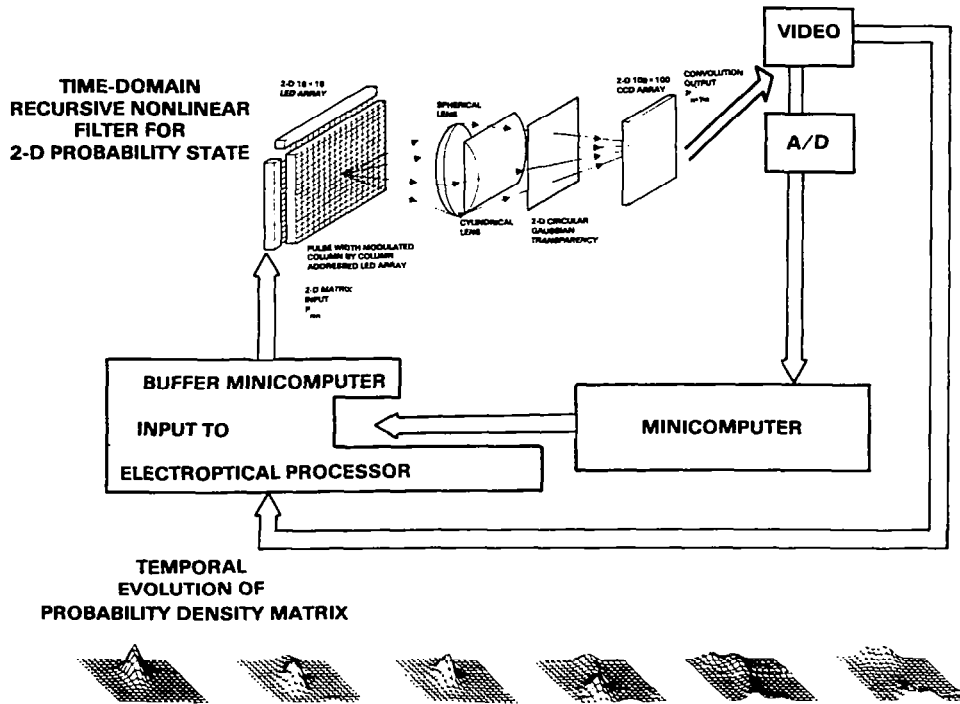TEMPORAL EVOLUTION OF PROBABILITY DENSITY MATRIX

Figure 6.- Phase estimation using hybrid optical/digital processor.

PRESENT: 2-YEAR EXPECTATION IN PARENTHESIS	MSLM	DMD	PROM	SI/PLZT	M-O LIGHT MOD	RUTICON	LCLV's	DARPA
MODULATING MATERIAL	ELECTRO-OPTIC CRYSTAL (LINBO$_3$)	DEFORMABLE MEMBRANE	ELECTRO-OPTIC CRYSTAL (BSO)	PLZT	MAGNETOOPTIC CRYSTAL (GARNET)	DEFORMABLE ELASTOMER	TWISTED NEMATIC IC	—
LIGHT SENSOR	PHOTOCATHODE	Si	BSO	SI PHOTOTRANSISTOR		PHOTOCONDUCTOR AMORPHOUS SE PVK: TNF	CdS	—
CURRENT FRAME TIME (MSEC)	30 (1)	8 (.1)	10 (1-2)	(.1)	.2	5-10 (5)	20 (10)	1
STORAGE TIME	WEEKS (MONTHS)	200 MSEC (1 SEC)	SEVERAL HOURS —	— (25 SEC)	LONG	15 MSEC	15 MIN	1 SEC
MAXIMUM NUMBER OF PIXELS	(10²)² PER IN²	(128)² PER (20mm)²	(350)² PER IN²	EXPECT (1000)²	(500)² PER (5CM)²	(1800)² PER IN²		(1000)²
RESOULTION (LP/MM) (@ 50% MOD.)	2.0 (30)	9.8	25	20		10	33	
PHASE DYNAMIC RANGE (RAD)	5	2	2	3	AMP (30dB)	0.2	2	30dB
PEAK CONTRAST	100:1 (1000:1)	30:1	—	100:1 (1875:1)	50:1 (1000:1)		100:1	1000:1

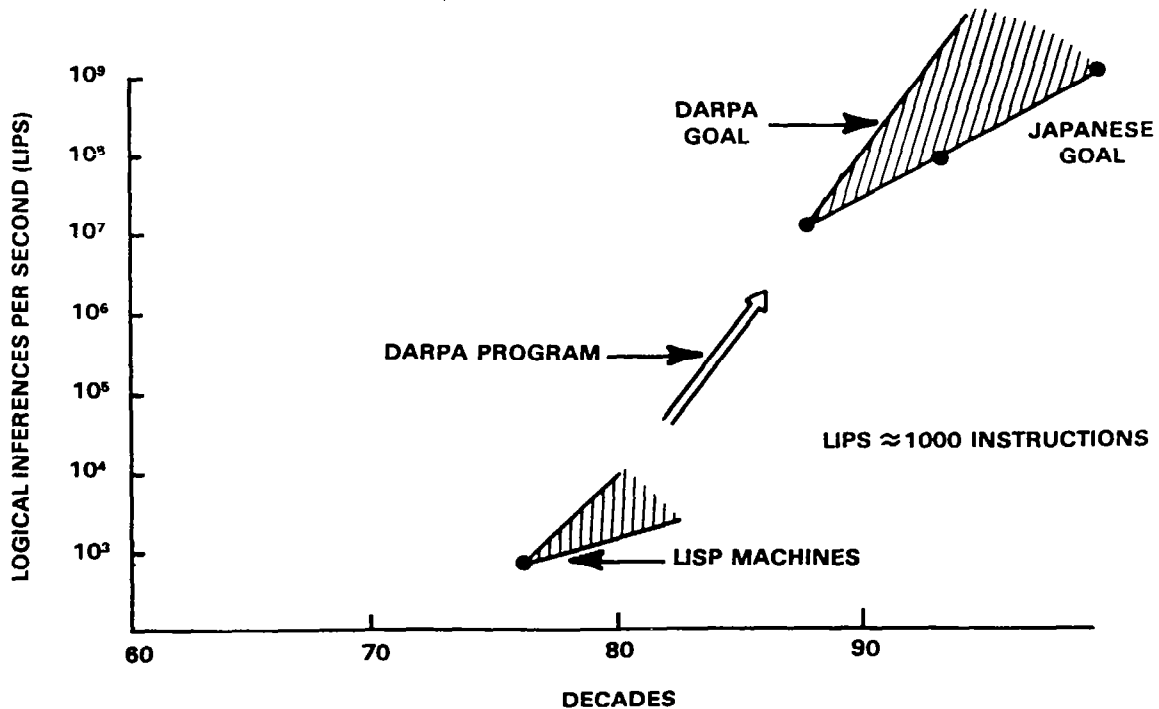Figure 7.- Comparison of SLM characteristics and DARPA goals.

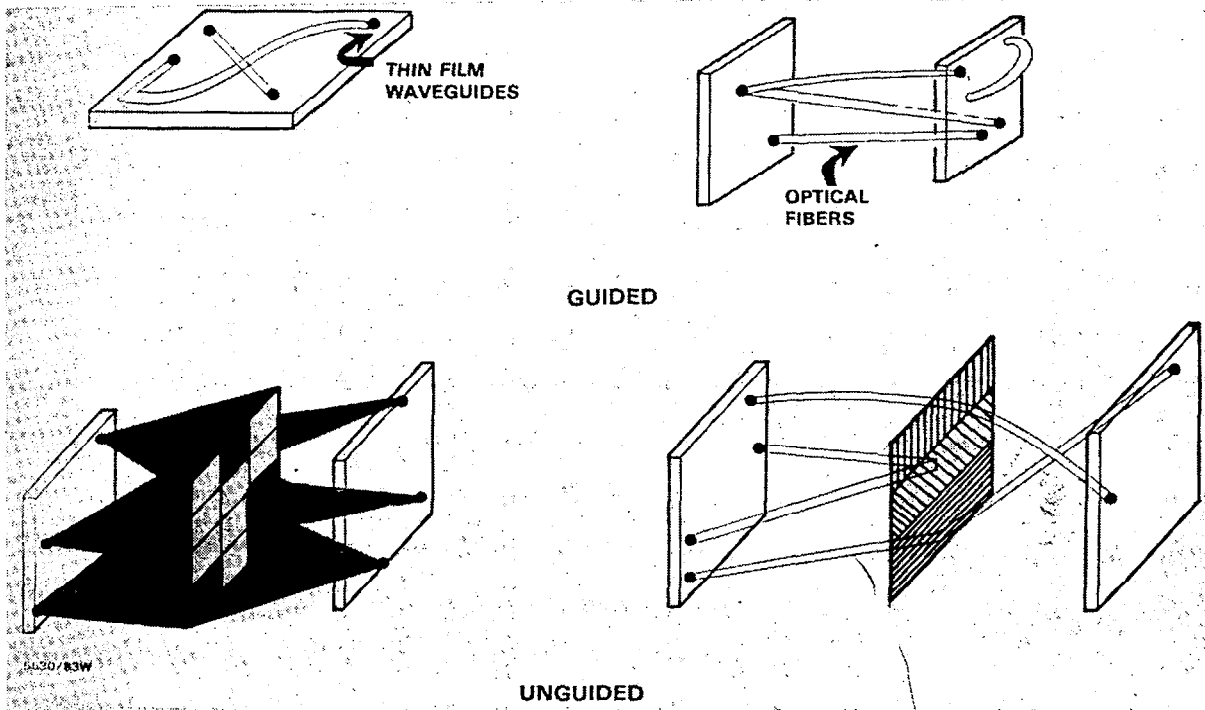Figure 8.- Supercomputer performance goals.

THIN FILM
WAVEGUIDES

OPTICAL
FIBERS

GUIDED

UNGUIDED

Figure 9.- Nonprogrammable optical interconnects for VLSI.

ELECTRONIC
ROUTING

SWITCHING

DEVICE CONTROL

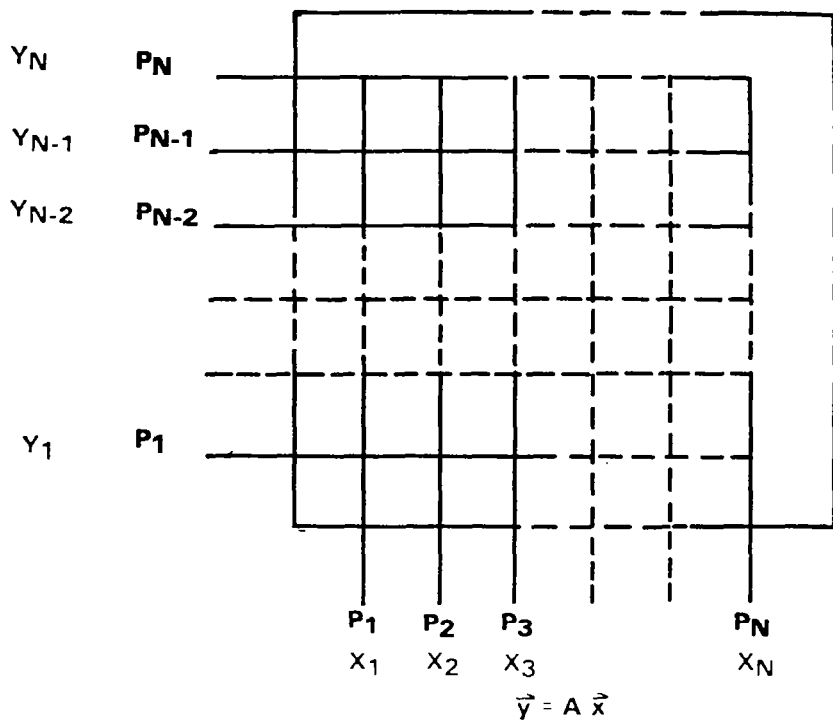Figure 10.- Laser assisted electronics.

$$\vec{y} = A \vec{x}$$

Figure 11.- Generalized crossbar.
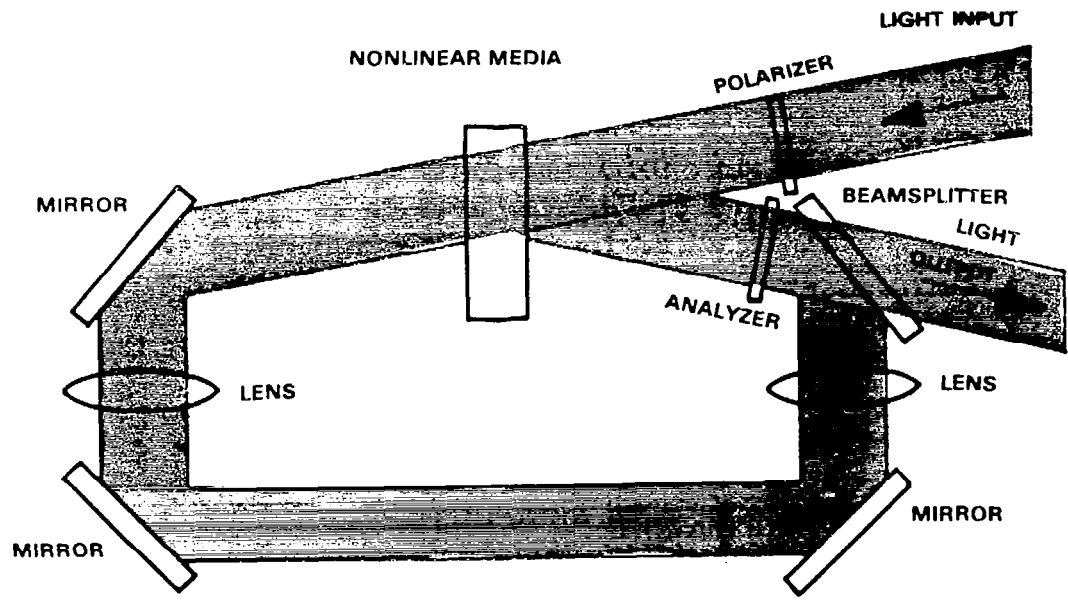
Figure 12.- Bistable switching array using external feedback.

CONVENTIONAL HOLOGRAPHY

DEGENERATE 4-WAVE MIXING
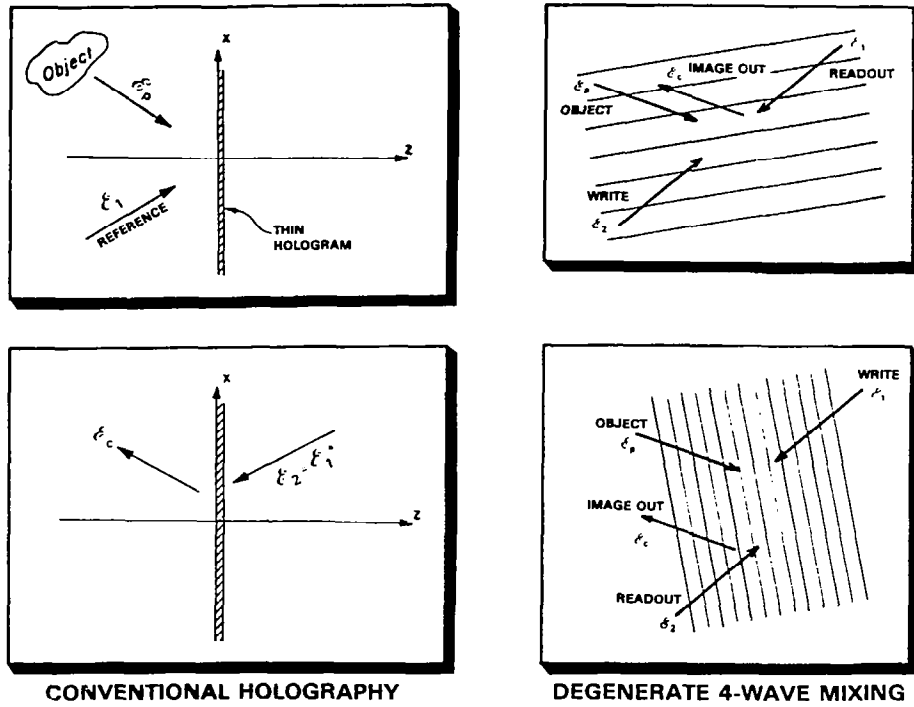
Figure 13.- Comparison of holography and degenerate 4-wave mixing.
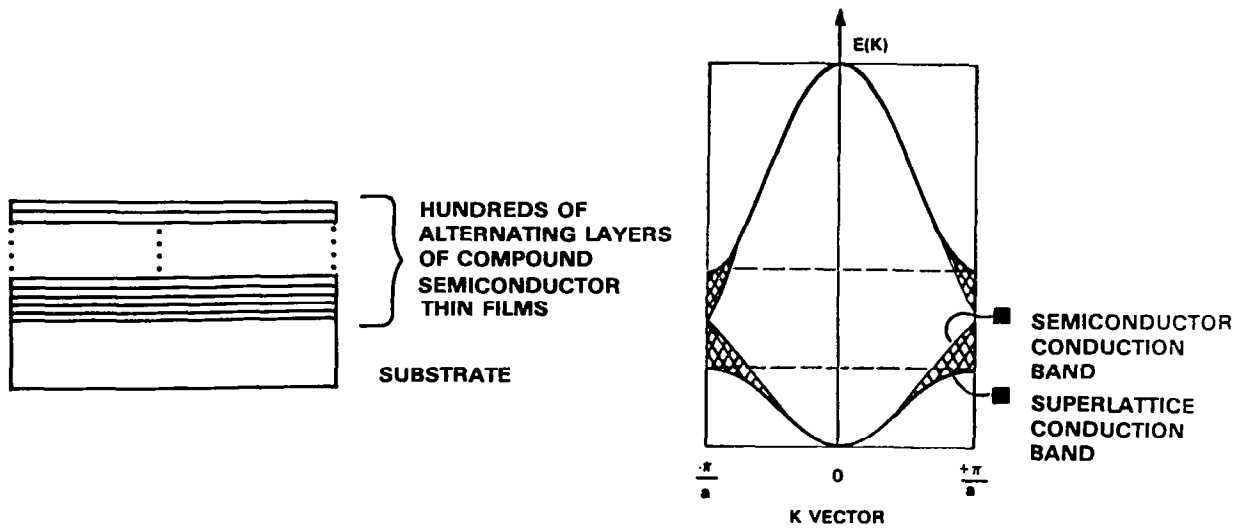
Figure 14.- Existence of nonparabolic conduction band in superlattices.
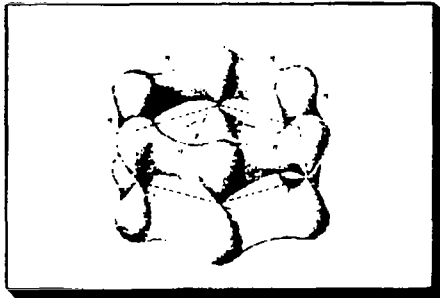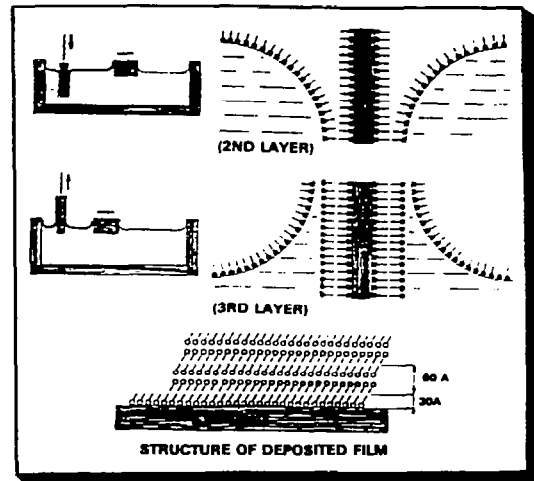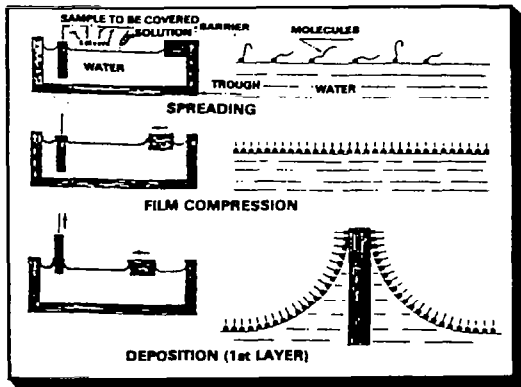
- **BUILD UP LAYER BY LAYER**
- **ACCURATELY CONTROLLED**
- **MULTILAYER STRUCTURES POSSIBLE**
- **LARGE NONLINEAR POLARIZABILITIES**

Figure 15.- Langmuir-Blodgett deposition of organic films.
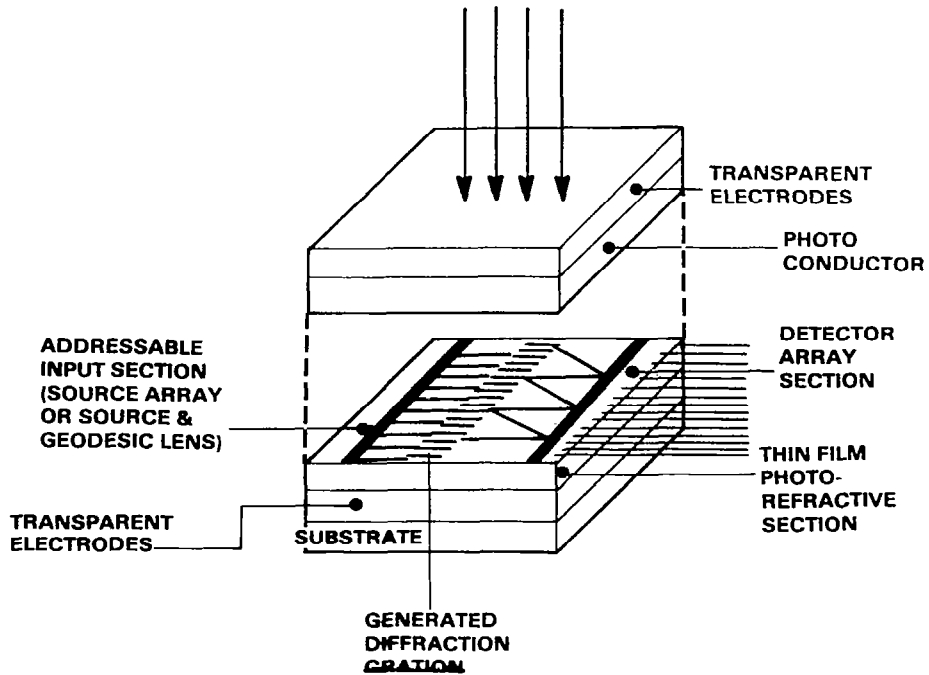
Figure 16.- Reconfigurable optical channels.

RECONFIGURABLE OPTICAL COMPUTER

DMA
DETECTOR PLANE

RAM
MEMORY PLANE
(SLM)

ADDRESSABLE
SOURCE
PLANE (LASER
OR LED ARRAY)

ADDVERSABLE
CPU
PLANE
(SLM)

SWITCHING
PLANE
(4-WAVE MEDIA)

DETECTOR
PLANE
(CCD ARRAY)

Figure 17.- Reconfigurable optical computer.

IMAGE-PLANE PROCESSING FOR IMPROVED COMPUTER VISION

F. O. Huck, C. L. Fales, and S. K. Park
NASA Langley Research Center
Hampton, Virginia

and

R. W. Samms
Information and Control Systems, Incorporated
Hampton, Virginia

SUMMARY

By properly combining optical design with image-plane processing, as suggested by the mechanism of human vision, it is possible to improve the performance of sensor-array imaging systems for edge detection and location. Two-dimensional band-pass filtering during image formation, instead of subsequent digital processing, optimizes edge enhancement and minimizes data transmission. It also permits control of the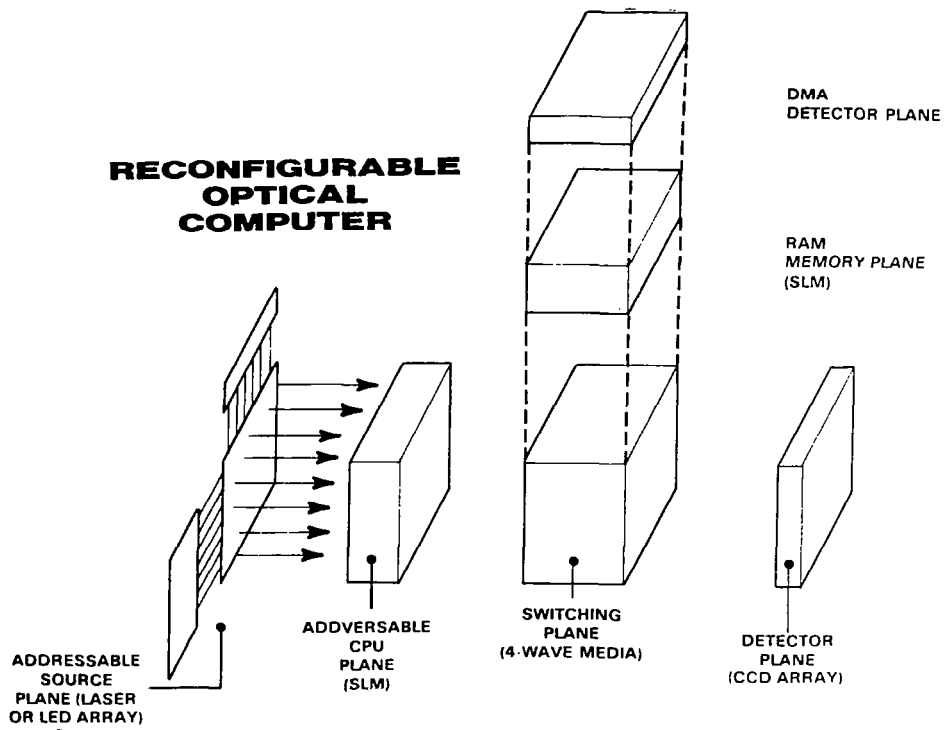 spatial imaging system response to trade-off edge enhancement for sensitivity at low light levels. Using information theory to optimize and assess performance leads to a spatial response shape close to that of human vision, and reveals that most of the information, up to about 94%, is contained in the signal intensity transitions from which the location of edges is determined for raw primal sketches. Furthermore, shading the lens transmittance to increase depth of field and using a hexagonal instead of square sensor-array lattice to decrease sensitivity to edge orientation improve edge information about 10%.

INTRODUCTION

Like human vision, most current approaches to computer, or robotic, vision include edge enhancement as an initial image processing step, i.e., they use the eye (presumably) to economically encode spatial information for the narrow dynamic range of nerve fibers,[1] and computer vision to outline shapes and surfaces for a raw primal sketch.[2] However, unlike the mechanism of human vision which performs edge enhancement during image formation, the current practice in computer vision is to perform edge enhancement by digitally processing image data after it has been acquired with conventional imaging systems, usually television cameras or sensor-array devices. Processing images during their formation (i.e., in the image plane), as in human vision, has several advantages: it improves edge enhancement by performing two-dimensional filtering prior to sampling; it minimizes the amount of data transmission and processing required for edge detection; and it permits control of the spatial response of the imaging system to trade edge enhancement for sensitivity at low light levels. The improved edge enhancement is realized because sampling introduces aliasing noise which, together with photosensor electronic noise, is often emphasized by subsequent edge enhancement.

The photoreceptors of the human eye are arranged in a roughly hexagonal pattern. Generally about 7 to 12 photoreceptors are interconnected in the retina[3] to form, together with blurring by the optical elements of the eye, a spatial

response[4,5] that is closely modeled by the difference-of-Gaussian (DOG) function.[6] Shanmugam et al.[7] have shown, for sufficiently sampled image data, that the DOG function is an optimum edge-enhancement filter in the sense that it produces maximum energy in the vicinity of the location of edges. The shape of this filter is very similar to the $\nabla^2 G$ function (where ∇^2 is the Laplacian operator $\partial^2/\partial x^2 + \partial^2/\partial y^2$ and G stands for the two-dimensional Gaussian distribution) that has been proposed by Marr and Hildreth[8] and Marr[9] as the mechanism by which the human eye detects intensity changes. Furthermore, the spatial response of the eye also appears to be sensitive to the magnitude of the incident radiance field, changing from an edge-enhancement filter at high light levels to a low-pass filter at very low light levels,[10] as illustrated in figure 1.

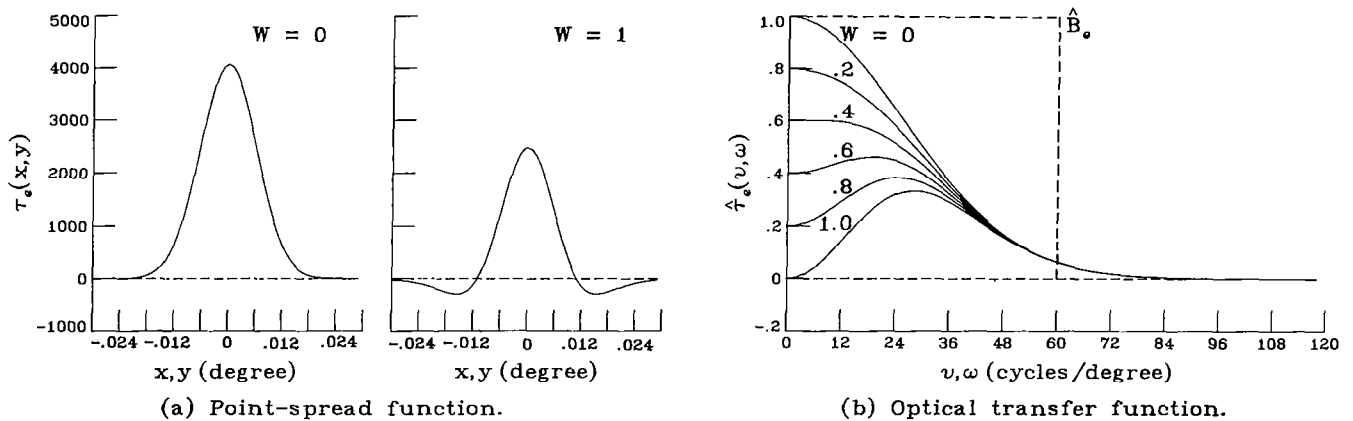
(a) Point-spread function. (b) Optical transfer function.

Figure 1.- Spatial response shape of human vision as approximated by the difference-of-Gaussian (DOG) function. Edge enhancement (W = 1) at high light levels is traded for sensitivity (W = 0) at low light levels. The parameter α = 1.6, for which the DOG (W = 1) PSF is most similar to the $\nabla^2 G$ function that has been proposed as the mechanism by which the human eye detects intensity changes:[9] the standard deviation σ = 6.3 x 10^{-3} degree, for which the OTF represents the highest of several band-pass responses of human vision based on a theoretical analysis of acuity and resolution;[9] and the effective sampling passband B_e = 60 cycles per degree is based on the mean center-to-center distance between photoreceptors of (120)$^{-1}$ degree.[11] The variables (x,y) are the rectangular (Cartesian) coordinates, and (υ,ω) are the associated spatial frequencies.

In this paper we assess the edge-enhancement, or band-pass filter, responses attainable with sensor-array imaging systems by combining high-pass filtering produced by image-plane signal processing with low-pass filtering produced by lens diffraction, lens transmittance shading, and defocus blur. The signal processing electronics permits the spatial response of the imaging system to be adjusted, approximately as illustrated in figure 1, either by a human operator or as it is in human vision, by the intensity of the radiance field.

Because the spatial response of optical apertures can never be negative, their associated spatial frequency response decreases gradually with frequency, generally without a finite cutoff (except for lens diffraction). These low-pass responses tend to blur small spatial detail and insufficiently bandlimit the radiance field prior to sampling.[12-14] Thus, even well-designed sensor-array imaging systems tend to undersample images during their formation and introduce aliasing noise. The human eye appears to minimize aliasing not only by blurring the image incident on

the eye's photoreceptors but also by slightly randomizing the basically hexagonal photoreceptor array lattice.[15] We use information theory analysis to resolve the inevitable trade-off between aliasing and blurring in favor of maximizing information acquisition. This approach would seem to be consistent with Marr's[9] emphasis on treating visual perception primarily as an information processing task. Mathematical details are omitted in this paper.

SPATIAL RESPONSE

Figure 2 illustrates the basic sensor-array imaging system concept to be analyzed. Both a square and regular hexagonal sensor-array pattern (fig. 3) will be considered, as well as optics with either a clear- or shaded-aperture transmittance.
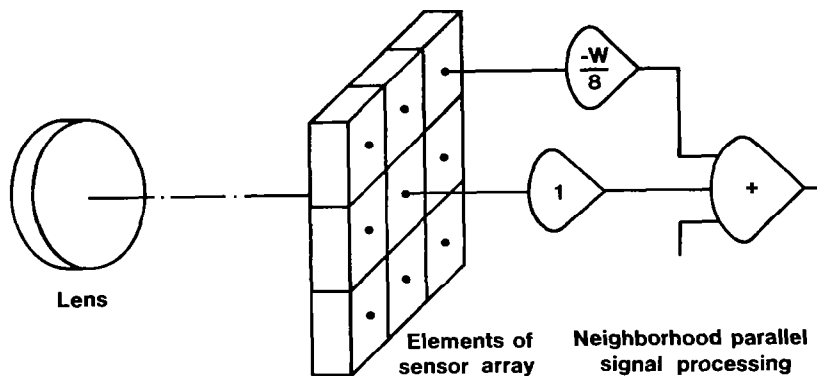

Figure 2.- Sensor-array imaging system concept for edge enhancement. The signal processing architectures can range from mostly serial to massive parallel, depending on the requirements and constraints of specific applications.

Sensor Array

Figures 4 and 5 illustrate the spatial response of the sensor-array apertures without (W = 0) and with (W = 1) image-plane processing. The areas of the square and regular hexagonal apertures and sampling passbands are equal when $\gamma_s = \sqrt{\sqrt{3}/2}$, $\gamma_r = 0.93 \gamma_r$, and $X_s = \sqrt{\sqrt{3}/2} X_r$. Furthermore, it is convenient for characterizing the spatial responses to let the aperture dimension $\gamma = \gamma_s = \sqrt{\sqrt{3}/2} \gamma_r = 1$, thereby reducing the number of units to be accounted for by one. This is equivalent to normalizing the spatial coordinates to units of γ_s.

Image-plane processing modifies the spatial response $\tau(x,y)$ by convolving it with a small mask to produce a spatial response denoted here by $\tau'(x,y)$. The response $\tau'(x,y)$ can be adjusted by the weighting parameter W. This adjustment could be controlled either by a human operator monitoring a real-time image display, or (as it is in human vision) by the intensity of the incident radiance field. In either case, a nonlinear, perhaps logarithmic, control may often be desirable. It is also conceivable that this adjustment could be
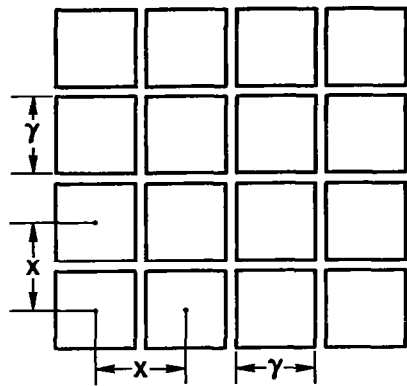
(a) Square apertures and sampling lattice.
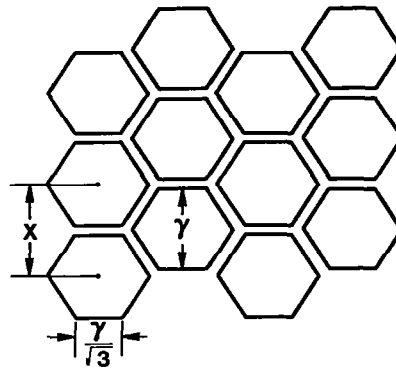
(b) Regular hexagonal apertures and sampling lattice.

Figure 3.- Sensor-array patterns. Aperture areas and sampling densities are equal when $Y_s = \sqrt{\sqrt{3}/2}$, $Y_r = 0.93\, Y_r$, and $X_s = \sqrt{\sqrt{3}/2}\, X_r$, where the subscripts s and r denote the square and regular hexagonal lattices, respectively.

Point-spread function:
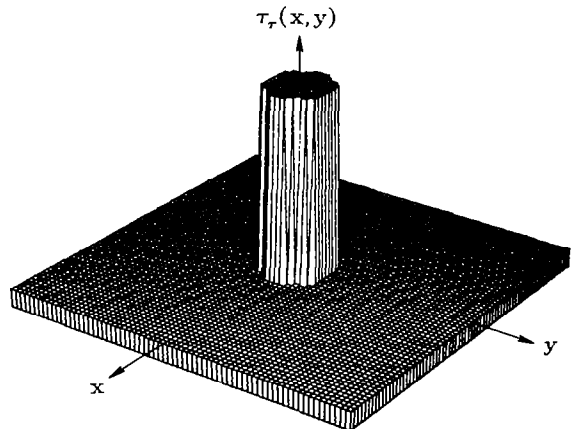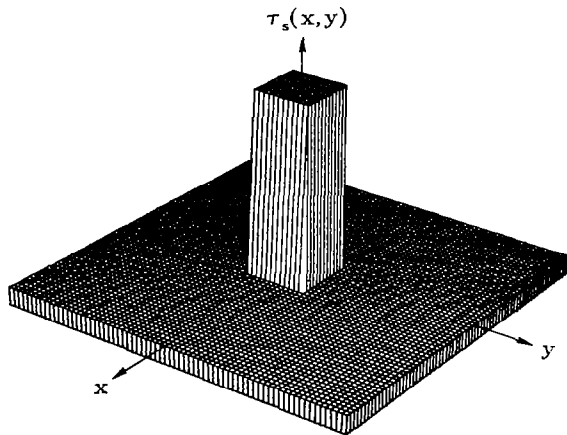
Optical transfer function:
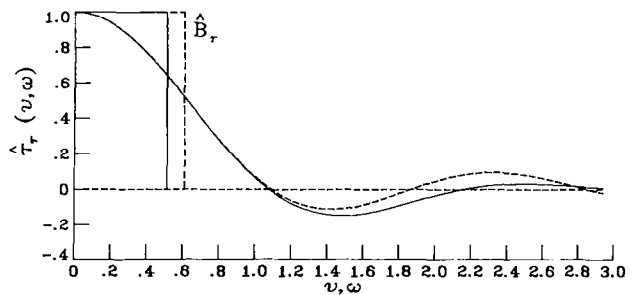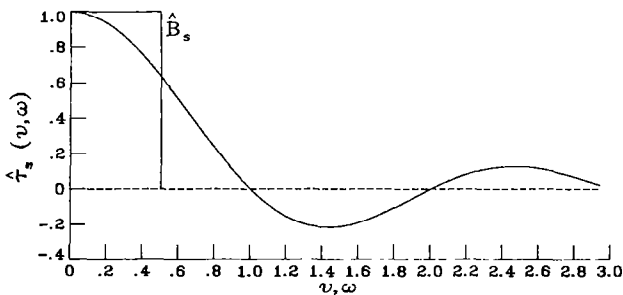
Figure 4.- Spatial response of sensor arrays with contiguous apertures (i.e., $Y = X = 1$). The aperture areas and sampling densities of the square and regular hexagonal sensor arrays are equal to each other.

Point-spread function:
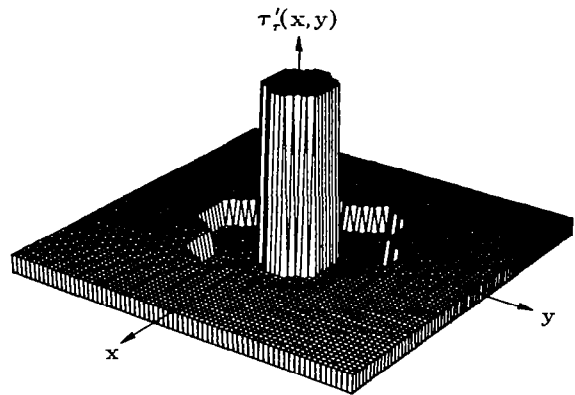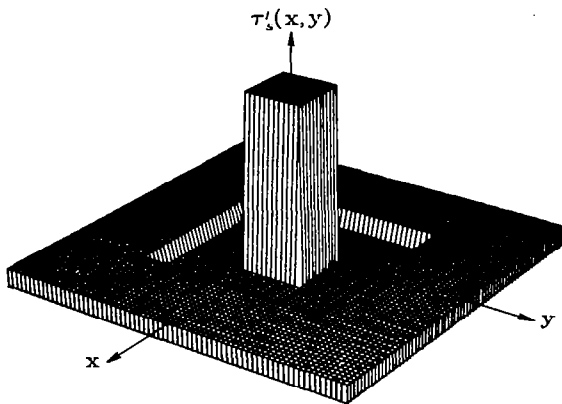
Optical transfer function:
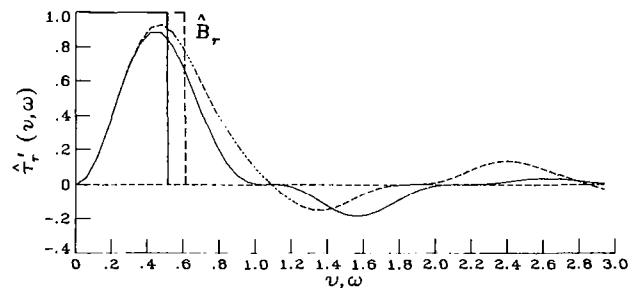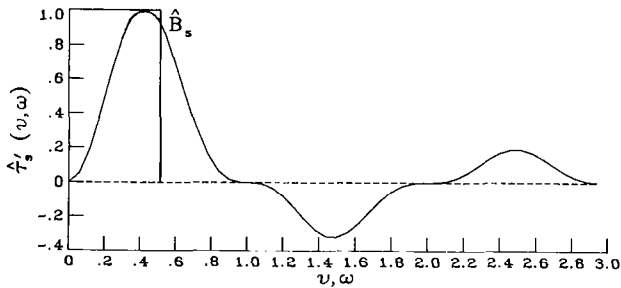
Figure 5.- Spatial response of sensor arrays with image-plane signal processing, using a neighborhood weighting W = 1. (Other characteristics are the same as in fig. 4.)

controlled by feedback from a computer vision system for autonomous scene analysis.

The undesirable spatial frequency response beyond the sampling passband can be reduced either by parallel processing of a larger number of spatially neighboring signals, or by appropriately shaping the optical transfer function (OTF) of the objective lens. The latter approach would be much more economical and is therefore investigated here.

Optics

The OTF of a defocused, diffraction-limited lens has been formulated by Hopkins[16] and Born and Wolf[17] for a clear aperture, and by Mino and Okano[18] for apertures with circularly symmetric transmittance shadings. Only one of the two shadings considered by Mino and Okano are of interest here, namely, that shading which reduces the lens transmittance from the center to the edge of the aperture, as given by $T(v,w) = 1 - (v^2 + w^2)$ for the geometrical coordinates Dv/2, Dw/2 of the lens. Figure 6 illustrates OTFs for the clear and shaded apertures. The aperture shading results in an OTF which has, compared to a clear aperture, an enhanced

response at low spatial frequencies, a suppressed response at high spatial frequencies, and, as was desired, an improved tolerance to defocus blur (i.e., an increased depth of field).

(a) Clear aperture.

(b) Shaded aperature.
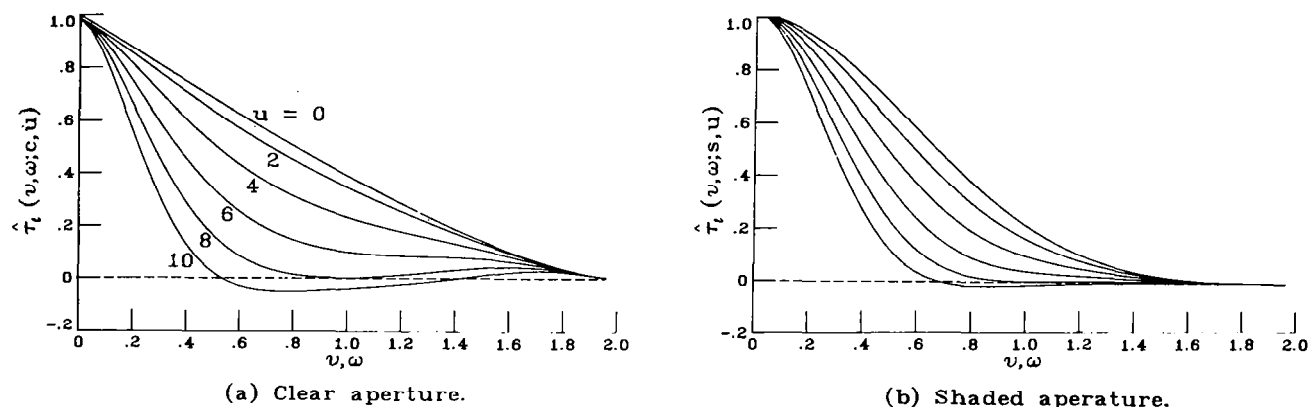
Figure 6.- Optical transfer functions of diffraction-limited lens with a coherent cutoff frequency $1/2\lambda F = 1$ and several values of defocus u.

Aperture transmittance shading, of course, reduces the amount of light transmitted to the photosensor. The ratio k of light transmitted through the shaded lens to a clear lens, or briefly the effective transmittance, is k = 0.33.

High spatial frequencies can also be suppressed by defocus blur. The defocus parameter u is

$$u \approx \frac{\pi \, \Delta \ell}{2\lambda F^2}$$

where $\Delta \ell = \left| \ell_i - \ell_p \right|$, ℓ_i and ℓ_p are the image and photosensor plane distances from the lens, respectively, $1/2\lambda F$ is the lens coherent cut-off frequency. F = f/D is the lens f-number, and f and D are the lens focal length and diameter, respectively.

Imaging System

The OTF of the imaging system is the product of the OTFs of the objective lens and the photosensor aperture (together with the effects of image-plane signal processing). Figure 7 illustrates OTFs for a somewhat arbitrarily selected lens cut-off frequency and several amounts of defocus. It may be observed that the OTF shapes obtained with image-plane processing (i.e., for W = 1) are similar to the OTF shape of the DOG function, as illustrated in figure 1, especially at spatial frequencies below peak response (i.e., $(\upsilon,\omega) < 0.4$). However, some of the system OTFs above peak response (i.e., $(\upsilon,\omega) > 0.4$) have the undesirable characteristic of

extending appreciably beyond the sampling passband (e.g.. beyond the frequency $1/2X_s = 0.5$). It is the subject of the following analysis, using information theory, to determine favorable system OTF shapes.

(a) $W = 0$.   (b) $W = 1$.
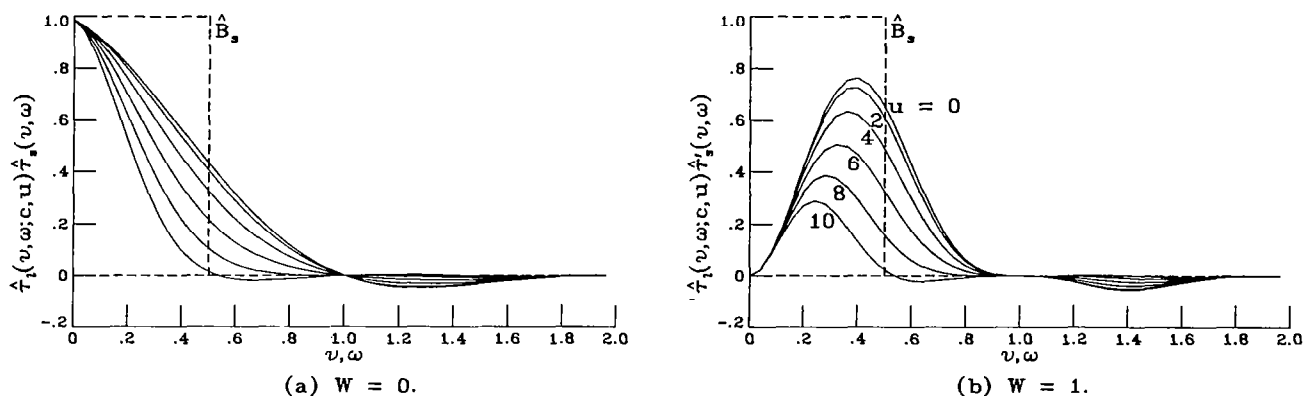
Figure 7.- Optical transfer functions and sampling passband of sensor-array imaging system with a square array of contiguous apertures (i.e., $Y = X = 1$), a clear lens with coherent cutoff frequency $1/2\lambda F = 1$, and several values of defocus u.

FIGURE OF MERIT

Since it generally is impractical to sufficiently bandlimit the radiance field prior to sampling by sensor-array mechanisms, it follows that sampled image data generally will be degraded by aliasing as well as blurring. Thus, the best one can hope to do is to shape the OTF with respect to the sampling passband so that an optimum compromise is reached between these two sources of degradation. Information theory provides an attractive approach for optimizing this trade-off because it combines the statistical properties of the radiance field with the spatial response, sensitivity, and sampling lattice of the imaging system into a single figure of merit. Formulations based on information theory are inevitably constrained by the assumption that the signal and noise amplitudes are Gaussian, ergodic, additive, and statistically independent. However, these assumptions, which are required for a rigorous derivation, lead to a robust expression that yields generally valid results for a wide range of practical conditions.

The information density (in binits per unit area) of the sampled signal is given by[14]

$$h_i = \frac{1}{2} \iint_{\hat{B}} \log_2 \left[1 + \frac{\hat{\Phi}'_L(\upsilon,\omega)\,|\hat{\tau}'(\upsilon,\omega)|^2}{\hat{\Phi}'_L(\upsilon,\omega)\,|\hat{\tau}'(\upsilon,\omega)|^2 \, *\widehat{III}(\upsilon,\omega;\, m,n\neq 0,0) + W'\left(\frac{K\sigma_L}{\sigma_N}\right)^{-2} |\hat{B}|^{-1}} \right] d\upsilon\, d\omega$$

where $\hat{B}$ is the sampling passband with area $|\hat{B}|$, $\hat{III}(\upsilon,\omega; m,n{\neq}0)$ locates the sampling sidebands, $\hat{\Phi}(\upsilon,\omega) = \sigma_L^2\hat{\Phi}_L'(\upsilon,\omega)$ is the Wiener spectrum of the radiance field with variance σ_L^2, σ_N^2 is the variance of the electronic noise, $\hat{\tau}'(\upsilon,\omega)$ is the OTF of the sensor-array imaging system with image-plane processing, $W' = 1 + W^2/8$ or $1 + W^2/6$ is a weighting parameter that accounts for the effect of image-plane processing on sensor noise for the square and hexagonal sensor array lattice respectively, and K is the steady-state gain of the conversion process of the spectral radiance into an electronic signal. The relationship between the parameters $\hat{\tau}'(\upsilon,\omega)$, W', and K is developed elsewhere.

We assume that the radiance field is both homogeneous and isotropic, and that its Wiener spectrum is modeled by the expression

$$\hat{\Phi}_L(\upsilon,\omega) = \frac{2\pi\mu_r^2\sigma_L^2}{\left[1 + (2\pi\mu_r\rho)^2\right]^{3/2}}$$

where $\rho^2 = \upsilon^2 + \omega^2$. The normalized Wiener spectrum $\hat{\Phi}_L'(\upsilon,\omega)$ is illustrated in figure 8 for several values of μ_r. The equation can be derived by assuming that the radiance field is a random set of two-dimensional pulses whose separation r obeys the Poisson probability density function with the (expected) mean separation, or spatial detail μ_r, and whose magnitude obeys the Gaussian probability density function with the (expected) variance σ_L^2.[19]
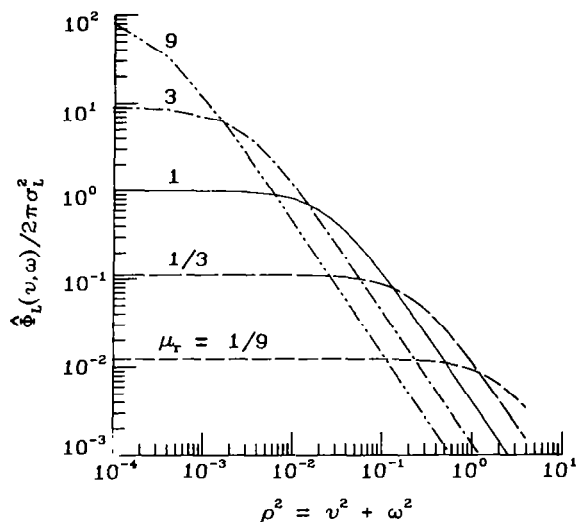
Figure 8.- Wiener spectrum of radiance field.

PERFORMANCE AND DESIGN

Without Image-Plane Processing

Figures 9 and 10 illustrate the variation of information density versus defocus and lens coherent cutoff frequency, respectively, and figure 11

illustrates the recommended relationship between realizable OTF shapes and the associated sampling passband, based on the results in figure 10.

(a) Clear-lens aperture.　　　　　　(b) Shaded-lens aperture.
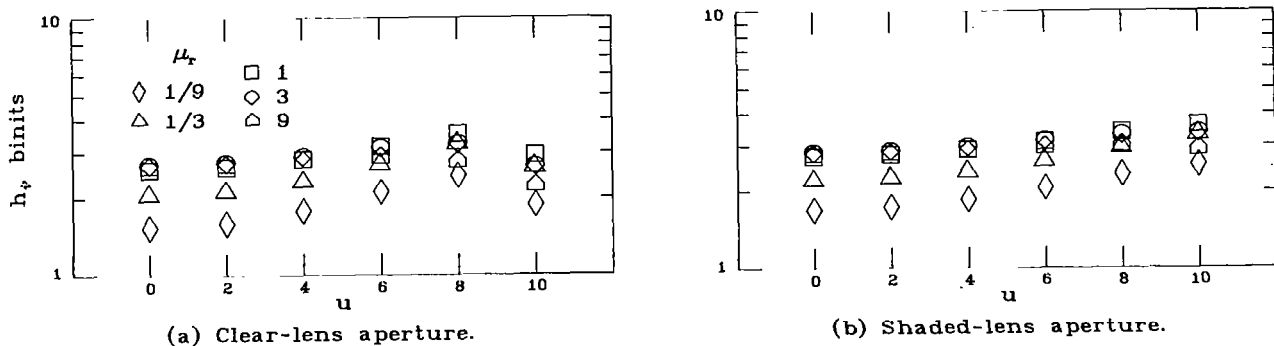
Figure 9.- Information density h_i versus defocus u for low-pass (W = 0) OTFs. Results are given for a lens with coherent cutoff frequency $1/2\lambda F = 1$, a SNR $K\sigma_L/\sigma_N = 128$, a square sensor array with contiguous apertures, and a radiance field with several mean spatial details μ_r.

(a) Clear-lens aperture.　　　　　　(b) Shaded-lens aperture.
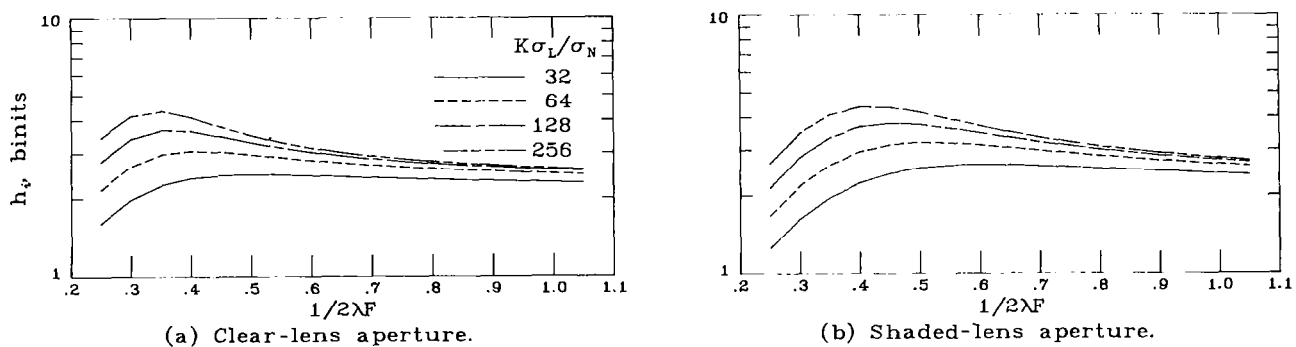
Figure 10.- Information density h_i versus lens coherent cutoff frequency $1/2\lambda F$ for low-pass (W = 0) OTFs. Results are given for several SNRs $K\sigma_L/\sigma_N$, a square sensor array with contiguous apertures, and a radiance field with mean spatial detail $\mu_r = 1$.

Information Density Versus Spatial Detail

Information density varies comparatively little with large variations in the mean spatial detail of the random radiance field. For example, variations of the mean spatial detail of nearly 2 orders of magnitude (from 1/9 to 9 times the photosensor aperture dimension) yield information density variations by less than a factor of 3. However, information density tends to be maximum when the mean spatial detail is approximately equal to or slightly larger than the photosensor aperture dimension. This result is consistent with the conditions that lead to the theoretical upper limit of information density. These conditions require that the OTF and sampling passband be matched to the Wiener spectrum of the radiance field.[13]

(a) Clear-lens aperture.   (b) Shaded-lens aperture.
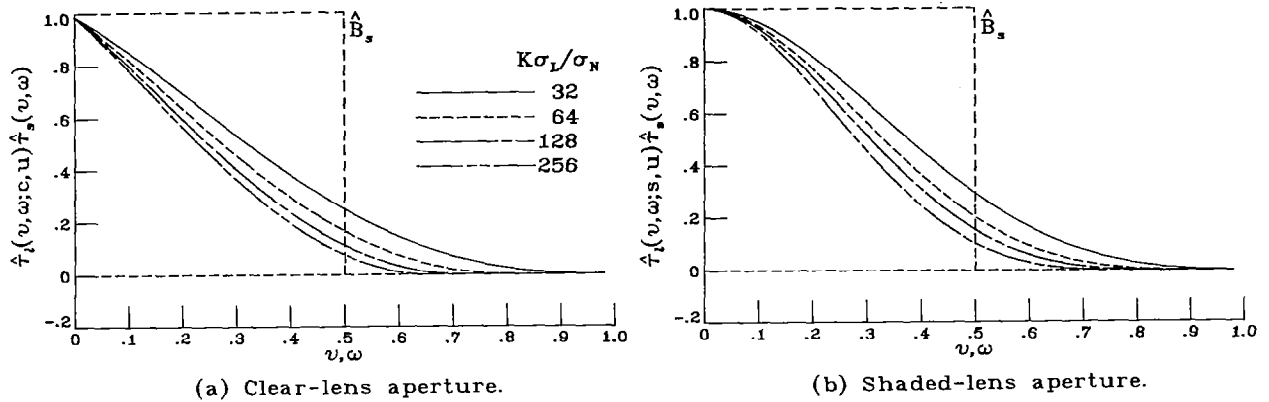
Figure 11.- Recommended relationship between realizable low-pass (W = 0) OTFs and sampling passband of sensor-array imaging systems with a square array of contiguous apertures.

Aliasing Versus Blurring

Information density, which tends to remain constant with increasing SNR for OTFs, permits appreciable aliasing, whereas information density that increases with increasing SNR for OTFs tends to suppress aliasing. These results reflect an important difference between aliasing and blurring. Whereas blurring is a source of degradation that permits the retrieval of information about all spatial frequency components for which the SNR is sufficiently high, aliasing is a source of noise that causes an irretrievable loss of information.

Thus, if it is desired to extract as much small spatial detail as possible, it becomes important to essentially limit the OTF to the sampling passband to minimize aliasing and to increase the SNR to permit the retrieval of the desired detail from the extensively blurred signal. These two objectives, to reduce the OTF cutoff frequency and to increase the SNR, are inherently contradictory. This contradiction arises because an increase in SNR is normally attained by increasing the lens aperture diameter which, for a fixed focal length and instantaneous field of view, increases (instead of decreases, as desired) the OTF cutoff frequency. The solution is to increase the lens diameter as needed to attain the desired SNR and then to defocus the optical system to reduce the OTF at the upper spatial frequencies.

Shaded Versus Clear Lens

By shading the lens aperture with a certain variable transmittance, it is possible not only to improve tolerance to defocus blur but also to increase the OTF at low spatial frequencies within the sampling passband and to decrease it at higher spatial frequencies outside the sampling passband. This leads to some improvement in information capacity, provided that a high SNR can be maintained in spite of the absorption by the lens aperture shading.

With Image-Plane Processing

Figure 12 reveals that the selection of lens, coherent cutoff frequency for maximum information density is not affected by image-plane processing. Figure 13 illustrates a favorable relationship between realizable OTF shapes and the associated sampling passband. The cutoff frequencies for the clear and shaded lens were selected so that the imaging system OTF values at the sampling passband limit would be equal to each other. Figures 14 to 16 illustrate various other performance characteristics.

(a) Clear-lens aperture.   (b) Shaded-lens aperture.
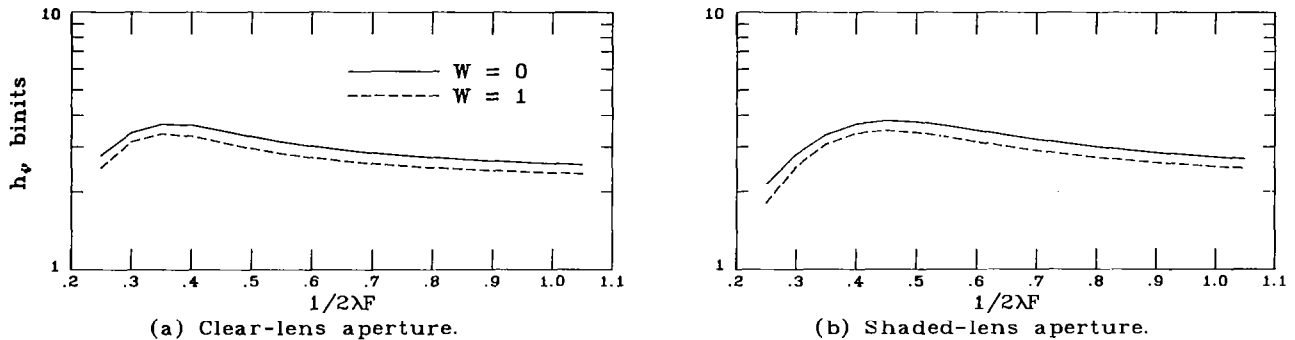
Figure 12.- Information density h_i versus lens coherent cutoff frequency $1/2\lambda F$ for low-pass (W = 0) and band-pass (W = 1) OTFs. Results are given for a SNR $K\sigma_L/\sigma_N = 128$, a square sensor array with contiguous apertures, and a radiance field with mean spatial detail $\mu_r = 1$.

Effect of Image-Plane Processing

Figure 14 characterizes the effect of image-plane processing on information density. The loss of information that occurs when only signal transitions are transmitted is small; the loss ranges from about 20% at low SNRs to only about 6% at very high SNRs. Otherwise, general performance characteristics and design guidelines are unchanged when image-plane processing is included.

Design Optimization

Figure 15 compares the performance attained with a clear-lens aperture and square sensor array to that with a shaded lens and a regular hexagonal array. the inherent advantage of lens aperture shading is the reduction of sensitivity to improper focusing; the advantage of hexagonal sampling is the reduction of sensitivity to edge orientation. Information density is improved typically about 10%. It should be noted that by changing lens cutoff frequency (and/or defocus blur), it is possible to select the SNR at which information density is most improved.
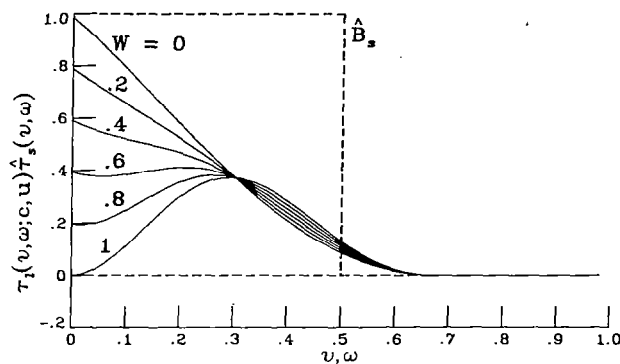
(a) Clear-lens aperture, $1/2\lambda F = 0.33$.
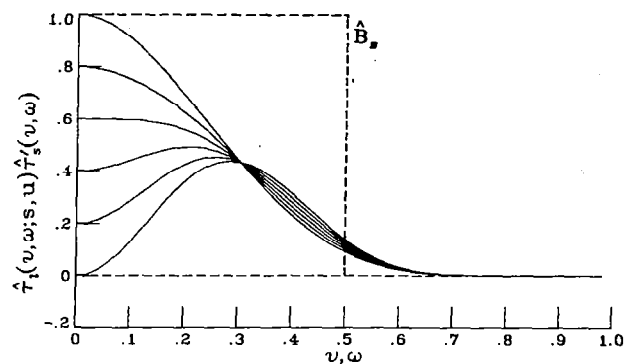
(b) Shaded-lens aperture, $1/2\lambda F = 0.41$.

Figure 13.- Spatial response of sensor-array imaging system with image-plane processing for several values of neighborhood weighting W. The curves illustrate the recommended relationship between OTFs and sampling passband for a square sensor array with contiguous apertures (i.e., $\gamma = X = 1$) and a rms SNR $K\sigma_L/\sigma_N = 128$.
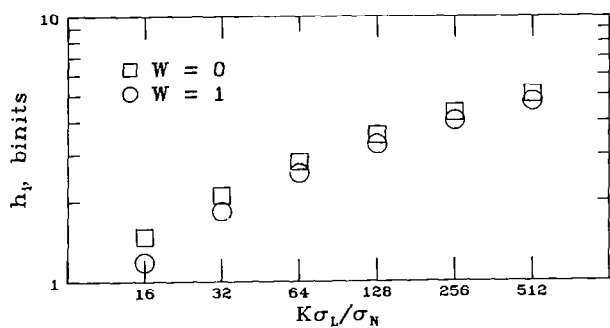
(a) Clear-lens aperture, $1/2\lambda F = 0.33$.
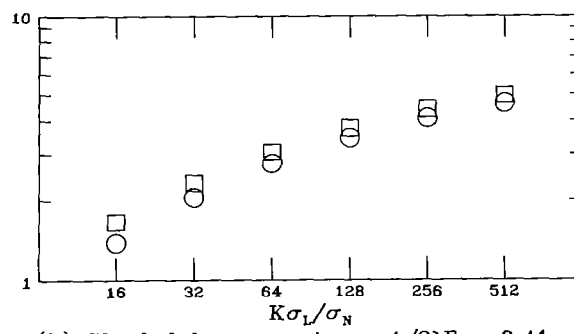
(b) Shaded-lens aperture, $1/2\lambda F = 0.41$.

Figure 14.- Information density h_j versus SNR $K\sigma_L/\sigma_N$ for low-pass (W = 0) and band-pass (W = 1) OTFs. Results are given for a lens with coherent cutoff frequency $1/2\lambda F$, a square sensor array with contiguous apertures, and a radiance field with mean spatial detail $\mu_r = 1$.

Comparison to Human Vision

According to recent models,[9,20,21] the mechanism of human vision encodes visual information in five spatial channels, also referred to as size-tuned filters or receptive field functions. The highest spatial frequency channel, according to the model by Marr,[9] corresponds to a point-spread function (PSF) which has a diameter d_0 (or W_{2-D} in his notation) of $1'2''$, or $0.022°$, between the zero crossings of the DOG function shown in figure 1. The spatial frequency ρ_m for which the corresponding OTF reaches its maximum value is $\rho_m = 27.6$ cycles per degree. The resulting spatial response shapes are shown in figure 1. The associated sampling passband is $\hat{B}_e = 60$ cycles per degree, based on the mean center-to-center distance between photoreceptors of $(120)^{-1}$ degree.[11]
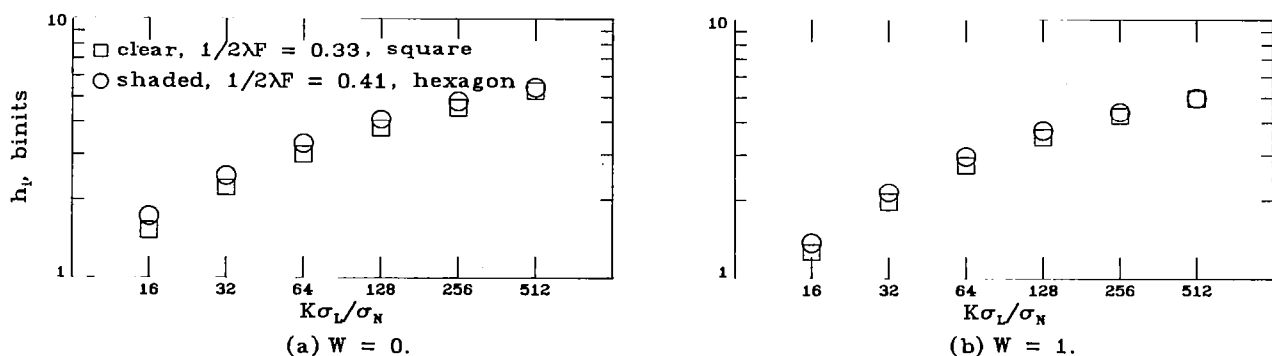
Figure 15.- Information density h_i versus SNR $K\sigma_L/\sigma_N$ for a clear lens with a square sensor array and a shaded lens with a regular hexagonal sensor array. Results are given for the conventional (W = 0) and band-pass (W = 1) OTFs, sensor arrays with contiguous apertures, and a radiance field with mean spatial detail $\mu_r = 1$.

Figure 16(a) compares the OTF of the human eye shown in figure 1 (but plotted against normalized spatial frequencies) with the OTFs shown in figure 13. It would appear from this comparison that the spatial response of the eye (i.e., its relationship to the sampling passband) permits less aliasing (at the cost of increased blurring) than the recommended responses for a SNR of $K\sigma_L/\sigma_N$ = 128. A closer fit between spatial responses can readily be obtained, as illustrated in figure 16(b), by slightly reducing the lens cutoff frequency. This response would be recommended on the basis of information theory for very high SNRs of about $K\sigma_L/\sigma_N$ = 512.

The relationship between objective lens cutoff frequency and sensor-array sampling passband is a critical design parameter. The limiting resolution (D/λ cycle/radian) set by the diameter of the eye's pupil (D, about 2.5 mm in bright light) and the wavelength of light used (λ = 0.56 μm) is D = 78 cycles/degree.[1] The coherent cutoff frequency 1/2λF, scaled by the ratio of the normalized

(a) Comparison with recommended responses for $K\sigma_L/\sigma_N$ = 128.

(b) Comparison with adjusted response.

Figure 16.- Comparison of OTF for human vision, based on a model by Marr,[9] with OTFs for sensor-array imaging system with image-plane processing and neighborhood weighting W = 1.

sampling passband $\hat{B}_s$ = 0.5 to the eye's sampling passband $\hat{B}_e$ = 60 cycles/degree, is (78/2)(0.5/60) = 0.33, close to the **shaded-lens** coherent cutoff frequency of 0.35 for which the imaging system OTF is shown in figure 16(b). Nearly the same relationship between optical **cutoff frequency and photoreceptor sampling passband** occurs in all eyes, including the simple eyes of invertebrates (in which the image is formed by reflection in a concave mirror) as well as the compound eyes of vertebrates.[1]

Despite this close agreement between the design and spatial response of the eye and of the imaging system when optimized for high sensitivity, it should be noted that we did not set out to obtain such an agreement. To do so, it would have been appropriate to start with a hexagonal array of slightly separated circular apertures to represent the photoreceptors, and with a lens transmittance shading that in its effect closely approximates the angular sensitivity of the photoreceptors (i.e., the Stiles-Crawford effect).

CONCLUDING REMARKS

Edge enhancement by digital processing of image data after it has been acquired with conventional imaging systems often emphasizes aliasing and electronic noise. Thus, processing images during their formation can be expected to improve performance as well as reduce data transmission and subsequent digital processing. The analysis in this paper has shown that:
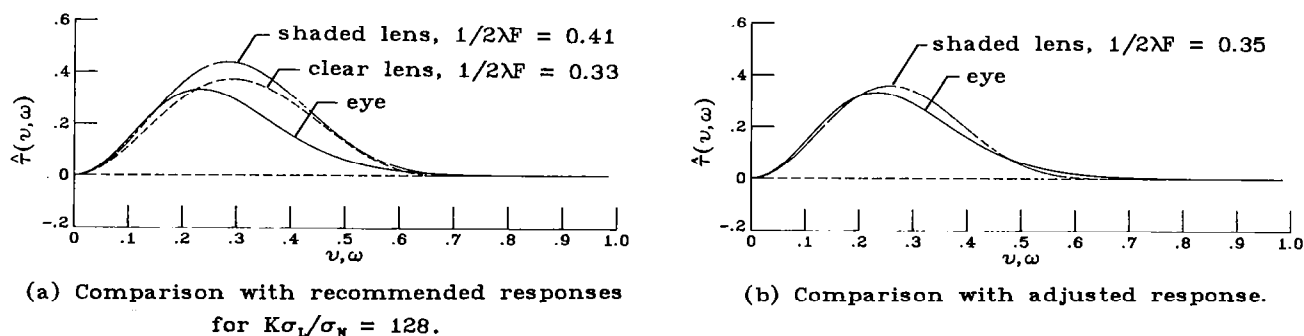
(1) the use of information theory to optimize the performance of sensor-array imaging systems with image-plane processing for edge enhancement leads to a spatial response shape close to that of human vision

(2) the design optimization tends to be independent of the statistical properties of incident radiance fields

(3) most information, up to about 94%, is contained in the signal intensity transitions (e.g., edges) rather than levels

(4) shading the lens transmittance to increase depth of field and using a hexagonal instead of square sensor-array lattice to decrease sensitivity to edge orientation improves the signal information density about 10%

The modest amount of information rejected by image-plane processing is concerned with low spatial frequency intensity levels; thus, it does not affect edge detection and location. However, the similarly modest amount of information gained by lens aperture shading and hexagonal sampling is specifically concerned with high spatial frequency intensity variations near the sampling passband limit; thus, it can be expected to improve edge detection and location for raw primal sketches.

It is reasonable to assume that the mechanism of human visual perception has been optimized by evolution within the constraints imposed by some basic biophysical limitations, and, consistent with this view, that a primary objective of this optimization for the eye has been the efficient encoding of visual information. This view is supported by the following observations:[1] (a) the dynamic range of the radiance field incident on the photoreceptors, even allowing for the changes in pupil diameter with changes in light levels, is several orders of magnitude higher than the dynamic range of the nerve fibers which transmit the

visual information from the eye to the visual cortex; (b) the attainment of high angular resolution apparently was not the major objective in the evolution of human vision since, for example, the eye of the eagle, although subject to the same biophysical constraints, has a 2 to 2.5 times higher acuity; and (c) visual processing occupies as much as 60% of the human brain, far exceeding the processing capacity of the eagle's brain. This apparent emphasis on information processing in human vision suggests that the requirement imposed on the eye to efficiently encode visual information has led to a spatial response that also happens to be optimum for edge enhancement. Thus, optimum edge enhancement and efficient encoding of visual information appear to be complementary results of a well-designed imaging system with image-plane processing.

From the point of view of efficient encoding of image data, the neighborhood image-plane processing can be regarded as a two-dimensional extension of the run length coding conventionally used for bandwidth compression when transmitting data over long distances (e.g., planetary missions[22]) and low bandwidth channels (e.g., picture transmission by facsimile over voice grade channels[23]). The advantage of two-dimensional processing, such as contour coding and algebraic picture transformation, has been recognized; however, the logic and buffer requirements for such schemes have been considered too expensive for many applications.[23] Image-plane processing may provide an opportunity for reducing these requirements by processing the signal while the imaging system stares at the scene. The buffer requirements can be completely avoided in optical-mechanical scanners and facsimile recorders by replacing their single photosensor with a 9-element square or 7-element hexagonal sensor array/neighborhood processor.

REFERENCES

1. H. B. Barlow, Proc. R. Soc. Lond., B 212, 1 (1981).

2. M. Brady, Computing Surveys, 14, No. 1, 3 (1982).

3. H. Kolb, Phil. Trans. R. Soc. Lond., B 258, 261 (1970).

4. H. R. Wilson and S. C. Giese, Vision Res., 17, 1177 (1977).

5. H. R. Wilson and J. R. Bergen, Vision Res., 19, 19 (1979).

6. M. E. Jernigan and R. W. Wardell, IEEE Transactions on Systems, Man, and Cybernetics, SMC-11, No. 6, 441 (1981).

7. K. S. Shanmugam, F. M. Dickey and J. A. Green, IEEE Trans. Pattern Anal. Mach. Intelligence, PAMI-1, No. 1, 37 (1979).

8. D. Marr and E. Hildreth, Proc. R. Soc. Lond., B 207, 187 (1980).

9. D. Marr, Vision (W. H. Freeman and Co. 1982).

10. H. B. Barlow, R. Fitzhugh and S. W. Kuffler, J. Physiol., 137, 338 (1957).

11. G. Osterberg, Acta Ophthal., Suppl. 6, 11 (1935).

12. F. O. Huck, N. Halyo and S. K. Park, Appl. Opt., 19, 2174 (1980).

13. F. O. Huck, N. Halyo and S. K. Park, Appl. Opt., 20, 1990 (1981).

14. F. O. Huck, et al., Optics and Laser Technology, 15, 21 (1983).

15. J. I. Yellott, Vision Res., 22, 1205 (1982).

16. H. H. Hopkins, Proc. Roy. Soc. (London), 231, No. 1184, 91 (1955).

17. M. Born and E. Wolf, Principles of Optics (Pergammon Press, 3rd ed., c. 1965).

18. M. Mino and Y. Okano, Appl. Opt., 10, 2219 (1971).

19. Y. Ikatura, Infrared Phys., 14, 17 (1974).

20. B. Sakitt and H. B. Barlow, Biol. Cybern., 43, 97 (1982).

21. S. Macelja, J. Opt. Soc. Am., 70, 1297 (1980).

22. R. F. Rice and J. R. Plaunt, IEEE Trans. on Comm. Techn., COM-19, 889 (1971).

23. H. Meyr, H. G. Rosdolsky and T. S. Huang, IEEE Trans. of Comm., COM-22, 826 (1974).

OPTICAL SYSTOLIC SOLUTIONS OF LINEAR ALGEBRAIC EQUATIONS[*]

Charles P. Neuman and David Casasent
Department of Electrical and Computer Engineering
Carnegie-Mellon University
Pittsburgh, PA   15213

ABSTRACT

Optical systolic array processors for performing matrix operations constitute a novel, attractive, general-purpose and flexible architecture for many linear algebraic operations and diverse engineering applications. In this paper, we review the philosophy and data encoding possible in our systolic array optical processor (SAOP). We then survey the multitude of linear algebraic operations achievable on this architecture. These operations include such linear algebraic algorithms as: matrix-decomposition, direct and indirect (iterative) solutions, implicit and explicit methods for partial differential equations, eigenvalue and eigenvector calculations, and singular value decomposition. This architecture can be utilized to realize general techniques for solving matrix linear and nonlinear algebraic equations, least mean-square error solutions (including gradient algorithms), FIR filters, and nested-loop algorithms for control engineering applications. We emphasize the data flow and pipelining of operations, design of parallel algorithms and flexible (matrix algebra) architectures, application of these architectures to computationally intensive physical problems, error source modeling (and accuracy achievable) of optical processors, and matching of the computational needs of practical engineering problems to the capabilities of optical processors.

1. INTRODUCTION

An optical matrix multiplier consists of input LED's, a two-dimensional (2-D) mask or acousto-optic cell, and output detectors [1-6]. Inclusion of electronic feedback (from the detectors to the LED's or acousto-optic cell) leads to versatile electro-optical processors which can realize a multitude of iterative algorithms for engineering applications. A fixed 2-D mask vector-matrix iterative optical processor (IOP) has been fabricated and tested in our optical computing laboratory [4]. We have applied this IOP to adaptive array processing, image deblurring and linear quadratic regulator (LQR) controller design [7-9]. Our current research is directed toward the hardware implementation of a frequency-multiplexed acousto-optic matrix-matrix systolic array optical processor (SAOP) [10]. The SAOP is an attractive general-purpose optical processor for iterative algorithms and direct matrix algorithms (such as LU and Cholesky [11-12] and QR [12] decomposition) for application to practical engineering problems in applied mechanics, control and signal processing.

Modern technology depends upon our capability to carry out substantial computations to explore the consequences of the laws of nature. Linear algebraic equations (LAE's) pervade modern technology. Natural origins of linear algebraic equations

include: the discretization of partial differential equations which are the stand-
ard mathematical models for engineering problems in applied mechanics (e.g., electro-
magnetics, fluid and heat flow, and structural design), networks (in electrical,
fluidic, mechanical, structural, and thermal systems), control engineering and signal
processing. The objective of this paper is to review the development of our systolic
array optical processor and its application to the solution of linear algebraic equa-
tions of modern technology. We introduce the phrase optical linear algebra to
connote this marriage of optical computing and linear algebra.

This paper focuses on our frequency-multiplexed acousto-optic matrix-matrix
systolic array optical processor (SAOP). The architecture of the SAOP [10] allows
enormous flexibility in data formatting, data flow and pipelining of operations, and
operations achievable. We address the optical and digital solutions to linear alge-
braic equations.

This paper is organized as follows. In Section 2, we review our iterative LAE
applications, which we presented at the First NASA Conference on Optical Information
Processing in August 1981 [7], and summarize our activities of the past two years.
Our significant progress is due, in large part, to the design and development of our
SAOP. We highlight (in Section 3) our frequency-multiplexed SAOP architecture and
indicate the flexibility and versatility of this architecture and our data encoding
schemes. In Section 4, we indicate the physical origins and structural characteris-
tics and properties of LAE's in applied mechanics, control engineering and signal
processing. We then turn to the solutions of LAE's on our SAOP.

In Section 5, we review our optical systolic direct (matrix decomposition) sol-
utions of LAE's. The final step involves the solution of a triangular system of LAE's.
We note that we can achieve this (back substitution) solution both optically and
digitally, and thus indicate the possibility of hybrid (optical and digital) direct
solutions of LAE's. In Section 6, we address iterative solutions of LAE's and summa-
rize our design approach for selecting the operational parameters of our algorithms.
We proceed (in Section 7) to apply our optical systolic direct and iterative algo-
rithms to the explicit and implicit solutions of partial differential equations. In
Section 8, we highlight our error source model and indicate its central role in the
design and development of advanced data processors. We conclude (in Section 9) with
guidelines for the development and application of optical processors.

2. OVERVIEW

In Table 1, we review the iterative LAE applications which we achieved on our
vector-matrix fixed mask IOP and highlighted at the First NASA Conference on Optical
Information Processing in August 1981 [7]. In Table 2, we summarize our activities
of the past two years and compare the LAE operations achievable on optical processors
with specific attention to our vector-matrix IOP and matrix-matrix SAOP. Since data
must be continuously fed to the acousto-optic (AO) cell, the design and development
of our flexible SAOP [10] has enabled the optical implementation of the plethora of
direct LAE solutions enumerated in Table 2. The reader is referred to the references
indicated throughout this paper for the technical details on the LAE applications and
solutions listed in Tables 1 and 2.

3. FREQUENCY-MULTIPLEXED AO SYSTOLIC PROCESSOR

The basic (space, time and frequency-multiplexed) systolic array optical processor (SAOP) is depicted schematically in Figure 1. The SAOP consists of a linear array of point modulators imaged through separate spatial regions of the AO cell and the Fourier transform of the resultant data is collected on an output linear detector array. The point modulator inputs can be time and space multiplexed and the AO cell inputs can be time and frequency-multiplexed. The SAOP can thus perform matrix-matrix multiplication, with one matrix-vector product (one column or row of a matrix-matrix product) produced in parallel every bit time T_B. The bit time T_B is the time required for the AO cell data to propagate between two spatially adjacent regions of the AO cell. The bit time T_B specifies the rate at which new data can be fed in parallel to the AO cell and to the linear point modulator input array.

We describe the operation of the SAOP through its calculation of the (3x3) matrix-matrix product

$$\underline{M}\,\underline{A} = \underline{C} \tag{1}$$

illustrated in Figure 2. We time and space multiplex the rows and columns of $\underline{M}$, and time and frequency-multiplex the rows and columns of $\underline{A}$, as depicted in Figure 2. After $3T_B$, the bottom $3T_B$ of the AO cell contains the entire $\underline{A}$ matrix. Point modulator inputs 3-5 are pulsed-on with the first row of $\underline{M}$. The first row $[c_{11}\ c_{12}\ c_{13}]$ of the matrix-matrix product $\underline{M}\,\underline{A} = \underline{C}$ is immediately produced in parallel on the output detector array. At the next T_B, the data input to the AO cell is shifted-up by T_B. We pulse-on point modulators 2-4, with the data input being the second row of the matrix $\underline{M}$ and immediately obtain the second row of $\underline{C}$ at the output of the system. This procedure is repeated until all rows of the matrix-matrix product $\underline{M}\,\underline{A} = \underline{C}$ have been produced. The data encoding scheme in Figure 2 [10] is ideally suited for matrix decomposition algorithms (highlighted in Section 5), which comprise the essential step in direct solutions [12-13] of linear algebraic equations.

In our optical linear algebra applications of this basic, yet flexible, matrix-matrix (or matrix-vector) SAOP architecture, we generally use (2N-1) LEDs and an AO cell with the time-aperture $T_A = (2N-1)T_B$. In each T_B, we form, in parallel, N vector inner products of N element vectors. Data flow and pipelining of operations is ideal in the SAOP depicted schematically in Figure 1 [10 and 12-15].

4. LINEAR ALGEBRAIC EQUATIONS (LAE's)

The model problem is to solve the system of N linear algebraic equations (LAE's)

$$\underline{A}_{[NxN]}\ \underline{x}_{[Nx1]} = \underline{b}_{[Nx1]} \tag{2}$$

for the N elements of the unknown (or solution) vector $\underline{x}_{[Nx1]}$. The physical origins of LAE's induce the structural characteristics and properties of the coefficient matrix $\underline{A}_{[NxN]}$. These attributes of physically-rooted LAE's are indicated in Table 3 and motivate the design and implementation of optical systolic parallel matrix algebra algorithms.

There are two distinct computational approaches for solving the LAE's in (2): direct algorithms and iterative (or indirect) algorithms [16]. We review our optical direct (matrix decomposition) solutions in Section 5 and our optical iterative solutions in Section 6.

5. DIRECT (MATRIX DECOMPOSITION) SOLUTIONS

Direct algorithms decompose (or factor) the coefficient matrix $A_{[NxN]}$ in (2) into the product of two (or more) matrices of special structure (such as diagonal, triangular and orthogonal) to allow subsequent rapid solutions of LAE's and easy calculation of pertinent quantities (e.g., eigenvalues and singular values). The direct solutions achievable on our SAOP include LU (Gauss elimination) and Cholesky decomposition [12] and QR decomposition [13]. Our Householder optical systolic parallel QR algorithm utilizes orthogonal transformations (which tend to be numerically stable) and computes the eigenvalues of the coefficient matrix $A_{[NxN]}$. We can thus realize matrix decomposition algorithms on our systolic acousto-optic matrix-matrix (and matrix-vector) processor through judicious data encoding in space, time and frequency.

We illustrate our direct solutions of the LAE's in (2) through our optical parallel LU decomposition algorithm which is depicted in Figures 3 and 4. The essential step is to transform the LAEs $\underline{A}\,\underline{x} = \underline{b}$ in (2) into the upper triangular system of LAEs

$$\underline{U}\,\underline{x} = \underline{b}^{*} \tag{3}$$

in which U is an upper triangular matrix. Optical parallel LU decomposition is thus equivalent to Gauss elimination. We then perform the back substitution in (3) to compute the solution vector $\underline{x}$ on our (vector inner product) SAOP or a dedicated electronic (vector inner product) processor [11].

In our optical systolic LU decomposition (Gauss elimination) algorithm [12], we operate simultaneously on both the coefficient matrix $\underline{A} = A_{[NxN]}$ and right-hand side vector $\underline{b} = \underline{b}_{[Nx1]}$ in (2). We compute directly (in Figure 3) the upper-triangular coefficient matrix $\underline{U}$ and transformed right-hand side vector $\underline{b}^{*}$ in (3) according to

$$[\underline{U} \mid \underline{b}^{*}] = \underline{M}_{(N-1)}\underline{M}_{(N-2)} \cdots \underline{M}_2\underline{M}_1 \; [\underline{A} \mid \underline{b}]$$

where the $\underline{M}_k$, for $k=1,2,\ldots,$ $(N-1)$, is a sequence of $(N-1)$ decomposition matrices [17].

The system of LAE's in (2) specifies the initialization $\underline{A}_0 = \underline{A}$ and $\underline{b}_0 = \underline{b}$ for our optical systolic LU decomposition algorithm. In each of the $(N-1)$ steps of our algorithm, we multiply the pair $[\underline{A}_{k-1} \mid \underline{b}_{k-1}]$ by the k-th decomposition matrix $\underline{M}_k$ and feedback immediately the product $[\underline{A}_k = \underline{M}_k\,\underline{A}_{k-1} \mid \underline{b}_k = \underline{M}_k\,\underline{b}_{k-1}]$ from the output detectors to the acousto-optic (AO) cell, as illustrated in Figure 3. The k-th step triangularizes the k-th column of $\underline{M}_k\,\underline{A}_{k-1}$, without affecting the triangular structure of the first (k-1) columns. After k steps of our optical systolic LU decomposition algorithm, we transform the coefficient matrix $\underline{A}$ in (2) into the partial triangular structure shown in (4) below, in which an asterisk (*) signifies a non-zero element:

$$\underline{A}_k =$$

	Full Matrix	k Rows

⊙ * * * *
  * * *
  * *
  *		

	Full Matrix	(N-k) Rows

k Columns (N-k) Columns

(4)

After (N-1) steps, we thus transform (2) into the upper triangular system of LAE's in (3) and compute the solution vector $\underline{x}$ by back substitution. We can therefore realize direct solutions of LAEs in a <u>fixed</u> finite number of steps on our matrix-matrix SAOP.

In our optical systolic parallel matrix decomposition algorithms, we operate <u>simultaneously</u> on both the coefficient matrix $\underline{A}_{[NxN]}$ (column-wise in LU decomposition and row-wise in QR decomposition) and the right-hand side vector $\underline{b}_{[Nx1]}$ in (2). We showed in Section 3 and illustrated in Figures 3 and 4 that the data flow and pipelining of operations in optical systolic parallel direct (and indirect [15]) algorithms are attractive. In each bit time T_B, one time-slot of data leaves the AO cell and the next time-slot of data is entered into the AO cell. When the aperture time T_A of the AO cell is matched to the physical problem, we find that the parallel output detected data can be processed and fed-back immediately to the AO cell input. In the realization of all of our algorithms [15], the output data are fedback immediately into the SAOP as they are produced.

Implementation of our optical systolic parallel matrix decomposition algorithms on the SAOP requires 2N LED's and N frequencies and detectors [12-13]. The total time is proportional to N^2 (where N is the number of LAE's) because the SAOP (in Section 3) computes N vector inner products in parallel (in each bit time T_B). The time reduction is thus from $O(N^3)$ in serial processors to $O(N^2)$ in parallel processors.

We conclude our review of direct algorithms by noting that the singular value decomposition (SVD) of the matrix $\underline{A}$ can also be achieved on our SAOP [18]. SVD arises naturally in principal component analysis of pattern recognition, least mean-squared (LMS) error data analysis, and rank determination of matrices. The singular value decomposition of the rectangular matrix $\underline{A}_{[NxM]}$ is

$$\underline{U}^T \underline{A} \underline{V} = \begin{bmatrix} \underline{\Lambda} \\ \underline{0} \end{bmatrix} = \begin{bmatrix} \underline{\Lambda} & \underline{0} \end{bmatrix} \qquad (5)$$

$$\underbrace{}_{N \geq M} \qquad \underbrace{}_{M \geq N}$$

where:

    $\underline{U}$ = (NxN) orthogonal matrix (columns are <u>left</u>-singular vectors or <u>principal components</u> of $\underline{A}$);

    $\underline{V}$ = (MxM) orthogonal matrix (columns are <u>right</u>-singular vectors of $\underline{A}$);

and

    $\underline{\Lambda}$ = (IxI) diagonal matrix <u>DIAGONAL</u> $[\lambda_1 \quad \lambda_2 \quad \ldots \quad \lambda_I]$ in which

        $\lambda_1 \geq \lambda_2 \geq \ldots \geq \lambda_I \geq 0$ are the <u>singular</u> values of $\underline{A}$ and I = Minimum (M,N).

We thereby add SVD to our repertoire of optical linear algebra operations achievable on our SAOP.

6. ITERATIVE SOLUTIONS

Iterative solutions of LAE's emerge from the additive splitting of the coefficient matrix $\underline{A}$ in (2) into [19]

$$\underline{A} = \underline{D} + \underline{L} + \underline{U} \tag{6}$$

in which $\underline{D}$ is diagonal (and non-singular), $\underline{L}$ is lower triangular and $\underline{U}$ is upper triangular [7]. The additive splitting of $\underline{A}$ leads to a multitude of flexible algorithms and processors for solving the LAE's in (2). The celebrated prototypal iterative solutions are the Jacobi, Gauss-Seidel and successive overrelaxation (SOR) algorithms for elliptic partial differential equations (Table 1). When the matrix $\underline{A}$ is stable (that is, when all of the eigenvalues of $\underline{A}$ lie strictly in the open left-half plane), we prefer the iterative Richardson algorithm [4,6,7,10,15,19]:

$$\underline{x}(j+1) = \underline{x}(j) - \omega \underline{A} \underline{x}(j) + \omega \underline{b} \qquad \text{for } j = 0,1,2\ldots \tag{7}$$

In (7), j is the iteration index (or time step) and ω is the acceleration parameter. We select the acceleration parameter $\omega = -1/\lambda_{max}(\underline{A})$, where $\lambda_{max}(\underline{A})$ is the largest eigenvalue (in absolute value) of $\underline{A}$, to insure the stability and convergence of our Richardson algorithm [4,7,15]. In [10], we described our realization of the iterative Richardson algorithm on the basic optical matrix-vector multiplier in Figure 1. When the matrix $\underline{A}$, vector $\underline{b}$ and acceleration parameter ω in (7) are time-varying (i.e., when $\underline{A} = \underline{A}(j)$, $\underline{b} = \underline{b}(j)$ and $\omega = \omega(j)$), our iterative Richardson algorithm in (7) becomes [7]

$$\underline{x}(j+1) = \underline{x}(j) - \omega(j) \underline{A}(j) \underline{x}(j) + \omega(j)\underline{b}(j) \tag{8}$$

which encompasses the stochastic (time-varying) gradient-following algorithms of adaptive filtering and signal processing [20]. We can thus implement iterative solutions of LAEs on our matrix-vector SAOP and realize gradient algorithms for signal processing and control engineering applications.

In contrast to direct solutions (which we realize in a fixed number of steps on our matrix-matrix SAOP), iterative solutions require many (an unknown number) steps on our matrix-vector SAOP (or any processor). Implementation of iterative algorithms requires careful selection of the operational parameters of the algorithm (such as the number of iterations in the iterative Richardson algorithm).

In our design of feedback regulators for the F100 turbofan engine, we developed a philosophy for operational parameter selection in iterative algorithms [8-9,21-23]. We summarize and apply our philosophy in the sequel to specify the fixed number of iterations in the iterative Richardson algorithm in (7).

The four salient steps of our operational parameter selection philosophy are:

(i)   Combine deterministic engineering analysis and digital simulation (in contrast to formal mathematical analysis which is valid "in-the-limit").

(ii) Develop analytical models (tight upper bounds) for the computational errors to characterize the convergence of the algorithm.

(iii) Apply the analytical models to interpret the digital simulation results and formulate practical engineering guidelines for operational parameter selection.

(iv) Apply the guidelines to evaluate (in digital simulation) the performance of the algorithm and processor in the presence of error sources and noise (Section 8).

To illustrate our operational parameter selection philosophy, we return to our iterative Richardson algorithm in (7). We define the computational error vector $\underline{e}(j)$ at the j-th iteration as the difference between the computed solution $\underline{x}(j)$ at the j-th iteration and the exact solution $\underline{x}^* = \underline{A}^{-1}\underline{b}$ of the LAEs in (2). The error vector

$$\underline{e}(j) = \underline{x}(j) - \underline{x}^* \tag{9}$$

thus evolves according to

$$\underline{e}(j+1) = [\underline{I} - \omega\underline{A}]\underline{e}(j) \tag{10}$$

where ω is the acceleration parameter in (7). After j iterations of the Richardson algorithm, the computational error is

$$\underline{e}(j) = [\underline{I} - \omega\underline{A}]^j \underline{e}(o) \tag{11}$$

where $\underline{e}(o)$ is the initialization error.

Specification of the fixed number of iterations for the Richardson algorithm requires a tight upper bound for the norm of the computational error in (11). The classical upper bound is

$$||\underline{e}(j)|| \leq ||[\underline{I} - \omega\underline{A}]||^j ||\underline{e}(o)|| \tag{12}$$

Our digital simulations [23] have led us to estimate the norm $||\underline{I} - \omega\underline{A}||$ by the spectral radius (i.e., largest eigenvalue (in absolute value)) of $[\underline{I} - \omega\underline{A}]$. The spectral radius of $[\underline{I} - \omega\underline{A}]$ is $[1-1/C(\underline{A})]$, where $C(\underline{A}) = \lambda_{max}(\underline{A})/\lambda_{min}(\underline{A})$ is the condition number of the coefficient matrix $\underline{A}$; i.e., the ratio of the largest eigenvalue (in absolute value) $\lambda_{max}(\underline{A})$ to the smallest eigenvalue (in absolute value) $\lambda_{min}(\underline{A})$ of $\underline{A}$. We thereby replace the norm of the matrix $[\underline{I} - \omega\underline{A}]$ in the classical upper bound in (12) by its spectral radius $[1-1/C(\underline{A})]$ to obtain our analytical model of the Richardson algorithm

$$||\underline{e}(j)|| \leq [1-1/C(\underline{A})]^j ||\underline{e}(o)|| \overset{\sim}{=} \exp[-j/C(\underline{A})]||\underline{e}(o)|| \tag{13}$$

Our analytical model in (13) indicates that the performance of the Richardson algorithm (for a fixed number of iterations) is governed completely by the condition number $C(\underline{A})$ of the coefficient matrix $\underline{A}$. Our digital simulations of the Richardson algorithm and its application to our nested Kleinman-Richardson algorithm for linear-quadratic regulator (LQR) design [8-9,21-23] indicates that a practical choice of the fixed number of iterations J is J = 1.5 $C(\underline{A})$ to 3 $C(\underline{A})$. Our digital simulations confirm that this fixed number of iterations remains a viable guideline in the presence of optical processor error sources and noise [21-23]. We have thus created a framework in which to develop and evaluate algorithms and optical processors for the iterative solution of linear algebraic equations.

7. PARTIAL DIFFERENTIAL EQUATIONS

Discretization of partial differential equations (which are the standard mathematical models for distributed systems in applied mechanics) leads to the formulation of systems of LAE's. The natural evolution from physical problems in distributed parameter systems to (steady-state and time-dependent) partial differential equations through discretization to LAE solutions is depicted in Figure 5.

Finite difference and finite element approximations of partial differential equations create finite systems of LAE's [16,24]. Finite differences discretize the continuous domain. We replace the continuum by a finite set of points (mesh or grid) and the partial derivatives by differences. The values of the approximate solution are then computed only at the grid points. Finite elements discretize the solution space. We approximate the solution by a finite linear combination of known (or assumed) basis functions (i.e., finite elements) and apply a weighted residual method (such as collocation, Galerkin or least-squares). We then compute the linear combination constants. Finite elements are functions which are zero except on a small part of the physical problem domain. Examples include piecewise polynomials and splines. The physical problem and (finite difference and finite element) approximation of the physical problem create the pattern and structure of the coefficient matrix $\underline{A}$ of the LAE's in (2).

The flow diagram in Figure 5 depicts the emergence of LAE's from partial differential equations (PDE's). Discretization of steady-state (e.g., elliptic) PDE's leads directly to LAE's (Section 4) which can be solved on our SAOP by direct algorithms (Section 5) or iterative algorithms (Section 6). Rice [16] notes the following advantages of finite elements over finite differences for elliptic PDEs: Finite elements have more flexible applicability (because finite differences are sensitive to the spatial domain), are more accurate and give rise to a smaller number of LAE's. What is noteworthy is that the gain in accuracy (in applying finite elements) more than offsets the increased computational effort in setting-up (which must be performed only once) and subsequent solutions of the resultant system of LAE's.

Discretization of time-dependent PDEs leads to explicit and implicit methods [13]. We illustrate these methods through the non-dimensional diffusion equation [24]

$$u_t = u_{xx} \tag{14}$$

If we apply forward differencing in time (t) and central differencing in space (x), we obtain the forward marching explicit algorithm

$$[\underline{U}(\text{All Space})]_{t+1} = \underline{M}[\underline{U}(\text{All Space})]_t \tag{15}$$

We thus compute (on our SAOP in Figure 1) the solution u of (14) at the next time point (t+1) for all spatial points (x) through the matrix-vector multiplication of the coefficient matrix $\underline{M}$ and the solution vector at the current time point (t). The regular structure of $\underline{M}$ emerges from the diffusion equation in (14) and the finite difference algorithm. Explicit methods are thus characterized by repeated matrix-vector multiplication (Section 2), rather than solutions of linear algebraic equations.

If we implement the implicit Crank-Nicolson algorithm (i.e., apply forward differencing in time and the trapezoidal approximation in space), we obtain a (banded triangular [6-7]) system of LAE's. We then proceed to solve these LAE's on our SAOP

(in Figure 1) by direct algorithms (Section 5), iterative algorithms (Section 6), or special purpose optical deconvolver architectures [6]. Implicit algorithms thus lead to solutions of LAE's. We can thereby achieve the explicit and implicit solutions of (finite difference and finite element) partial differential equations on our flexible and versatile SAOP.

8. ERROR SOURCE MODELING

Error source modeling is a central step in the design of algorithms and architectures for optical processors. In [15], we advanced the first error source model for an optical systolic array processor. Our model indicates that the actual observed output $\hat{C}$ of the matrix-matrix product $\underline{MA} = \underline{C}$ in (1) is

$$\hat{\underline{C}} = \left\{ \begin{array}{l} \text{Detector} \\ \text{Spatial} \\ \text{Errors} \end{array} \right\} * \left\{ \begin{array}{l} \text{AO Cell} \\ \text{Frequency} \\ \text{Response} \end{array} \right\} * \left\{ \begin{array}{l} \text{Data} \\ \text{Matrix} \\ \underline{A} \end{array} \right\} * \left\{ \begin{array}{l} \text{LED} \\ \text{Spatial} \\ \text{Errors} \end{array} \right\} * \left\{ \begin{array}{l} \text{AO Cell} \\ \text{Attenuation} \end{array} \right\} * \left\{ \begin{array}{l} \text{Data} \\ \text{Matrix} \\ \underline{M} \end{array} \right\}$$

(16)

$$+ \text{ Detector Dark Current } + \text{ (Time-Varying) Detector Noise.}$$

Our multiplicative error source model in (16) is thus specified by the cascade of the AO cell attenuation, input (LED and AO cell) spatial errors, AO frequency response and output (detector) spatial errors.

In [15], we applied our error source model, along with digital simulation, to evaluate the performance of direct and indirect solutions of LAE's on our SAOP. In these initial studies, we found that AO cell acoustic attenuation is the dominant error source in our SAOP and that a direct solution is less sensitive to such optical system error sources than is an indirect solution.

9. CONCLUDING REMARKS AND GUIDELINES

In this paper, we reviewed the application of our frequency-multiplexed SAOP to the solution of linear algebraic equations arising in modern technology. We noted that the versatility of our systolic array optical architecture and the flexibility of our data encoding schemes can be utilized to achieve a multitude of optical linear algebra operations required in applied mechanics, control engineering and signal processing.

We have reviewed the central issues of systolic array optical processors:

(i)   Data flow and pipelining of operations;

(ii) Design of parallel algorithms;

(iii) Design of flexible (matrix algebra) architectures;

(iv) Application of optical processors to computationally intensive $O(N^3)$ physical problems (e.g., Kalman filtering [10]); and

(v)   Error source modeling and accuracy achievable on optical processors.

The engineering trade-off is the selection between direct and indirect solutions. In our optical systolic <u>direct</u> solutions (Section 5), we operate simultaneously on the coefficient matrix $\underline{A}$ and right-hand side vector $\underline{b}$ in (2) to produce the upper triangular system of LAE's in (3). Iterative solutions (Section 6) require careful selection of the <u>operational parameters</u> of the algorithm (including the initialization, choice of the acceleration parameter and specification of the number of iterations).

The solution depends upon the physical problem, dynamic (changing) characteristics of the matrix $\underline{A}$, speed requirements of the physical problem, speed available in the optical processor, solution accuracy required and the errors in the processor. Physical problems lead to different coefficient matrices and systems of linear algebraic equations --- with different properties and structures.

REFERENCES

[1]   M. Monahan, K. Bromley and R. Bocker, "Incoherent Optical Correlators," <u>Proceedings of the IEEE</u>, <u>65</u> (1), pp. 121-129, January 1977.

[2]   J. W. Goodman, A. Dias and L. Woody, "Full Parallel, High-Speed Incoherent Optical Method for Performing Discrete Fourier Transforms," <u>Optics Letters</u>, <u>2</u>(1), pp. 1-3, January 1978.

[3]   D. Psaltis, D. Casasent and M. Carlotto, "Iterative Color-Multiplexed Electro-Optical Processor," <u>Optics Letters</u>, <u>4</u>(11), pp. 348-350, November 1979.

[4]   M. Carlotto and D. Casasent, "Microprocessor-Based Fiber-Optic Iterative Optical Processor," <u>Applied Optics</u>, <u>21</u>(1), pp. 147-152, January 1982.

[5]   H. J. Caulfield, et al., "Optical Implementation of Systolic Array Processing," <u>Optics Communications</u>, <u>40</u>(2), pp. 86-90, December 1981.

[6]   D. Casasent, "Acousto-Optic Transducers in Iterative Optical Vector-Matrix Processors," <u>Applied Optics</u>, <u>21</u>(10), pp. 1859-1865, May 1982.

[7]   D. Casasent and C. P. Neuman, "An Iterative Optical Processor: Selective Survey of Operations Achievable," <u>Proceedings of the NASA Langley Conference on Optical Data Processing for Aerospace Applications</u>, NASA Conference Publication 2207 (NTIS, Springfield, VA), pp. 105-118, August 1981.

[8]   D. Casasent, C. P. Neuman and M. Carlotto, "An Electro-Optical Processor for Optimal Control," <u>Proceedings of the Society of Photo-Optical Instrumentation Engineers</u>, <u>295</u>, pp. 176-183, August 1981.

[9]   C. P. Neuman, D. Casasent and R. Baumbick, "An Electro-Optical Processor for the Optimal Control of F100 Aircraft Engines," <u>Proceedings of the Electro-Optical Systems Design Conference</u>, Anaheim, CA, pp. 311-320, November 1981.

[10]   D. Casasent, J. Jackson and C. Neuman, "Frequency-Multiplexed and Pipelined Iterative Optical Systolic Array Processors," <u>Applied Optics</u>, <u>22</u>(1),

pp. 115-124, January 1983.

[11] A. Ghosh and D. Casasent, "Triangular System Solutions on an Optical Systolic Processor," Applied Optics, 22(12), pp. 1795-1796, June 1983.

[12] D. Casasent and A. Ghosh, "LU and Cholesky Decomposition on an Optical Systolic Array Processor," Optics Communications, 46(5-6), pp. 270-273, July 1983.

[13] D. Casasent and A. Ghosh, "Optical Linear Algebra," Advances in Optical Information Processing, Proceedings of the Society of Photo-Optical Instrumentation Engineers, 388, January 1983.

[14] D. Casasent and A. Ghosh, "Direct and Implicit Optical Matrix-Vector Algorithms," Applied Optics (in press).

[15] D. Casasent, A. Ghosh and C. P. Neuman, "Direct and Indirect Optical Solutions to Linear Algebraic Equations: Error Source Modeling," Real-Time Signal Processing VI, Proceedings of the Society of Photo-Optical Instrumentation Engineers, 431, August 1983.

[16] J. R. Rice, Numerical Methods, Software and Analysis. New York: McGraw-Hill, 1983.

[17] J. H. Wilkinson, The Algebraic Eigenvalue Problem. Oxford: Clarendon Press, 1965.

[18] B.V.K. Vijaya Kumar, "Singular Value Decomposition Using Iterative Optical Processors," Applied Optics, 22(7), pp. 962-963, April 1983.

[19] D. M. Young, Iterative Solution of Large Linear Systems. New York: Academic Press, 1971.

[20] D. C. Farden, "Tracking Properties of Adaptive Signal Processing Algorithms," IEEE Transactions on Acoustics, Speech, and Signal Processing, ASSP-29(3), pp. 439-446, June 1981.

[21] C. P. Neuman, D. Casasent and M. Carlotto, Electro-Optical System Controller and Processor, Interim Report (Phase I) for Grant NAG 3-5, NASA Lewis Research Center, Cleveland, Ohio 44135, 26 November 1980.

[22] D. Casasent, C. P. Neuman and A. Ghosh, Electro-Optical System Controller and Processor, Interim Report (Phase II), for Grant NAG 3-5, NASA Lewis Research Center, Cleveland, Ohio 44135, 1 March 1982.

[23] D. Casasent, A. Ghosh and C. P. Neuman, Electro-Optical System Controller and Processor, Final Report (Phase III) for Grant NAG 3-5, NASA Lewis Research Center, Cleveland, Ohio 44135, 10 December 1982.

[24] G. E. Forsythe and W. R. Wasow, Finite-Difference Methods for Partial Differential Equations. New York: John Wiley and Sons, Inc., 1960.

TABLE 1

LAE APPLICATIONS ON VECTOR-MATRIX IOP
NASA LANGLEY   (AUGUST 1981)

CONTROL ENGINEERING AND SIGNAL PROCESSING APPLICATIONS	ALGORITHMS
LMS (STATE AND PARAMETER ESTIMATION)	BIPOLAR AND COMPLEX-VALUED DATA
DECONVOLUTION	ITERATIVE LAE SOLUTIONS (RICHARDSON, JACOBI, GAUSS-SEIDEL AND SUCCESSIVE OVERRELAXATION)
EIGENVALUE-EIGENVECTOR COMPUTATION (POWER METHOD)	SIMULATION OF LINEAR DYNAMIC SYSTEMS
	MATRIX-MATRIX MULTIPLICATION
ADAPTIVE PHASED-ARRAY RADAR SIGNAL PROCESSING	MATRIX INVERSION
LQR-ARE OPTIMAL CONTROL DESIGN (KLEINMAN-RICHARDSON NESTED LOOP ALGORITHM)	LINEAR MATRIX-MATRIX EQUATION SOLUTIONS
	NONLINEAR MATRIX EQUATION SOLUTIONS

TABLE 2

LAE SOLUTIONS ACHIEVABLE
NASA LANGLEY (AUGUST 1983)
TWO YEARS OF PROGRESS

DIRECT	IOP	SAOP
LU DECOMPOSITION		V
CHOLESKY DECOMPOSITION		V
QR DECOMPOSITION		V
FORWARD AND BACKWARD SUBSTITUTION		V

ITERATIVE	IOP (1981)	SAOP
RICHARDSON	V	V
JACOBI	V	V
GAUSS-SEIDEL	V	V
SUCCESSIVE OVERRELAXATION	V	V

(Choice Depends Upon Matrix Structure
and Properties)

ALGORITHM	APPLICATION	IOP	SAOP
POWER METHOD	EIGENVALUES AND EIGENVECTORS	V	V
QR	EIGENVALUES		V
SVD	PRINCIPAL COMPONENTS		V
KLEINMAN	LQR-ARE OPTIMAL CONTROL DESIGN	INDIRECT	DIRECT/INDIRECT
KALMAN FILTER	STATE ESTIMATION (LINEAR)		V
EXTENDED KALMAN FILTER	STATE ESTIMATION (NONLINEAR)		V
EXPLICIT PDE's	PHYSICAL PROBLEMS	V	V
IMPLICIT PDE's	PHYSICAL PROBLEMS	INDIRECT	DIRECT/INDIRECT

TABLE 3

PHYSICAL ORIGIN AND PROPERTIES OF LAE's

PHYSICAL ORIGIN	COEFFICIENT MATRIX
Partial differential equations and finite differences (Standard mathematical models for applied mechanics problems)	Sparse, banded and regular
Physical structures	Banded and less regular
Networks	Banded and less regular yet
Signal processing	Symmetric --- Toeplitz
Least Mean-Squared (LMS) Error	Symmetric
Control engineering	Full

48
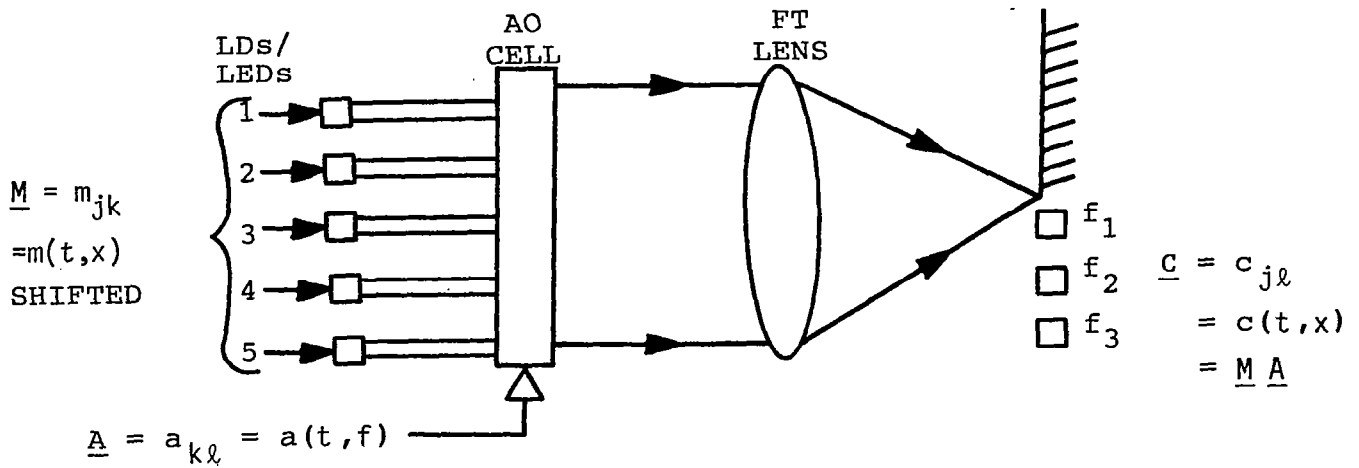
Figure 1.- Schematic diagram of (space, time and frequency-multiplexed) SAOP.
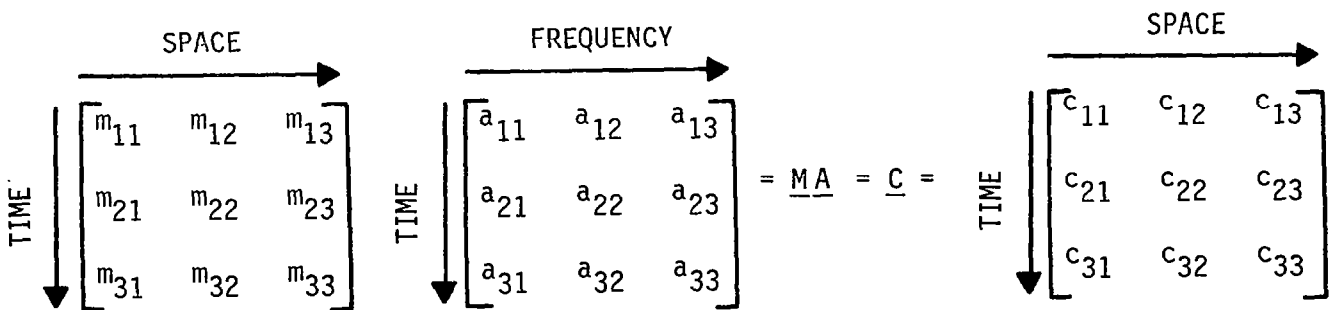
Figure 2.- SAOP data encoding for matrix-matrix product $\underline{M}\,\underline{A} = \underline{C}$.
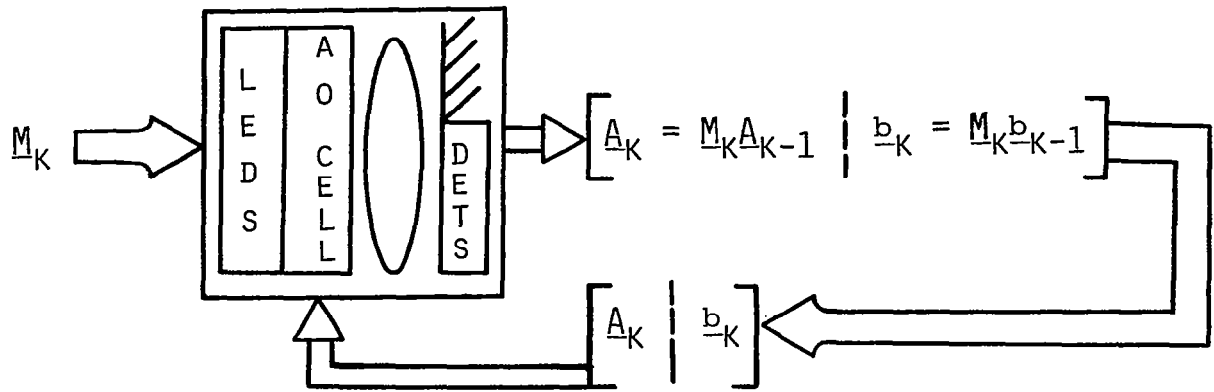
Figure 3.- Optical systolic LU decomposition.
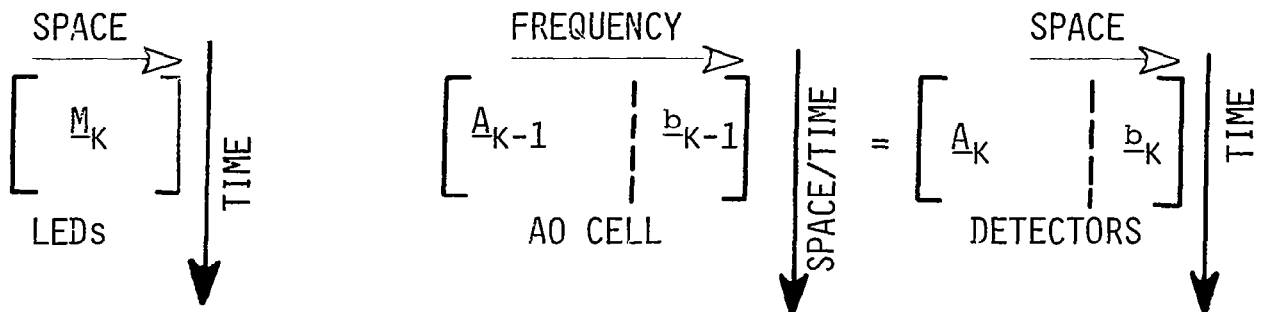
Figure 4.- Data encoding (space, time and frequency)
for optical systolic LU decomposition.
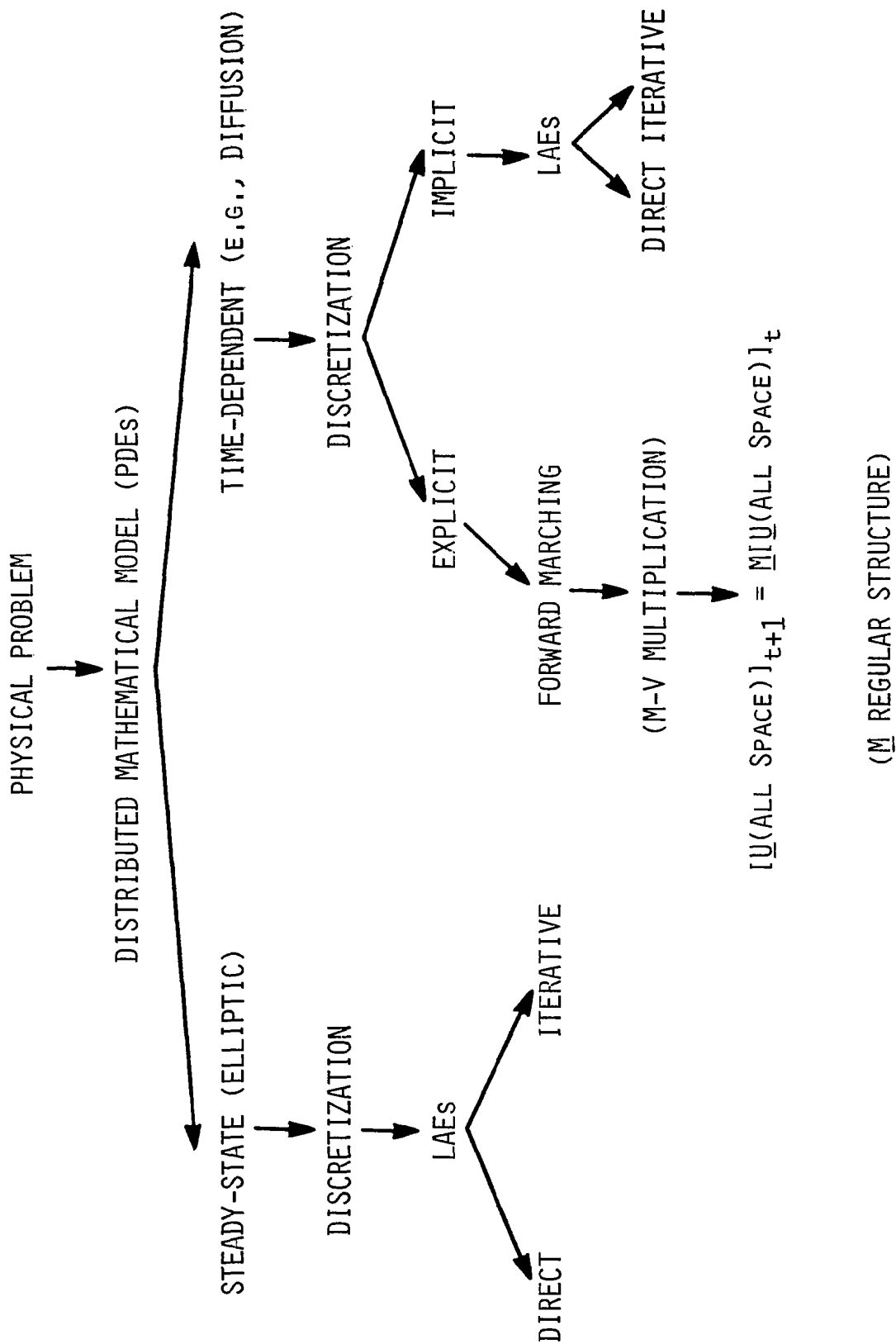
Figure 5.- Physical problems and linear algebraic equations.

ADVANCES IN WHITE-LIGHT OPTICAL SIGNAL PROCESSING*

F. T. S. Yu
Electrical Engineering Department
The Pennsylvania State University
University Park, Pennsylvania 16802

SUMMARY

A technique that permits signal processing operations to be carried out by white-light source is described. This method is capable of performing signal processing that obeys the concept of coherent light rather than incoherent optics. Since the white-light source contains all the color wavelengths of the visible light, the technique is very suitable for color signal processing. Some of its recent advances in white-light signal processing will be illustrated.

INTRODUCTION

The use of coherent light enables optical systems to carry out many sophisticated information processing operations (ref. 1). However, coherent optical processing systems are plagued with coherent artifact noise, which frequently limits their processing capability. Although many optical information processing operations can be implemented by systems that use incoherent light (refs. 2-5), there are other severe drawbacks. The incoherent processing system is capable of reducing the inevitable artifact noise, but it generally introduces a dc-bias buildup problem, which results in poor noise performance. Techniques have been developed for coherent operation with light of reduced coherence (refs. 6,7); however, these techniques also possess severe limitations.

Attempts at reducing the temporal coherence requirements on the light source in optical information processing fall into two general categories: one, the use of incoherent instead of coherent optical processing has been pursued by Lowenthal and Chavel (ref. 8) and Lohmann (ref. 9), among others. The other, the reduction of coherence while still operating in the linear-in-amplitude, has been pursued by Leith and Roth (ref. 10) and by Morris and George (ref. 11).

Since the invention of laser (i.e., a strong coherent source), it has become a fashionable tool for many scientific applications particularly as applied to coherent optical signal processing. However coherent optical signal processing systems are plagued with coherent noises, which frequently limit their processing capability. As noted by the late Gabor, the Nobel prize winner in physics in 1970 for his invention of holography, the coherent noise is the number one enemy of the Modern Optical Signal Processing (ref. 12). Aside from the coherent noise, the coherent sources are usually expensive, and the coherent processing environments are very stringent. For example, heavy optical benches and dust free environments are generally required.

Recently, we have looked at the optical processing from a different standpoint. A question arises, is it necessarily true that all optical signal processing required

a coherent source? The answer to this question is that there are many optical signal processings that can be carried out by a white-light source (ref. 13). The advantages of the proposed white-light signal processing technique are: 1. It is capable of suppressing the coherent noise; 2. White-light source is usually inexpensive; 3. The processing environment is not very demanding; 4. The white-light system is relatively easy and economical to maintain; and 5. The white-light processor is particularly suitable for color image processing.

One question that the reader may ask, since the white-light system offers all these glamorous merits, is why has it been ignored for so long? The answer to this question is that it was a general acceptance that an incoherent source cannot process the signal in complex amplitude. However, none of the practical sources are strictly incoherent, even a white-light source. In fact, we were able to utilize the partial coherence of a white-light source to perform the complex amplitude processing. The proposed white-light processor, on one hand, is capable of suppressing the coherent noise like an incoherent processor, and on the other hand, it is capable of processing the signal in complex amplitude like a coherent processor.

There is however a different approach toward the utilization of a white-light processor. In coherent processing, virtually no one evaluates the coherence requirement, since the laser provides a very good coherent source. However, in white-light processing, the evaluation of the coherence requirement is usually called for.

In white-light signal processing we should approach the problem from a different standpoint. First, we should have the a priori knowledge of the signal processing operation we would encounter. For example, is it a 1-D or 2-D processing? Is the signal filtering a point or point-pair concept? What is the spatial bandwidth of the signal? Then we would be able to evaluate the coherence requirements at the Fourier and at the input planes. From the evaluated results, we would be able to design a signal sampling function and a source encoding mask to obtain these requirements. The objective of using a signal sampling function is to achieve a high degree of temporal coherence in Fourier plane so that the signal can be processed in complex amplitude for the entire spectral band of the light source. And for the source encoding, it is to alleviate the inability of an extended source.

In the following, we shall discuss in detail the source encoding, signal sampling and spatial band filtering as applied to white-light signal processing.

WHITE-LIGHT OPTICAL SIGNAL PROCESSING

We shall now describe an optical signal processing technique that can be carried out by a white-light source, as illustrated in Fig. 1. The white-light signal processing system is similar to that of a coherent system, except for the use of a white-light source, source encoding mask, signal sampling grating, multispectral filters and achromatic transform lenses. For example, if we place a signal transparency $s(x,y)$ in contact with a sampling phase grating, the complex light field for every wavelength λ behind the achromatic transform lens L_1 would be

$$E(p,q;\lambda) = \int\int s(x,y) \, \exp(ip_o x)\exp[-i(px+qy)]dxdy = S(p-p_o,q) \qquad (1)$$

where the integral is over the spatial domain of the input plane P_1, (p,q) denotes the angular spatial frequency coordinate system, p_o is the angular spatial frequency

of the sampling phase grating, and $S(p,q)$ is the Fourier spectrum of $s(x,y)$. If we write Eq. (1) in the form of linear spatial coordinate system (α,β), we have,

$$E(\alpha,\beta;\lambda) = S(\alpha - \frac{\lambda f}{2\rho} p_o, \beta) \tag{2}$$

where $p = (2\pi/\lambda f)\alpha$, $q = (2\pi/\lambda f)\beta$, and f is the focal length of the achromatic transform lens. Thus, we see that the Fourier spectra would disperse into rainbow color along the α axis, and each Fourier spectrum for a given wavelength λ is centered at $\alpha = \pm(\lambda f/2\pi)p_o$.

In signal filtering, we assume that a sequence of complex spatial filters for various λ_n are available, i.e., $H(p_n,q_n)$, where $p_n = (2\pi/\lambda_n f)\alpha$, $q_n = (2\pi/\lambda_n f)\beta$. In practice, all the processing signals are spatial frequency limited; the spatial bandwidth of each spectral band filter $H(p_n,q_n)$ is also bandlimited, such as

$$H(p_n,q_n) = \begin{cases} H(p_n,q_n), \alpha_1 < \alpha < \alpha_2 \\ \\ 0, \quad \text{otherwise} \end{cases} \tag{3}$$

where $\alpha_1 = (\lambda_n f/2\pi)(p_o + \Delta p)$ and $\alpha_2 = (\lambda_n f/2\pi)(p_o - \Delta p)$ are the upper and the lower spatial limits of $H(p_n,q_n)$, and Δp is the spatial bandwidth of the input signal $s(x,y)$.

The limiting wavelengths of each $H(p_n,q_n)$ can be written as

$$\lambda_\ell = \lambda_n \frac{p_o + \Delta p}{p_o - \Delta p} \text{ , and } \lambda_h = \lambda_n \frac{p_o - \Delta p}{p_o + \Delta p} \tag{4}$$

The spectral bandwidth of $H(p_n,q_n)$ is therefore

$$\Delta\lambda_n = \lambda_n \frac{4p_o\Delta p}{p^2 - (\Delta p)^2} \simeq \frac{4\Delta p}{p_o} \lambda_n \tag{5}$$

If we place this set of spectral band filters side-by-side positioned over the smeared Fourier spectra, then the intensity distribution of the output light field can be shown as

$$I(x,y) \simeq \sum_{n=1}^{N} \Delta\lambda_n |s(x,y;\lambda_n) * h(x,y;\lambda_n)|^2 \tag{6}$$

where $h(x,y;\lambda)$ is the spatial impulse response of $H(p_n,q_n)$ and $*$ denotes the convolution operation. Thus, the proposed white-light signal processor is capable of processing the signal in complex amplitude. Since the output intensity is the sum of the mutually incoherent narrow band spectral irradiances, the annoying coherent artifact can be eliminated. Furthermore, the white-light source contains all the color wavelengths; the processor is very suitable for color signal processing.

SPECTRAL BAND FILTERING, SIGNAL SAMPLING AND SOURCE ENCODING

As stated earlier, in white-light signal processing we would approach the problem from a different standpoint. For example, if signal filtering is two-dimensional (e.g., 2-D correlation operation), we would synthesize a set of narrow spectral band filters for each λ_n for the entire smeared Fourier spectra, as illustrated in Fig. 2(a). On the other hand, if the signal filtering is one-dimensional (e.g., deblurring due to linear motion), a broadband fan-shape spatial filter, to accommodate the scale variation due to wavelength, can be utilized as illustrated in Fig. 2(b). Since the filtering is taking place with the entire spectral band of the light source, the artifact noise can be suppressed and the white-light processing technique is also suitable for color image processing.

There is, however, a temporal coherence requirement imposed upon the signal filtering in Fourier plane. Since the scale of the Fourier spectrum varies with wavelength, a temporal coherence requirement should be imposed on each spatial filter at the Fourier plane. Thus, the spectral spread over each filter $H(p_n, q_n)$ is imposed by the temporal coherence requirement, i.e.,

$$\frac{\Delta\lambda_n}{\lambda_n} = \frac{4\Delta p}{P_o} << 1 \tag{7}$$

From this inequality, a high degree of temporal coherence is achievable in the Fourier plane by simply increasing the spatial frequency of the sampling grating. Needless to say, the same tempoal coherence requirements of Eq. (7) can also be applied for a broadband fan-shape filter.

There is also a spatial coherence requirement imposed at the input plane of the white-light signal processor. The spatial coherence function at the input plane can be shown (refs. 14,15),

$$\Gamma(\vec{x}-\vec{x}') = \int\int\gamma(\vec{x}_o)\exp[i2\pi \frac{\vec{x}_o}{\lambda f}(\vec{x}-\vec{x}')]d\vec{x}_o \tag{8}$$

which essentially is the Van Cittert-Zernike Theorem (refs. 16,17), where $\gamma(\vec{x}_o)$ denotes the intensity distribution of the source encoding function.

From the above equation, we see that the spatial coherence and source encoding functions form a Fourier transform pair, i.e.,

$$\gamma(\vec{x}_o) = \mathcal{F}[\Gamma(\vec{x}-\vec{x}')] \tag{9}$$

and

$$\Gamma(\vec{x}-\vec{x}') = \mathcal{F}^{-1}[\gamma(\vec{x}_o)] \tag{10}$$

where $\mathcal{F}$ denotes the Fourier transformation. This Fourier transform pair implies that if a spatial coherence function is given then the source encoding function can be determined with the Fourier transformation and vice versa. We note that source encoding function can consist of apertures of any shape or complicated gray scale

transmittance. However the source encoding function is only limited to a positive real quantity which is restricted by the following physical realizable condition:

$$0 \le \gamma(\vec{x}_o) \le 1 \tag{11}$$

In white-light signal processing, we would search for a reduced spatial coherence requirement for the processing operation. With reference to this reduced spatial coherence function, a source encoding function that satisfies the physical realizability condition can be obtained. One of the basic objectives of the source encoding is to alleviate the inability of a physical white-light source. Furthermore the source encoding also improves the utilization of the light power such that the optical processing can be carried out by an extended source.

We shall now illustrate an application of the source encoding, signal sampling, and filtering for a white-light signal processing. Let us now consider a polychromatic image subtraction (ref. 18). The image subtraction of Lee (ref. 19) that we would consider is essentially a one-dimensional processing operation, in which a 1-D fan-shape diffraction grating should be utilized, as illustrated in Fig. 3. We note that the fan-shape grating (i.e., filter) is imposed by the temporal coherence condition of Eq. (7). Since the image subtraction is a point-pair processing operation, a strictly broad spatial coherence function at the input plane is not required. In other words, if one maintains the spatial coherence between the corresponding image points to be subtracted at the input plane, then the subtraction operation can be carried out at the output image plane. Thus instead of using a strictly broad spatial coherence function, a reduced spatial coherence function may be utilized, such as

$$\Gamma(y-y') = \delta(y-y'-h_o) + \delta(y-y'+h_o) \tag{12}$$

where $2h_o$ is the main separation between the two input color transparencies. The source encoding function can therefore be evaluated by through the Fourier transform of Eq. (9), such as

$$\gamma(y_o) = 2 \cos(\frac{2\pi h_o}{\lambda f} y_o) \tag{13}$$

Unfortunately Eq. (13) is a bipolar function which is not physically realizable. To ensure a physically realizable source encoding function, we let a reduced spatial coherence function with the point-pair coherence requirement be (ref. 20)

$$\Gamma(|y-y'|) = \frac{\sin(\frac{N\pi}{h_o} |y-y'|)}{N\sin(\frac{\pi}{h_o} |y-y'|)} \text{ sinc } (\frac{\pi w}{h_o d} |y-y'|) \tag{14}$$

where $N \gg 1$, a positive integer, and $w \ll d$. Equation (14) represents a sequence of narrow pulses which occur at every $|y-y'| = nh_o$, where n is a positive integer, and their peak values are weighted by a broader sinc factor, as shown in Fig. 4(a). Thus, a high degree of spatial coherence can be achieved at every point-pair between the two input color transparencies. By taking the Fourier transformation of the reduced spatial coherence function of Eq. (14), the corresponding source encoding

function is

$$\gamma(|y|) = \sum_{n=1}^{N} \text{rect} \frac{|y-nd|}{w} \qquad (15)$$

where w is the slit width, $d = (\lambda f/h_o)$ is the separation between the slits, and N
is the number of the slits. Since $\gamma(|y|)$ is a positive real function which
satisfies the constraint of Eq. (11), the proposed source encoding function of
Eq. (15) is physically realizable.

In view of Eq. (15), we also note that the separation of slit d is linearly
proportional to the λ. The source encoding is a fan-shape type function, as shown
in Fig. 4(b). To obtain lines of rainbow color spectral light sources for the
signal processing, we would utilize a linear extended white-light source with a
dispersive phase grating, as illustrated in Fig. 3. Thus with the described broad-
band source encoding mask, sampling grating, and fan-shape sinusoidal grating,
a color substracted image can be seen at the output image plane.

RECENT ADVANCES IN WHITE-LIGHT PROCESSING

It would occupy lengthy pages to describe most advances in white-light signal
processing. We would however have to restrict our discussion to a few recent
results that are considered interesting. Since the white-light signal processor is
particularly suitable for color signal processing, we shall provide the results
mostly in color images.

We shall first demonstrate a color image deblurring result due to linear mo-
tion. Since linear motion is a 1-D processing operation and its deblurring filter
is a point-by-point filtering, a fan-shape deblurring filter can be utilized
(ref. 21). Figure 5(a) shows a color picture of a blurred image due to linear
motion of an F-16 fighter plane. The body of this fighter plane is painted in navy
blue-and-white colors, the wings are mostly painted in red, the tail is also navy
blue-and-white, and the ground terrain is generally bluish-green color. From this
figure, we see that the plane is severely blurred due to motion. Figure 5(b) shows
the color image deblurring result obtained with the white-light signal processing
technique. From this result, the letters and overall shape of the entire airplane
are more distinctive than the blurred one. The river, the highways, and the
forestry of the ground terrain are far more visible. We note that the color
reproduction of the deblurred image is spectacularly faithful and coherent artifact
noise is virtually nonexistent.

Let us now provide a color image subtraction utilized by the source encoding
technique with extended incoherent sources (ref. 18) as described in previous
sections. Figure 6(a) and 6(b) show two color image transparencies of a parking lot
as input color objects. Figure 6(c) shows the color subtracted image obtained by
the source encoding technique with extended incoherent source. In this figure, the
profile of a (red) subcompact car can be seen at the output image plane. The
shadow and the parking line (in yellow color) can also be readily identified.
However, we note that this color image subtraction result is obtained by two
narrow spectral band extended incoherent sources. Extension toward the entire
spectral band of a white-light source is currently under investigation.

We shall now illustrate our experimental result that a multicolor sound spectrogram (ref. 22) can be generated by a white-light processing technique, as illustrated in Fig. 7. Figure 8(a) shows a typical 1-D intensity modulated speech signal obtained by focusing its CRT scanner onto a moving photographic film by a film transport. If the recorded format transparency is transporting over a rectangular optical window at the input plane of Fig. 7, a frequency color encoded sound spectrogram can be recorded at the output plane. Figure 8(b) shows a typical frequency color coded speech spectrogram obtained with this technique. The frequency content is encoded from red for high frequency, green for intermediate frequency, to blue for low frequency. This color encoded speech spectrogram represents a sequence of English words spoken by a male voice. These words are "testing, one, two, three, four." From this color encoded speech spectrogram, we see that excellent character-ization of format variation can readily be seen. Because of the use of a white-light source, the artifact noise is avoided. As compared with the electronic and digital counterparts, its white-light signal processing technique simplified the processing technology and the system is rather versatile to operate. Although the result provided is rather preliminary, it is the first color-coded speech spectrogram being generated.

We shall now illustrate a computer controlled white-light density pseudocolor encoder, as proposed in Fig. 9. The spatial encoding is made by multiplexing a positive, a negative, and a product image onto a black-and-white photographic film, as illustrated in Fig. 10. Figure 11 shows a sketch of the normalized transmittance as a function of gray scale. If the encoded transparency is inserted at the input plane of a white-light processor of Fig. 9, then a density color coded image can be obtained by color filtering at the Fourier plane.

We stress that this white-light pseudocolor encoder offers several advantages over the digital counterpart. The encoder is far less expensive and in principle the technique offers a higher image resolution.

Figure 12 shows a set color coded image of a woman's pelvis. The x-ray was taken following a surgical procedure. A section of the bone between the sacroiliac joint and spinal column has been removed. In Fig. 12(a), the positive image is encoded in red, the negative image is encoded in blue, and the product image is encoded in green. By comparing the pseudocolor coded image with the original black-and-white x-ray picture, it appears that the soft tissues can be better differen-tiated by the color images as demonstrated by the fact that the image contrast in the region containing the gastrointestinal tracts is evidently superior in the color image. On the other hand, there seems to be a degradation in the resolution in the color image along edges of the hard tissues. This is perhaps caused by two reasons: Firstly, high frequency information may be eliminated due to the low spatial frequency encoding gratings (40 lines/mm and 26.7 lines/mm) employed. Secondly, the image may be smeared due to the film development process. These two problems can be easily corrected by selecting higher frequency encoding gratings and by gaining more experience in film processing.

Another point worthwhile to note is that a reversal of the color encoding can be easily implemented as shown in Fig. 12(b), where the positive and negative images are encoded in blue and red while the product image remains in green. This color mixture capability could be beneficial because an image in different color combination may reveal subtle features which are otherwise undetected. For instance, the air pockets in the colon of the patient can be identified more easily with Fig. 12(b) than with Fig. 12(a). Moreover, a wide variety of other pseudocolor

encoded images can also be obtained by simply alternating the color filters in the Fourier plane of the white-light processor.

CONCLUSION

In conclusion we would stress that source encoding is to provide an appropriate, reduced spatial coherence function at the input plane so that the signal processing can be carried out by an extended white-light source. The effect of the signal sampling is to achieve a higher temporal coherence at the Fourier plane so that the signal can be processed in complex amplitude. If the filtering operation is two-dimensional, a multi-spectral-band 2-D filters should be utilized. If the filtering operation is one-dimensional, a fan-shape filter can be used. In summary, the white-light signal processor is capable of processing the signal in complex amplitude as a coherent processor and, on the other hand, it suppresses the artifact noise as an incoherent processor. Since the white-light source contains all the visible wavelengths, it has been shown very suitable for color signal processing.

REFERENCES

1. A. Vander Lugt, "Coherent Optical Processing," Proc. IEEE, 62, 1300 (1974).

2. G. L. Rogers, "Non-coherent Optical Processing," Opt. Laser Technol., 7, 153 (1975).

3. K. Bromley, "An Optical Incoherent Correlation," Opt. Acta, 21, 35 (1974).

4. M. A. Monahan, K. Bromley, and R. P. Bocker, "Incoherent Optical Correlations," Proc. IEEE, 65, 121 (1977).

5. G. L. Rogers: Noncoherent Optical Processing, John Wiley, New York, 1977.

6. E. N. Leith and J. Upatnieks, "Holography with Achromatic-Fringe Systems," J. Opt. Soc. Am., 57, 975 (1967).

7. R. E. Brooks, L. O. Weflinger, and R. F. Wuerker, "Pulsed Laser Holograms," IEEE, J. Quantum Electron., QE-2, 275 (1966).

8. S. Lowenthal and P. Chavel, in R. Wiener and J. Shamir, Eds., Proc. of ICO Jerusalem 1976, Conference on Holography and Optical Processing, Plenum Press, New York, 1977.

9. A. Lohmann, "Incoherent Optical Processing of Complex Data," Appl. Opt., 16, 261 (1977).

10. E. N. Leith and J. Roth, "White-Light Optical Processing and Holography," Appl. Opt. 16, 2565 (1977).

11. G. M. Morris and N. George, "Space and Wavelength Dependence of a Dispersion-Compensated Matched Filter," Appl. Opt., 19, 3843 (1980).

12. D. Gabor, "Laser Speckle and Its Elimination," IBM, J. Res. Develop., 14, 509 (1970).

13. F.T.S. Yu, Optical Information Processing, Wiley-Interscience, NY, 1983.

14. M. Born and E. Wolf: Principles of Optics, 2nd rev. ed., Pergamon Press, New York, 1964.

15. F.T.S. Yu, S. L. Zhuang, and S. T. Wu, "Source Erroding for Partially Coherent Optical Processing," Appl. Phys., B27, 99 (1982).

16. P. H. Van Cittert, "Die Wahrscheinlicke Schwingungs verteilung in einer von einer lichtquelle direkt Oden Mittels einer linse," Physica 1, 201 (1934).

17. F. Zernike, "The Concept of Degree of Coherence and Its Application to Optical Problems," Physica 5, 785 (1938).

18. F.T.S. Yu and S. T. Wu, "Color Image Contradiction with Extended Incoherent Source," J. Opt., 13, 183 (1982).

19. S. H. Lee, S. K. Yao, and A. G. Milnes, "Optical Image Synthesis (Complex Amplitude Addition and Subtraction) in Real-Time by a Diffraction-Grating Interfere Metric Method," J. Opt. Soc. Am., 60, 1037 (1970).

20. S. T. Wu and F.T.S. Yu, "Image Subtraction with Encoded Extended Incoherent Source," Appl. Opt., 20, 4082 (1981).

21. T. H. Chao, S. L. Zhuang, S. Z. Mao and F.T.S. Yu, "Broad Spectral Band Color Image Deblurring," Appl. Opt., 22, 1439 (1983).

22. F.T.S. Yu, K. B. Xu, T. N. Lin and T. H. Chao, "White-Light Optical Speech-Spectrogram Generation," J. Opt. Soc. Am., 72, 1722 (1982).
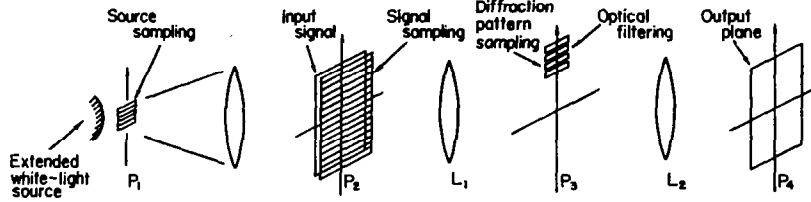
Figure 1. A white-light optical signal processor.
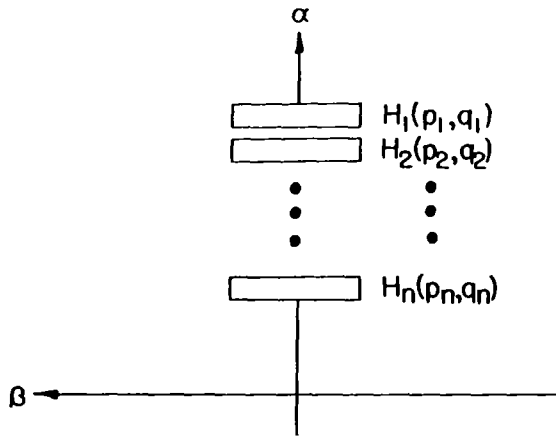
Figure 2(a). A multi spectral-band filter.
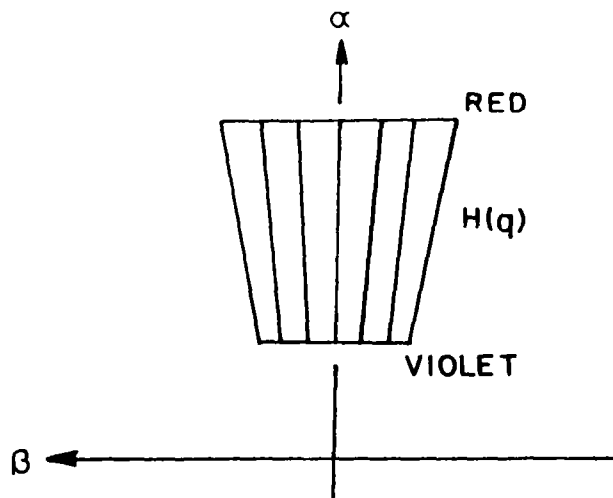
Figure 2(b). A fan-shape filter.
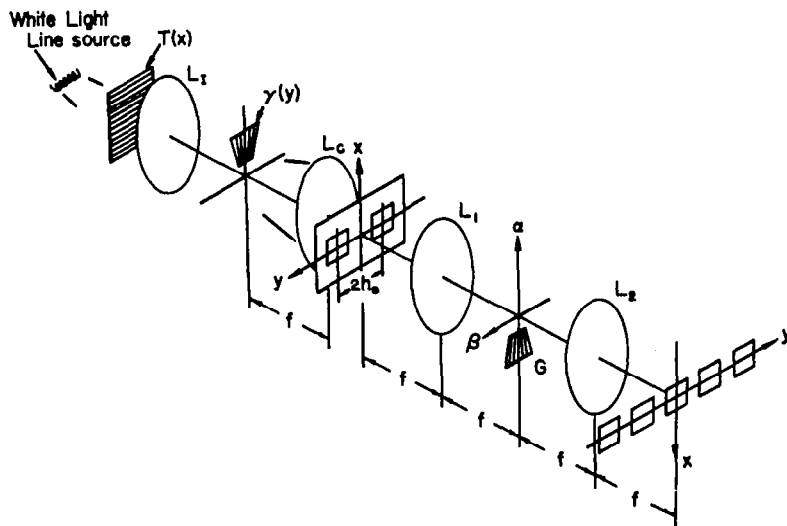
Figure 3.   A white-light image subtraction processor. $T(x)$; phase grating, L_I; image lens, L_C; collimated lens, L_1 and L_2; achromatic transform lenses, $\gamma(y)$; source encoding mask, G; fan-shape diffraction grating.
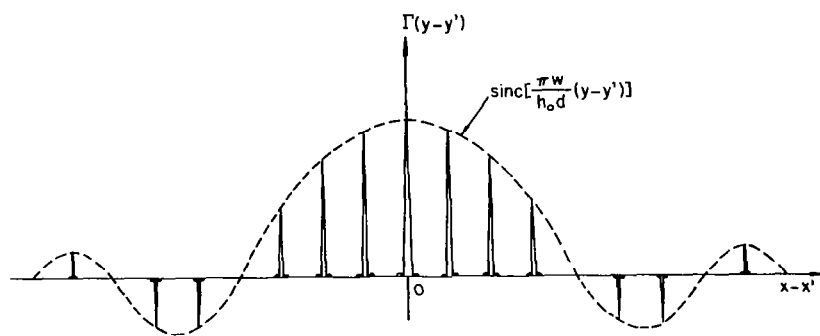
Figure 4(a).   A spatial coherence function.
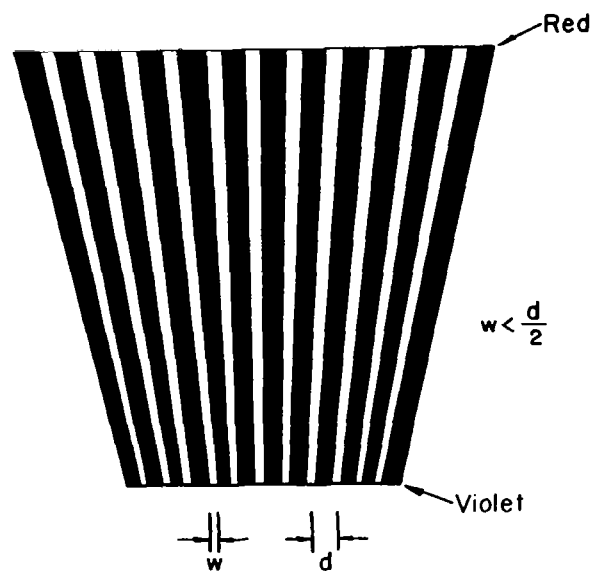
Figure 4(b).   A source encoding mask.

Figure 5(a). A black-and-white blurred color image.
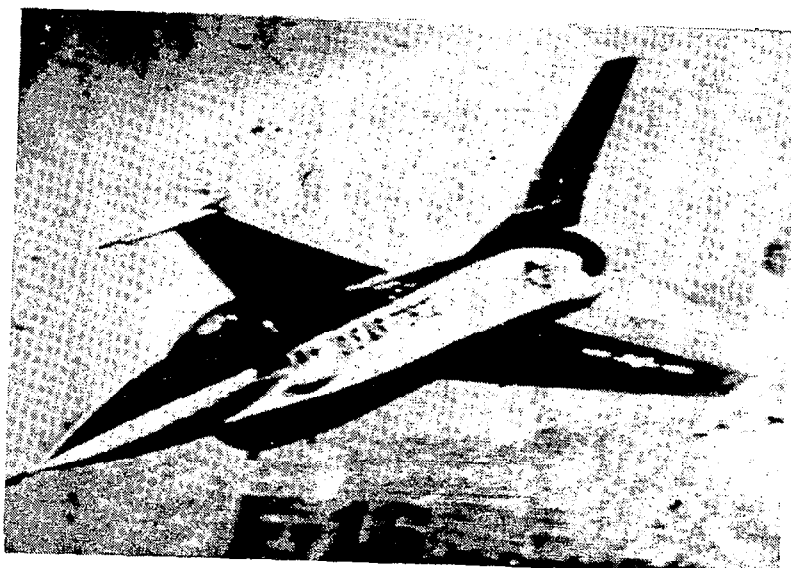
Figure 5(b). A black-and-white deblurred color image.

Figures 6(a) and (b). Black-and-white pictures of the input color objects.

Figure 6(c). A black-and-white subtracted color image.
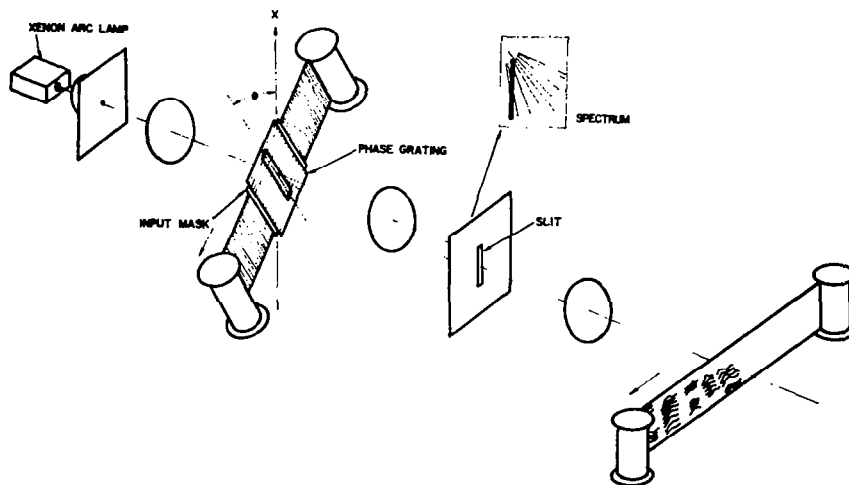
Figure 7. A white-light optical speech spectrograph.
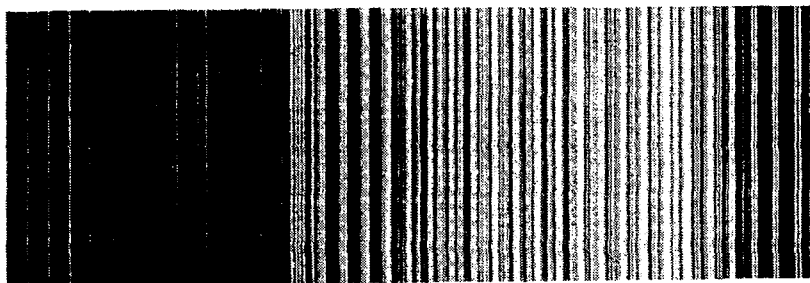
Figure 8(a). An intensity modulated format.

Figure 8(b). A black-and-white frequency color coded speech spectrogram.
This spectrogram represents a sequence of English words
"testing, one, two, three, four" spoken by a male voice.
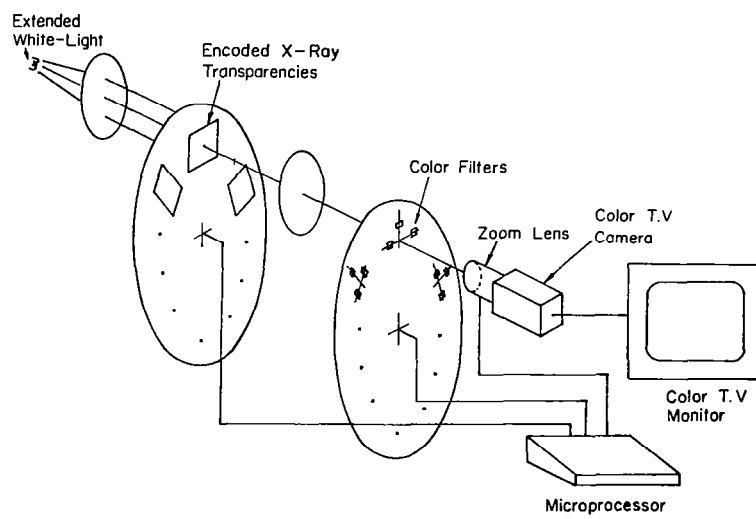
Figure 9. A computer controllable white-light density pseudocolor encoder.
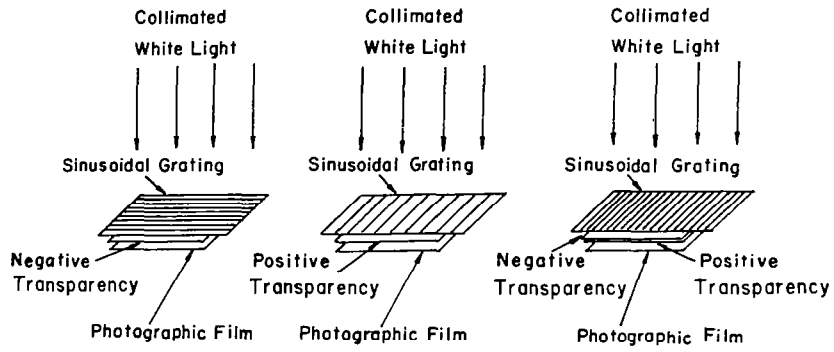
Figure 10. Spatial encoding.
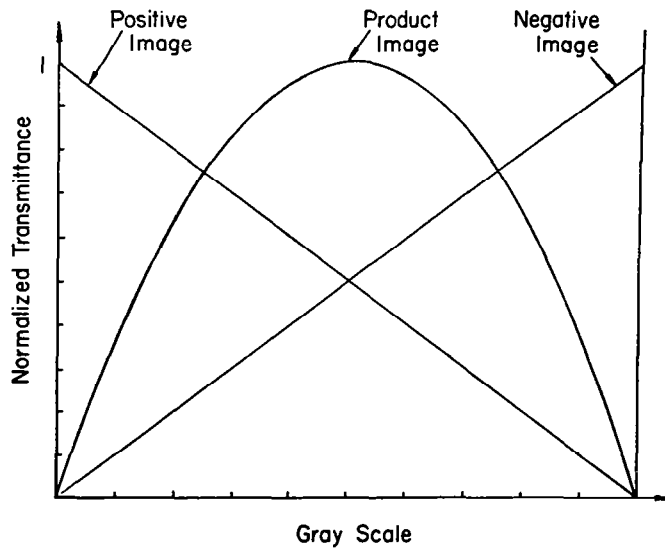
Figure 11. Normalized transmittance as a function of gray scale.

68
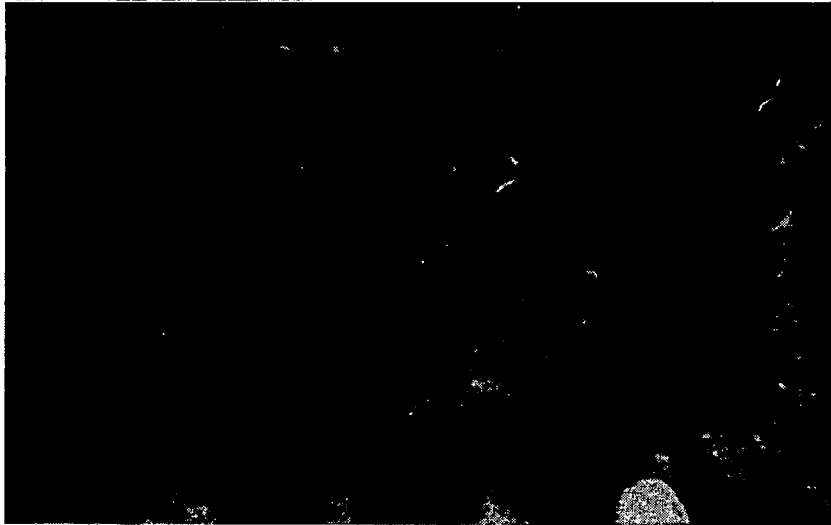
Figure 12(a). A black-and-white picture of a color coded picture.
Positive image is encoded in red, negative image is
encoded in blue, and product image is encoded in green.

Figure 12(b). A black-and-white picture of a reversal of primary color
coded image of (b).

69

SPATIAL INTERFEROMETRY FOR

WHITE LIGHT PROCESSING:

THE COHERENCE INTERFEROMETER*

J. B. Breckinridge
Jet Propulsion Laboratory
· Pasadena, CA 91109

ABSTRACT

An optical systems design approach is given for a parallel optical processor that has an information throughput capacity in excess of one petabit per second. This system will enable predetection processing of white-light, passively illuminated scenes. Integrated with a programmable Van der Lugt filter, this system is an effective data compression method. A program to implement this parallel optical processing by interferometry system is discussed.

INTRODUCTION

Observational systems record vast amounts of data for scientific, earth resources, and environmental analysis purposes. These large amounts of data are digitally processed, stored, and then analyzed by interpreters (scientists and engineers) to convert the data into information. Accurate interpretation of data often requires long hours of tedious work by a highly skilled individual. To decrease the amount of human interaction, many successful research efforts using digital data analysis methods have been completed.

The volume of data to be processed over the next 20 years will exceed the physical capacity limits of digital-type computers. Fundamental research into new computational architectures is needed to create the new technologies required to handle the very large volumes of data planned for NASA missions, such as the multispectral linear array (MLA) and imaging spectrometer, during the next 20 years (ref. 1).

In this paper we build upon the observation that an optical system performs operations on a large two-dimensional data set (an image), in parallel, at the speed light takes to traverse the system. Here, we introduce a design approach for a processing system and present a progress report on a specific implementation. We recognize that the number of operations performed by optical interference is limited when compared to those available using the digital approach and suggest that under certain conditions the hyper-throughput capability of parallel optical processing by interferometry compensates for the limited processing algorithms.

71

The recent technologies of high-speed, large-format two-dimensional charge-coupled device (CCD) detectors and of high-speed, large-format two-dimensional amplitude and phase filters, and the new invention of the white-light two-dimensional optical Fourier transform device are integrated into a parallel optical processing by interferometry system.

ANALYSIS

The computational throughput of a system using parallel optical processing by interferometry is calculated and compared to a state-of-the-art digital computer system.

Figure 1 shows a schematic of a parallel optical processing by interferometry system, configured for a Van der Lugt filter operation. Plane 1 indicates the entrance pupil of the fore-optic system that relays an image from object space onto a field stop located at the image plane 2. A collimator at plane 3 relays the pupil at plane 1 into an optical interferometer that performs a two-dimensional white-light spatial frequency Fourier transform which is displayed at plane 4. The lens at plane 5 relays the output of the interferometer at plane 4 onto the complex (amplitude and phase) (Van der Lugt) filter mask at plane 7. The system at plane 7 forms an image of the processed two-dimensional information at plane 2 as modified by the filter onto plane 8 for readout by a two-dimensional array detector system. At plane 8 appears the cross-correlation between the scene and the spectrum of the a priori information at the filter.

The optical interferometer that performs the two-dimensional white-light spatial frequency Fourier transform has been extensively analyzed in the literature and will not be redescribed here (refs. 2-6). It is capable of transforming a white-light, passively illuminated scene. Details of its operation are given in the next section.

Processing capacity of the optical system between planes 4 and 6 in figure 1 is now calculated. Assume the diffraction limit of the optical system is such that the linear dimension across the zeros of the Airy diffraction pattern is denoted by ℓ, and assume that the field stop at plane 2 in figure 1 has diameter D_2. The number of Airy patterns, A_n, across the portion of the image plane admitted by the field stop is then

$$A_n = [D_2/\ell]^2 \tag{1}$$

The Fourier transform operation is performed by the device at plane 4 as a consequence of white-light image formation, or the white-light interference phenomenon. The Fourier transform of the two-dimensional irradiance distribution across plane 2 is performed in the length of time light takes to travel from plane 2 to plane 7 in figure 1. For a physical distance, L, in meters within the optical system, this time, t, is given by

$$t = (L/3) \times 10^{-8} \text{ seconds} \tag{2}$$

To quantify the amount of data, Q, at the image plane 2, we need to assume that each of N independent samples across the image is represented by a quantum of bits, b. The amount of data, Q, at plane 2 is then,

$$Q = Nb \qquad (3)$$

and the data throughput, T, of the system expressed as data rate (bits per unit time) or bandwidth is

$$T = Q/t \qquad (4)$$

A realistic value for T, the throughput, is now computed.

The linear dimension across the Airy diffraction pattern, ℓ, at the image plane 2 is

$$\ell = 2.44\lambda f_1/D_1 \qquad (5)$$

where f_1 is the focal length of the lens at plane 1 in figure 1 whose diameter is D_1. For the system in figure 1 we assume that the lens at plane 3 is large enough to transmit all the rays, with no spatial frequency vignetting onto plane 4.

To identify samples at the image plane 2 that are _independent_ and not correlated at, say, the 1% level, the spacing of the samples, d, must be approximately,

$$d = 4\ell$$

where ℓ is defined in equation 5.

The number, N, of _independent_ samples across the image plane number 2 in figure 1 is then,

$$N = \left[\frac{D_1 D_2}{10\lambda f_1}\right]^2 \qquad (6)$$

If we assume the quantum number of bits - that is, the number of binary levels used to represent intensity levels within an independent spatial sample at the image plane - to be 10, then, from equation 3

$$Q = 10[D_1 D_2/10\lambda f_1]^2 \qquad (7)$$

The throughput, T, in units of bits per second is obtained by placing equations 7 and 2 into equation 4, to give,

$$T = \frac{3 \times 10^7}{L} \left[\frac{D_1 D_2}{\lambda f_1} \right]^2 \tag{8}$$

where the variables are in units of meters.

If we assume that the entrance aperture diameter of the optical system, D_1, is 0.1 m, that the diameter at the field stop, D_2, is 0.1 m, that the focal length, f_1, is 1.0 m, that the length of the entire optical system, L, is 3.0 m, and that the wavelength, λ, is 500 nm, then the processing throughput of the system, T, is found to be

$$T = 4 \times 10^{15} \text{ bits per second}$$

or 4 peta (peta = 10^{15}) bits per second.

This data processing rate represents an approximate upper bound theoretical limit for parallel optical processing by interferometry. This rate is several orders of magnitude above current predictions for the more classical digital architectures. If this capacity is realizable in a system, a new dimension in information processing is opened up. The throughput in equation 8 is per unit of the broadband wavelength interval of the "white-light" signal. Wavelength multiplexing can be used to increase the system information throughput beyond that given above by up to a factor of 100.

SPECIFIC IMPLEMENTATION

An interferometric optical element that performs the two-dimensional white-light Fourier transform was originally developed by Breckinridge (refs. 2-4) and used for measurements of the turbulent properties of the atmosphere (refs. 5,7) and for imaging through turbulence (ref. 8). This instrument, with fixed, 180-degree shear, enables the measurement of the spatial frequency mutual coherence function and is called coherence interferometer. Roddier et al. (refs. 9,10) developed an interferometer similar to the coherence interferometer but with capability for variable rotational shear and with chromatic correction for off-axis field points.

Breckinridge and Roddier (ref. 6), in a design study, applied this interferometer design approach to the modeling of the reconstruction of stellar images in the visible with the strongly aberrated far-infrared large deployable reflector (LDR) telescope. This interferometer concept, which has been successfully used for scientific research in optics, atmospheres, and astronomy for the past 10 years, is now applied to the study of parallel optical processing by interferometry.

The interferometer is similar to the Kosters (ref. 11) prism interferometer, but modified extensively to enable operations over a two-dimensional, rather than the limited one-dimensional, field. The manner in which the interferometer folds wave fronts to make the white-light hologram, or to perform the cosine Fourier transform operation, is given in figure 2, which shows, on the left-hand side, an optical

instrument containing the coherence interferometer. In the lower left-hand corner, an x-y coordinate system is shown with the letter F in the +x, +y quadrant. The image of this letter F was projected onto this image plane by a fore-optics system off the lower left side of the paper. To be consistent with the notation used in figure 1, which shows the schematic of the system, we label plane 2 as the image plane containing the letter F in figure 2.

The lens at plane 3 collimates the radiation at the image plane and relays an image of the system pupil into the roofs of the coherence interferometer (rotational shear interferometer) shown at plane 4 in both figures 1 and 2. An enlarged and rotated sketch of the coherence interferometer (interferometer prisms) is shown in the right position of figure 2.

A plane wave enters the interferometer. A portion of the energy in the wave front that is reflected into the left arm of the interferometer is reflected through the prism roofs where it is rotated or flipped about the axis of the roof line and returns to the beam splitter. The remaining portion of the energy in the wave front is transmitted, reflects through a separate prism roof, is rotated or flipped about the axis of the roof line, and returns to combine with the wave front coming from the other interferometer arm. The two complex amplitude wave fronts then leave the interferometer. The path lengths in both paths of the interferometer are equal, and, therefore, the wave fronts are rotationally sheared by 180 degrees (in this case), and are in phase in the white-light sense.

The lens at plane 5 in figure 2 takes the collimated light and forms an image at the image plane 6. As shown in figure 2, the single letter F has been mapped by the prism system into two letters F with a point symmetry lying on the system axis.

Figure 3, which gives a detail of plane 6, shows the two letters F in position in the aspect of point symmetry. Small elements of each of the letters F are identified by Δx and Δy. Specific elements are identified as $\Delta x'$, $\Delta y'$ and $\Delta x''$, $\Delta y''$. Note that for each point on that letter F in the second quadrant there exists an identical point on that letter F shown in the fourth quadrant. By the method of construction of the prism assembly, with equal paths in both arms, each point on the letter F in quadrant 2 is coherent with the "image" of that point on the letter F in quadrant 4. Recall that "coherent" means that interference fringes are formed by the interference of wave fronts from each pair of image points. That is, since both images of the letter F originate from the same object, the electromagnetic fields radiating from one F are correlated with those radiating from the other.

The original letter F is illuminated by white light. Radiation from a particular point on the letter F is <u>not</u> coherent, that is, not correlated, with radiation from any other point on the same letter F. Only radiation from points pairwise identical between the F "image" in quadrant 2 and the F "image" in quadrant 4 are correlated and thus contribute to a modulation or fringe field at plane 7.

The intensity $I_7(\xi,\eta)$ at plane 7 is therefore given by

$$I_7(\xi,\eta) = \frac{1}{2}[<I_7>]$$

$$+ \frac{1}{2} \int_{-\infty}^{+\infty} \int_{-\infty}^{+\infty} I_2(x,y) \cos(4\pi\xi x + 4\pi\eta y)dxdy \qquad (9)$$

where $I_2(x,y)$ is the intensity distribution across plane 2. The intensity at plane 7 is therefore a uniform illumination across which are intensity variations, the envelope of which is the cosine Fourier transform of the white light scene information at plane 2.

Analysis of this interferometer system is detailed in reference 4, where the quasimonoplanatic analog of the quasimonochromatic assumption is discussed. That this interferometer system produces the spatial frequency Fourier transform of the white light source is demonstrated both by analysis and by several laboratory measurements described in reference 5.

INFORMATION EXTRACTION

Spatial information will be extracted from the signal by positioning a programmable spatial amplitude and/or phase filter at plane 7, retransforming the multiplication of the filter times the Fourier transform of the observed spatial information using an optical subsystem, and reading out the subsequent two-dimensional correlation signal with a two-dimensional array detector positioned at plane 8 in figure 1.

APPLICATION

The application of the parallel optical processing by interferometry is for pre-detection processing of two-dimensional scenes. For example, an optical system onboard a satellite might be required to determine the number density of certain spatial structures. For example, the density of trees: To record a picture of all the trees, transmit the data to the ground, and perform digital analysis of the data is far more inefficient than preprocessing the data before detection and transmitting from the spacecraft to the ground cross-correlation coefficients.

PROGRESS

The instrument system shown schematically in figure 1 is now under construction at JPL. The coherence interferometer (rotational shear interferometer) prisms are being built in the optical shop of the Université de Nice, France. The alignment jig is being built at JPL. A two-dimensional CCD array detector with liquid nitrogen cooling was purchased.

If sufficient funds are available in FY'84, the prisms will be assembled into their jig, programming of a microcomputer to read the CCD will begin, a detailed optical system design will be completed and parts ordered, and research to identify a commercially available, high-speed, high-resolution programmable filter will be initiated.

REFERENCES

1. Wellman, J.B., J.B. Breckinridge, P. Kupferman, R.P. Salazar, and K. Sigurdson (1982); S.P.I.E. 345.

2. Breckinridge, J.B. (1972), Applied Optics 11, 2996-2998.

3. Breckinridge, J.B. (1974), Applied Optics 13, 2670-2762.

4. Breckinridge, J.B. (1976a), The Spatial Structure Analyzer and Its Astronomical Applications, Ph.D. dissertation, University of Arizona, Tucson, Arizona.

5. Breckinridge, J.B. (1976b), J. Opt. Soc. Amer. 66, 1240-1242.

6. Breckinridge, J.B. and F. Roddier (1982), J. Opt. Soc. Amer. 72, 1970.

7. Breckinridge, J.B. (1976c), J. Opt. Soc. Amer. 66, 143-144.

8. Burke, J.J. and J.B. Breckinridge (1978), J. Opt. Soc. Amer. 68, 67-77.

9. Roddier, F., C. Roddier, and J. Demarcq (1978), J. Optics (Paris) 9, 145-149.

10. Roddier, C., F. Roddier, F. Martin, A. Baranne, and R. Brun (1980) J. Optics (Paris) 11, 149-152.

11. Saunders, J.B. (1954), Journal of Research of the National Bureau of Standards 58, 27-31.

Figure 1. Schematic of the parallel optical processing by interferometry system. The marginal ray is given as a series of short dashed lines and the chief ray is given as a broken line.

Figure 2. Optical system containing the coherence interferometer. The notation used here is the same as that used in figure 1. An enlarged and rotated view of the coherence interferometer prisms is shown in the upper right-hand portion.
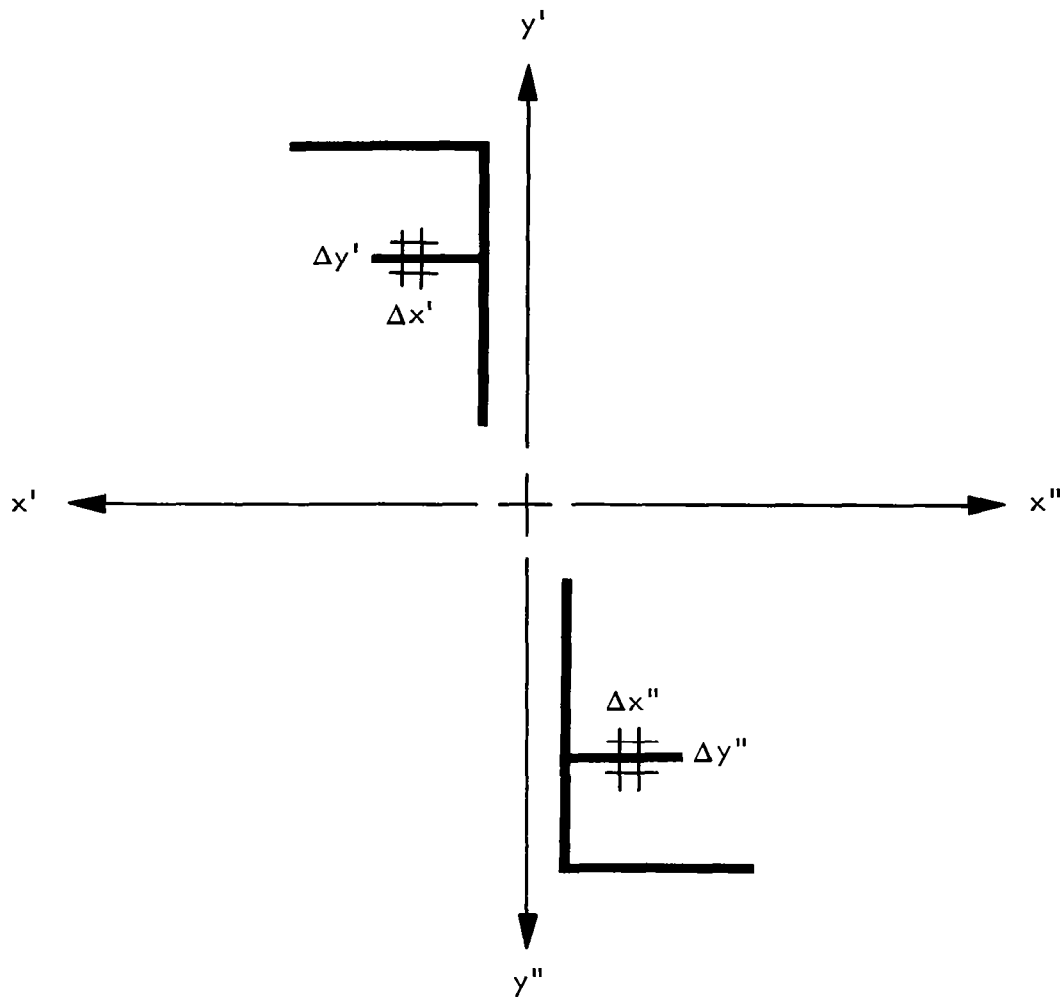
Figure 3. Sketch of the "double" image plane at plane 6 in figure 2. The single letter F at the image plane 2 is shown mapped by the coherence interferometer into two letters F with a point of symmetry lying on the system axis. Elements $\Delta y'$ $\Delta x'$ and $\Delta x''$ $\Delta y''$ are images of the same point in plane 2 and therefore are coherent with each other and contribute to the fringe field at plane 7 in figure 2.

Figure 1. Schematic of the parallel optical processing by interferometry system. The marginal ray is given as a series of short dashed lines and the chief ray is given as a broken line.

Figure 2. Optical system containing the coherence interferometer. The notation used here is the same as that used in figure 1. An enlarged and rotated view of the coherence interferometer prisms is shown in the upper right-hand portion.

Figure 3. Sketch of the "double" image plane at plane 6 in figure 2. The single letter F at the image plane 2 is shown mapped by the coherence interferometer into two letters F with a point of symmetry lying on the system axis. Elements $\Delta y'$ $\Delta x'$ and $\Delta x''$ $\Delta y''$ are images of the same point in plane 2 and therefore are coherent with each other and contribute to the fringe field at plane 7 in figure 2.

A HYBRID SILICON MEMBRANE SPATIAL LIGHT MODULATOR FOR OPTICAL INFORMATION PROCESSING

Dennis R. Pape and Larry J. Hornbeck
Texas Instruments Incorporated
Central Research Laboratories
Dallas, Texas 75265

SUMMARY

A new two-dimensional, fast, analog, electrically addressable, silicon-based membrane spatial light modulator (SLM) has been developed for optical information processing applications. This SLM, the Deformable Mirror Device (DMD), consists of a 128 × 128 array of deformable mirror elements addressed by an underlying array of MOS transistors. Coherent light reflected from the mirror elements is phase modulated producing an optical Fourier transform of an analog signal input to the device. The DMD architecture and operating parameters related to this application are presented. A model is developed that describes the optical Fourier transform properties of the DMD. The calculated peak first-order diffraction efficiency of 8.2% is in good agreement with the value of 8.4% obtained from experimental optical Fourier transform measurements.

INTRODUCTION

An integral component of an optical information processor is a spatial light modulating device[1]. Such a device may be used to input information into the object plane of the processor or filter information in an image or Fourier plane. Present devices each have limitations affecting their use in these applications. Some of these limitations include slow response time[2], inherent one-dimensionality[3], and inherent digital operation[4]. This paper describes the use of a new two-dimensional, fast, analog, electrically addressable, silicon-based spatial light modulator, the DMD.

The first section of the paper describes the device. A more complete description is given elsewhere[5]. A model of the mirror deflection is given in the second section. In the third section, we present a model of the Fourier transform of an image imposed on the device. Again, a more complete description is given elsewhere[6]. Experimental data are presented and compared with this model in the fourth section. Finally, we outline future development of the device in the fifth section.

DEVICE DESCRIPTION

A perspective view of the DMD is shown in figure 1. The device consists of an X-Y array of deformable mirror elements that can be addressed by an underlying array of MOS transistors. Each of the two devices described in this paper has an array size of 128 × 128 pixels with pixel elements 51 μm square. This gives a resolution of 9.8 p/mm. Device A has an active (deformable) area of 23 μm × 36 μm and an air gap dimension of 620 nm. Device B has an active area of 28 μm × 33 μm and an air gap dimension of 800 nm.

Figure 2 shows the line-addressed organization of the DMD. Video data are fed to an off-chip serial-to-parallel converter that is connected to the 128 drain lines of the MOS transistors. These lines are charged to a potential $(\phi_d)_{nm}$. A decoder, connected to the 128 gate lines, selects one gate to be turned on. The floating sources of all the MOS transistors in that particular gate line are then charged to the potential of their respective drains. The gate is then turned off. The mirror is held at a fixed voltage V_M. An electrostatic force then exists on the mirror proportional to $V_M - (\phi_d)_{nm}$ causing the mirror element to deflect. The mechanical response time of the mirror and hence the line settling time are approximately 25 μs. The membrane response time can be improved by operating the device under vacuum. Figure 3 shows membrane response time as a function of pressure. In vacuum, the response time is approximately 5 μs. Once the sources have been set, the next line of video is transferred onto the drain lines and the next gate line is selected by the decoder. The source storage time is approximately 200 ms. This line-address process continues at standard video TV line rates of 63.5 μs. Because the DMD has a line settling time less than the TV line rate, the device may be applied to taking continuous transforms at TV rates. The DMD may be operated at much higher line rates consistent with the line propagation delays estimated to be 0.5 μs.

Chip photomicrographs are shown in figure 4. Figure 4a shows a corner of the central array. Bond pads are on the left-hand side of the figure. Figure 4b is a magnified view of one side of the chip, showing air channels etched in the polysilicon to allow air to escape when the membrane is placed on the chip.

Considerable progress has been made in improving the performance of the DMD. The first demonstration of the device concept occurred in July of 1980 using a 16 × 16 array. In February of 1982, a 128 × 128 array device was demonstrated. Improvements in the 128 × 128 device have now resulted in devices with defect levels less than 1.0%.

Figure 5 shows schlieren projection images of Device B generated at TV rates. A checkerboard pattern of blocks of 16 elements is shown in figure 5a. Figure 5b shows horizontal bars consisting of alternating sections of 16 elements ON and 16 elements OFF. Figure 5c demonstrates the resolution of the device. The upper left quadrant of figure 5c shows all pixels ON. The upper right and lower

left quadrants show alternating pixels ON. The lower right quadrant of figure 5c shows a checkerboard pattern of pixels ON. Figure 5d shows all elements OFF. Nonuniformities in these images are caused primarily by the projection optics. Brightness nonuniformity of the device is approximately ±5% and the defect level is approximately 0.4%.

MEMBRANE DEFLECTION MODEL

The characteristics of the deflection of the DMD membrane can be approximated using an electro-mechanical model for membrane modulators[7]. This model assumes the membrane has a circular support boundary of radius R and air gap t. The membrane is uniformly loaded by an electrostatic field in which end effects are ignored. The membrane tension T_o is assumed constant and acts only in a tangential direction. It is also assumed no pressure differential exists across the membrane. The numerical analysis solution of this model shows that for small peak membrane deflections Δ_o,

$$\Delta_o/t = V^2 R^2 / T_o t^3 \qquad (1)$$

where V is the air gap voltage. When Δ_o/t exceeds 0.44, the membrane tension can no longer counteract the electrostatic force and the membrane collapses. The voltage at which collapse occurs, V_c, is given by

$$V_c^2 \propto T_o t^3 / R^2 \qquad (2)$$

Typical DMD parameters are t = 0.62 μm, T_o = 5 N/m, $(\Delta_o)_{collapse}$ = 0.27 μm, and V_c = 28 V. An effective radius is used for R,

$$R = \sqrt{(WL/\pi)} \qquad (3)$$

where W and L are the width and length of the air gap opening.

Figure 6a is a graph showing membrane deflection versus voltage. The extremely nonlinear behavior will be seen later in the Fourier transform data. Figure 6b is a graph of collapse voltage versus membrane radius.

The application of this model to the present device breaks down due to the noncircular air gap opening and the existence of a pressure differential across the membrane. A rectangular membrane deflection model is being developed, but is not used in this paper.

Consider a wave of complex amplitude $U(x,y)$ and wavelength λ incident on the DMD. The field $G(x,y)$, representing the spatially modulated and reflected wave immediately in front of the DMD, is given by

$$G(x,y) = U(x,y)\ S(x,y) \qquad (4)$$

where $S(x,y)$ is the complex reflectance amplitude function describing the surface of the DMD mirror. In the following analysis, we have scaled $S(x,y)$ by the reflectance of the mirror.

The function $S(x,y)$ is pictorially represented in figure 7. It consists of a unit cell convolved with an X-Y array of delta functions. The unit cell, $S_u(x,y)$, can be written as

$$S_u(x,y) = S_s(x,y) + S_M(x,y) \qquad (5)$$

where $S_s(x,y)$ (describing a flat mirror over a polysilicon support structure of width P and length Q with a central opening of width W and length L) is given by

$$S_s(x,y) = [\text{Rect}(x/P)\text{Rect}(y/Q) - \qquad (6)$$
$$\text{Rect}(x/W)\text{Rect}(y/L)]$$

and $S_M(x,y)$ describes a deformed mirror of maximum central deflection Δ_o bounded by the central rectangular opening. We assume the mirror is deformed parabolically. With the mirror deflection Δ given by

$$\Delta = \Delta_o(1-4x^2/W^2)\ (1-4y^2/L^2) \qquad (7)$$

the second term of $S_u(x,y)$ is

$$S_M(x,y) = [\text{Rect}(x/W)\text{Rect}(y/L)]\ \exp\ \{-i\ \phi_o(1-4x^2/W^2)\ (1-4y^2/L^2)\} \qquad (8)$$

where

$$\text{Rect}(x/a) \equiv \begin{cases} 1 & |x| < a/2 \\ 0 & |x| > a/2 \end{cases} \qquad (9)$$

and

$$\phi_o = 4\pi\Delta_o/\lambda \qquad (10)$$

The delta function array $S_D(x,y)$ with delta functions on centers P and Q and bounded by width G and length H is represented by the function

$$S_D(x,y) = (1/PQ)\text{Comb}(x/P)\text{Comb}(y/Q)\text{Rect}(x/G)\text{Rect}(y/H) \qquad (11)$$

where

$$\text{Comb}(x/a) = \sum_{m=-\infty}^{+\infty} \delta(x/a - m) = a\ \Sigma\ \delta(x - ma) \qquad (12)$$

Combining equations 5, 6, 8, and 11, $S(x,y)$ is written as

$$
\begin{aligned}
S(x,y) &= S_u(x,y) * S_D(x,y) \\
&= \Big[\ \text{Rect}(x/P)\text{Rect}(y/Q) - \text{Rect}(x/W)\text{Rect}(y/L) \\
&\quad + \text{Rect}(x/W)\text{Rect}(y/L)\ \exp\{-i\ \phi_o(1-4x^2/W^2)\ (1-4y^2/L^2)\}\Big] \\
&\quad * \Big[\ (1/PQ)\text{Comb}(x/P)\text{Comb}(y/Q)\text{Rect}(x/G)\text{Rect}(y/H)\ \Big]
\end{aligned}
\qquad (13)
$$

The reflected wave now undergoes Fraunhofer diffraction. The field distribution $F(x,y)$, a distance Z from the DMD, is given by

$$
F(x,y) = \frac{1}{i\lambda Z}\ \exp\left[i\ \frac{2\pi Z}{\lambda} + \frac{i\pi}{\lambda Z}(x^2 + y^2)\right]\ \times
$$
$$
\int_{-\infty}^{+\infty} \int_{-\infty}^{+\infty} G(x_1,y_1)\ \exp\frac{(2\pi i x x_1)}{\lambda Z}\ \exp\frac{(2\pi i y y_1)}{\lambda Z}\ dx_1\ dy_1
\qquad (14)
$$

which we recognize, aside from multiplicative phase and amplitude factors, as the Fourier transform (F.T.) of $G(x,y)$ evaluated at the spatial frequencies $u = x/\lambda Z$ and $v = y/\lambda Z$ and denoted by $G(u,v)$. It is convenient to normalize $G(u,v)$ to the Fourier transform of the field distribution from an undeformed DMD ($\Delta = 0$) at $(u,v) = (0,0)$,

$$G_N(u,v) = G(u,v) / G_o(0,0) \qquad (15)$$

Since it is the energy spectrum and not the wave amplitude that one measures in the Fourier plane, the modulus squared of $G_N(u,v)$ is evaluated. The normalized Fourier transform energy spectrum of the DMD is then

$$
\left|G_N(u,v)\right|^2 = \Big|\ \Sigma_M\ \Sigma_N\ \Big[\ [PQ\ \text{Sinc}(M)\text{Sinc}(N) - WL\ \text{Sinc}(WM/P)\text{Sinc}(LN/Q)
$$
$$
+ \int_{-L/2}^{+L/2}\int_{-W/2}^{+W/2} \exp\{-i\phi_o(1-4x^2/W^2)(1-4y^2/L^2)\}\exp\{2\pi i Ny/Q\}\exp\{2\pi i Mx/P\}dxdy]\ \times
$$
$$
[GH/PQ\ \text{Sinc}(G(u-M/P))\ \text{Sinc}(H(v-N/Q))]\ \Big]\ \Big/\ GH\ \Big|^2
\qquad (16)
$$

The integral in the above expression must be evaluated numerically. In the following analysis, we have used an adaptive Romberg method to evaluate this integral over its two-dimensional region. Finally, the energy spectrum $\left|G_N(u,v)\right|^2$ is computed for comparison with experimental data.

A diagram of the apparatus used to measure the optical Fourier transform of the DMD is shown in figure 8. We have used the converging beam technique to avoid the aberrations and noise inherent in the traditional parallel beam Fourier transform lens system[8]. A converging 2.5-mW Gaussian beam from a He-Ne laser is reflected off a pellicle beam splitter onto the DMD. Much higher beam intensities may be used due to the effective light blocking layer of the floating field plate in the well of each pixel. The beam, with a diameter of approximately 5500 μm, illuminates approximately 9000 DMD pixels. The spatially modulated beam, reflected from the DMD mirror, passes through the pellicle beam splitter onto a CCD detector array located in the Fourier plane of the system. The photographs in the next section were taken from an x-y monitor connected to the video output from the CCD camera. Each video line has been offset to give the appearance of three-dimensionality to the frame of video data displayed on the x-y monitor. The energy spectrum of intensity data, which was compared with model calculations in the next section, was obtained with the video output from the CCD camera connected to an oscilloscope.

DMD OPTICAL FOURIER TRANSFORM RESULTS

Fourier transform images of a uniformly deflected DMD (Device B) at three different drain voltage levels are shown in figure 9. For these measurements, the mirror was held with a fixed negative bias of -28 V, and the substrate at -4 V. Figure 9a shows the image with 0 V on the drains, the condition for all pixels OFF. Note the absence of any signal for the higher order peaks. This demonstrates the high signal-to-noise ratio of this device, to be discussed later. Figure 9b shows the maxima in the first-order occurring at +16.9 V, and figure 9c shows the minima in the zeroth-order occuring at +21.8 V for this particular device.

Figure 10 shows quantitatively the zeroth-order and maximum first-order normalized peak diffraction intensities as a function of air gap voltage for Device A. The nonlinearity of the mirror deflection as a function of air gap voltage, shown in figure 6, is responsible for the small change in I_0 and I_1 below an air gap voltage of about 16 V. Unlike the step grating case, the minima in I_0 do not coincide with the maxima in I_1. This is caused by the fact that the shape of the diffracting surface, the deformed membrane, is not flat but has an x,y dependence. It is expected that the location of the minima in I_0 and maxima in I_1 will occur at a greater central membrane deflection than that for the step grating. Mirau interferometric measurements of the DMD mirror deflection show that indeed the minima in I_0 occur at 325 nanometers and the maxima in I_1 occur at 275 nanometers. The measured first-order peak diffraction efficiency of this

device is 8.4%. The model gives a value of 8.2%. These values are in contrast to the 19.8% efficiency of the step grating, the maximum possible efficiency for this geometry.

Figure 10 also shows, in solid lines, the calculated values of I_0 and I_1 from equation 16. We used the Mirau interferometric mirror deflection measurements to relate the amplitude of the membrane deflection to the air gap voltage for these graphs. Although the calculated intensities of I_0 and I_1 agree well with experimental values, the location of the minima and maxima in the curves does not. This indicates that the membrane deflection has less curvature than predicted by a parabolic shape.

Figure 11 shows the Fourier transform image of Device B at the Nyquist frequency. Figure 11a is the central line of the video frame displayed in figure 11b. The half width of the zeroth order peak in figure 11a is 10% of the Nyquist frequency. Therefore, the usable spatial frequency range of this device is from 10% to 100% of the Nyquist frequency.

The signal-to-noise (S/N) ratio is defined as the maximum sinusoidal signal at 1/4 Nyquist frequency (f_N) capable of being sampled before spurious frequency components appear in the Fourier plane divided by the minimum detectable signal. The present device is driven by an off-chip digital serial-to-parallel converter, limiting inputs to digital signals. Therefore, we define the S/N ratio for a square wave at f_N as the maximum first-order peak diffraction intensity at f_N divided by the noise at f_N. The noise from periodic defects at the pixel frequency is at twice f_N and is small as can be seen in figure 9a. The noise at f_N is predominantly caused by random defects in the membrane surface. This noise, however, is spread into all frequency components and, thus, its contribution at any one frequency is also small. For this device, the S/N was measured to be in excess of 57 dB. Our measurement was limited by the temporal noise in the CCD camera electronics.

Figure 12 demonstrates optical Fourier transforms of the four image conditions shown on Device B in figure 5c. All photographs were taken with the zeroth order saturated in order to enhance the amplitude of the higher order peaks. Figure 12a shows all pixels ON. Figures 12b and 12c show vertical and horizontal bars, respectively, at the Nyquist frequency. Figure 12d shows a checkerboard pattern at the Nyquist frequency.

FUTURE DEVELOPMENT

A program is underway to reduce the particulate contamination between the membrane and the silicon substrate, the major cause of defects in the device. Another program has begun to develop on-chip address circuitry for the device. A hermetic package is being developed that will allow operation of the device in a

vacuum. Finally, a new optically addressed DMD is in development.

CONCLUSIONS

The Deformable Mirror Device is a two-dimensional, fast, analog, spatial light modulator integrated on silicon. The device operating parameters useful for optical information processing applications have been presented. A model has been developed to characterize the Fourier transform properties of the DMD. Optical Fourier transform data were taken using the DMD. The modeled diffraction efficiency behavior was compared with the experimental data with some differences discussed. The calculated value of the peak first-order diffraction efficiency, 8.2%, is in good agreement with the measured value of 8.4%.

A S/N ratio in excess of 57 dB was measured at the Nyquist frequency. Finally, the usable spatial frequency range of the device was measured to be from 10% to 100% of the Nyquist frequency.

REFERENCES

1) Casasent, D., Proc. IEEE 65 (1), 143 (1977).

2) Little, M. J., Braatz, P. O., Efron, U., Grinberg, J., and Goodwin, N. W., SID Digest, 250 (1982).

3) Sprague, R. A., Turner, W. D., and Flores, L. N., Proc. SPIE 299, 68 (1982).

4) Ross, W. E., Psaltis, D., Anderson, R. H., Proc. SPIE 341, 191 (1982).

5) Hornbeck, L. J., IEEE Trans. Electron Devices ED-30 (5), 539 (May 1983).

6) Pape, D. R., and Hornbeck, L. J., Proc. SPIE 388, 65 (1982) and Optical Engineering 22 (6), 675 (Nov./Dec. 1983).

7) Meyer, R. A., Grant, D. G., and Queen, J. L., Technical Memorandum TG 1193A, John Hopkins University, (1972).

8) Joyeux, D., and Lowenthal, S., Applied Optics 21, 4368 (1 December 1982).
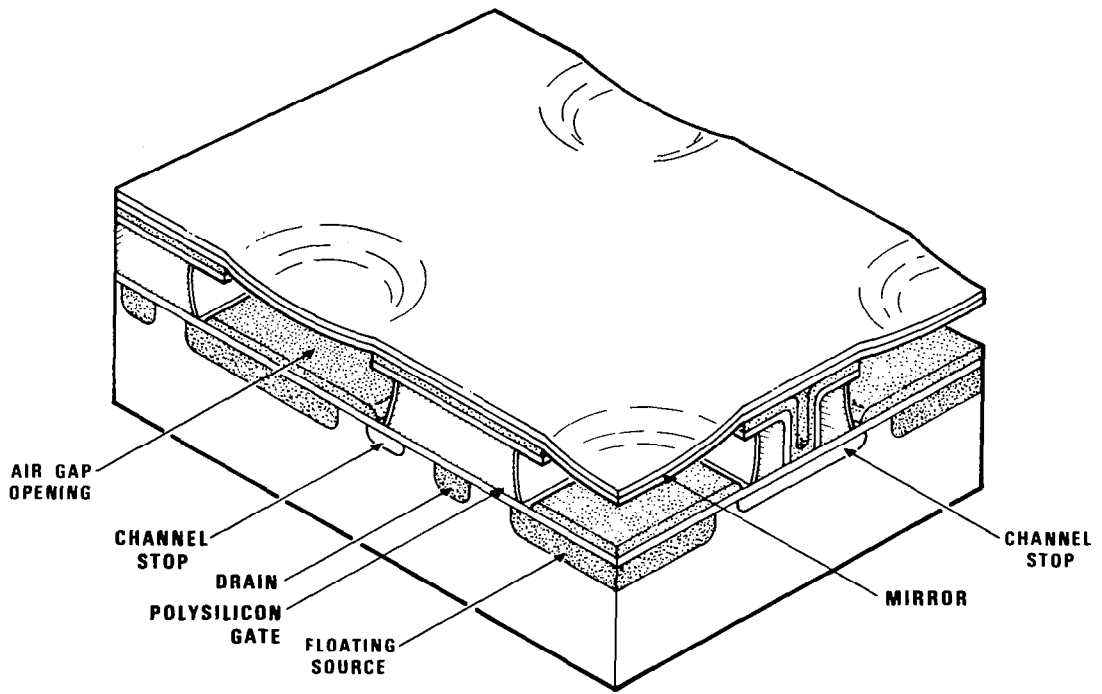
Figure 1.- Perspective view of the deformable mirror device (DMD).

AIR GAP OPENING

CHANNEL STOP

DRAIN

POLYSILICON GATE

FLOATING SOURCE

CHANNEL STOP

MIRROR

DATA INPUT

SERIAL/PARALLEL CONVERTOR

STORAGE REGISTER

LINE DRIVER AMPLIFIERS

DECODER

CELL nm

G_{m+1}

V_M

$(\phi_d)_{nm}$

G_m

D_n

D_{n+1}
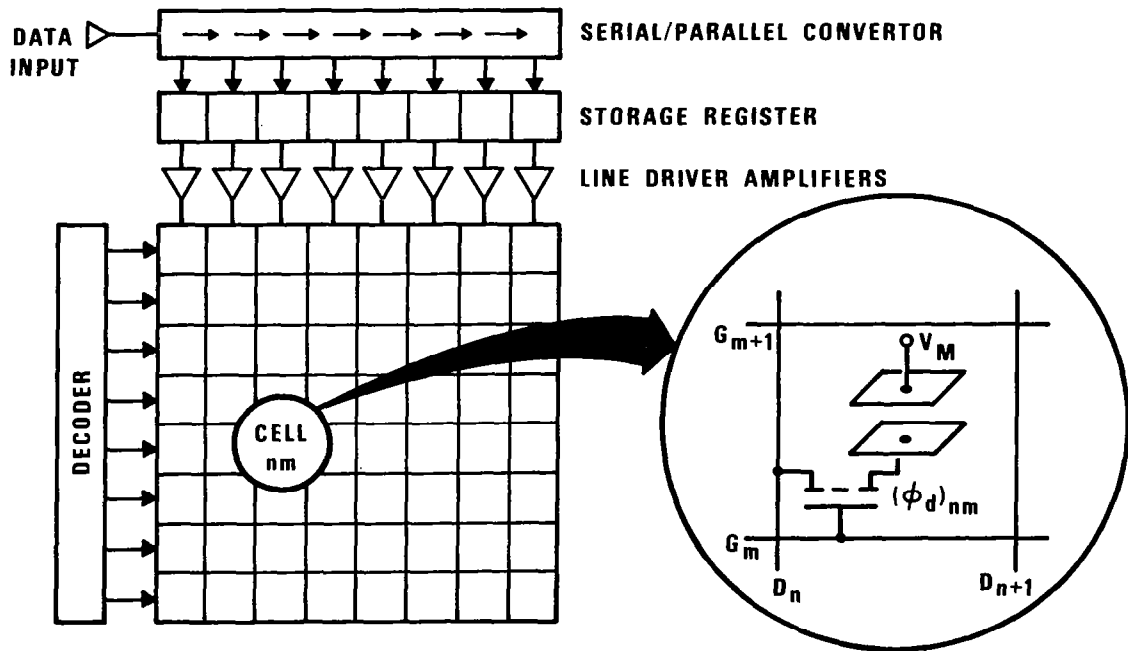
Figure 2.- Line-addressed organization of the DMD.
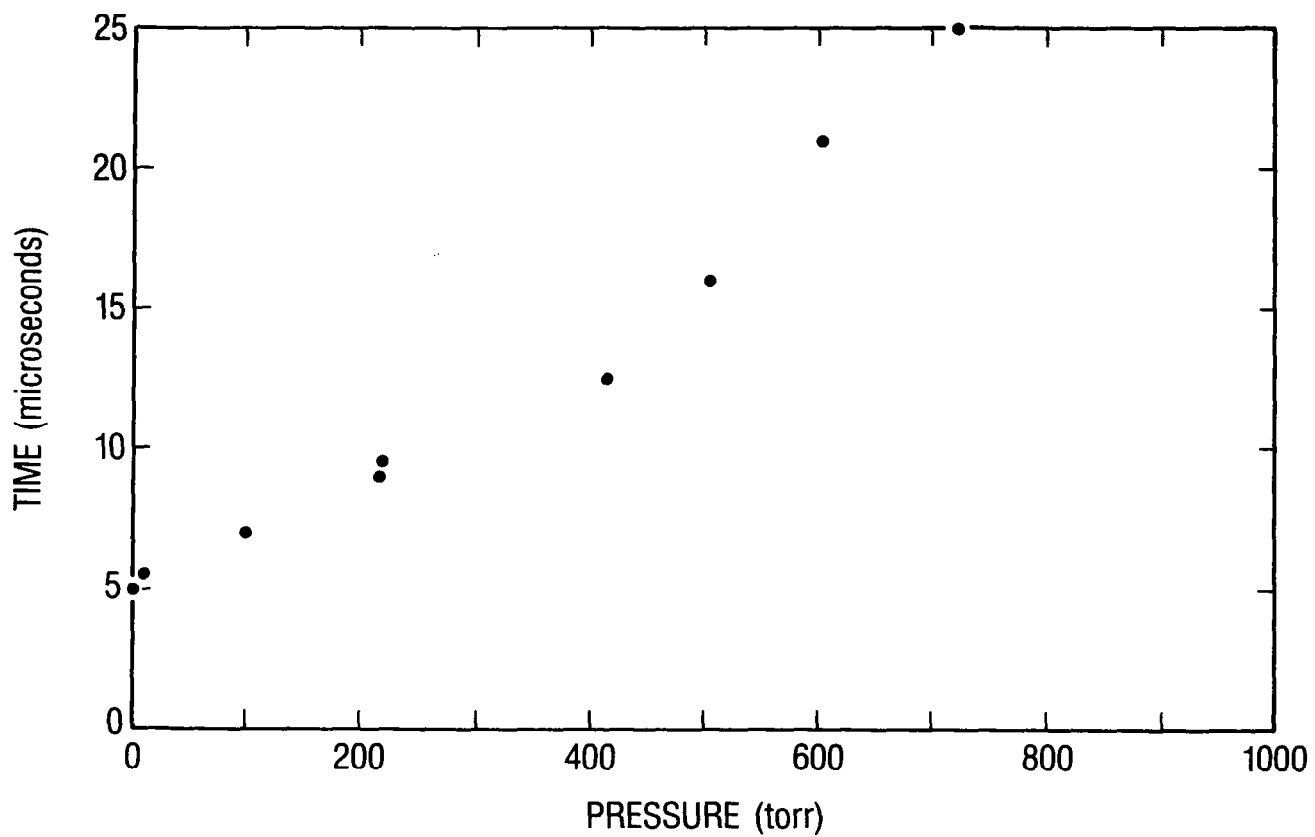
Figure 3.- Membrane response time versus pressure.
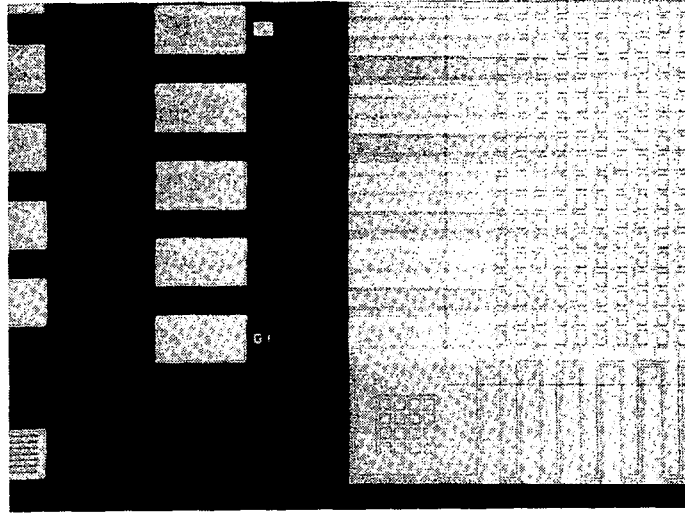
(a) Corner.
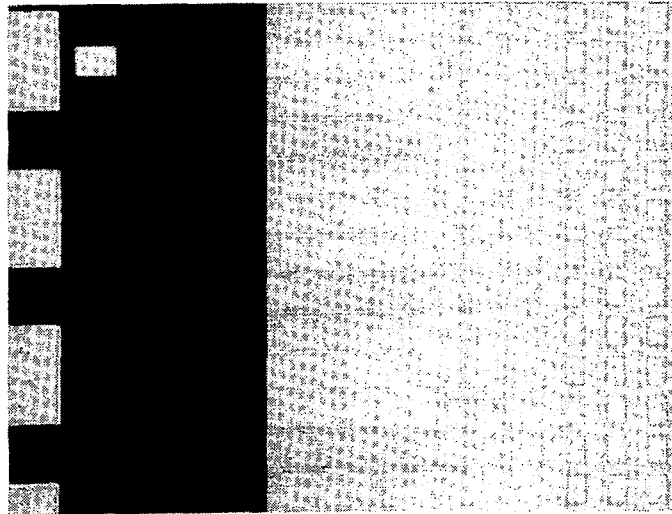
(b) Side of the central array.

Figure 4.- Photomicrographs of the DMD.
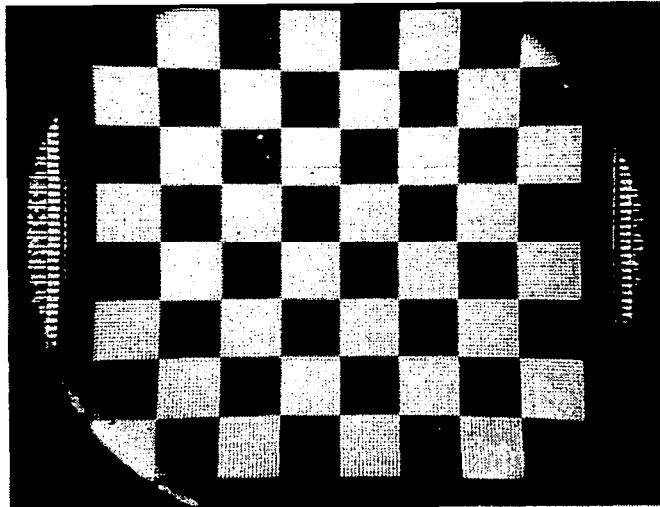
(a) Checkerboard.
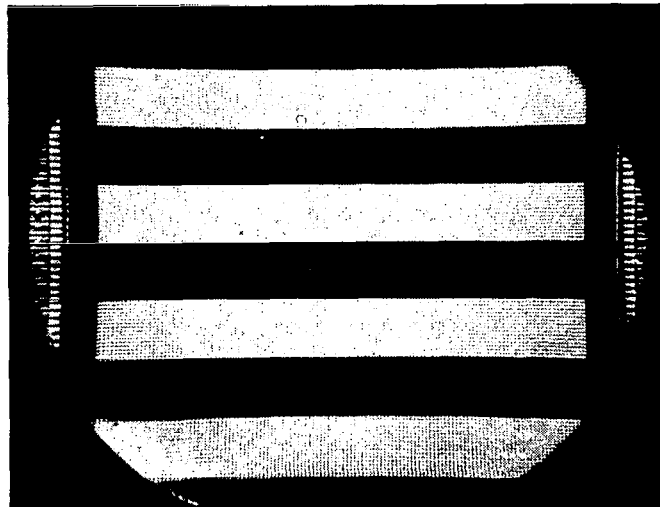
(b) Horizontal bars.

Figure 5.- Schlieren images of the DMD.
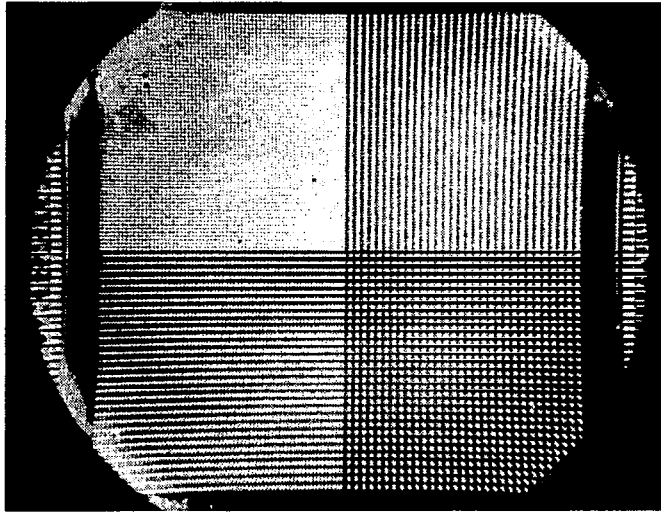
(c) Quadrants showing all cells ON,
horizontal and vertical bars,
and checkerboard.
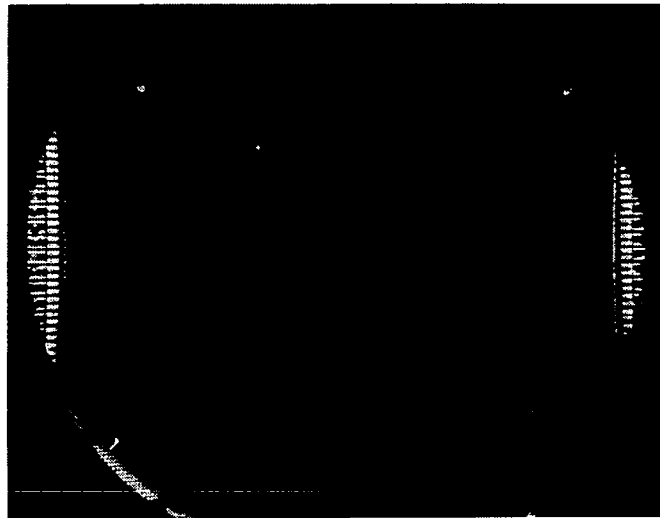
(d) All cells OFF.

Figure 5.- Concluded.
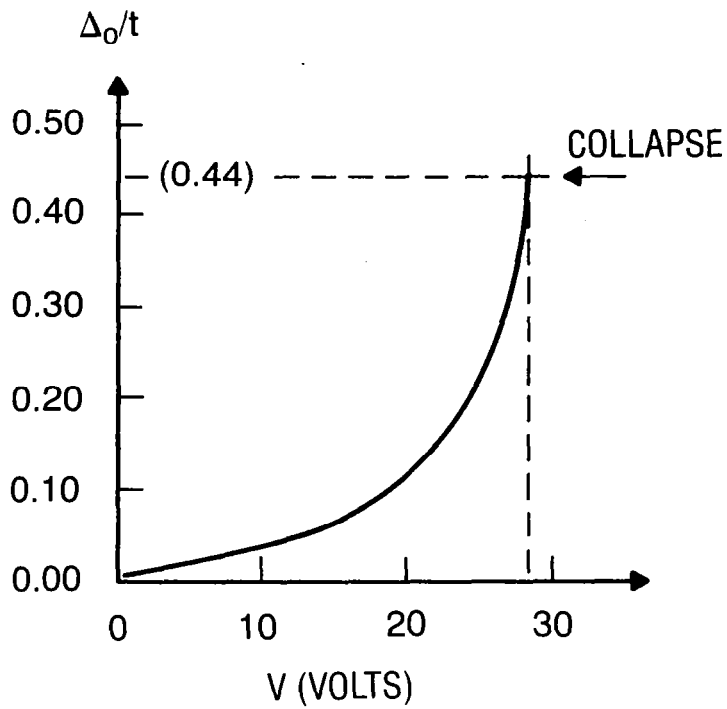
(a) Normalized deflection versus voltage.
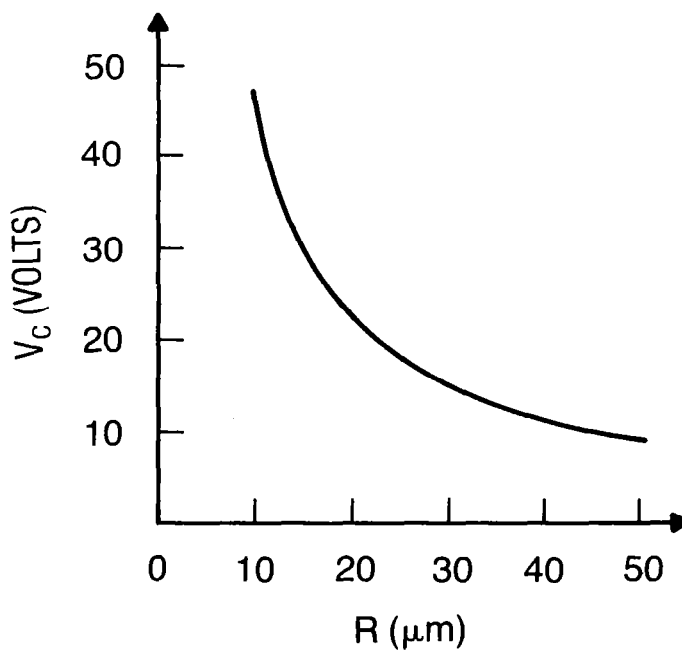
(b) Collapse voltage versus support radius.

Figure 6.- Membrane deflection model.
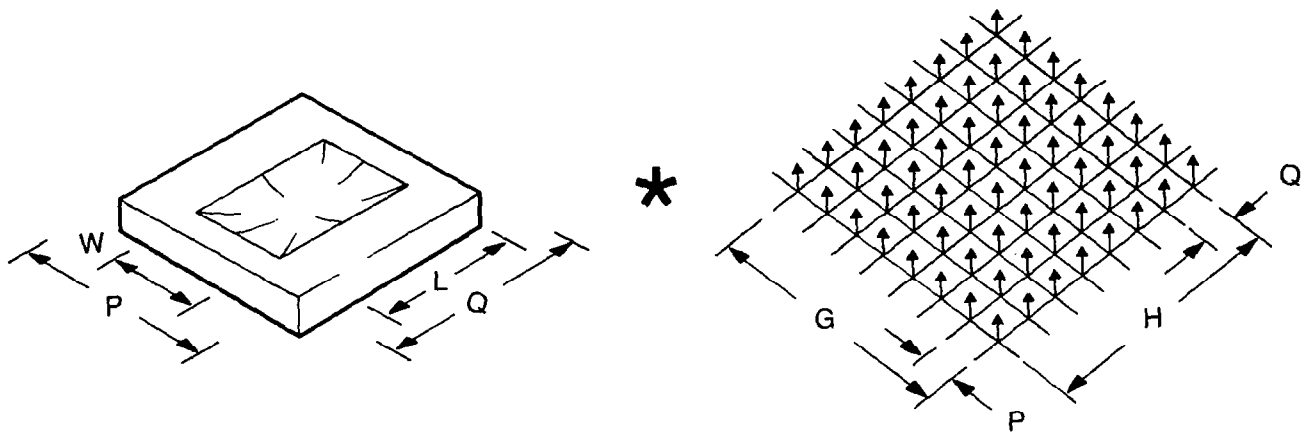
Figure 7.- A pictorial representation of the function $S(x,y) = S_u(x,y) * S_D(x,y)$ used in the Fourier transform model.
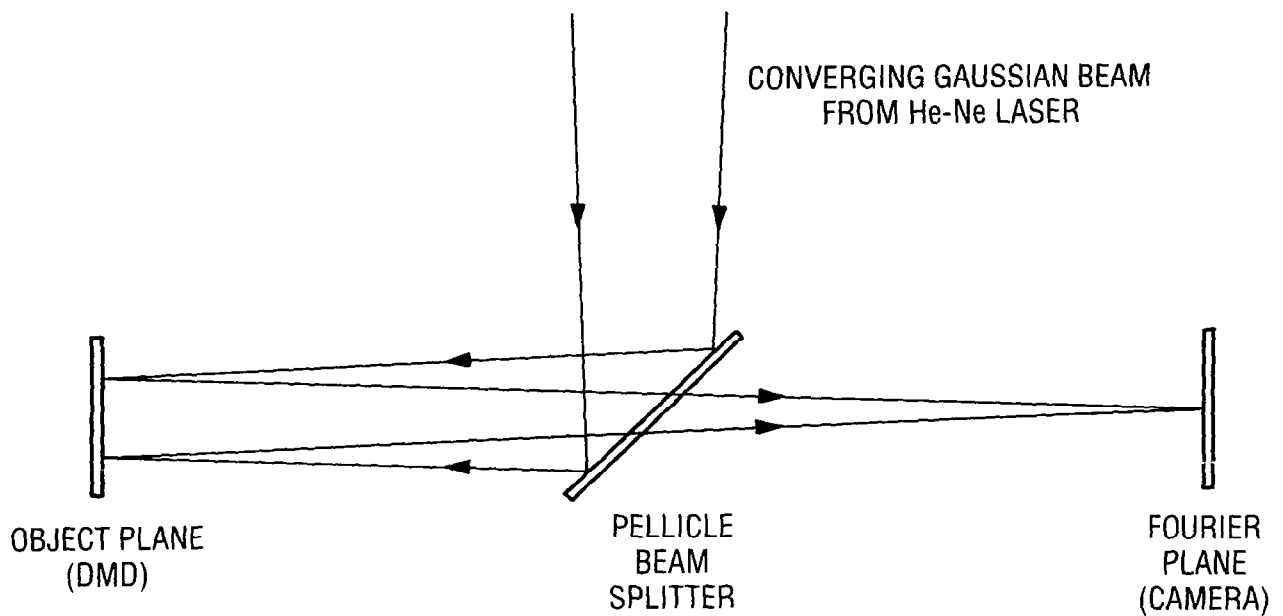
Figure 8.- Fourier transform optical setup.
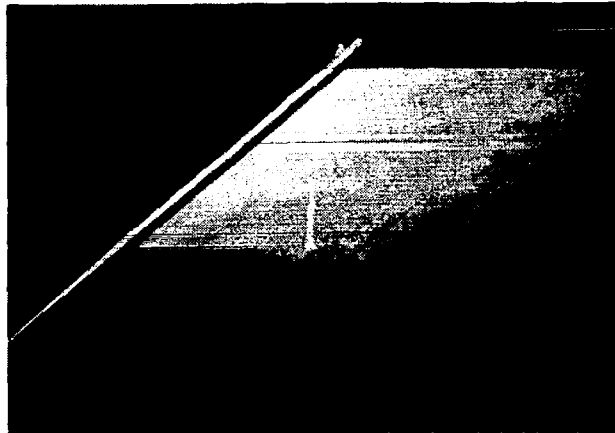
(a) All pixels OFF.
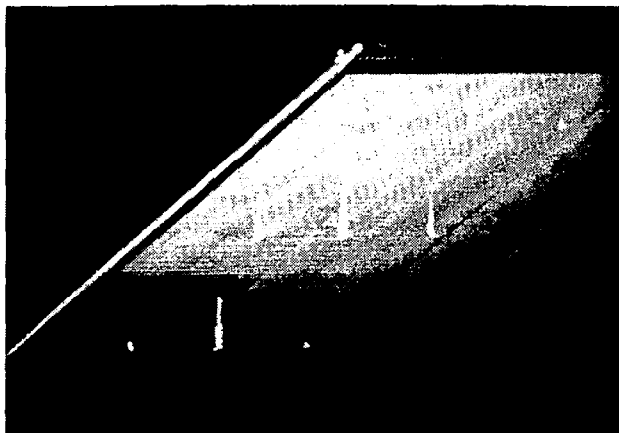
(b) Maxima in first order.

Figure 9.- Optical Fourier transform images of a DMD.
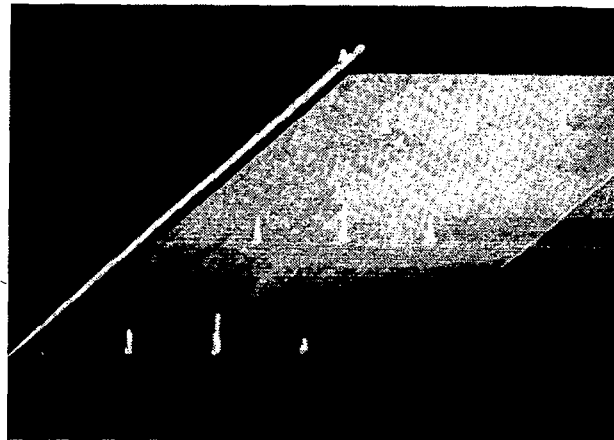
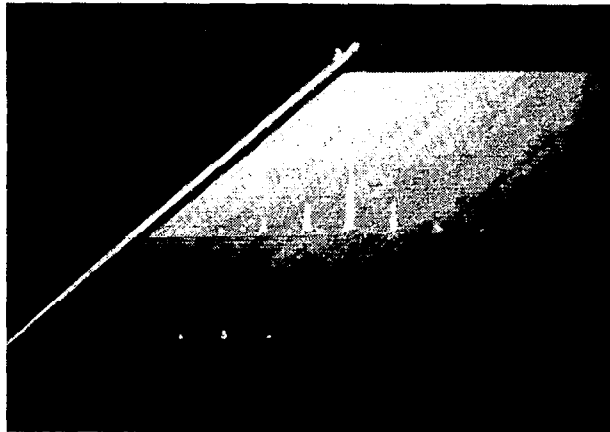(c) Minima in zeroth order.

Figure 9.- Concluded.

AIR GAP VOLTAGE (VOLTS)
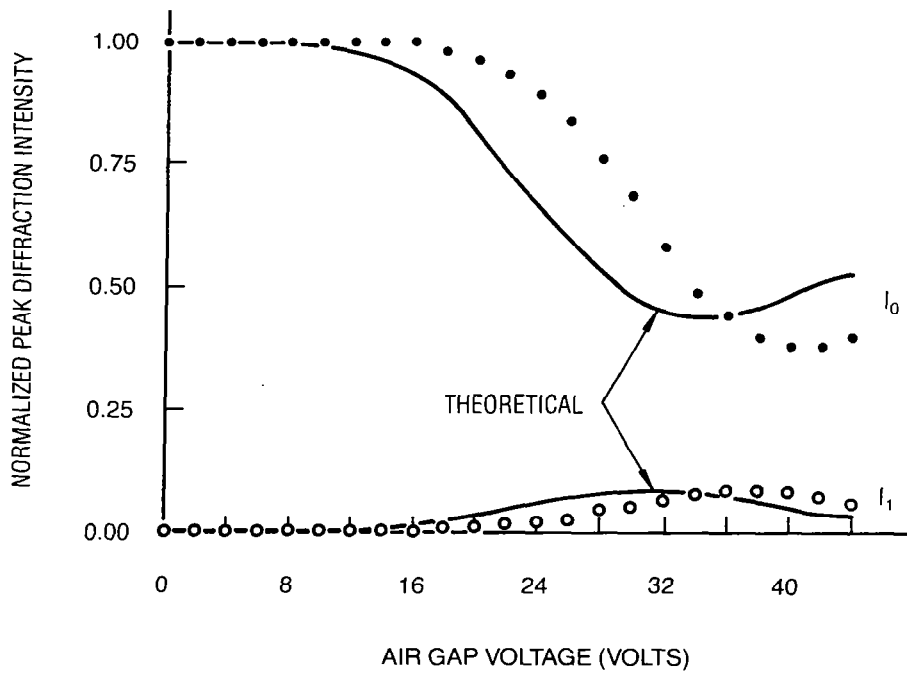
Figure 10.- Zero and first-order diffraction intensity versus air gap voltage for a DMD with all pixels ON.
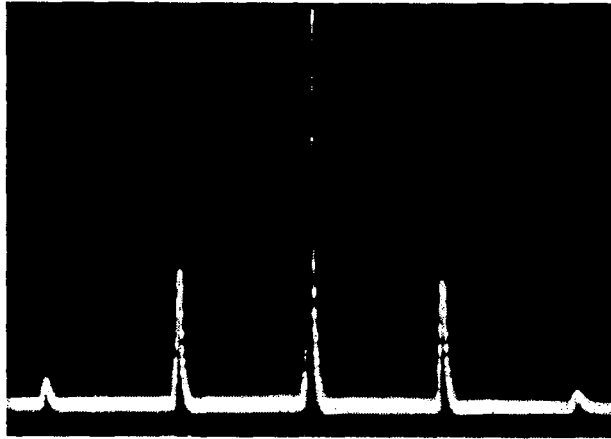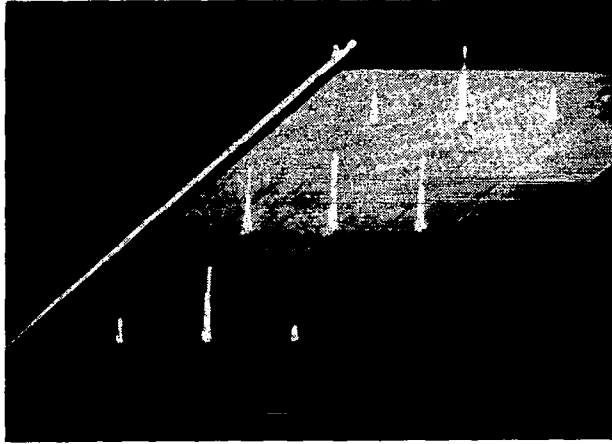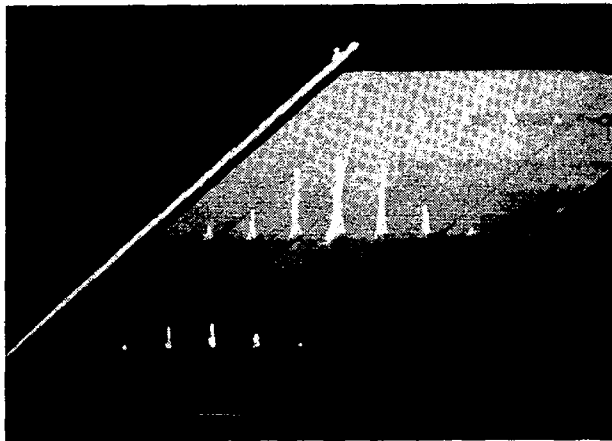
(a) Central video line.

(b) Full video frame.

Figure 11.- Optical Fourier transform image of a DMD
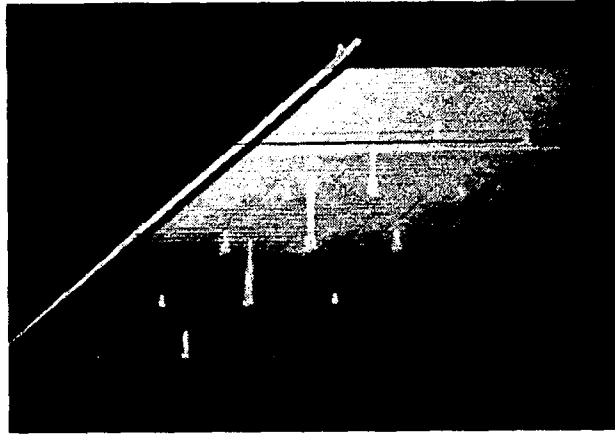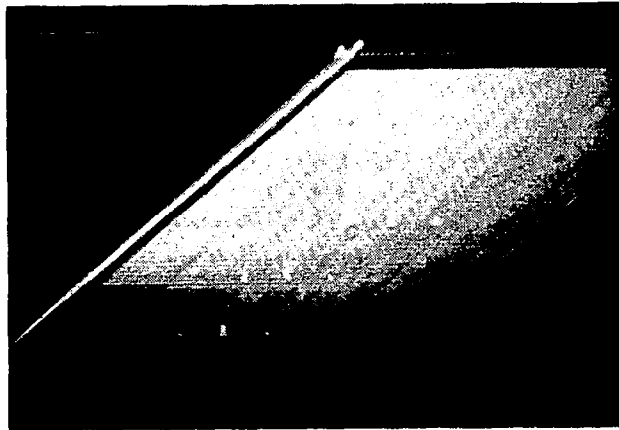at the Nyquist frequency.

(a) All pixels ON.

(b) Vertical bars.

Figure 12.- Optical Fourier transform images of a DMD.

(c) Horizontal bars.

(d) Checkerboard pattern at the
Nyquist frequency.

Figure 12.- Concluded.

THE APPLICATIONS OF SILICON LIQUID CRYSTAL LIGHT VALVES TO

OPTICAL DATA PROCESSING: A REVIEW

U. Efron and B. H. Soffer
Hughes Research Laboratories
Malibu, CA 93065

and

H. J. Caulfield
Aerodyne Research, Inc.
The Research Center at Manning Park
Billerica, MA 01821

ABSTRACT

The applications of the photo-activated, the CCD-addressed, and the variable-grating mode liquid crystal light valves (LCLVs) to optical data processing are described. These applications include image correlation, level slicing, spectral analysis and correlation, bi-spectral image division, and matrix-matrix multiplication.

INTRODUCTION

Coherent optical data processing (CODP) (ref. 1) offers many potential advantages in image processing as well as in the processing of wide bandwidth electrical signals which are amenable to two-dimensional (2-D) form. One of the main limitations of this technology has been the lack of a fast, high-resolution, real-time spatial light modulator (SLM) (refs. 2, 3). These devices impose, on a coherent optical beam, a 2-D image that is derived from either an incoherent optical source (photoactivated SLM) or directly from a properly formatted electrical input signal (electronically addressed SLM). While the first of these tasks can be accomplished with the photoactivated hybrid field-effect mode (HYFEM) liquid crystal light valve (LCLV) (ref. 4), the second can be implemented by the use of the charge-coupled device (CCD)-addressed LCLV (ref. 5).

The first generation, CdS-based photoactivated device is already in production at Hughes. A second-generation, fast-response silicon photoconductor-based device is currently under development at Hughes Research Laboratories. These types of devices operate in conjunction with an optical input source, such as a CRT or a laser scanner to provide a real-time coherent output image (ref. 6). The novel, photoactivated silicon LCLV (Figure 1) with its high-broadband input sensitivity may also be used for direct imaging of the scene and subsequent image processing (e.g., for robotics).

In CODP applications (such as radar signal processing or real-time matched filters), it is desirable to convert the electrical input directly to an optical output image without the intermediate step of first converting to an input image via a CRT. To realize this function, we have designed and developed a novel type of CODP inputting device that uses a CCD array to serially load and store a full frame of analog electrical information which is subsequently transferred in parallel to a liquid crystal (LC) layer (Figure 2). The elimination of the CRT (or equivalent process) from the ODP system greatly simplifies the system; in particular, it eliminates several of the drawbacks associated with it, such as geometrical distortions, stability, and jitter. This device can be used with both coherent and incoherent readout sources, extending in spectral range from the near ultraviolet to the near infrared.

In the following section, some applications of both the silicon photoactivated LCLV and the electronically addressed CCD-LCLV to ODP will be described. These applications include image correlation and level slicing, spectral analysis and correlation, bi-spectral image division, and matrix-matrix multiplication.

OPTICAL PROCESSING APPLICATIONS OF THE SILICON LIGHT VALVES

Image Correlation and Level Slicing

Optical data processing is applicable in two main categories of data processing: the processing of wideband serial signals, and in 2-D or image processing. The photoactivated device is most effectively used in image processing applications, while the CCD-addressed spatial light modulator can be used in both of these categories.

One example of image processing is that of correlating an image with a reference pattern, as shown in Figure 3. Here the images analyzed, A(t) (in video form), and the reference image, B(t), are correlated using a joint-transform technique (ref. 7). The two CCD-SLMs are used as the electro-optic transducers to generate real-time coherent optical images in which amplitudes are superimposed in the Fourier plane. The intensity at the input to the photoactivated device contains, among other terms, the multiplied amplitudes of the two Fourier-transformed images. The photoactivated LCLV is then used to retransform the multiplication image, resulting in the correlation required.

An important application of the photoactivated silicon LCLV is direct-scene imagery followed by coherent processing. This function is required, e.g., in robot vision systems. Here, one can utilize the two important features of the silicon device: (1) its broadband sensitivity (400 to 1,100 nm, with typically 50 $\mu W/cm^2$ at 540 nm); and (2) its fast time response, permitting fast scenery changes to be processed. In the configuration shown in Figure 4, the input scene is imaged and converted to coherent modulation using the Si-LCLV, and is subsequently correlated with a matched pattern using the CCD-LCLV as a programmable matched filter.

The use of the silicon photoactivated device for such direct image processing further permits the dual-frequency mode of the liquid crystal activation to be applied (ref. 8). This may result in cutting the response time from the current 16 ms to 1 to 2 ms.

Another powerful application of optical processing is with the use of a special photoactivated device: the variable grating mode (VGM) SLM (ref. 9). The device is based on the formation of grating-type regions in the LC, the spatial frequency of which is determined by the voltage drop across the LC. Since a very high-impedance photoconductor is required for this light valve, the silicon-MOS configuration is a potential candidate.

A useful application of the device is intensity-to-spatial frequency conversion, shown in Figure 5. Here, the device is used to level slice an input image (shown in three levels: I_1, I_2, I_2). Filtering at the frequency plane with $F = F_2$ (corresponding to $I = I_2$) results in the generation of the $I = I_2$ level of the input image at the output plane.

Large Time-Bandwidth Spectrum Analyzer

We have demonstrated a real-time rf spectrum analyzer with an extraordinarily high resolution and time-bandwidth product using the LCLV, with resolution $<10^2$ Hz. The scheme of the apparatus is shown in Figure 6. The rf signals were amplified and displayed in raster fashion on a CRT. The signals were obviously asynchronous with the raster scan of $\omega_s = 20 \times 10^3$ sec^{-1} and a frame time of 7×10^{-2} sec. The incoherent optical display was focused on the photoconductive input of the LCLV which acted as a coherent-to-incoherent transformer as the output of the LCLV was illuminated with a coherent HeNe laser. This transformation permitted an optical Fourier transformation to be performed. It is well known that the Fourier transform of a raster pattern in time is a raster pattern in frequency, as shown in Figure 6. Low-frequency, Morse-coded tone-modulated rf signals from oil field transmitters displayed the simple textbook A.M. spectral pattern of a carrier and two pulsating sidebands. More complex modulations were also evident in the display. The theoretical resolution is given by the ratio of ω_s to the number of lines, which with $N = 1.4 \times 10^3$ lines is 14 Hz. Because of the falloff in resolution of the LCLV and associated optics, the resolution achieved was somewhat less (80 Hz). An obvious improvement of this system will be the replacement of the CRT-imaging lens with a CCD-addressed LCLV.

In this case, the ultimate, 1,000 array CCD-LCLV would provide 10^6 point resolution over 100 MHz bandwidth at (real-time) frame rates of 100 Hz. Comparable performance, taking into account size and power requirements, will not be achievable by even the most advanced digital technology currently in development (i.e., VHSIC).

A Real-Time Spectrum Analyzer/Correlator

Another important application is real-time spectrum analysis of a given scene. A silicon light valve-based system that can perform this operation is shown in Figure 7. The operation of this system is described below.

The radiation from the scene to be analyzed, I(W), is split by the beam splitter in a Michelson interferometer configuration. Two mirrors, a standard one and a staircase one, are used. The interference pattern at the output of the interferometer (i.e., at the input to the LCLV) is the (spatial) Fourier transform of the input spectrum. This is analogous to a conventional Fourier transform spectrometer (FTS) (ref. 10), in that each of the staircase steps represents one mirror location in a moving mirror spectrometer. The subsequent spatial Fourier transform of the output of the light valve results in the spectral analysis of the input beam at the imaging array. Figure 7 shows the operation of the spectral correlator. The readout laser beam is spatially modulated by the Fourier

transformed reference spectrum using the CCD light valve. This modulated beam is then used as a readout light for the photoactivated light valve. At the input of the photoactivated light valve, the spatial interferogram of the input beam is present. The emerging output beam consists of a multiplication of the input and the reference, Fourier-transformed spectra presented by the CCD-LCLV. The subsequent inverse Fourier transformation carried out by the lens results in the appearance of correlation and convolution terms of the two spectra at the imaging array. This system, which is based on the FTS principle, benefits from two important advantages of the FTS system, namely, the multiplexing, or the Felgett's advantage in signal-to-noise ratio, and the throughput, or the Jaquinot's advantage.

An attractive feature of this system is that it can be used for pattern recognition purposes with a flip of a mirror. In this way, the pattern of the incoming beam, rather than its spectral content, can now be analyzed and correlated with a suitable reference image presented by the CCD light valve, as in Figure 4. The system can thus perform both spectral and pattern correlations of the scene.

The spectral range of this system is limited by the photoactivated light valve since it must be sensitive in the spectral range used. The existing silicon light valve enables us to use the 400-nm to 1,200-nm range. Since the detection of longer wavelengths may require cooling of the light valve, the LC will be the limiting component for such a longer wavelength light modulator. It is estimated that operation up to 3 μm can be achieved using LC operating at low temperatures. Possible photoconductor candidates for such IR light valves are Ge, InAs, InSb, or extrinsic silicon, depending on the cutoff wavelength required.

The spectral resolution largely depends on the manufacturing of the staircase mirror. One could conceive more than 10,000 elements of resolution. It should be pointed out that for the photoactivated and CCD-addressed light valves, a resolution on the order of 10^6 elements is possible.

One obvious limitation for the application above is the intensity of the input beam, or the radiation level from the scene analyzed. Using the silicon light valve, a rough estimate for the input illumination level required is 100 μW/cm^2 in the visible spectral region. Projected performance of such a correlator for two spectral regions is presented in Table 1. Finally, it should be pointed out that other, possibly more efficient methods of self-interference of the incoming analyzed beam have been previously suggested (ref. 11).

A particularly important type of signal processing in which the CCD-LCLV may be used is radar signal processing. This field encompasses ambiguity-function generation and synthetic aperture radar (SAR) processing.

An ambiguity-function generation system using two LCLVs was previously described (ref. 12). The replacement of the photoactivated LCLV by a CCD-addressed LCLV will significantly improve the system, elimating the CRT and the acousto-optic units required.

The Bi-Spectral Imaging/Image Division System

Another potential application of the Si-LCLV for combined spectral and scene analysis is the Bi-Spectral Imaging/Image Division System. The purpose of this system is to obtain the (logarithmic) image of the intensity ratio of the scene at two wavelengths in the 400-nm to 1100-nm spectral range. This operation results in

the enhancement of specific textures in the scene. Thus, it has applications in texture recognition such as the remote Earth-features identification system currently under development by NASA (ref. 13). The schematics of the Si-LCLV-based system are shown in Figure 8. The operation is as follows. The scene imaged by the input optics is split into two channels which are each wavelength filtered in the two spectral regions (λ_1, λ_2) required (400 nm < λ_1, λ_2 < 1100 nm). Then the filtered images are spatially modulated by logarithmic halftone screens with different spatial frequency for each channel, λ_1-F$_1$ and λ_2-F$_2$. A variable attenuation compensator placed at one of the channels acts to compensate for intensity imbalance between the two channels. The two images, each modulated by a different spatial carrier, are then recombined at the input to the silicon liquid crystal light valve. Thus, each of the two images at the two different wavelengths is "tagged" with a different spatial frequency modulation. The photoactivated silicon liquid crystal light valve acts as a sensitive, broadband, incoherent-to-coherent image converter. A spatial Fourier transform is then performed on the data readout by the laser beam. The diffractions of the two wavelength images will now appear separately in the Fourier plane, due to the different spatial carriers for each of those images. Spatial filters corresponding to each of the two halftone screens are placed at the appropriate locations in the Fourier plane. This results in the formation of logarithmic intensity images following a retransforming lens (ref. 14). A 180° phase retardation plate placed at one of the filter locations will result in one of the logarithmic images (λ_2) having a reversed phase with respect to the other. Thus, the amplitude of this image formed at the video detector plane will be proportional to

$$A_{out} = A_1(x,y) + A_2(x,y) \; \alpha \; \log I_1(x,y) - \log I_2(x,y) = \log \left[I_2/I_2 \right]$$

where $I_1(x,y)$ and $I_2(x,y)$ are the intensities of the input images at λ_1 and λ_2, respectively. The image amplitude following reconstruction at the vidicon input will be proportional to $\log [I(\lambda_2)/I(\lambda_1)]$, i.e., to the (logarithmic) ratio of the images at λ_1 and λ_2. Due to the high sensitivity of the silicon photoconductor in the silicon light valve configuration (about 40 μW/cm^2), the imaging system is expected to have sufficient sensitivity for direct imaging of Sun-illuminated scenes.

It should be noted that the same physical region of the light valve is utilized in both channels. This is done in order to minimize non-uniformities in the ratio image obtained by the wavefront substraction. Thus, non-uniformities associated with amplitude or phase defects originating in the light valve will be automatically substrated. The "penalty", however, is the need to use two different spatial frequencies, reducing the bandwidth available for image information.

The Spectral Range of the bi-spectral imaging/image division system is limited by the silicon LCLV (400 nm to 1100 nm). As indicated above, it may be possible to extend the spectral range of the silicon device into the 3- to 5-μm region.

The Dynamic Range of this system is limited by the Si-LCLV, which is typically 100:1. An important advantage of this optical processing system is that the output ratio is presented by a coherent light. This enables a straightforward use of optical post-processing (e.g., ratio image correlation).

The Spatial Resolution of this system depends on the spatial frequencies employed, as well as on the Si-LCLV performance. Taking Fo = 25 cycles/mm at 30%

modulation as the current performance of the Si-LCLV, and using the two carrier frequencies, as: Fo/4 and 3Fo/4, it is found that over 500 pixels of resolution are available using the 43-mm aperture device, with ΔF = Fo/2.

Application of the CCD-LCLV to Systolic Array Processing

Optical numerical processing offers a unique application of CCD-addressed LCLVs. For high speed, an optical numerical processor must utilize spatial parallelism. A two-dimensional data array offers great parallelism but can entail a significant addressing problem. If, however, data could be entered a line at a time and be made to march across the LCLV at the chosen clock rate, a single $N \times 1$ CCD line could address a full $N \times N$ data array. The use of moving electronic data in a plane for such numerical operations was popularized as "systolic array processing" by Kung (ref. 15). The first extension of systolic array processing to the optical domain used one-dimensional transducers (acousto-optic delay lines and CCD detectors) in direct analogy with VLSI transducers (ref. 16). Recently, Bocker et al. (ref. 17) proposed the use of optics for systolic array processing in three dimensions, which electronics cannot do. Their Rapid Unbiased Incoherent Calculator cube (or RUBIC cube) uses two electronically addressed spatial light modulators to move components of matrices A and B across the spatial light modulator at certain clock rates. One possible configuration is shown in Figure 9. Because two pixels are needed for real-number representation, we can multiply the two $(N/2) \times (N/2)$ matrices together with the RUBIC cube in $(N-1)$ clock periods. The cube's ability to multiply very large matrices very rapidly with low power consumption should make the RUBIC cube very important. To use the CCD-addressed LCLV for the RUBIC cube, one must use an external buffer memory which will feed the CCD-LCLV with one line/column displacement in each frame. Alternatively, it may be possible to modify the structure of the CCD-LCLV to incorporate an internal buffer memory. This will enable the line/column clocking operation required. This possibility, although not a simple task, may also be desirable for other applications of the CCD-SLM.

REFERENCES

1. D. Casasent: Coherent Optical Pattern Recognition, Proc. IEEE 67, 813 (1979).

2. D. Casasent: Spatial Light Modulators, Proc. IEEE 65, 143 (1977).

3. D. Casasent: Performance Evaluation of Spatial Light Modulators, Appl. Optics 18, 2445 (1979).

4. J. Grinberg et al.: A New Real-Time Noncoherent-to-Coherent Light Image Converter, Opt. Eng. 14, 217 (1975).

5. M. J. Little et al.: CCD-Addressed Liquid Crystal Light Valve, Soc. Info. Display 1982 Tech. Digest, 250 (1982).

6. U. Efron, P. O. Braatz, M. J. Little, R. N. Schwartz, and J. Grinberg: Silicon Liquid Crystal Light Valves: Status and Issues, Opt. Eng. 22, 682 (1983).

7. J. E. Rau: Detection of Differences in Real Distributions, J. Opt. Soc. Am. 56, 1490 (1966).

8. C. S. Bak et al.: Fast Decay in a Twisted Nematic Induced by Frequency Switching, J. Appl. Phys. 46, 1 (1975).

9. B. H. Soffer et al.: Variable Grating Mode Liquid Crystal Device for Optical Processing, Proc. SPIE, Devices and Systems for Optical Signal Processing 218, 81 (1980).

10. P. R. Griffith: Chemical Infrared Fourier Transform Spectroscopy (J. Wiley and Sons, 1975), Chapter 1.

11. H. J. Caulfield: Holographic Spectroscopy, in Advances in Holography, Vol. 2, N. H. Farhat, ed. (M. Dekker, Inc., N.Y., 1976), p. 151.

12. W. P. Bleha et al.: Applications of the Liquid Crystal Light Valve to Real-Time Optical Data Processing, Opt. Eng. 17, 371 (1978).

13. R. Gale Wilson and W. Eugene Sivertson, Jr.: Earth Feature Identification and Tracking Technology Development, Proc. SPIE, Smart Sensors 178, 185 (1979).

14. S. R. Dashiel and A. A. Sawchuk: Nonlinear Optical Processing: Analysis and Synthesis, Appl. Opt. 16, 1009 (1977).

15. H. T. Kung: Special-Purpose Devices for Signal and Image Processing: an Opportunity in Very Large Scale Integration (VLSI), Proc. SPIE 241, 76 (1980).

16. H. J. Caulfield, W. T. Rhodes, M. J. Foster, and S. Horvitz: Optical Implementation of Systolic Array Processing, Opt. Commun. 40, 86 (December 1981).

17. R. P. Bocker, H. J. Caulfield, and K. Bromley: Rapid Unbiased Bipolar Incoherent Calculator Cube, Appl. Opt. 22, 804 (1983).

TABLE 1.– PROJECTED SPECIFICATIONS OF THE Si–LCLV–BASED FOURIER TRANSFORM SPECTROPHOTOMETER/CORRELATOR

1. VISIBLE RANGE: 400 nm $<$ λ $<$ 1200 nm

    BANDWIDTH: Δf = 16,700 cm^{-1}

    NO. OF RESOLUTION ELEMENTS: N = 100 X 100

    SPECTRAL RESOLUTION: δf = 1.67 cm^{-1}

    MAXIMUM "STROKE": δD_{MAX} $\simeq$ $1/\delta f$ = 0.6 cm

    "ROUGH" STEPS: δD_X = 0.6 cm/100 = 60 μm

    "FINE" STEPS: δD_Y = 60 μm/100 = 0.6 μm

2. 1.5-μm TO 4.5-μm REGION

    BANDWIDTH: Δf = 4440 cm^{-1}

    NO. OF RESOLUTION ELEMENTS: N = 100 X 100

    SPECTRAL RESOLUTION: δf = 0.44 cm^{-1}

    MAXIMUM "STROKE": δD_{MAX} = 1/0.44 = 2.27 cm

    "ROUGH" STEPS: δD_X = 227 μm

    "FINE" STEPS: δD_Y $\simeq$ 2.27 μm

STEPS DIMENSION (BOTH CASES) $\simeq$0.5 mm X 0.5 mm FOR 50-mm APERTURE
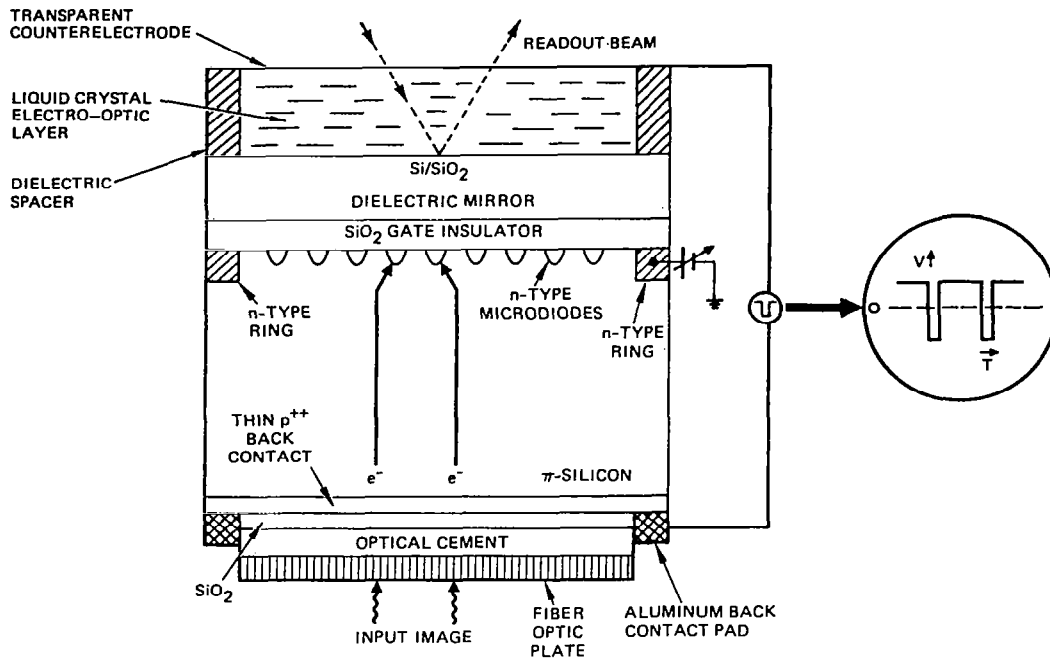
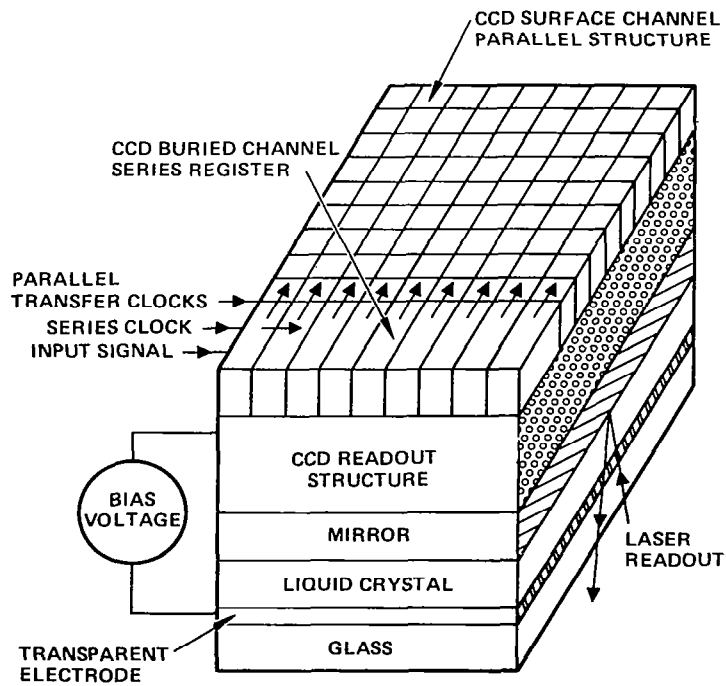Figure 1.- A cross section of the photoactivated silicon liquid crystal light valve.

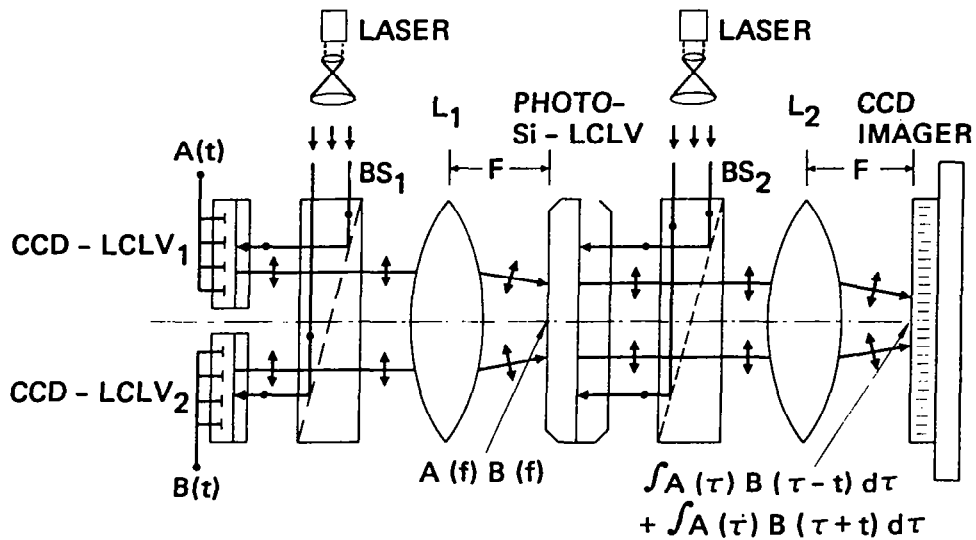Figure 2.- Structure of the CCD-addressed liquid crystal light valve.

Figure 3.- A joint transform-based image correlation system
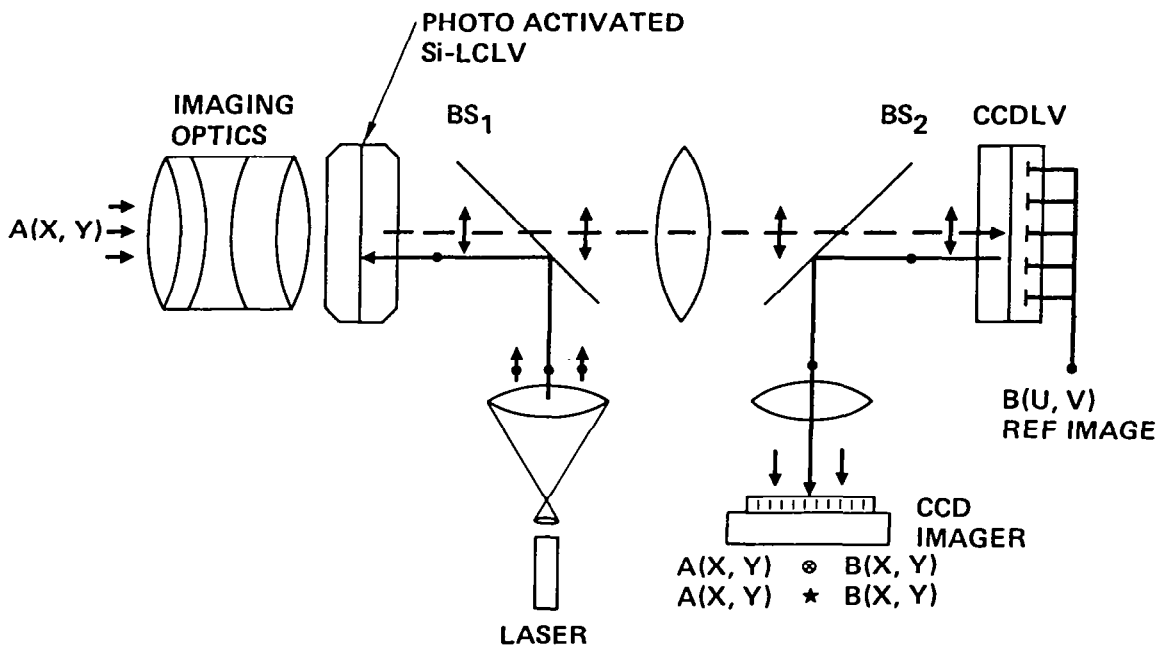using CCD-addressed and photoactivated devices.

Figure 4.- An imaging/scene correlation system using the
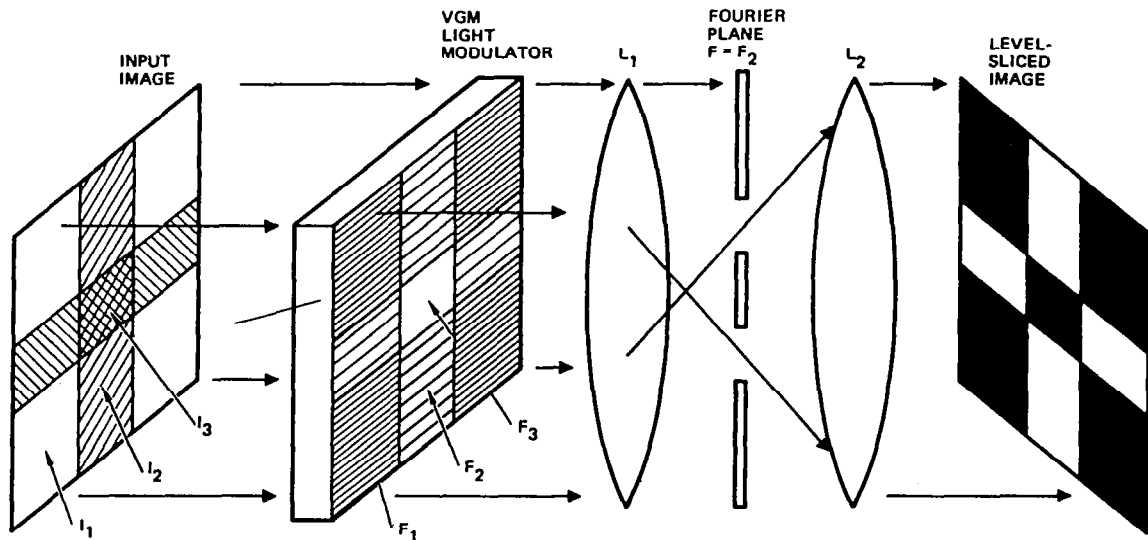silicon liquid crystal light valves.

Figure 5.- Intensity level slicing of an image using the VGM modulator.
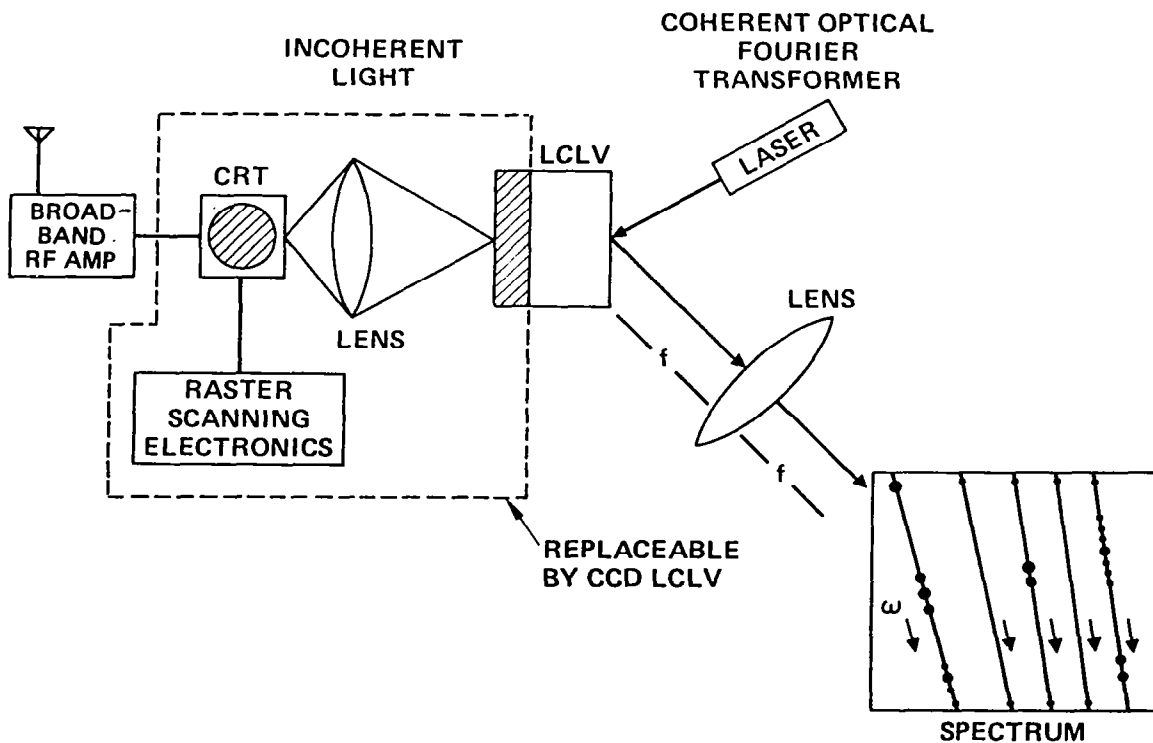The $I = I_2$ level is reproduced at the output.

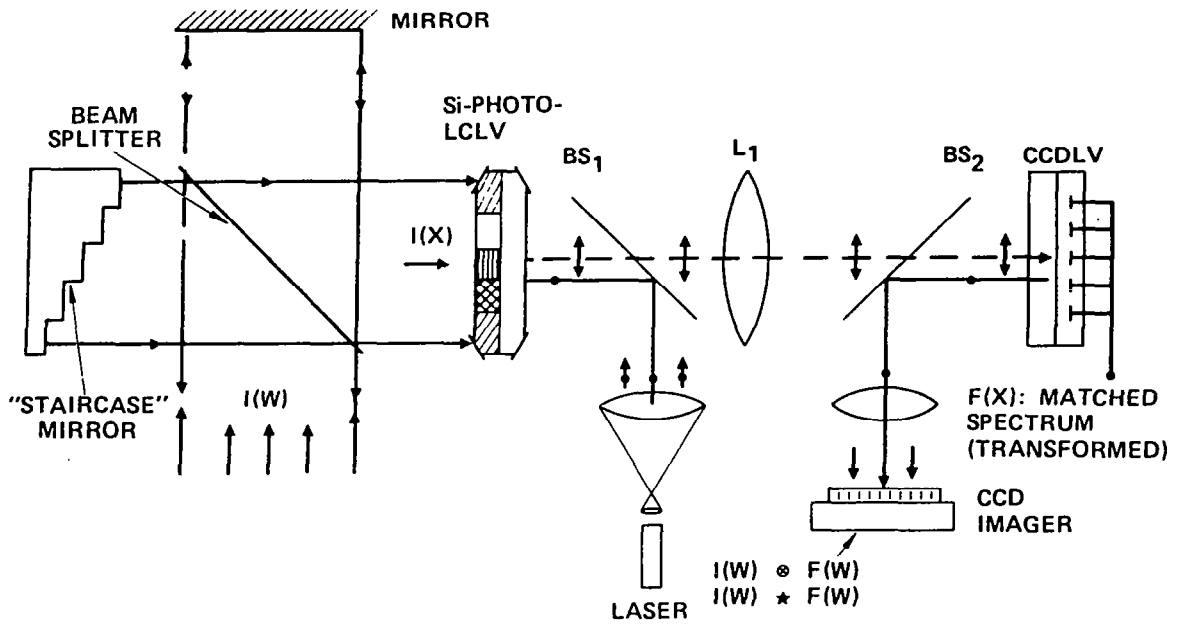Figure 6.- Real-time, large time-bandwidth spectrum analysis.

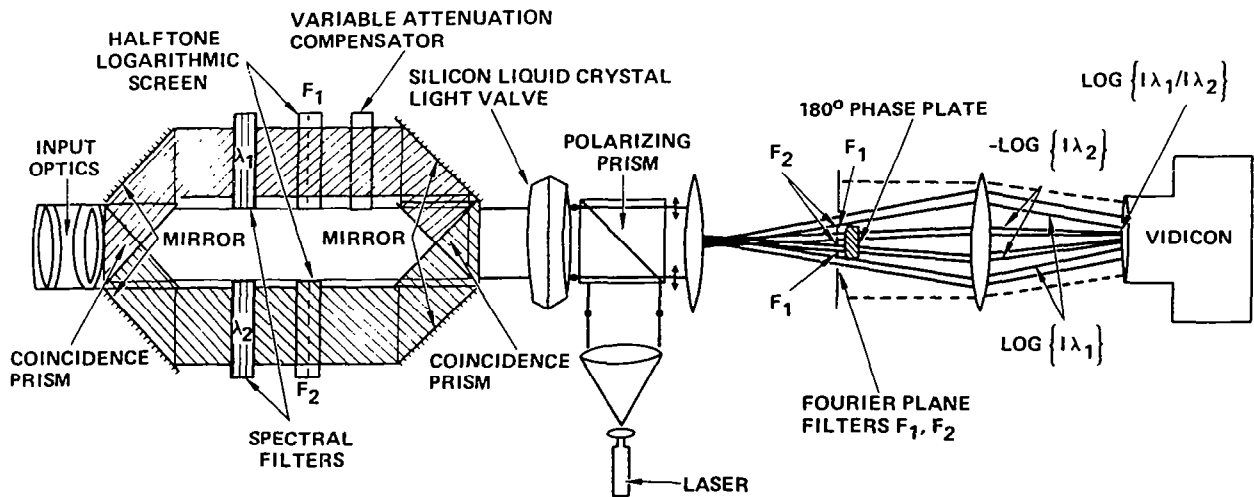Figure 7.- A correlation system using the silicon LCLV.

Figure 8.- A bi-spectral imaging/image division system based
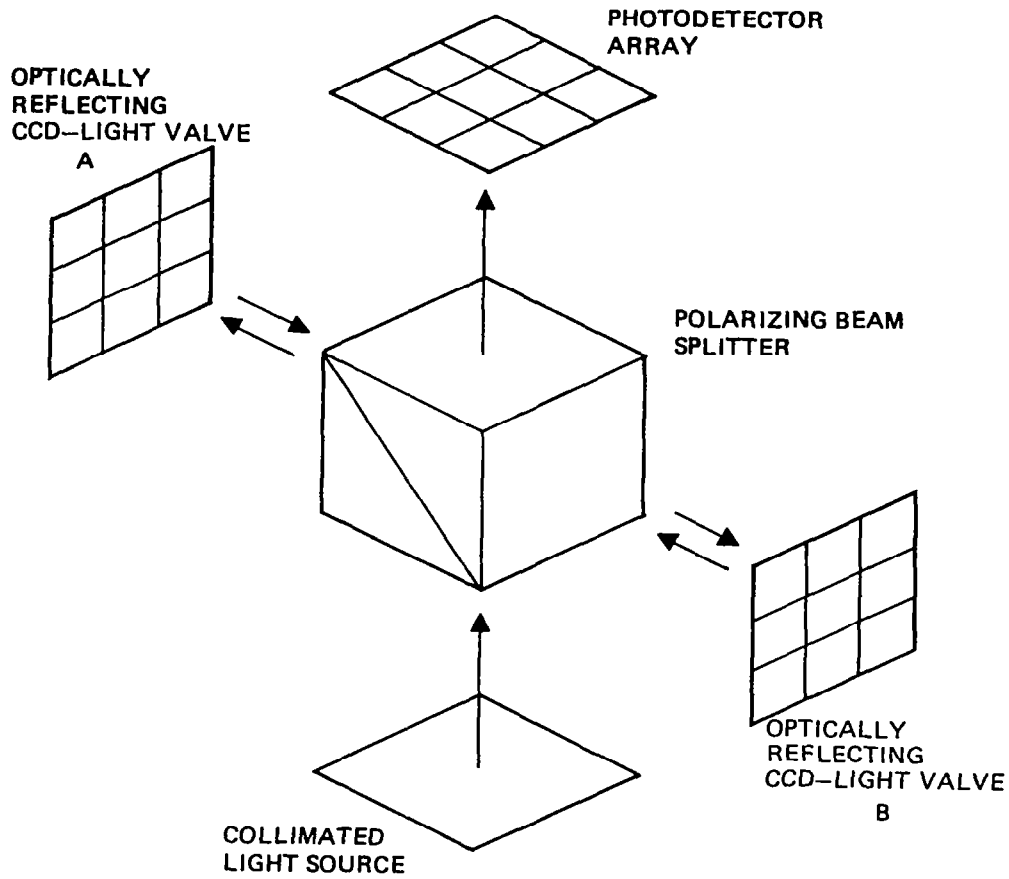on the silicon LCLV.

Figure 9.- The application of the CCD-addressed LCLV's
in a "RUBIC cube" system.

MAGNETO-OPTIC GARNET AND LIQUID CRYSTAL OPTICAL SWITCHES*

J. A. Krawczak, E. J. Torok, W. A. Harvey,
F. G. Hewitt, and G. L. Nelson

Sperry Corporation, Computer Systems, Defense Systems Division
Box 43525, St. Paul, MN 55164-0525

SUMMARY

Magnetic stripe domain and liquid crystal devices are being developed and evaluated as fiber optic switches that can be utilized for nonblocking type nxm optical matrix switches in networking and optical processing. Liquid crystal switches are characterized by very low insertion loss and crosstalk, while stripe domain switches commutate in less than one microsecond. Both switches operate on multimode, randomly polarized fiber light with potentially large values for (n,m).

INTRODUCTION

Fiber optics is emerging as the solution to many systems' interconnect problems, including optical processing and local area networks. The advantages of fiber optics over wire interconnects are well known; however, networking systems that are now appearing fail to take full advantage of the vast data rate capability offered by the fiber optic alternative.

An envisioned data network that portrays the current direction of fiber system interconnects is shown in Figure 1. This is basically a contention ring topology with compatible as well as incompatible subscribers. A subscriber is, in general, any component that has access to the ring; mainframes, terminals, sensors, satellite up/down links are all within subscriber space. These networks can be quite complex. Some subscribers connect directly to the ring, others to the ring via bus tapoff sections that feed a small number of users. Interface units are often necessary to translate data for the various diverse users. One central feature of this network is the lack of immediate access – a subscriber has to wait until the ring is free of traffic before attempting communications. This has led to the need for data collision avoidance circuitry. In addition, to achieve even modest data transfer rates, all subscribers must be equipped with high speed data transfer circuitry. Another salient feature is that the data exchange between a subscriber pair is available to all subscribers. Thus, sophisticated coding techniques are required

to protect sensitive data. A spread spectrum technique that would supply protection as well as eliminate data collision difficulties has been suggested, but the spreading ratio is greater than 100 for just a few subscribers so that real information transfer rates are severely limited, even with fiber optics.[1]

A fiber optic network topology that offers immediate access to all subscribers and also insures data privacy is obviously advantageous. Such a topology is shown in Figure 2 in simplified schematic form. A nonblocking optical switch controls interconnects between subscriber pairs or even amongst subscribers in a conferencing mode. This is a true star arrangement rather than a typical fiber star topology that is actually a logical bus. Like the general ring topology, a true star may have short bus tapoffs for a few remote subscribers.

In order to realize the general architecture of Figure 2 it is necessary to have available nxm optical matrix switches where (n,m) values could range from 1 to 1024. Certain desirable properties for any candidate switch technology are delineated in Figure 3. Brief reviews and recent results in liquid crystal and stripe domain garnet nonblocking matrix switches are the subject of this paper.

LIQUID CRYSTAL SWITCHING

Brief Review

Two different techniques have been studied for liquid crystal switching. One is based on twisted nematics where the liquid crystal acts like a half-wave plate. A polarizing prism diverts light along one of two possible directions depending on whether the active half-wave plate is present or is erased by a voltage across the liquid crystal.[2] The second type depends on a voltage induced change in the index of refraction of a liquid crystal to accomplish switching and will be discussed more thoroughly.[3]

As seen in Figure 4, a randomly polarized input beam of free laser light or of collimated multimode fiber light impinges on the left interface between the liquid crystal and the dove prisms. This point is a passive polarizing beam splitter so that the perpendicular and parallel components of the light field traverse separate paths inside the switch. At the right-hand, active interface in Figure 4A, the index of refraction of the parallel component is much greater in the glass than in the liquid crystal causing total internal reflection. Hence, parallel light emerges through the upper prism. For the perpendicular component, the index is only slightly lower in the liquid crystal so that at the angle of incidence the light is transmitted in parallel with the parallel component. Upon application of a voltage above a threshold level the

index changes for the parallel and perpendicular component provide full transmission through the lower prism (4B). Thus, this liquid crystal device switches unpolarized multimode light with nearly zero loss because the losses of liquid crystal materials are small at useful wavelengths.

Typically, the voltage across the liquid crystal is applied to transparent, conductive electrodes such as deposited indium-tin-oxide. An audio frequency a.c. voltage is preferred to minimize chemical deterioration of the liquid crystal. Current levels are in microamps and switching time is near one millisecond. Figure 5 indicates that the voltage build-up to total switching is gradual. For instance, near V = 5 vrms there are approximately equal amounts of light in each output position. This means that the device exhibits an active star coupler mode. The device is 1 to 1 or 1 to 2, depending on the applied voltage.

(1,4) and (4,4) Models

Although the basic liquid crystal switch is a symmetric 2x2, more elaborate models have been constructed and evaluated. A 1x4 switch, along with measured data, is shown in Figure 6. With this switch there is a 3 dB polarization loss which is included in the measured loss. However, the unswitchable component can be picked off at the front end of the switch with a polarizing beam splitter and sent to a parallel 1x4. This would amount to a 1x8 switch or two 1x4's. Like the 1x2 switch, the 1x4 also has an active star coupler feature in that input light can be distributed to all outputs simultaneously or individually, depending on the voltages at the electrical control points.

On concatenating two 1x4 switches, it is possible to construct a 4x4 matrix switch with nonblocking capability.[4] This is depicted in Figure 7 where the 32 electrical control points have been suppressed in the interest of clarity. There are 24 distinct output states corresponding to all possible pairings between input and output. Also included in the figure is performance data at .633 microns.

MAGNETO-OPTIC SWITCH

Brief Review

The active component of this deflector is a dynamically alterable, solid-state phase diffraction grating that is the energetically favored domain structure of properly configured magnetic materials. The light deflector materials of current interest are bismuth substituted rare earth iron garnet films grown by high temperature liquid phase epitaxy on garnet substrates similar to the substrates used in magnetic bubble memories. Several papers,[5,6] have discussed the operating principles of the stripe domain grating structure; thus only a brief description will be presented here.

One of the natural magnetic states of bismuth garnet expitaxial films is an array of stripes of alternating magnetic vector. This is schematized in Figure 8 where the relevant magnetic and optical vectors have been included. The width of each stripe d is between 0.5 and 5 μm, the length can extend to centimeters, and the film thickness is usually < 50 μm. The parallel and antiparallel nature, $M_{\pm}$, of the periodic normal components ot the magnetization together with the enhanced Faraday effect in bismuth garnet, produce phase diffraction of an incident plane wave of visible or near-infrared radiation. This is because the direction of the optical electric field is rotated clockwise in up stripes and counterclockwise in down stripes as the wave progresses through the material. Thus, the emerging electric vector fluctuates at the spatial frequency of the magnetic stripe domains. Because the Faraday effect is a manifestation of circular magnetic birefringence, the interaction of the light with the garnet is independent of incident polarization. Figure 9 is a photograph of a stripe array in the ferrimagnetic film, YIG, observed under Faraday microsopy. In the far-field emerging light adds constructively at angles m, given by

$$\sin\theta_m = \frac{m\lambda}{\Lambda},$$

where m is the order number, λ the incident wavelength, and Λ the grating period. In the special case where each stripe has the same width, even orders are suppressed. Magnetic apodization at the transitions between even and odd stripes can discourage higher orders, as well.

Light intensity in each of the two first-order conjugate beams is governed by the rule

$$\frac{I}{I_o} = 0.405 \exp(-\alpha T) \sin^2 FT,$$

where α is the optical absorption of the material, T the film thickness, and F the specific Faraday rotation. As much as 81% of the incident intensity can be passed to the first order if the material is lossless and if the Faraday effect produces an exact $\pm$ 90° rotation of the optical electric field. Thus, 3 separate factors can be manipulated to maximize diffracted intensity. Reductions in optical absorption in garnet films have been obtained through doping techniques.[7] Enhancements in Faraday rotation are currently being sought using bismuth substituted garnet on large lattice substrates. Finally, in the near infrared where garnet is transparent, multipass optics has been used to provide the optimal path length of many times the actual film thickness.[8] The diffraction efficiency of a large lattice sample with multipass optics is shown in Figure 10. This curve is the result of calculations made on single pass absorption and Faraday rotation measurements taking the sum of all the diffracted orders.

The direction and period of the magnetic grating are controllable by a magnetic field H that is applied in the plane of the film. Typically H is derived from two small Helmholtz pairs or stripline coil sets oriented perpendicularly so that any field direction in the plane is attainable by programming the coil

currents. Required field intensities are around 100 gauss, which is similar to what is required for electron beam deflection in cathode ray tubes, although much lower electrical power is required since the field volume can be 1 cm^3. Switching times of less than 150 nanoseconds have been achieved.

Though there exist a number of applications for solid state, two-dimensional light deflectors, switching of randomly polarized, multimode fiber light is most suited to stripe domain technology. A stripe domain deflector can serve as an nxm switch for switchboard PABX's or certain optical processing functions or it can serve as a 1xm switch with active star coupling.

Garnet Integrated Fiber Optic Switchboard

Ruggedized, nonvolatile nxm fiber optic switchboards with submicrosecond switching time are expected to find use in such applications as field communications systems, shipboard distributed computing systems and airborne and space computing or display systems. In shipboard computing systems, in which any subscriber can transfer data to any other and all can transfer data simultaneously, the desired number of inputs and outputs may approach 200. For field communications the number may approach 1000. The magneto-optic system described next is a way of achieving switchboards that can service a large number of subscribers.

Figure 11 shows an integrated nxm fiber optic switchboard, using a single magneto-optic film with a mirror on the back. The area of the film is divided into n areas corresponding to the n input fibers. Each area has a set of two striplines (shown in Figure 12) that can supply a field in any in-plane direction to that area alone without disturbing the neighboring areas. Thus, in effect, the single stripe domain film an inch in diameter becomes an array of many independent light deflectors.

Each input fiber has its own separate input lens. This may be a short focal length conventional lens (e.g. a microscope objective) or a gradient index lens. Both have been tested; the former causes less attenuation; the latter is easier to assemble. The purpose of the input lens is to collimate the diverging light from the input fiber. Thus the input fibers and input lenses may be set a considerable distance back from the stripe domain film, and still the light from a given fiber will fall on only the small spot corresponding to one of the integrated deflectors.

Each output fiber has its own output lens. The purpose of an output lens is to demagnify the beam being sent to an output fiber so that all the light from that beam will enter the fiber.

There is a single long focal length lens in front of the stripe domain film.

The purpose of this lens is to ensure that if all the integrated deflectors are in the same residual magnetic state (i.e. no applied field and the stripes everywhere have the same orientation) then the light from each will go to one and only one output fiber. The reason that this works is simply that a lens focuses all collimated light to a single point a focal length away. Since in this reflective configuration the light passes twice through the lens, the effective focal length is half that for a single pass. This lens makes non-volatile operation possible and furthermore maximizes the number of possible output fibers. With this lens one need know only the address of the desired output fiber to determine the proper field pulse for any input fiber.

Matrix - Matrix Multiplication

The integrated fiber optic switchboard can also be used as a matrix - matrix multiplier.[9] The variable mask is the garnet film and the variation in intensity can be accomplished by causing the light beam to partially miss the fiber end. Such experiments on matrix - matrix multiplication have not yet been performed, however.

Garnet 1xm Switch With Active Star Coupling

In the 1xm mode of operation, there is a single input bus fiber and several output fibers arranged around a circle with radius corresponding to the natural zero field deflection angle of the grating.[10] Normally, advantage is taken of microoptic devices such as gradient index lenses to improve the coupling. Rotation of the grating to connect the selected output fiber to the bus fiber can be accomplished in submicrosecond times using pulse currents in the deflection coils. Sustaining currents are not required to lock the grating into the new orientation because the stripe domain field is stable at any orientation in the plane. Thus switching power can be quite low. Because of grating reciprocity, light is transferable from the output fibers onto the bus fiber for bidirectional communications. Figure 13 reports the experimental results obtained from a working model of a garnet 1xm switch at .633 microns. The high insertion loss reflects the relatively high absorption of bismuth garnet in the visible. Using improved materials and possibly interference filter techniques that transfer zeroth order light to first order should reduce insertion loss substantially. Switching times on this model were inductance limited due to the bulk drive coils. More recently a switching time of 140 nsec has been observed using deposited stripline coils.

In addition to the conventional rotations of the linear stripe domain array that provides for 1xm switching the grating is also dynamically configurable to a 1 to m switch where first order light is divided equally amongst all outputs.

This makes for an active star coupler option. To accomplish this, the stripe domain grating is altered from linear to radial with constant periodicity. A mechanical grating of this sort would be very difficult to generate. However, a stripe domain grating achieves this quite simply by forming short, truncated domains that point toward the center of the array.

The angular spectrum of a general grating of this type is discrete in the radial spatial coordinate but continuous in azimuth. That is, the far-field diffracted light appears as thin, uniformly illuminated annuli with radii

$$r_m = \ell \tan \left[\sin^{-1} \frac{m\lambda}{\Lambda} \right],$$

where ℓ is the distance from the grating to the plane of observation. The continuous distribution for first order light is depicted in Figure 14.

Figure 15 shows an apparatus for inducing a constant period radial grating in a stripe domain array. A pulsed, point magnetic pole oriented perpendicular to the plane of the array provides the appropriate field geometry to establish the grating. It was seen that the grating could be altered from linear to constant period radial with a single 10 microsecond current pulse. A Faraday microscopy photograph of the resulting grating is presented in Figure 16. On attempting to return the grating to linear the ferrite needle was seen to short circuit the field from the (x,y) drive coils. This was eliminated by replacing the ferrite needle with a small spiral stripline drive coil bonded directly to the sample. Then the switching of the grating from linear to radial occured in 5 microseconds and there was no difficulty returning to the linear grating.

Ultimately, it is planned to fabricate the (x,y) coils and the spiral coil on one overlay. This should result in a fast, solid state switch that has an active star coupler option and occupies approximately 1 cubic centimeter.

CONCLUSIONS

Fiber optic networking problems could benefit immensely from the development of large capacity optical mode matrix switches that have most of the properties of their electronic counterparts, yet operate at the bandwidth routinely available to fiber optics. Both liquid crystals and magnetic stripe domains are candidate technologies for matrix switching. Further work is necessary though, to perfect these technologies and fit them into data processing interconnects.

REFERENCES

1. Smythe, C.; Spracklen, C. T.: A High Speed Local Area Network Using Spread Spectrum Code Division Multiple Access Techniques. Proceedings of FOC/LAN 83, Oct. 1983, P. 131.

2. Wagner, R. E.; Cheng, T.: Electrically Controlled Optical Switch For Multi-Mode Fiber Applications. Applied Optics, Vol. 19 No. 17, Sept. 1980, P. 2921.

3. Soref, R. A. ; McMahon, D. H. ; Total Switching Of Unpolarized Fiber Light With A Four-Port Electro-Optic Liquid-Crystal Device. Optics Letters, Vol. 5, No. 4, April, 1980, P. 147.

4. Soref, R. A.: Electrooptic 4x4 Matrix Switch For Multimode Fiber-Optic Systems. Applied Optics, Vol. 21, No. 8, April, 1982, P. 1386.

5. Johansen, T. R.; Norman, D. E.; Torok, E. J.: Variations Of Stripe-Domain Spacing In A Faraday Effect Light Deflector. Journal Of Applied Physics, Vol. 42, No. 4, March, 1971, P. 1715.

6. Scott, G. B.; Lacklison, D. E.: Magnetooptic Properties and Applications Of Bismuth Substituted Iron Garnets. IEEE Transactions On Magnetics, Vol. MAG-12, No. 4, July 1976, P. 292.

7. Nelson, G. L.; Harvey, W. A.: Optical Absorption Reduction In Bi, $Lu_2 Fe_5 O_{12}$ Garnet Magneto-Optical Crystals. Journal Of Applied Physics, Vol. 53, No. 3, 1982, P. 1687.

8. Krawczak, J. A.; Torok, E. J.: A Three Mirror Cavity For A Magneto-Optic Light Deflector. IEEE Transactions On Magnetics, Vol. MAG-16, 1980, P.1200.

9. Dias, A. R.: Incoherent Optical Matrix – Matrix Multiplier. Proceedings Of The First NASA Conference On Optical Information Processing For Aerospace Applications, NASA Publication 2207, 1981, P. 71.

10. Sauter, G. F.; Honebrink, R. W.; Krawczak, J. A.: Alterable Grating Fiber Optic Switch. Applied Optics, Vol. 20, No. 20, Oct., 1981, P. 3566.
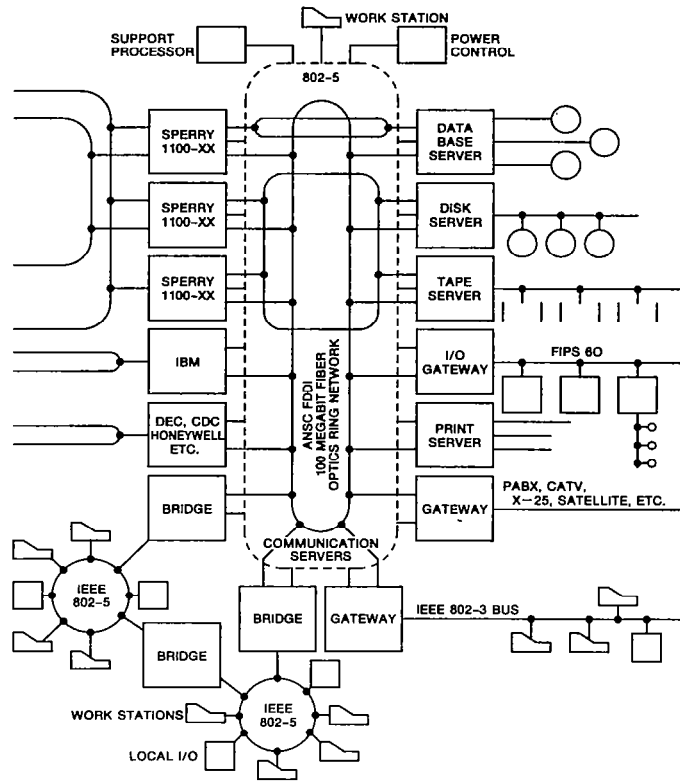
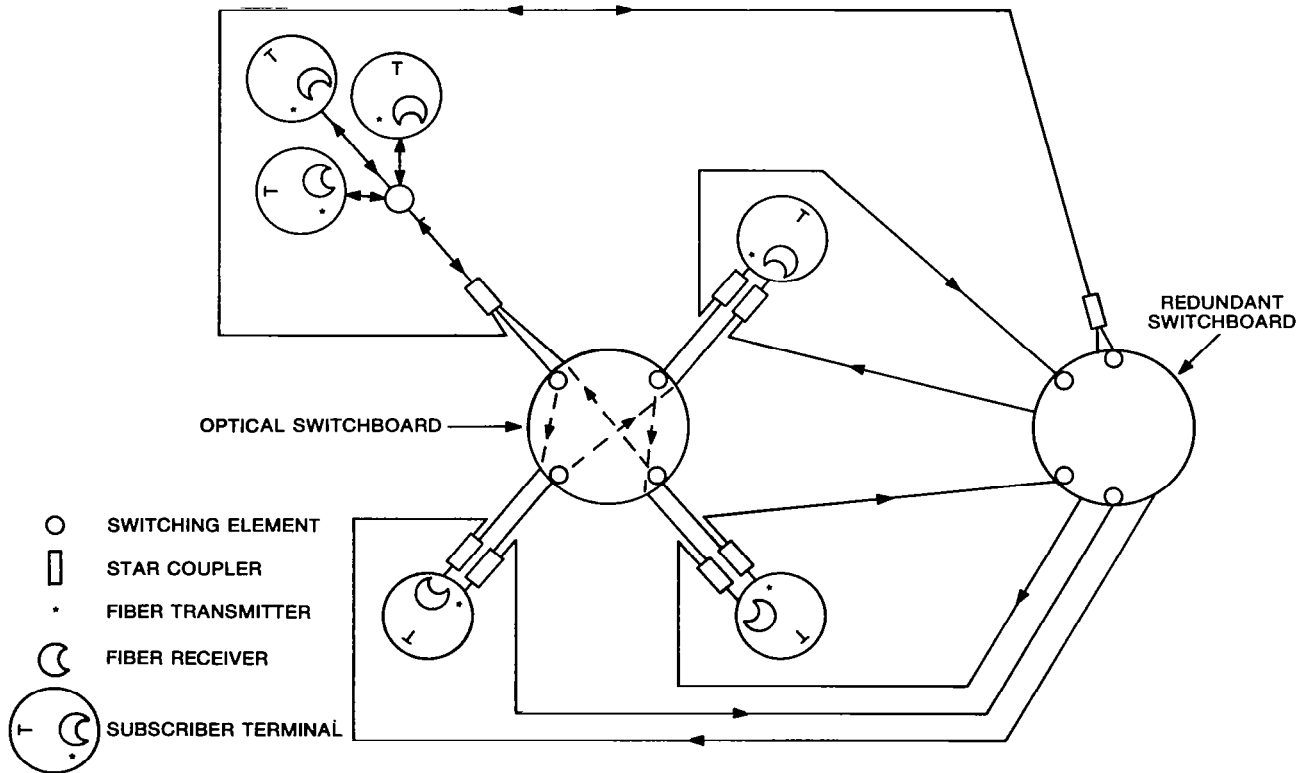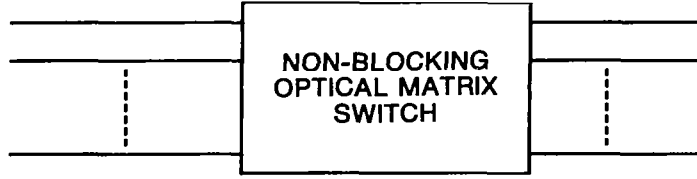Figure 1.- Emerging fiber optic ring type local area network.

O   SWITCHING ELEMENT

⬚   STAR COUPLER

•   FIBER TRANSMITTER

☾   FIBER RECEIVER

⊙   SUBSCRIBER TERMINAL

Figure 2.- Fiber optic star network with active switchboard.

```
                    ┌─────────────────┐
  ────────────────  │                 │  ────────────────
  ─ ─ ─ ─ ─ ─ ─ ─ ─ │  NON-BLOCKING   │  ─ ─ ─ ─ ─ ─ ─ ─ ─
   N                │ OPTICAL MATRIX  │                  M
 INPUT       ┊      │     SWITCH      │      ┊        OUTPUT
 FIBERS             │                 │                FIBERS
  ────────────────  │                 │  ────────────────
                    └─────────────────┘
```

DESIRABLE FEATURES

RUGGEDIZED, NONMECHANICAL FIBER SWITCHING TECHNOLOGY
SWITCHING OF WIDE BANDWIDTH FIBER OPTIC SIGNALS
LOW LOSS AND CROSSTALK
SWITCHING OF UNPOLARIZED, MULTIMODE FIBER LIGHT
OPTO-ELECTRONIC/ELECTRO-OPTIC CONVERSIONS ELIMINATED AT SWITCHING NODES
SIMULTANEOUS COMMUNICATIONS AMONGST ALL POSSIBLE INPUT/OUTPUT PAIRINGS
INFORMATION AVAILABLE ONLY TO SELECTED OUTPUT OR CONFERENCING
(N, M) VALUES TO (1024, 1024)

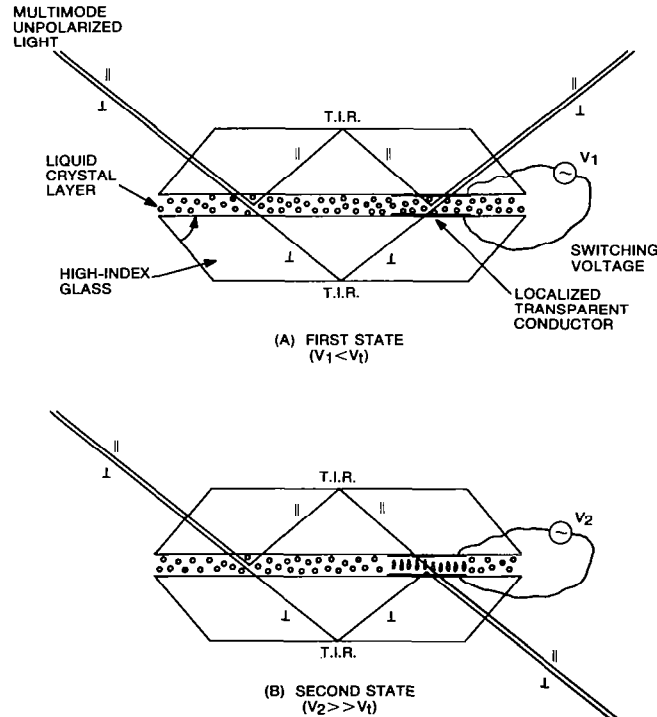Figure 3.- Desirable properties for optical switchboards.

Figure 4.- Operating principles of double-pass switch. Light paths for
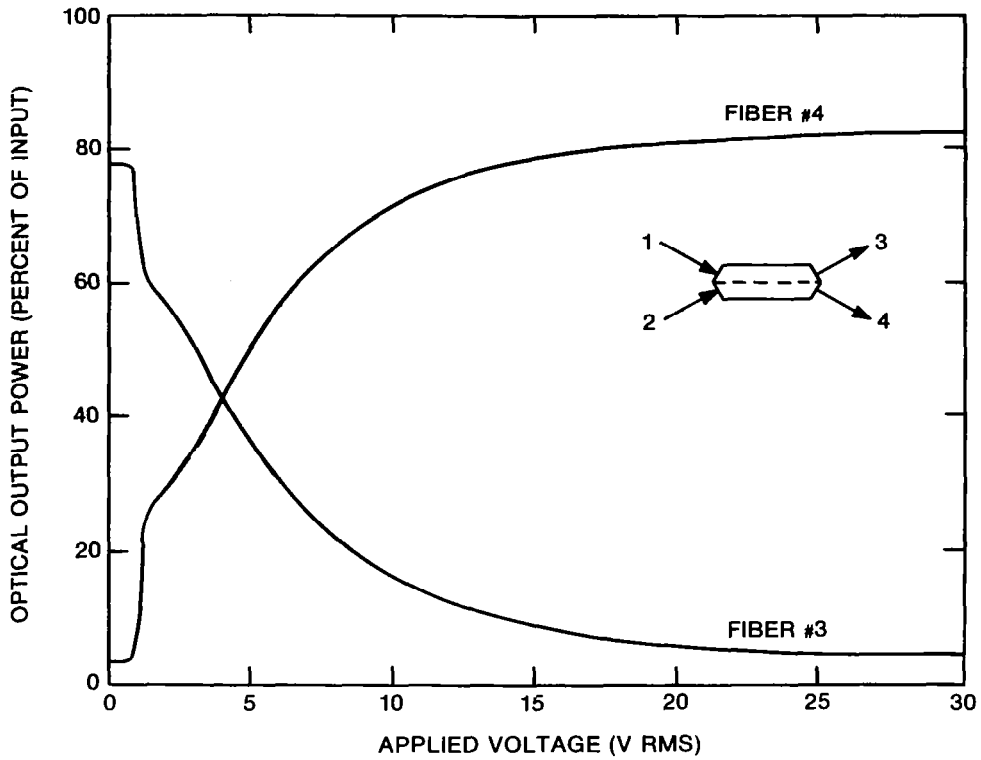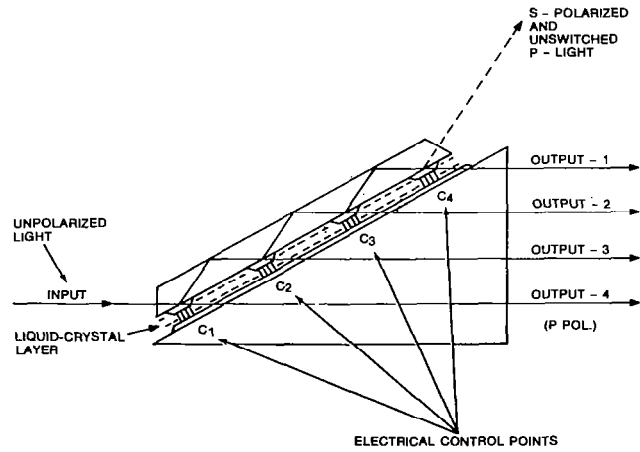both polarization-components are shown.

Figure 5.- Observed electro-optical performance of double-pass 4-fiber switch.
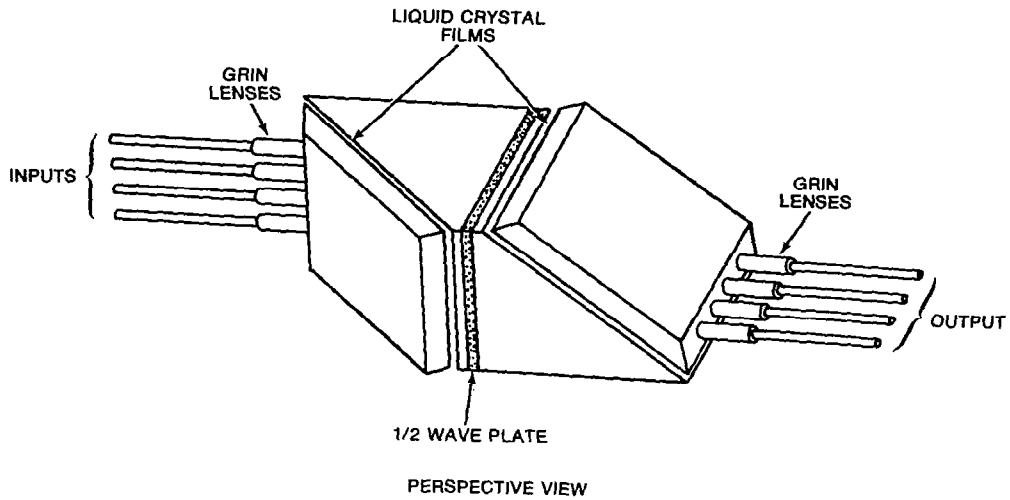

MEASURED PROPERTIES

OPTICAL

λ. MICRONS	LOSS (db.)	CROSSTALK (db.)
.81	3.5 – 5.4	−50
1.3	4	−37

ELECTRICAL

RESPONSE TIME	4ms.
ELECTRICAL POWER	<1 mw.

Figure 6.- Performance of 1x4 liquid crystal switch.

MEASURED PROPERTIES AT .663 MICRONS

INSERTION LOSS	5 DB.
CROSSTALK	40 DB.
SWITCHING TIME	5 MSEC.
SWITCHING POWER	<1 MILLIWATT

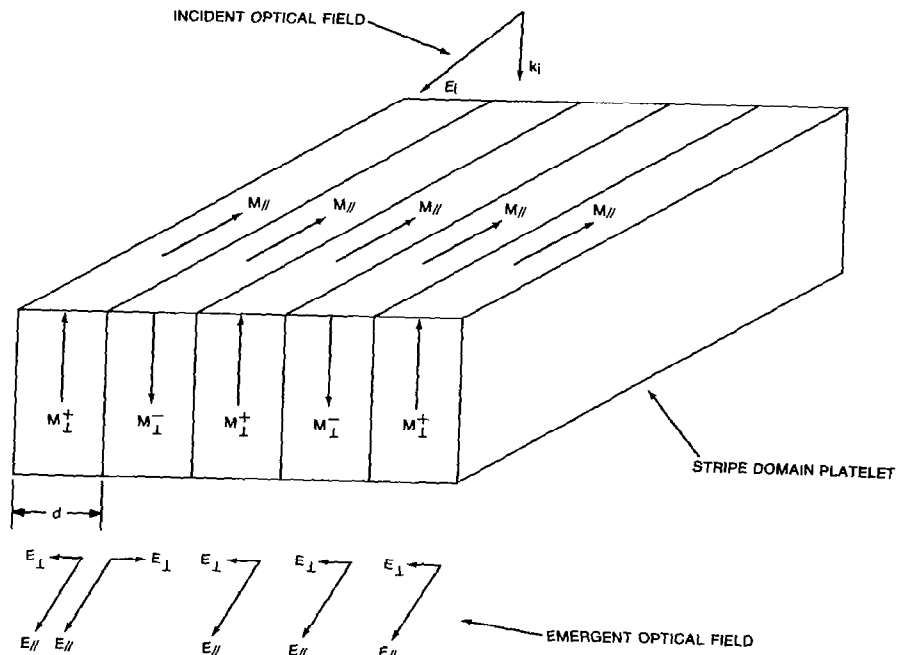Figure 7.- Performance of 4x4 liquid crystal matrix switch.

Figure 8.- Optical and magnetic vectors in stripe domain material.

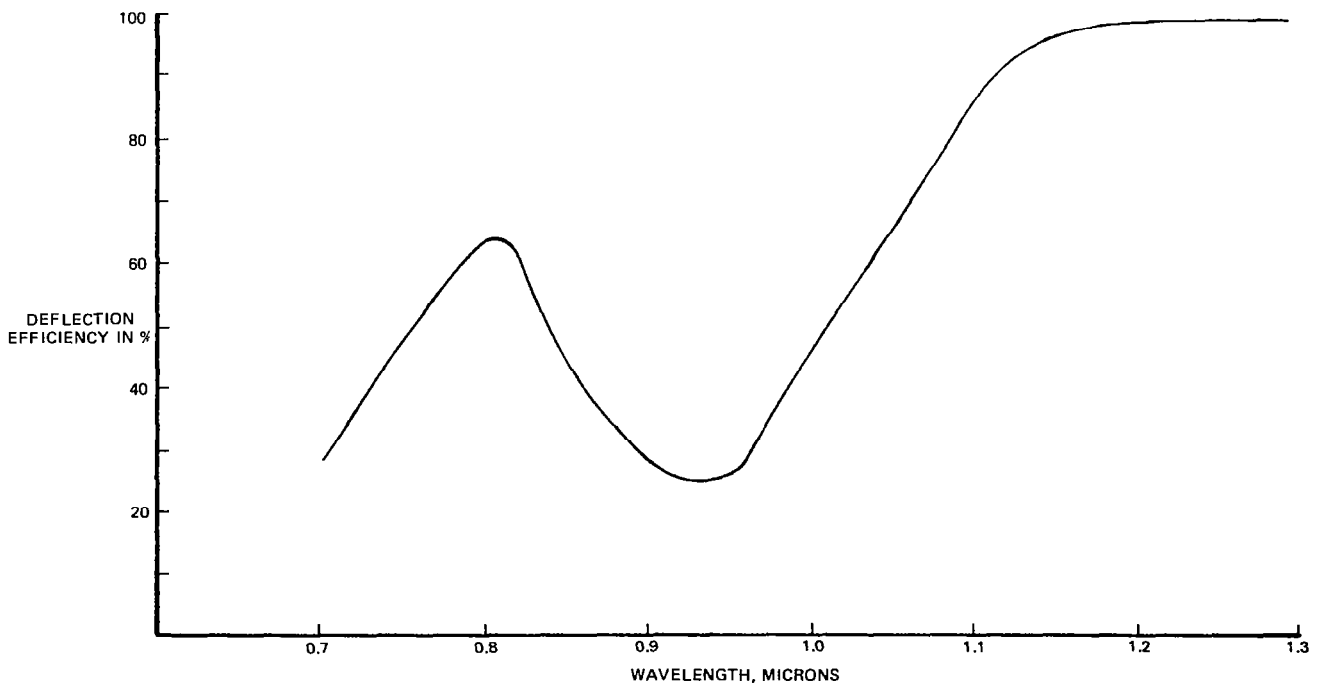Figure 9.- Stripe domain in YIG. Domain width is 6 microns.

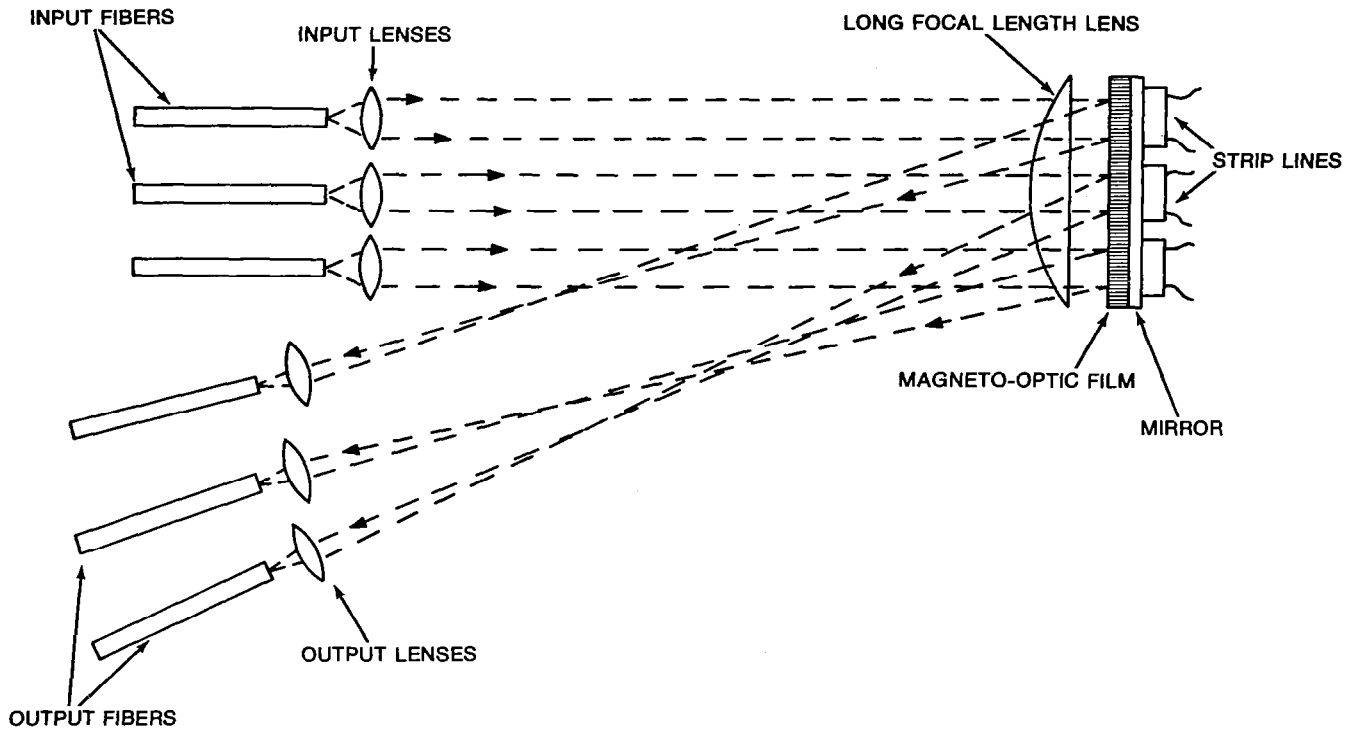Figure 10.- Calculated diffraction of optimized stripe domain garnet film.

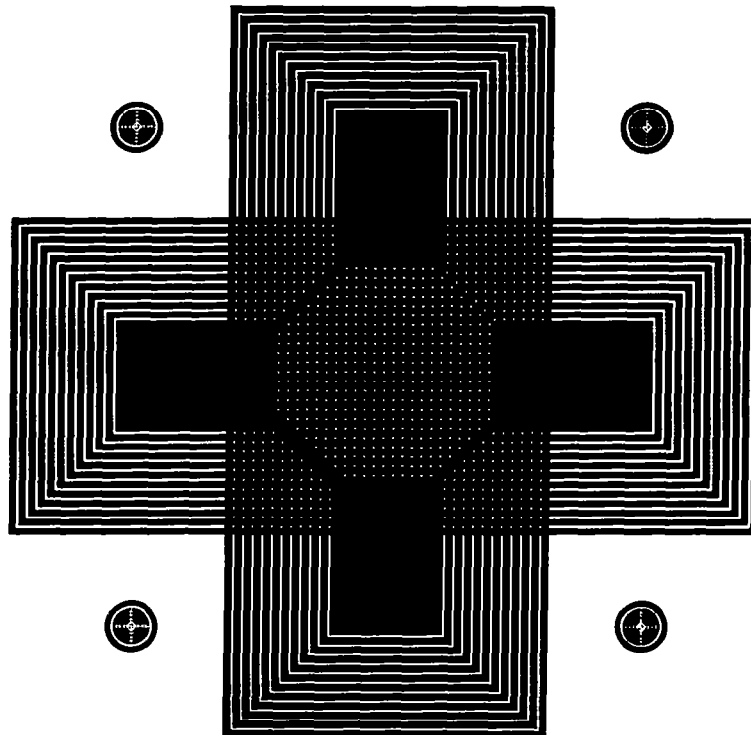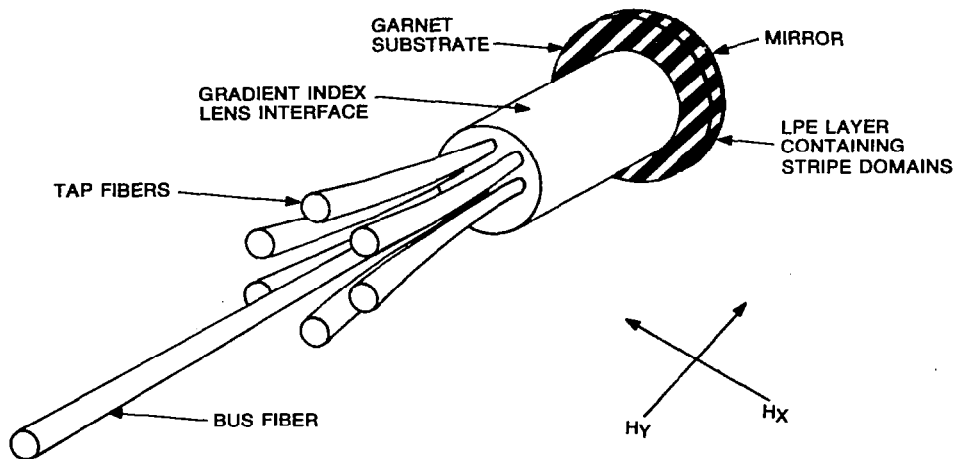Figure 11.- nxm magneto-optic stripe domain fiber optic switchboard.

Figure 12.- Stripeline coil set. Line width is 100 microns.

GARNET SUBSTRATE

MIRROR

GRADIENT INDEX LENS INTERFACE

LPE LAYER CONTAINING STRIPE DOMAINS

TAP FIBERS

BUS FIBER

H_Y

H_X

MEASURED PROPERTIES AT .633 MICRONS.

INSERTION LOSS 12 DB.

CROSSTALK 36 DB.

SWITCHTIME 2 MICROSEC.

SWITCHING CURRENT 600 MA.

M → 20

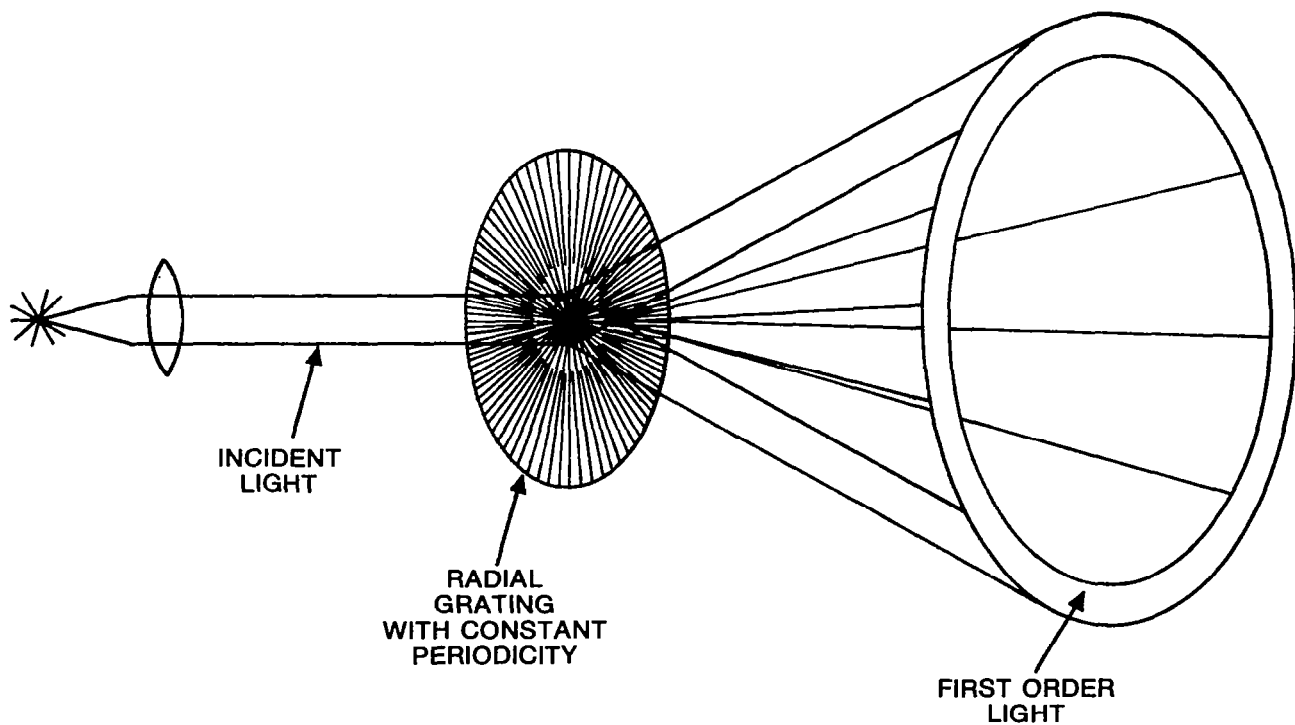Figure 13.- Performance of garnet 1xm optical switch.

INCIDENT LIGHT

RADIAL GRATING WITH CONSTANT PERIODICITY

FIRST ORDER LIGHT

Figure 14.- First order angular spectrum of radial grating with constant periodicity.
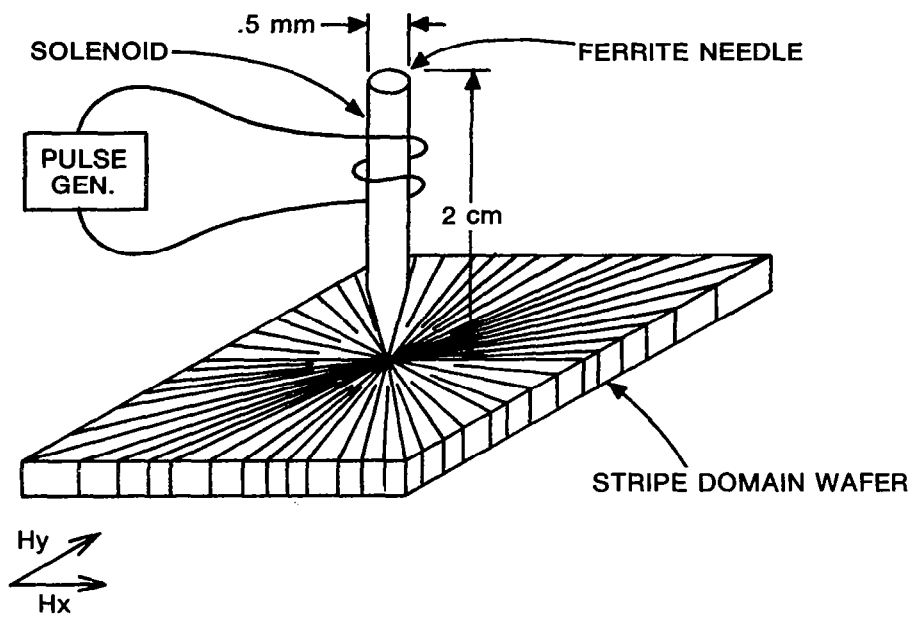
133

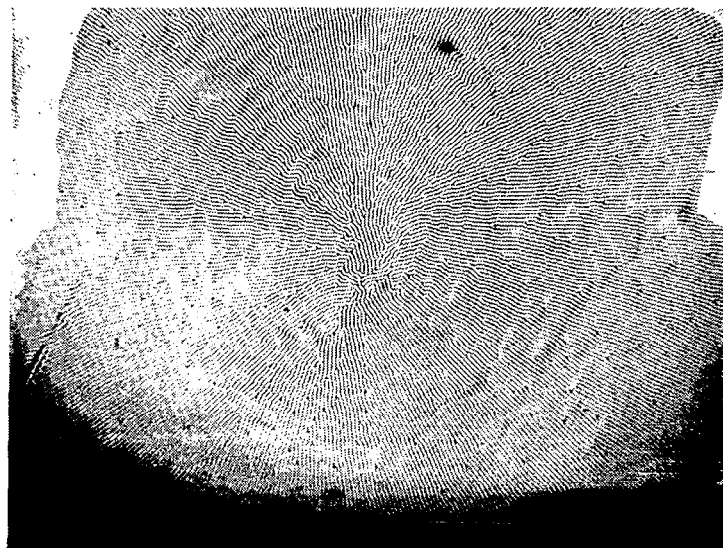Figure 15.- Apparatus for generating radial grating in garnet film.

Figure 16.- Induced radial grating in garnet.
Domain width is approximately
2 microns.

OPTICAL BISTABILITY: A NOVEL APPROACH TO
OPTICAL SIGNAL PROCESSING AND COMMUNICATIONS*

N. Peyghambarian
Optical Sciences Center, University of Arizona
Tucson, Arizona 85721

SUMMARY

        Optical bistability and its potential for optical signal processing and communications are reviewed. Recent experimental results in semiconductor optical bistability are presented. In particular, optical bistability in GaAs-AlGaAs superlattices and CuCl, ZnS, and ZnSe is discussed.

INTRODUCTION

        Optical bistability (OB) is a phenomenon in which a nonlinear medium responds to an optical input beam by changing its transmission abruptly from one value to another (references 1-5). A device is said to be optically bistable if two stable output states exist for the same value of the input over some range of input values. For example, in figure 1, the transmitted intensity through a semiconductor bistable device is plotted as a function of incident intensity. For each cycle of the incident intensity I_{in}, the transmission of the device remains low until I_{in} is increased beyond some critical value $I_\uparrow$. The transmission then remains high even as I_{in} is decreased back down until another critical value $I_\downarrow$ ($<I_\uparrow$) is reached, and the device jumps to the "off" state. This type of hysteresis is considered evidence for optical bistability.

        Picosecond optical pulses can be generated easily, and optical fibers permit transmission of these pulses with low loss. Therefore, the missing component in all-optical signal processing is an optical logic element in which one light beam controls another. Optically bistable devices have many desirable characteristics in this regard. They can perform a number of logic functions such as optical memory, optical transistor, optical discriminator, optical limiter, optical oscillator, etc. They also have the potential for subpicosecond switching, greatly exceeding the capability of electronics. Figure 2(a) demonstrates how such a device can serve as an optical memory element, as either one of two output states can be maintained indefinitely by an input beam of intensity between the two critical values $I_\uparrow$ and $I_\downarrow$. Under slightly modified operating conditions, the same device can be used as an optical transistor, as shown in figure 2(b). For intensities close to I_g, a small change in the input produces a large change in the output. The device in figure 2(b) can be also used as an optical limiter, since for input intensities above I_g, increasing the input does not change the output.

Finally, the device can serve as an optical discriminator; input intensities above I_g are transmitted with little attenuation, while those below I_g are highly attenuated.

For optical data processing, the ideal practical device should be small (micrometer or submicrometer) and fast (picosecond), require very little switching energy (10^{-15} J) and low holding power ($\simeq$ mW), and operate at a convenient temperature (room temperature) and a convenient wavelength (1.3 μm where optical fibers transmit with minimal loss). It should be able to be incorporated into an integrated system and be operable by a tiny laser diode. No device has yet achieved all of these characteristics. However, semiconductor etalons have already reached some of these goals, and the prospects for satisfying most, if not all, of these requirements are high with further development.

Optical data processing has several advantages over electronic processing. Optical circuitry is more immune to electromagnetic interference and cross talk than is electronics. It has the potential for subpicosecond switching (switching in the 0.1- to 10-ps regime is only possible optically) and is capable of performing high-speed parallel processing and/or optical imaging by integrating an array of devices onto the same chip.

Optical bistability is usually achieved by inserting a nonlinear medium inside a Fabry-Perot etalon. The nonlinear medium, normally a thin semiconductor slab, has an intensity-dependent index of refraction. The slab has flat, parallel faces that are high-reflectivity dielectrically coated, forming a Fabry-Perot etalon which provides the optical feedback. Semiconductor etalons have the attractive property of providing adequate absorption ($\alpha L \simeq 1$) in very short ($\simeq 1$ μm) lengths. A short length provides a faster cavity build-up time causing a fast switching time. It also permits tighter focusing before beam walk-off losses become significant, thus reducing input powers and switching energies. Our semiconductor OB research involves four materials: GaAs-AlGaAs multiple-quantum-well (MQW) superlattices, CuCl, ZnS, and ZnSe. We discuss the characteristics of each of these devices in turn.

GaAs-AlGaAs SUPERLATTICES

The first observation of optical bistability in a bulk semiconductor was reported in GaAs by Gibbs et al. (reference 6). The nonlinearity in this material is due to the existence of an exciton absorption feature just below the band edge which saturates at high input intensity. An exciton is a bound state of an electron and a hole, formed by absorption of a photon of energy just below the band gap, and bound through Coulomb attraction. In GaAs, the exciton binding energy is about 4.2 MeV and its Bohr radius is 140 Å. At high optical intensities, the exciton wave functions begin to overlap, screening the Coulomb attraction between the electron and the hole, and saturating the exciton resonance.

Most of our experiments at present are performed on GaAs-AlGaAs MQW superlattices which are grown by molecular beam epitaxy (reference 7) on a GaAs substrate (etched away after growth). MQW's are thin alternating layers of GaAs and AlGaAS, as shown in figure 3. The band gap of AlGaAs is larger than that of GaAs (1.75 eV compared with 1.5 eV, respectively, at 2 K), so that the low energy carriers are confined in the GaAs layers. This confinement causes a quantization of the

carrier motion in the direction normal to the layers, yielding a set of discrete energy levels, and a step-like density of states function instead of the usual parabolic shape (reference 8). The confinement of the carriers in the GaAs layers causes the exciton to behave like a two-dimensional hydrogen atom with smaller Bohr radius and larger binding energy. For example, an MQW with 336 Å GaAs wells and 401 Å AlGaAs layers has a binding energy of 6 MeV and a radius of 60 Å compared with 4.2 MeV and 140 Å for the bulk GaAs (reference 9).

Optical bistability was first observed at room temperature (reference 9) in MQW samples, and has since been observed in bulk GaAs (figure 4). A preliminary comparison between the two shows no significant difference in switching power and performance at room temperature. However, MQW's have the advantage of being able to operate at different wavelengths depending on the well size. The minimum switching power obtainable was about 3 mW. Lower powers should be possible by improved etching techniques (e.g. plasma etching), thus providing flatter samples and reducing scattering losses, and/or by lowering the impurity concentration by using better growth techniques.

The large room temperature nonlinearity in an MQW and the shift of the exciton resonance toward shorter wavelength with reduced well thickness suggest the use of a diode laser instead of a dye laser as a light source for bistability. The operating wavelength of a 66 Å MQW is comparable to that of available diode lasers. We have used an Hitachi HLP 1400 single-mode laser diode operating at 838 nm and about 10 mW power to switch a room-temperature MQW consisting of 300 periods of 66 Å GaAS and 64 Å $Al_{0.3}Ga_{0.7}As$ (figure 5). This is the first reported observation of OB with a laser diode (reference 10).

It is desirable to be able to switch an optical bistable device (OBD) externally. The switch-on time is limited by how fast the exciton feature saturates. Since the exciton screening occurs in less than 1 ps (reference 11) and the cavity build-up time is also ≈ 1 ps, a switch-on time of a few picoseconds is expected. A cavity-dumped dye laser, synchronously pumped by a mode-locked argon laser, produced 10-ps, 600-nm, 1-nJ pulses which were used to externally switch on the OBD in a detector-limited time of 200 ps (reference 12). Since the switching pulse is above the band gap in energy, it generates free carriers which remove the exciton contribution to the index of refraction by screening the Coulomb interaction. The creation of free carriers in this fashion thus has the same effect on the index as a sudden change in the input light intensity.

External switch-off was achieved in about 20 ns by thermally shifting the Fabry-Perot peak with a 7-ns, 600-nm, 300-nJ heating pulse (reference 12). Both external switch-on and switch-off were performed on a single input pulse as shown in figure 6. This operation is equivalent to an optical flip-flop with one light beam controlling another. The switch-off time is limited by how fast the exciton feature recovers, which depends on the carrier lifetime (about 21 ns, reference 13). A switch-off time of a few nanoseconds has been observed with a triangular input pulse (reference 14).

When the input pulse was lengthened to several microseconds, the output oscillated between high and low transmission states (figure 7). These regenerative pulsations (reference 15) are attributed to competition between thermal and excitonic nonlinearities with different time constants. This effect to date has precluded CW

operation of bistability. Various heat sinking materials (indium, transistor paste) have been tried, but all failed, presumably because they tended to absorb light from the transmitted beam, further increasing the generated heat. However, we intend to try diamond, which holds promise as a suitable material for heat sinking.

CuCl

CuCl is another direct band gap semiconductor with a band gap energy of about 3.4 eV at 5 K. The existence of the biexciton resonance in this material is well established (references 16, 17). A biexciton is a bound state of two excitons, analogous to a hydrogen molecule. In CuCl, the biexciton has a binding energy of ∿30 MeV and a resonance frequency of 3.1861 eV (3890 Å) at 5 K. Bistability in CuCl is of particular interest, as Hanamura (reference 18) has predicted picosecond switching using the biexciton two-photon resonance. Koch and Haug (reference 19) suggested that 0.1 MW/cm^2 input power should be adequate to switch a 1-μm-thick CuCl device with natural reflecting surfaces. However, they neglected the background absorption at the biexciton frequency due to the exciton tail as well as the broadening of the biexciton resonance with intensity. Including these two effects, we predicted (reference 20) a switching intensity of ∿ 10 MW/cm^2 for a 10-μm-thick sample with 90% reflecting surfaces (figure 8). We have observed optical limiting and bistability in CuCl (references 21, 22) consistent with the predictions of our theoretical analysis. Namely, using a 12-μm-thick CuCl film sandwiched between 90% dielectrically coated mirrors, we observed bistability with an input intensity of about 14 MW/cm^2 (figures 9, 10). Our results are also consistent with hysteresis loops seen by Hönerlage et al. (reference 23). In the future, we hope to make quantitative studies of the switching times as a function of laser detuning from the resonance.

ZnS AND ZnSe

Russian workers (reference 24) reported optical bistability in a thin-film semiconductor using a room temperature interference filter containing an intermediate ZnS layer of thickness λ/n (∿ 0.22 μm). They reported switching times of ∿ 10 μs with intensities on the order of 300 W/cm^2, and suggested that the switching can be even faster (submicrosecond). The nonlinearity was thought to be due to two-photon photorefraction involving structural effects in thin films. We have observed OB in similar interference filters with ZnS and ZnSe spacers (references 25, 26), but the nonlinearity is apparently thermal with slow switching times (≈200 μs) and much larger switching intensities (≈ 10 kW/cm^2, figure 11). The disparity in results is likely to be related to differing growth techniques. We are beginning studies to look at the effects of deliberately introducing impurities and/or lattice defects during the film growth, which should create surface states and thereby decrease switching times. Thin-film interference filters may prove valuable for parallel processing if the switching is actually rapid and powers are as low as reported by the Russian group. Ease of production of interference filters and their simple room temperature operation make these materials especially appealing.

138

REFERENCES

1. Gibbs, H. M., McCall, S. L., and Venkatesan, T. N. C.: Optical bistability. Opt. News, vol. 5, 1979, p. 6; and, Optical bistable devices: the basic components of all-optical systems? Opt. Eng. vol., 19, 1980, p. 463.

2. Abraham, E., and Smith, S. D.: Optical bistability and related devices. Rep. Prog. Phys., vol. 45, 1982, p. 815.

3. Smith, P. W., and Tomlinson, W. J.: Bistable optical devices promise subpicosecond switching. IEEE Spect., vol. 18, 1981, p. 26.

4. Miller, D. A. B.: Bistable optical devices: physics and operating characteristics. Laser Focus, vol. 18, no. 4, 1982, p. 79.

5. Arecchi, F. T., and Salieri, P.: Optical bistability. Phys. Bull., vol. 33, 1982, p. 20.

6. Gibbs, H. M., McCall, S. L., Venkatesan, T. M. C., Gossard, A. C., Passner, A., and Wiegmann, W.: Optical bistability in semiconductors. Appl. Phys. Lett., vol. 35, 1979, p. 451.

7. Gossard, A. C.: GaAs/GaAlAs layered films. Thin Solid Films, vol. 57, 1979, p. 3.

8. Dingle, R.: Confined carrier quantum states in ultrathin semiconductor hetrostructures. In Festkörperprobleme XV, Advances in solid state physics, H. J. Queisser, ed. (Pergamon, Vieweg, Braunschweig), vol. 15, 1975, p. 21.

9. Gibbs, H. M., Tarng, S. S., Jewell, J. L., Weinberger, D. A., Tai, K., Gossard, A. C., McCall, S. L., Passner, A., and Wiegmann, W.: Room-temperature excitonic optical bistability in GaAs-GaAlAs superlattice etalon. Appl. Phys. Lett., vol. 41, 1982, p. 221.

10. Gibbs, H. M., Jewell, J. L., Moloney, J. V., Tai, K., Tarng, S. S., Weinberger, D. A., Gossard, A. C., McCall, S. L., Passner, A., and Weigmann, W.: Optical bistability, regenerative pulsations, and transverse effects in room-temperature GaAs-AlGaAs superlattice etalons. Int. Workshop on Optical Phase Conjugation and Instabilities. Sept. 20-24, 1983, Corsica, invited paper, J. Physique, vol. 44, C2, 1982, p. 195, and also, Tarng, S. S., Gibbs, H. M., Jewell, J. L., Peyghambarian, N., Gossard, A. C., and Wiegmann, W.: Use of a laser diode to observe room-temperature, low power optical bistability in a GaAs-AlGaAs etalon. Appl. Phys. Lett., February 1984.

11. Shank, C. V., Fork, R. L., Leheny, R. F., and Shah, J.: Dynamics of photoexcited GaAs band-edge absorption with subpicosecond resolution. Phys. Rev. Lett., vol. 42, 1979, p. 112.

12. Tarng, S. S., Tai, K., Jewell, J. L., Gibbs, H. M., Gossard, A. C., McCall, S. L., Passner, A., Venkatesan, T. N. C., and Wiegmann, W.: External off and on switching of a bistable optical device. Appl. Phys. Lett., vol. 40, 1982, p. 205.

13. Miller, D. A. B., Chemla, D. S., Eilenberger, D. J., Smith, P. W., Gossard, A. C., and Tsang, W. T.: Large room-temperature optical nonlinearity in $GaAs/Ga_{1-x}Al_xAs$ multiple quantum well structures. Appl. Phys. Lett., vol. 41, 1982, p. 679.

14. Jewell, J. L., Tarng, S. S., Gibbs, H. M., Tai, K., Weinberger, D. A., Ovadia, S., Gossard, A. C., McCall, S. L., Passner, A., Venkatesan, T. N. C., and Wiegmann, W.: Advances in GaAs bistable optical devices. In Optical Bistability II, C. M. Bowden, H. M. Gibbs, and S. L. McCall, eds., Plenum Press, 1983.

15. Jewell, J. L., Gibbs, H. M., Tarng, S. S., Gossard, A. C., and Wiegmann, W.: Regenerative pulsations from an intrinsic bistable optical device. Appl. Phys. Lett., vol. 40, 1982, p. 291.

16. Gale, G. M., and Mysyrowicz, A.: Direct creation of excitonic molecules in CuCl by giant two-photon absorption. Phys. Rev. Lett., vol. 32, 1974, p. 727.

17. Chase, L. L., Peyghambarian, N., Grynberg, G., and Mysyrowicz, A.: Direct creation of a high density of biexcitons at k=0 in CuCl. Opt. Commun., vol. 28, 1979, p. 189.

18. Hanamura, E.: Optical bistable system responding in picosecond. Solid State Commun., vol. 38, 1981, p. 939.

19. Koch, S. W., and Haug, H.: Two-photon generation of excitonic molecules and optical bistability. Phys. Rev. Lett., vol. 46, 1981, p. 450.

20. Sarid, D., Peyghambarian, N., and Gibbs, H. M.: Analysis of biexcitonic optical bistability in CuCl in the presence of collision broadening. Phys. Rev. B., Rapid Commun., vol. 28, 1983, p. 1184.

21. Peyghambarian, N., Gibbs, H. M., Rushford, M. C., and Weinberger, D. A.: Observation of biexcitonic optical bistability and optical limiting in CuCl. Phys. Rev. Lett., vol. 51, 1983, p. 1692.

22. Peyghambarian, N., Gibbs, H. M., Weinberger, D., Rushford, M. C., and Sarid, D.: Optical nonlinearity and bistability due to the biexciton two-photon resonance in CuCl. In Optical Bistability II, C. M. Bowden, H. M. Gibbs, and S. L. McCall, eds., Plenum Press, 1983.

23. Hönerlage, B., Bigot, Y. J., and Levy, R.: Optical bistability in CuCl. Ibid.

24. Karpushko, F. V., and Sinitsyn, G. V.: An optical logic element for integrated optics in a nonlinear semiconductor interferometer. J. Appl. Spect. (U.S.S.R.), vol. 29, 1978, p. 1323; and, The anomalous nonlinearity and optical bistability in thin-film interference structures. Appl. Phys. B., vol. 28, 1982, p. 137.

25. Weinberger, D. A., Gibbs, H. M., Li, C. F., and Rushford, M. C.: Room-temperature optical bistability in thin-film interference filters and dye-filled etalons. Annual Meeting of the Optical Society of America, Tucson, Arizona, Oct. 1982.

26. Rushford, M. C., Weinberger, D. A., Gibbs, H. M., Li, C. F., and Peyghambarian, N.: Room-temperature thermal optical bistability in thin-film interference filters and dye-filled etalons. Air Force Office of Scientific Research, Army Research Office's Topical Meeting on Optical Bistability, Rochester, New York, June 15-17, 1983.

27. Gibbs, H. M.: Optical bistability. McGraw-Hill Yearbook of Science and Technology, New York, 1982 (McGraw-Hill Books), p. 136.

28. Jewell, J. L., Gibbs, H. M., Gossard, A. C., Passner, A., and Wiegmann, W.: Fabrication of GaAs bistable optical devices. Matl. Lett., vol. 1, 1983, p. 148.
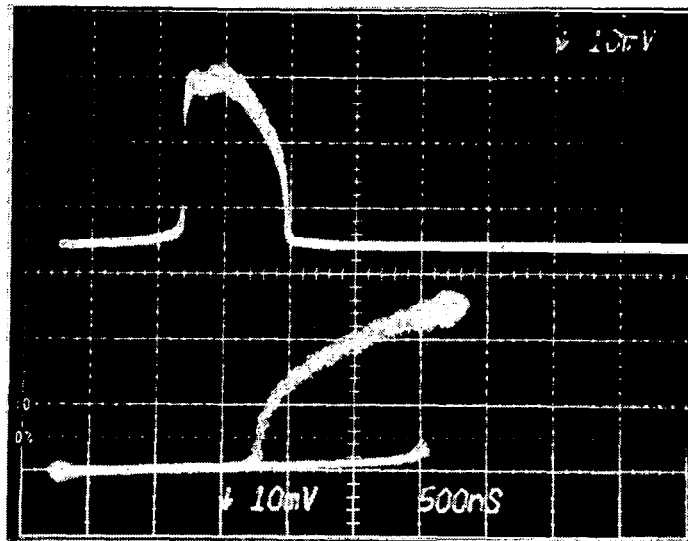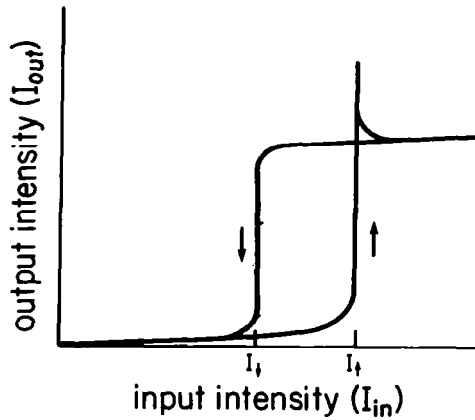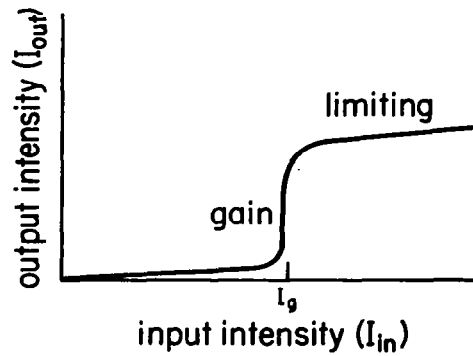
Figure 1.- Room temperature optical bistability in a GaAs-AlGaAs multiple-quantum-well etalon. The top trace is a transmission of device (output) versus time. The bottom trace is the output versus input, showing hysteresis. Input is a triangular pulse.

(a) Under conditions of bistability (memory).

Figure 2.- Transmission of a typical bistable optical device (reference 27).

(b) Under conditions of high ac gain (optical transistor, discriminator, or limiter).

Figure 2.- Concluded.

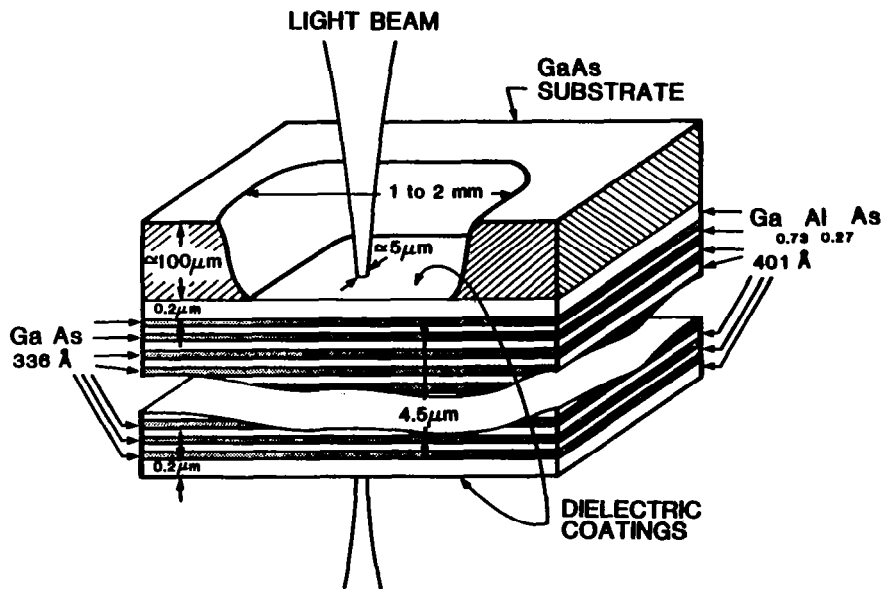Figure 3.- Diagram of a 336-$\overset{\circ}{A}$ superlattice sample. In our present samples, the entire GaAs substrate is etched away, and the remaining "flake" is either sandwiched between dielectric mirrors or directly coated for high reflection (reference 28).
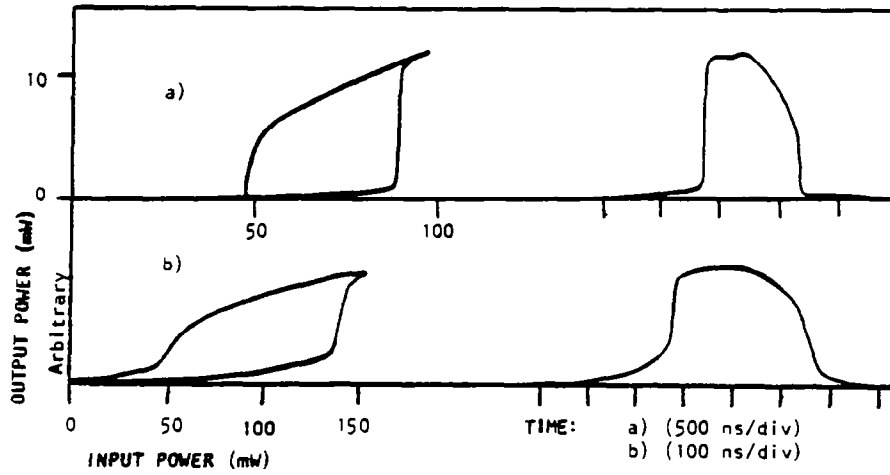
Figure 4.- Room temperature bistability in (a) 336-Å MQW and (b) bulk GaAs devices.
Recent experiments have demonstrated no significant difference in performance
between the superlattice and bulk devices.
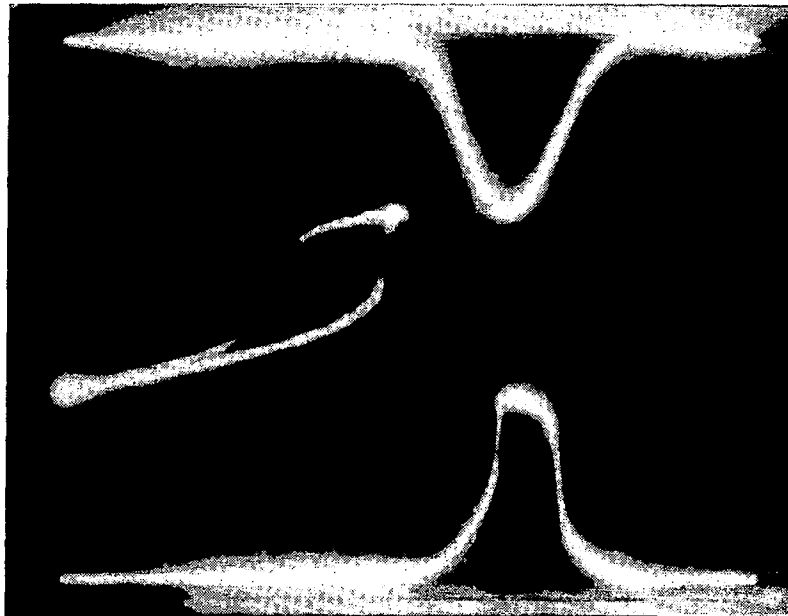
Figure 5.- Room temperature optical bistability in a GaAs MQW etalon using a diode
laser at 830 nm.

Figure 6.- External switch-on and switch-off during a single-input pulse.
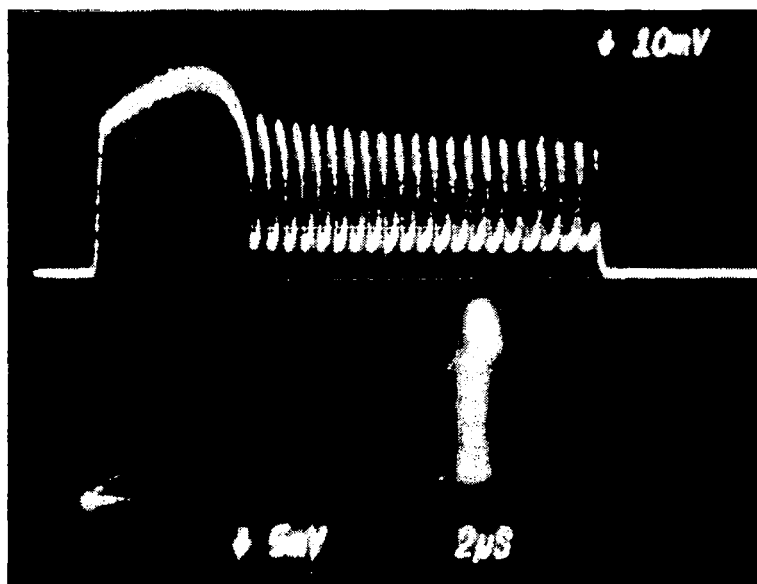
Figure 7.- Regenerative pulsations at a frequency at about 2 MHz with an input wavelength of approximately 882 nm.
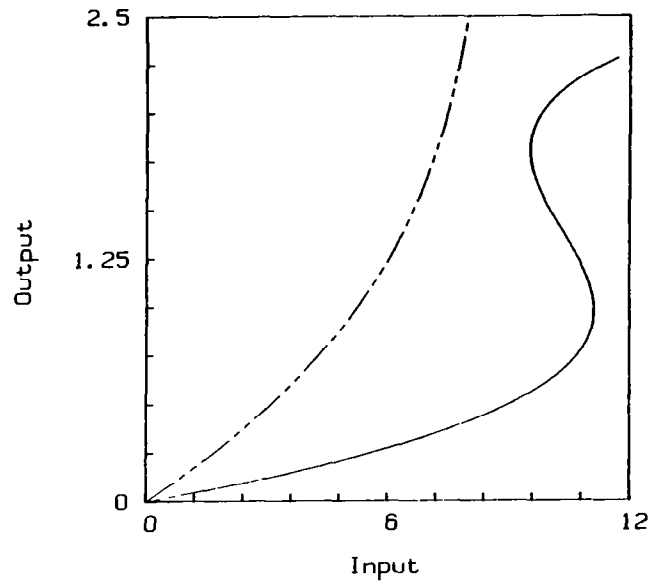
Figure 8.- Calculated output intensity versus input intensity (MW/cm^2) of a 10-μm-thick CuCl etalon with R = 0.9 (full line) and R = 0.8 (dashed line).
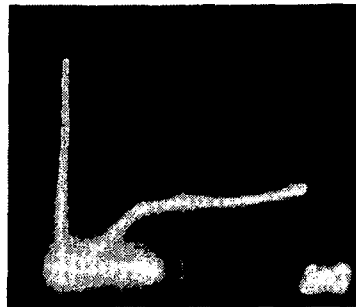
(a) Output versus input intensity.
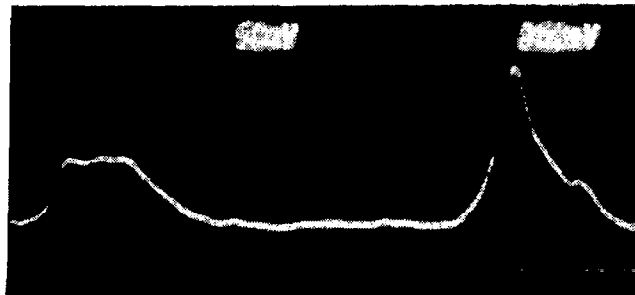
(b) Input pulse (right) and clipped output pulse (left) versus time.

Figure 9.- Limiting action in a 10-μm-thick CuCl etalon. (Time scale 2 ns/division.)
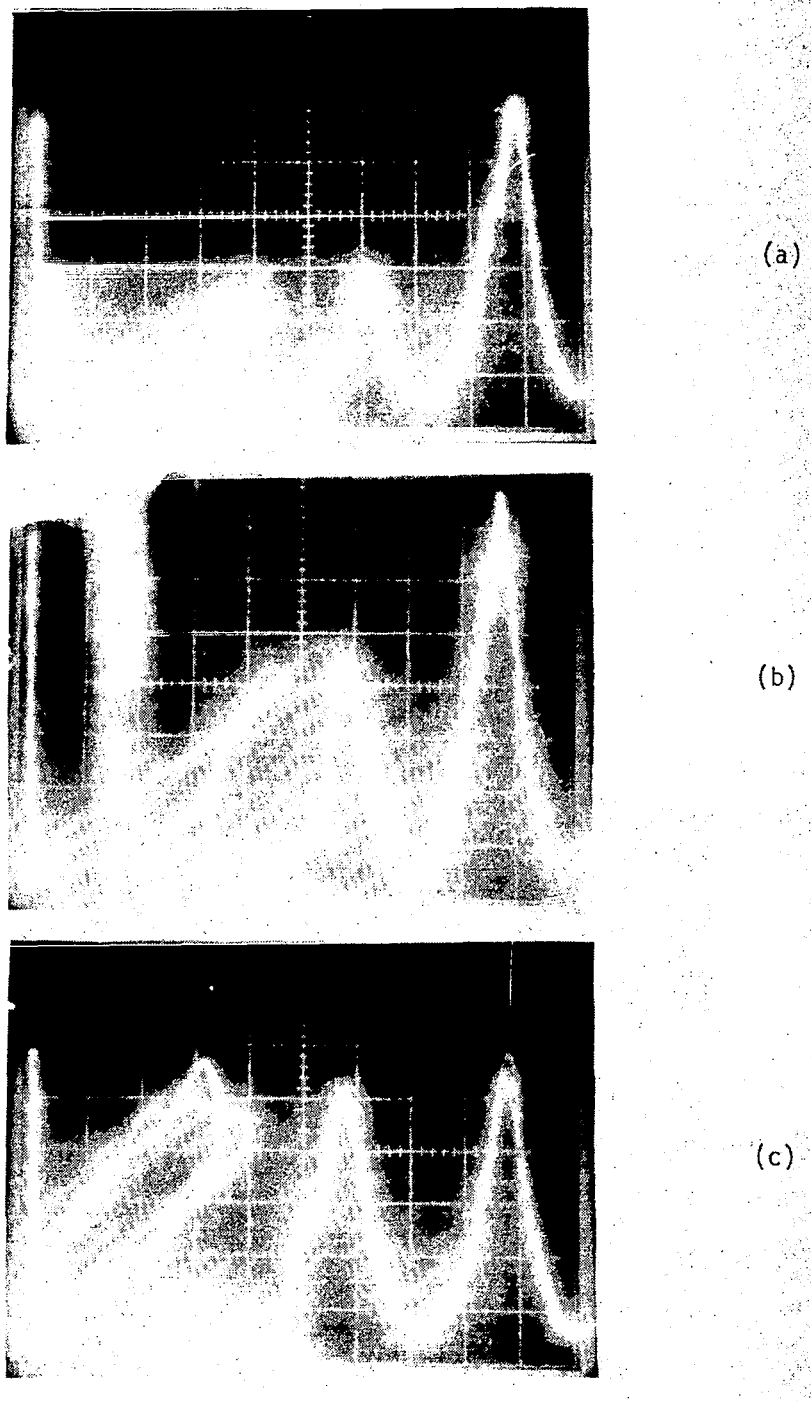
Figure 10.- Switch-on in a 12-μm-thick CuCl etalon. The laser frequency is gradually increased (corresponding to a fraction of a milli-electron volt change) in the sequence of photos (a) - (c). Each photo shows hysteresis loop, output pulse (center), and input pulse (right). Note only (b) shows switch-on. Switch-off is not resolved in (b) as the input dye laser pulse falls too steeply. The time scale is 5 ns/division.
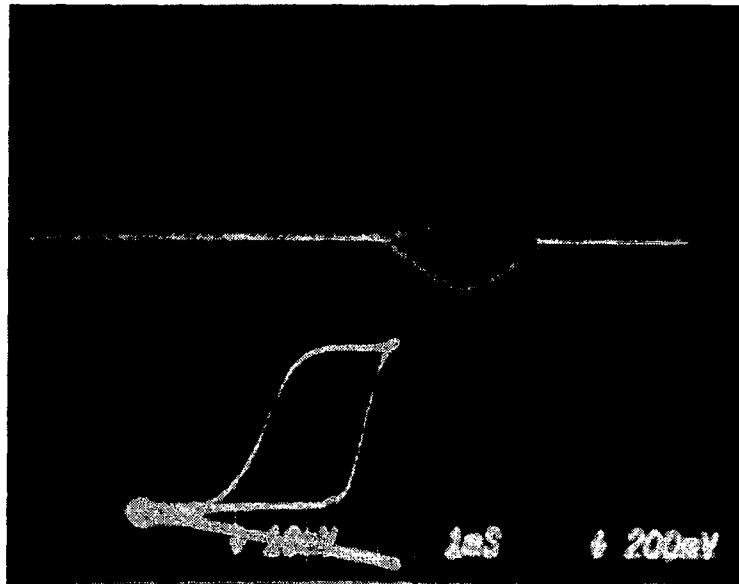
(a) ZnS. The switch-on time is ≈200 µs, the fastest we have observed to date in these devices.
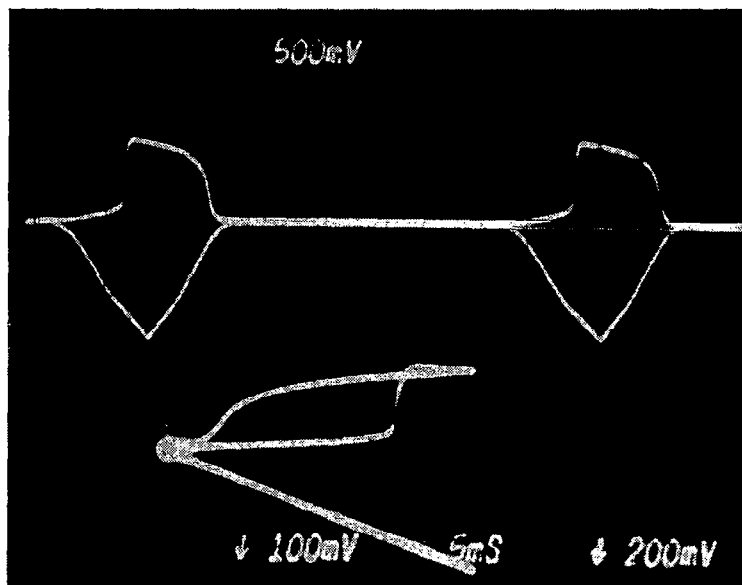
(b) ZnSe.

Figure 11.- Thermal optical bistability in ZnS and ZnSe thin-film interference filters.

HYBRID INTEGRATED OPTIC MODULES FOR REAL-TIME SIGNAL PROCESSING*

Chen S. Tsai
Department of Electrical Engineering
University of California, Irvine

ABSTRACT

This paper reports the most recent progress on four relatively new hybrid integrated optic device modules in LiNbO$_3$ waveguides and one in YIG/GGG waveguide that are currently being studied at the author's laboratory. The five hybrid modules include a time-integrating acoustooptic correlator, a channel waveguide acoustooptic frequency shifter/modulator, an electrooptic channel waveguide TIR modulator/switch, an electrooptic analog-to-digital converter using a Fabry-Perot modulator array, and a noncollinear magnetooptic modulator using magnetostatic surface waves. All of these devices possess the desirable characteristics of very large bandwidth (GHz or higher), very small substrate size along the optical path (typically 1.5 cm or less), single-mode optical propagation, and low drive power requirement. The devices utilize either acoustooptic, electrooptic or magnetooptic effects in planar or channel waveguides and, therefore, act as efficient interface devices between a light wave and temporal signals. Major areas of application lie in wideband multichannel optical real-time signal processing and communications. Some of the specific applications include spectral analysis and correlation of RF signals, fiber-optic sensing, optical computing and multiport switching/routing, and analog-to-digital conversion of wide RF signals. The common technical problems that require further research and development include fabrication yield, fiber-waveguide and diode laser-waveguide couplings, and resistance to optical damage.

INTRODUCTION

Recent advancements on the performances of individual guided-wave optical devices, basic building blocks, their interconnections, coupling to and from waveguide, and specific real-world applications have been quite significant. Together with the recent progress on fabrication of miniature laser sources, waveguide lenses and photodetectors, integration of all passive and active components on a single substrate or a small number of substrates is becoming a reality. This emerging technology can be utilized to implement integrated optic modules for wideband multichannel optical communications and signal processing systems. Clearly, such future integrated optic modules should share a number of attractive features, such as very large bandwidth, low electrical drive power, small size, light weight, less susceptibility to environmental effects, and potentially less cost in fabrication. In this paper five new hybrid integrated optic modules currently being explored at the author's laboratory are reported together with most recent results.

TIME-INTEGRATING ACOUSTOOPTIC CORRELATOR

Time-integrating correlation of RF signals using bulk-wave isotropic acousto-optic (AO) Bragg diffraction has become a subject of great interest because of its applications in radar signal processing and communications. Some encouraging results with the experiments which utilize guided-wave isotropic Bragg diffraction was reported earlier (ref. 1). Subsequently, hybrid and monolithic structures for integrated optic implementations were suggested (ref. 2). In a conventional configuration that utilizes either bulk-wave or guide-wave <u>isotropic</u> Bragg diffraction, a pair of imaging lenses and a spatial filter are used to separate the diffracted light beam from the undiffracted light beam. We are presently exploring a new and novel hybrid structure which utilizes guided-wave <u>anisotropic</u> Bragg diffraction and hybrid integration (See Fig. 1) (ref. 3). This new structure can conveniently incorporate a thin-film polarizer to separate the diffracted light from the undiffracted light prior to detection and, therefore, eliminate the need of imaging lenses and spatial filter. As a result, the acoustooptic time-integrating correlator is not only much smaller in dimension along the optical path and capable of providing a larger time window and a lower optical insertion loss, but it is also easier to implement in integrated optic format. A laser diode and a thin-film polarizer/photodetector array (CCPD) composite are butt-coupled to the input and the output end faces of a Y-cut $LiNbO_3$ plate (2mm x 12mm x 15.4mm), respectively. A single geodesic lens (with 8mm focal length) is used to collimate the input light beam prior to interaction with the surface acoustic wave (SAW). The SAW propagates at 5 degrees from the X-axis of the $LiNbO_3$ plate to facilitate anisotropic Bragg diffraction between TE_0 and TM_0 modes. In operation, the correlation between the two signals $S_1(t)$ and $S_2(t)$ is performed by separately modulating the laser diode and the RF carrier to the SAW transducer. Finally, the time-integrating correlation waveform is read out from the detector array by the charged-coupled device.

The preliminary experiment carried out earlier with the correlator of incomplete hybrid integration at 0.6328μm wavelength and the SAW at 391 MHz center frequency had demonstrated a bandwidth of 60 MHz, a time bandwidth product of 4.2×10^5, and a dynamic range of −27dB (ref. 3). A considerably larger bandwidth can be realized as it is now possible to design and fabricate GHz bandwidth planar acoustooptic Bragg cells (ref. 4) and it is also possible to modulate the diode laser at GHz rates. Fig. 2 shows the $LiNbO_3$ substrate of the module with the geodesic lens located at the center and the SAW transducer at the right end. Most recently, complete hybrid integration using a diode laser at 0.78μm wavelength and the SAW at 314 MHz center frequency was accomplished. Some preliminary results have been obtained but the aperture of the collimated guided-light beam needs to be enlarged in order to perform a meaningful evaluation of this hybrid integrated correlator module.

CHANNEL WAVEGUIDE ACOUSTOOPTIC DEFLECTOR/MODULATOR

While <u>planar</u> waveguide AO devices have already reached some degree of sophistication and found immediate applications (ref. 5), <u>channel</u> waveguide AO devices, which result from acoustooptic deflection in channel waveguides, have only started to receive interest and attention (ref. 6). This interest was motivated by the fact that comparable cross sections of the channel waveguide and the optical fiber would greatly facilitate the interfacing of the resultant AO channel devices with fiber optic systems. One interaction configuration of particular interest is shown in Fig. 3. Two identical channel waveguides in a Y-cut $LiNbO_3$ substrate are crossed at an angle

ψ to form a 2Δn straight intersection (ref. 7). Unlike the conventional Δn inter-
section, the retractive index change in the crossover region is twice that in the
other parts of the channel waveguide. As a result, the light wave is also guided in
the crossover region and the crosstalks between the two channel waveguides can be
significantly smaller. An interdigital transducer is symmetrically positioned so
that the SAW generated propagates in the intersection region. The center frequency
of the SAW is such that the corresponding Bragg angle is equal to one half of the
intersection angle. An optical wave incident at guide 1 is diffracted by the moving
optical grating induced by the SAW. Consequently, a portion of the incident light is
deflected into guide 3. The frequency of the deflected light is up-shifted by an
amount equal to the acoustic frequency. Similarly, an optical wave incident at guide
2 will have a portion of its intensity deflected into guide 4 and have the frequency
of the deflected light down-shifted by the same amount. Such a device module should
find a variety of applications in future integrated and fiber optic systems. In the
application for heterodyne detection, the frequency-shifted light can be conveniently
used as a reference signal (local oscillator) in connection with optical communica-
tions and fiber optic sensing.

A high diffraction efficiency was demonstrated earlier in a preliminary
experiment (ref. 8) with multimode crossed-channel waveguides of 30μm channel width
in a Y-Cut LiNbO$_3$ substrate and a SAW operating at 634 MHz center frequency. We have
recently extended this experimental study to single-mode crossed-channel waveguides
of 10μm channel width, and have obtained similarly encouraging results (ref. 6).
Specifically, a 50% diffraction efficiency and a bandwidth of 13.4 MHz were obtained
with 0.13 watt of acoustic power centered at 320 MHz. This result clearly indicates
the feasibility for realization of an active integrated optic module with a 50-50
power split and a tunable frequency offset. Consequently, this crossed-channel AO
module should find a variety of applications in integrated and fiber optic systems.
Fig. 4 is a photograph of the resultant module. Located in the center of the device
holder is the LiNbO$_3$ plate which has the dimensions 0.2 x 1.0 x 1.4 cm. A pair
of RF connectors for excitation and detection of the SAW are also shown. While both
prism-and edge-couplings of the light beam have been utilized successfully, a more
rigid coupling using single-mode fibers is being pursued.

ELECTROOPTIC CROSSED CHANNEL WAVEGUIDE TIR MODULATOR AND 4 X 4 SWITCHING NETWORK

A variety of channel waveguide electrooptical (E-O) devices in LiNbO$_3$ substrates
have demonstrated desirable characteristics, including low RF drive power, small
sizes, and high switching speed or large modulation bandwidth. Consequently, such
E-O devices should provide essential functions for realization of single-mode optical
fiber communication and optical signal processing systems. One of the guided-wave
E-O devices that has received increasing interest utilizes the electrically-induced
total internal reflection (TIR) in a crossed-channel waveguide (ref. 9). The basic
device configuration is shown in Fig. 5. The crossed-channel waveguide employed in
this TIR device is similar to that employed in the channel waveguide acoustooptic
device described in the last section. A pair of parallel metal electrodes are de-
posited in the middle of the crossover region. In absence of an applied voltage, an
incident light from port 1, for example, will transmit rather freely through the
layer defined by the parallel electrodes and exit at port 4. However, when a voltage
of appropriate polarity is applied, the refractive index in the layer is reduced due
to the linear electrooptic effect. Two refractive index interfaces are thus created
electrically. A total internal reflection (TIR) of the light will occur at the first
interface if the incident angle is larger than the critical angle θ_c. Therefore, if

the intersection angle of the channel waveguides and, consequently, the incident angle of the light beam is chosen to be in the neighborhood of the critical angle, the ratio of the reflected (switched) light power to the transmitted (unswitched) light power becomes a sensitive function of the applied voltage (ref. 9). It is clear that the very small length of the parallel electrode pair suggests a very small capacitance and thus a very large base bandwidth for the device. For example, an electrode length of 1mm and 50-ohm termination will provide a theoretical base bandwidth of 20 GHz. It was also previously shown that by using a suitable intersection angle both low drive voltage and low crosstalk could be simultaneously achieved (ref. 6).

We had earlier fabricated and tested such TIR modulators and switches in multi-mode crossed channel waveguides in Y-cut LiNbO$_3$ substrates (ref. 6). We have recently realized a single-mode multigigahertz bandwidth TIR modulator and a simple 4 x 4 switching network which consists of five such basic modulators, again in the Y-cut LiNbO$_3$ substrates (ref. 10). The channel width and the intersection angle of the crossed channel waveguide are 10μm and 1.5 degrees, respectively. The length of the basic modulator along the optical path is 2.2mm. The best measured results for the basic modulator at 6328 Å wavelength are a base bandwidth greater than 2.0 GHz (limited by the availability of high-speed electronics testing equipment), a drive voltage of 18 volts for 90% switching efficiency, a crosstalk of -15 dB, and an estimated insertion loss of 1 dB. A simple scheme which employs a cascade of three identical devices for reduction of the crosstalks by a factor of two in dB, namely, from -15 dB to -30 dB, was also verified experimentally.

Fig. 6 is a photograph of the finished basic modulator module and the microscope objectives at right and left for edge-coupling of the light beam in actual experiment. The LiNbO$_3$ plate and the RF connector to the coplanar microstrip transmission on it are positioned at the top and a 50-ohm termination at the bottom.

Channel waveguide optical switching networks or matrices (ref. 11,12) are expected to provide a variety of high-speed operations, such as multiport routing and multiplexing in single-mode fiber optic communication and signal processing systems. Fig. 7(A) shows the geometry of a simple 4 x 4 optical switching network which was fabricated and tested (ref. 10). The total length of the switching network along the optical path is 0.74cm. This very small dimension is attributed to the fact that all individual switches are very small along the optical path and that only straight channel waveguides are required for their interconnections.

Multiport beam switching and routing experiments were carried out with the light incident at the second input port and subsequently modulated by switch S_1 at 1 KHz. Routing of the light to any of the four output ports was accomplished by setting switches S_2, S_4 and S_5 at appropriate switching states as indicated. Since the amplitudes of all four output waveforms as shown in Fig. 7(B) are practically the same, it is reasonable to conclude that the optical insertion loss associated with each individual route is also practically the same. Furthermore, since the total lengths of channel waveguides in all routes are almost identical, it is reasonable to suggest that the insertion loss of the switch was the same for all and was estimated to be at most 1 dB. This insertion loss for the switch was determined by comparing the output waveform of the route involving switches S_1, S_5 and S_2. Finally, the measured crosstalks at the unintended ports are typically -15 to -17 dB.

In summary, various single-mode crossed channel waveguide TIR device configurations, including single, cascaded, and matrix modulator/switches, have been realized in a Y-cut LiNbO$_3$ substrate. A bandwidth greater than 2 GHZ has been demonstrated in the single modulator. Since only straight channel waveguides are required, such

TIR devices possess the advantage of being very small in dimensions along the optical path which in turn results in very low insertion loss and high packing density. Various potential applications of such TIR devices are possible. For example, optical computation using an array of such TIR devices has been suggested (ref. 13,14). Some of the more obvious applications of such devices include high-speed multiport switching and routing in single-mode fiber optical communication and signal processing systems as well as data routing in electronic computer networks.

ELECTROOPTIC ANALOG-TO-DIGITAL CONVERTER USING CHANNEL WAVEGUIDE FABRY-PEROT MODULATOR ARRAY

One of the important signal processing applications that utilizes guided wave electrooptic (E-O) devices lies in analog-to-digital (A/D) conversion of wideband RF signals (ref. 15,16). Several types of electrooptic A/D converters which utilize guided-wave E-O devices in $LiNbO_3$ have been demonstrated (ref. 17-21).

We are currently studying a new type of E-O A/D converter (ref. 22) which utilizes an array of channel waveguide Fabry-Perot modulators (ref. 23) in a X-cut $LiNbO_3$ substrate. A 4-bit converter has been fabricated and the experimental results obtained with a He-Ne laser at 6328 Å have demonstrated some of its desirable features. The elements of this integrated E-O A/D converter are depicted in Fig. 8. A set of parallel electrode pairs to which the analog voltage is applied electrically in parallel is designed such that the electrode lengths of adjacent modulators differ by a factor of two for a binary-code representation. Activation of this apodized electrode array by the analog voltage will result in modulation of the refractive index and thus the phase shift of the light and the optical transmission characteristic in each channel waveguide. Thus an E-O Fabry-Perot modulator (ref. 24) is formed in each waveguide. It can be shown that the shape of the transmission characteristic versus the applied analog voltage or the total phase shift in each channel waveguide is periodic and its periodicity is inversely proportional to the length of the electrode. Accordingly the periodicity of modulation as a function of the applied voltage is reduced by a factor of two between adjacent channel waveguides. It is to be noted that each channel waveguide modulator is also incorporated with an electrooptic phase shifter to provide independent adjustment of its static phase shift. The depth of modulation in the transmitted light of each Fabry-Perot modulator is determined by the reflectivity of the two identical mirror facets and the attenuation coefficient in the channel waveguide. A series of plots generated by a computer calculation has shown that a significant modulation depth in the transmitted light intensity is achievable in the aforementioned $LiNbO_3$ substrate if the reflectivity of the mirrors and the optical attenuation coefficient are sufficiently low. Specifically, a reflectivity of 0.14 (which results from the difference in refractive index between the air and the X-cut $LiNbO_3$ channel waveguide) and an attenuation coefficient of up to 2.0 dB per cm are sufficient for this purpose. To summarize, the readily achievable modulation depth in the periodic dependence of the output light as a function of the applied voltage and the electrode length in a channel waveguide Fabry-Perot modulator suggests that a suitable light intensity threshold may be chosen to establish the "1" and "0" states for each element of the modulator array.

Referring to Fig. 8 again, a suitable laser diode array (ref. 25) is edge-coupled to one end face of the $LiNbO_3$ plate to provide the sampling optical pulses at a very high rate by direct modulation of injection current. At the output end an array of high-speed avalanche photodetectors, edge-coupled to the other end face of the $LiNbO_3$ plate, serve to convert the optical signals into electrical signals. If

necessary, the resultant electrical signals may also be enhanced by amplifiers. Finally, the high-speed electronic comparators which follow the amplifiers serve to compare the electrical signals with appropriate reference thresholds and generate the digital outputs.

In the experimental study, a 4-bit converter which consists of four parallel single-mode channel waveguides along the Y-axis was first designed and fabricated in a X-cut LiNbO$_3$ substrate using the conventional Ti-diffusion method (ref. 26). While the separation between adjacent waveguides is 500 μm, the separation of all electrode pairs in the apodized electrode array is 10 μm. The length of the longest electrode pair (for the LSB) is 10.0mm and the length of the static phase shifter in each waveguide is 2.0mm. Fig. 9 is a photograph of the LiNbO$_3$ substrate with the channel waveguide Fabry-Perot modulator array. A cw He-Ne laser (Fig. 10) shows the 22 KHz ramp analog test signal and the corresponding outputs from both the photomultiplier and the comparator for all bit channels of the 4-bit converter. It is seen that the period of the 2nd bit is twice that in the LSB as expected. This observation is valid for all adjacent bits. Since the maximum peak voltage of the ramp test signal was limited to 30 volts while the measured half-wave voltage for the LSB was 6.6 volts, some of the voltage levels were not digitized in this particular experiment.

In summary, a new electrooptic analog-to-digital converter which utilizes an array of channel waveguide Fabry-Perot modulators in a X-cut LiNbO$_3$ substrate has been studied using a 4-bit converter in a binary-code representation. The experimental results obtained have shown that it is feasible to fabricate Fabry-Perot modulator array with uniform quality. The length of the LiNbO$_3$ substrate used in this preliminary converter is 2.5cm; however, it can be easily reduced to 1.5cm in future design. Although this preliminary converter would require a peak-to-peak voltage of 52.8 volts to generate all digital words, this voltage requirement can be easily reduced by a factor of four in future design. Since only straight channel waveguides are required, this type of E-O A/D converter should possess the inherent advantages of simple geometrical layout, small substrate size, and low optical insertion loss as the number of bit precision is higher than, say, four. A preliminary analysis indicates that such converters should be capable of providing 1 GHz sampling rate with six to eight bits precisions.

NONCOLLINEAR MAGNETOOPTIC MODULATOR USING MAGNETOSTATIC SURFACE WAVE

Magnetostatic Surface Waves (MSSW) result from the electron spins precessing around a DC magnetic field but with its energy confined in a thin layer of ferromagnetic material such as YIG (Yttrium iron garnet) on a suitable substrate such as GGG (Gadolinium gallium garnet). MSSW can be readily generated by applying a microwave signal to a short-circuited metallic strip. The center frequency of the MSSW can be simply tuned, typically from 1.0 to 20 GHz, by varying an external DC magnetic field (ref. 27-29). Other potential advantages of the MSSW in comparison to the SAW include: 1) simple transducers not requiring critical photolithography, typically 50 μm wide; 2) lower propagation losses at the higher frequencies; and 3) both dispersive and nondispersive properties of the magnetostatic waves can be utilized. Since, like the SAW, the MSSW will induce a moving optical grating in the YIG film waveguide, a guided-light wave can be modulated by diffraction.

An interaction configuration of particular interest that has been identified is shown in Fig. 11. Note that in this non-collinear configuration, the propagation

direction of the lightwave is nearly orthogonal to that of the MSSW, in contrast to the collinear configuration (in which the light waves and the MSSE propagate in the same line) that was recently reported (ref. 30). Like guided-wave acoustooptics, non-collinear guided-wave magnetooptic interactions are expected to be much more versatile in application than the collinear interactions.

The dimensions of the YIB/GGG waveguide and the MSSW are shown in Fig. 11. A DC magnetic field of about 600 Gauss was applied to excite a MSSW with the center frequency at 3.9 GHz. Fig. 12 shows the waveform of the square-wave modulated light at 1.15 μm wavelength. An RF bandwidth of 250 MHz and a dynamic range of 15 dB have been measured in this preliminary experiment. Refined experiments are in progress.

In summary, noncollinear guided-wave magnetooptic diffraction using magnetostatice surface waves has been observed for the first time. This diffraction phenomenon should result in a number of integrated optic devices for wideband communication and signal processing systems with a center frequency much higher than that of acousto-optic devices.

CONCLUSION

Encouraging performance figures in terms of base bandwidth and device substrate sizes have been experimentally demonstrated with four single-mode hybrid integrated optic device modules in $LiNbO_3$ waveguide substrates and one in YIG/GGG substrates. Consequently, such device modules should act as efficient interface devices between a light wave and wideband temporal signals in optical communication and real-time signal processing systems. Although the present fabrication yield of such $LiNbO_3$-based modules has been less than desirable, increased yield should be possible through improvement in fabrication skills and facility. Both prism- and edge-couplings have been successfully employed to couple the He-Ne laser light at 6328 Å and 11500 Å wavelengths to the waveguide substrates. However, such coupling methods required delicate and time-consuming alignment and adjustment. A more robust approach, such as fiber-waveguide coupling, should enhance the practicality and utility of such device modules. Finally, a total hybrid integration of the devices requires coupling of a single-diode laser or an array of the same to the waveguide substrate. Such diode lasers should also greatly reduce the susceptibility of the devices to optical damage.

REFERENCES

1. I.W. Yao and C.S. Tsai, "A Time-Integrating Correlator Using Guided-Wave Acousto-optic Interactions," 1978 IEEE Ultrasonics Symposium Proc., pp. 87-90, IEEE Cat. No. 78CH1344-1SU.

2. C.S. Tsai, J.K. Wang and K.Y. Liao, "Acoustooptic Time-Integrating Correlators Using Integrated Optics Technology." SPIE-Symp. on Real-Time Signal Processing II, SPIE, Vol. 180, pp. 160-162, 1979.

3. K.Y. Liao, C.C. Lee and C.S. Tsai, "Time-Integrating Correlator Using Guided-Wave Anisotropic Acoustooptic Bragg Diffraction and Hybrid Integration," 1982 Topical Meeting on Integrated and Guided-Wave Optics, Jan. 6-8, 1982, Pacific Grove, CA., Technical Digest, pp. WA4-1 to -4, IEEE Cat. No. 82CH1719-4.

4. C.C. Lee, K.Y. Liao, and C.S. Tsai, "Acoustooptic Time-Integrating Correlator Using Hybrid Integrated Optics," 1982 IEEE Ultrasonics Symp. Proc., pp. 405-407, IEEE Cat. No. 82CH1823-4.

5. C.S. Tsai, "Guided-wave acoustooptic Bragg modulators for wide band integrated optic communications and signal processing," IEEE Trans. Circuits and Systems, Vol. CAS-26, 1072-1098 (Dec. 1979).

6. C.S. Tsai, C.T. Lee, and C.C. Lee, "Efficient Acoutooptic Diffraction in Crossed Channel Waveguides and Resultant Integrated Optic Module," 1982 IEEE Ultrasonics Sym. Proc., IEEE Cat. No. 82CH1823-4, pp. 422-425.

7. F.R. El-Akkari, C.L. Chang and C.S. Tsai, "Electrooptical Channel Waveguide Matrix Switch Using Total Internal Reflection," Topical Meeting On Integrated and Guided Wave Optics, Jan. 28-30, 1980, Incline Village, Nevada. Technical Digest, pp. TuE 4-1 to -4, IEEE Cat. No. 80CH1489-4QEA.

8. C.S. Tsai, C.L. Chang, C.C. Lee, and K.Y. Liao, "Acoustooptic Bragg Deflection in Channel Optical Waveguides," 1980 Topical Meeting on Integrated and Guided-Wave Optics, Technical Digest of Post Deadline Papers, pp. PD7-1 to -4, IEEE Cat. No. 80CH1489-4QEA.

9. C.S. Tsai, B. Kim, and F.R. El-Akkari, "Optic Channel Waveguide Switch and Coupler Using Total Internal Reflection," IEEE J. Quantum Electron., Vol. QE-14, 513-517 (1978).

10. C.L. Chang and C.S. Tsai, "GHz Bandwidth Optical Channel Waveguide TIR Switches And 4x4 Switching Networks," 1982 Topical Meeting on Integrated and Guided-Wave Optics, Jan. 6-8, Pacific Grove, CA, Technical Digest, pp. ThD-1 to -4, IEEE Cat. No. 82CH1719-4.

11. H.F. Taylor, "Optical Waveguide Connecting Networks," Electron. Lett., Vol. QE-14, 513-517 (1978).

12. R.V. Schmidt, "Experimental 4x4 Optical Switching Network." Electron. Lett., Vol. 12, 575-577 (1976).

13. A. Huang, Y. Tsunoda, J.W. Goodman, and S. Ishihara, "Optical Computers Using Residue Arithmatics," Appl. Opt., Vol. 18, pp. 149-159 (1979).

14. J.N. Polky and D.D. Miller, "Optical Waveguide Circuit Design of an Adaptive Filter in the Residue Number System," Appl. Opt., Vol. 21, pp. 3539-3551 (1982).

15. S. Wright, I.M. Mason, and M.G. Wilson, "High-Speed Electrooptic Analogue-Digital Conversion," Electron. Lett., Vol. 10, pp. 508-509, Nov. 28, 1974.

16. H.F. Taylor, "An Electrooptic Analog-To-Digital Converter," Proc. IEEE, Vol. 63, pp. 1524-1525, Oct. 1975.

17. P. Saunier, C.S. Tsai, I.W. Yao, and Le T. Ngugen, "Electrooptic Phased-Array Light Beam Deflector With Application To Analog-To-Digital Converter," 1978 Topical Meeting on Integrated and Guided-Wave Optics, Jan. 16-18, Salt Lake City, Utah, Technical Digest, pp. TuC 2-1 to 2-4, IEEE Cat. No. 78CH1280-7.

18. H.F. Taylor, M.J. Taylor, and D.W. Bauer, "Electro-Optic Analog-To-Digital Conversion Using Channel Waveguide Modulators," Appl. Phys. Lett., Vol. 32, pp. 559-561, 1978.

19. C.D.H. King and J.D. Jackson, Proc. 6th European Conf. on Opt. Comm., 256, 1980.

20. F.J. Leonberger, C.E. Woodward, and R.A. Becker, "4-bit 828 Megasample/s Electro-Optic Guided Wave Analog-To-Digital Converter," Appl. Phys. Lett., Vol. 40, pp. 565-568, 1982.

21. S. Yamada, M. Minabata, and J. Noda, "High Speed 2-Bit Analogue-Digital Converter Using LiNbO$_3$ Waveguide Modulator," Electron Lett., Vol. 17, pp. 259-260, 1981.

22. C.L. Chang and C.S. Tsai, "An Integrated Optical Analog-To-Digital Converter Using An Array of Channel Waveguide Fabry-Perot Modulators," Paper presented at the International Conference on Integrated Optics and Optical Fiber Communication, June 27-30, 1983, Tokyo, Japan.

23. P.W. Smith, I.P. Kaminow, P.J. Maloney, and L.W. Stulz, "Integrated Bistable Optical Devices," Appl. Phys. Lett., Vol. 33, pp. 24-26, 1978.

24. E.I. Gordon and J.D. Rigden, "The Fabry-Perot Electrooptic Modulator," Bell Syst. Tech. Jour., Vol. 42, pp. 155-179, 1963.

25. D. Botex, J.C. Connolly, D.B. Gilbert , M.G. Harvey, and M. Ettenberg, "High-Power Individually Addressable Monolithic Array of Constricted Double Heterojunction Large-Optical-Cavity Lasers," Appl. Phys. Lett., Vol. 41, pp. 1040-1042, 1982.

26. R.V. Schmidt and I.P. Kaminow, "Metal Diffused Optical Waveguides In LiNbO$_3$," Appl. Phys. Lett., Vol. 25, pp. 458-460, 1974.

27. J.D. Adam and J.H. Collins, "Microwave Magnetostatic Delay Devices Based on Epitaxial Yttrium Iron Garnet," Proc. IEEE, 64, 794-800 (May 1976).

28. J.M. Owens, R.L. Carter, C.V. Smith and J.H. Collins, "Magnetostatic Waves, Microwave SAW," 1980 IEEE Ultrasonics Symp. Proc., Cat. No. 80C1602-2, 506-513.

29. L.R. Adkins and H.L. Glass, "Propagation of Magnetostatic Surface Waves in Multiple Magnetic Layer Structures, "Electronics Letters, Vol. 16, No. 15, 590-592 (July 17, 1980).

30. A.D. Fisher, J.N. Lee, E.S. Gaynor, and A.B. Tveten, "Optical Guided-Wave Inter-actions with Magnetostatic Waves at Microwave Frequencies," Appl. Phys. Lett., Vol. 41, pp. 779-781 (Nov. 1982).
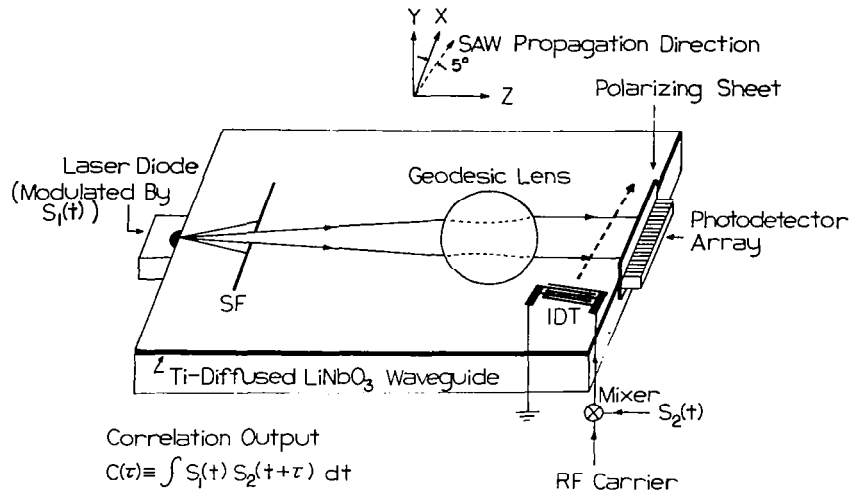
Figure 1.- Acoustooptic time-integrating correlator using anisotropic Bragg diffraction and hybrid optical waveguide structure.
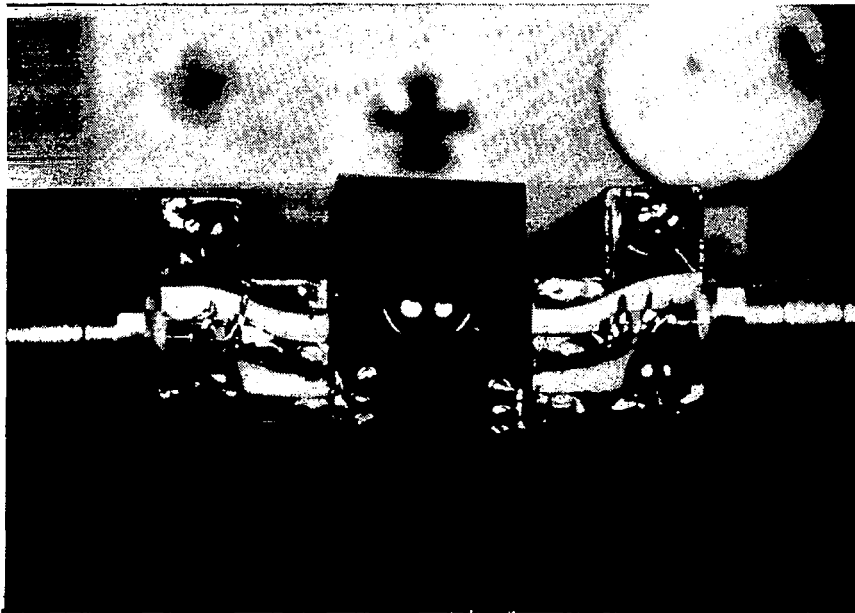

Figure 2.- Hybrid integrated module for acoustooptic time-integrating correlation.
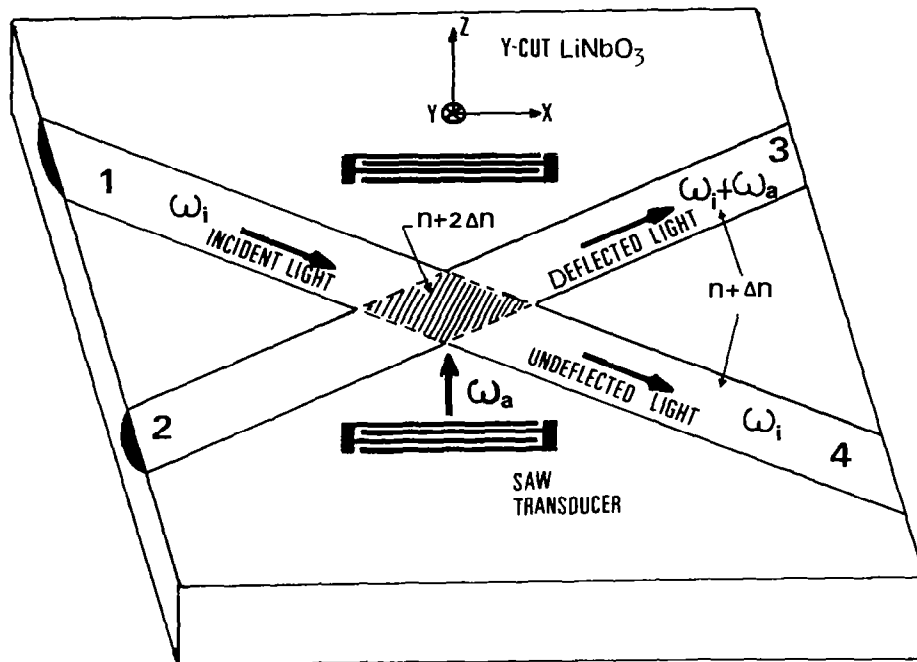
Figure 3.- Acoustooptic diffraction from surface acoustic wave in crossed-channel waveguides.
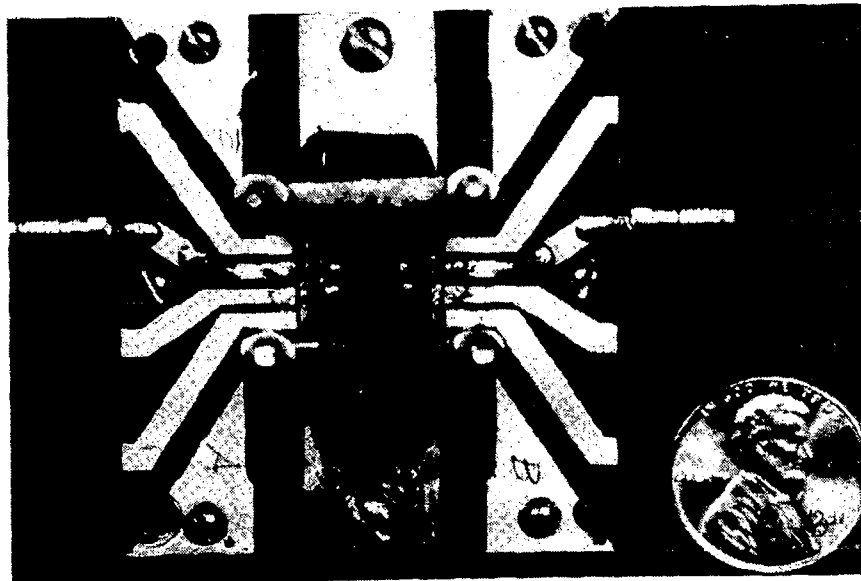
Figure 4.- Single-mode crossed-channel waveguide acoustooptic modulator/ deflector in LiNbO₃substrate.
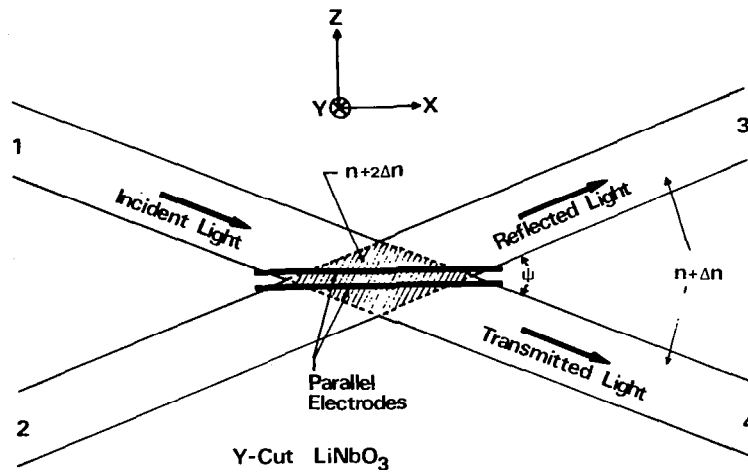
Figure 5.- Electrooptic total internal reflection in crossed-channel
          waveguide in LiNbO$_3$ substrate.
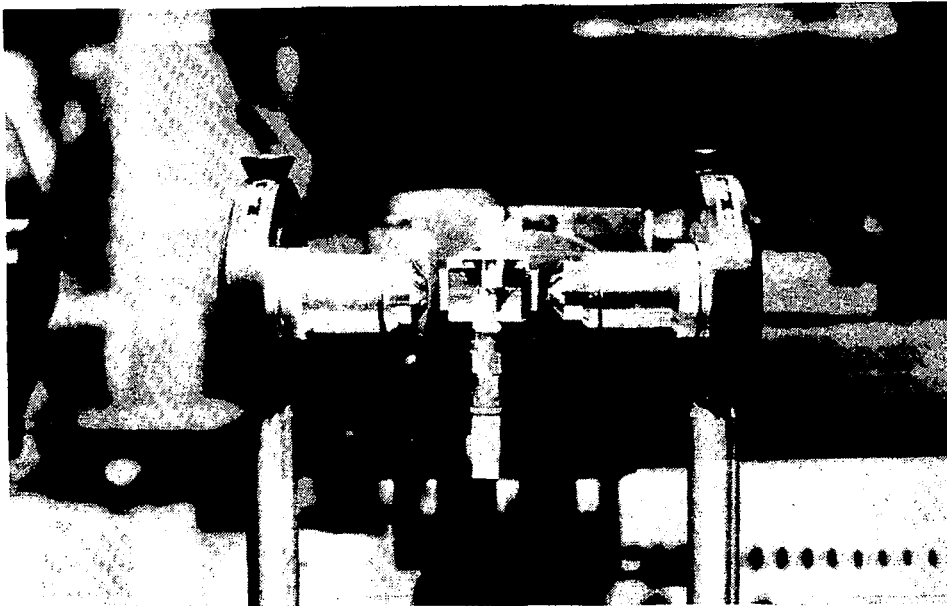
Figure 6.- Basic electrooptic TIR modulator/switch module in crossed-
          channel waveguide showing LiNbO$_3$plate in Middle and Microscope
          objectives at right and left for edge-coupling of light beam.
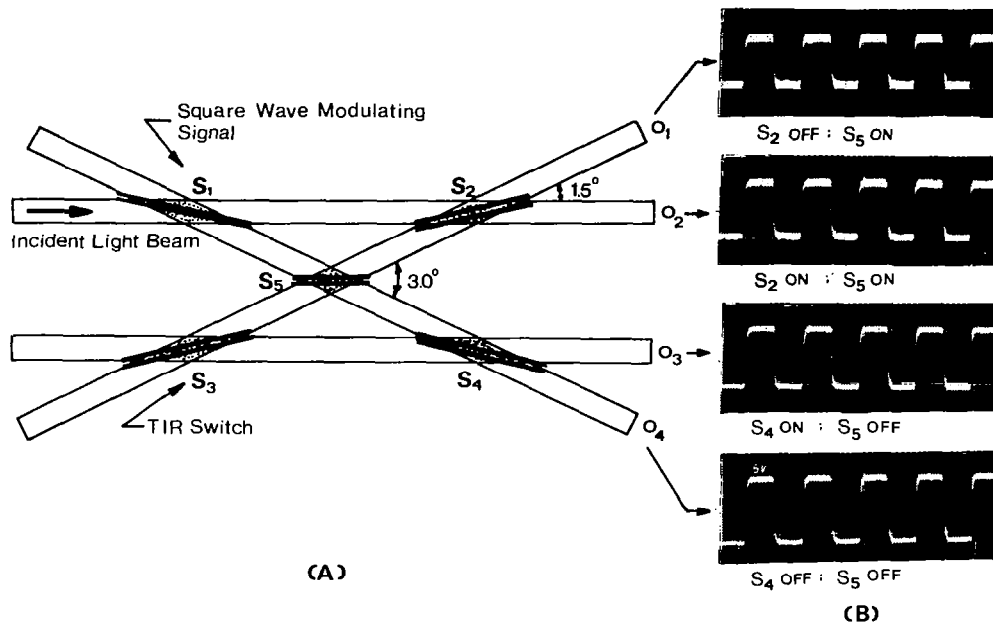
Figure 7.- 4 x 4 optical switching network using crossed-channel waveguide
TIR switches (A) and output waveforms for four switching states (B).
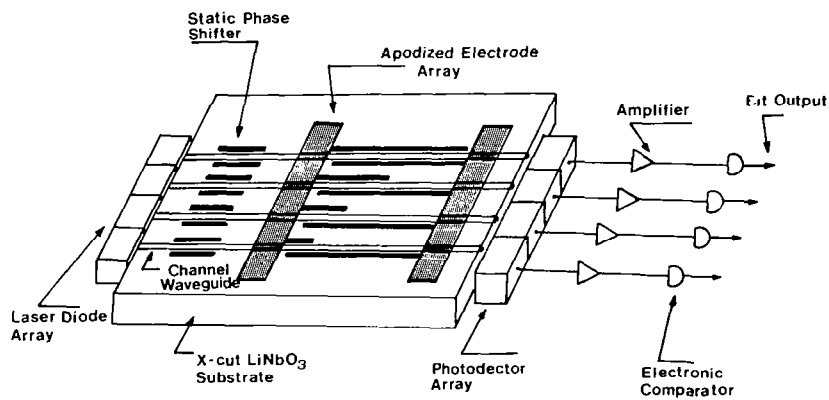
Figure 8.- Schematic diagram of electrooptic A/D converter utilizing array
of Fabry-Perot modulators.
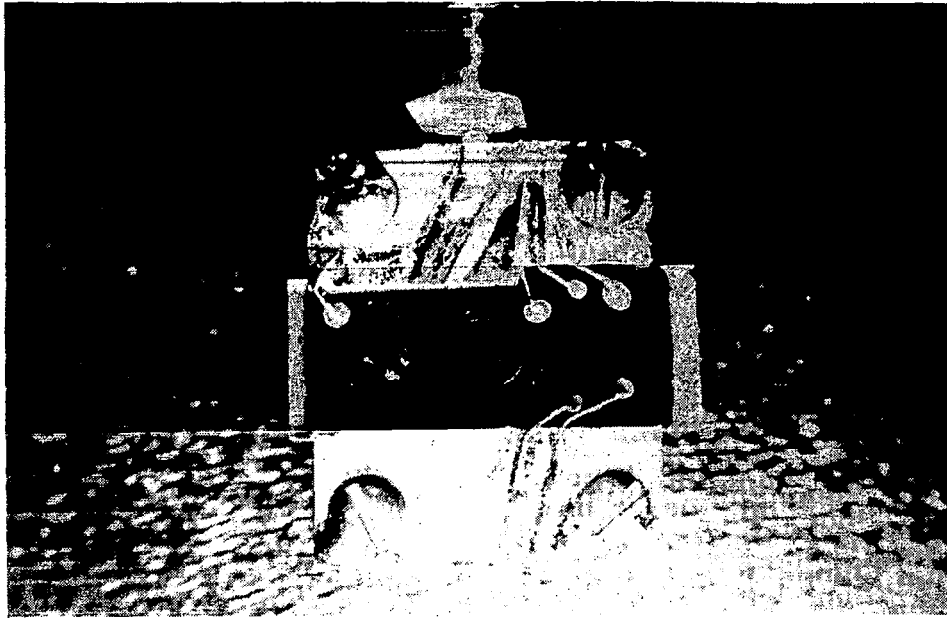
Figure 9.- Photograph showing LiNbO$_3$ plate with four parallel channel waveguide Fabry-Perot modulators for analog-to-digital conversion.
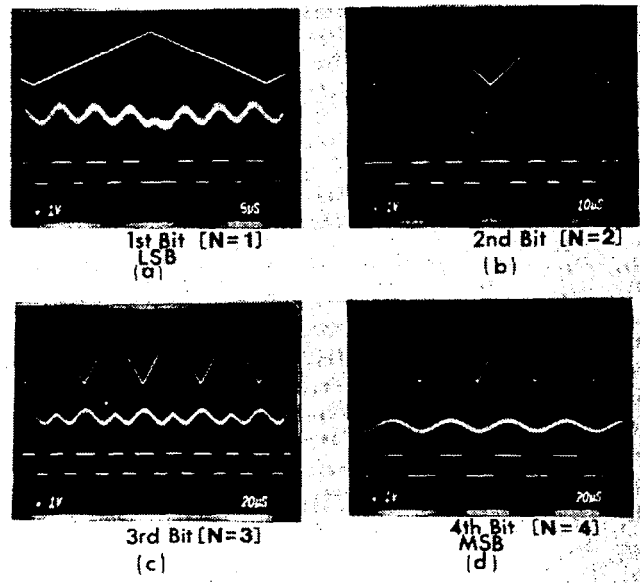
Figure 10.- Experimental results of a 4-bit electrooptic A/D converter using channel waveguide Fabry-Perot modulator array in figs (a) to (d).
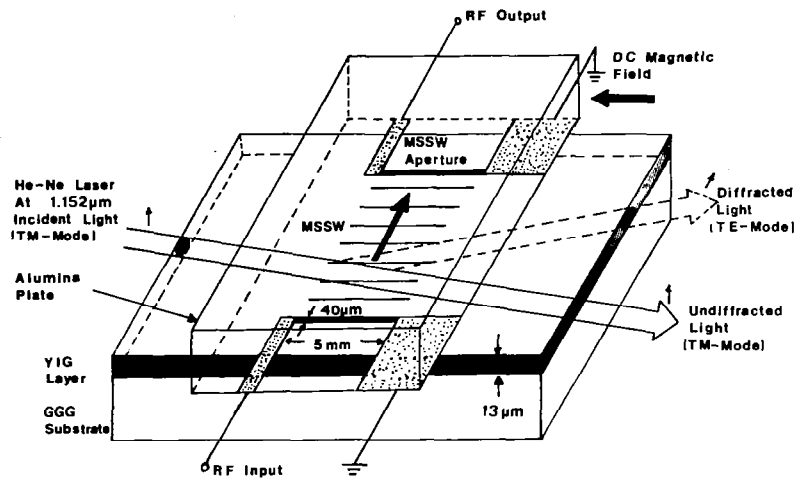
Figure 11.- Device geometry for guided-wave noncollinear anisotropic magneto-
optical diffraction using magnetostatic surface wave.
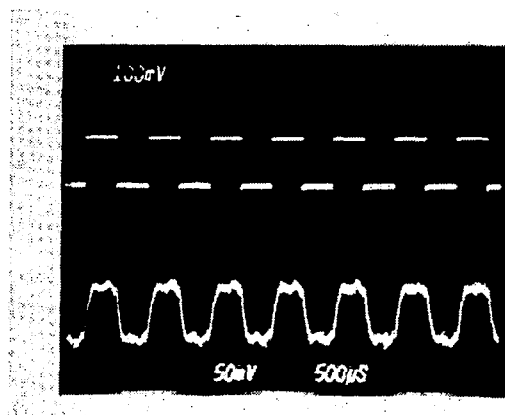
Figure 12.- Guided-wave noncollinear anisotropic magnetooptic diffraction
from magnetostatic surface wave: 1.4 KC square-wave modulated
magnetostatic surface wave at 3.9 GHz carrier frequency (top
trace); diffracted light waveform (bottom trace).

A NEW MULTIFUNCTION ACOUSTO-OPTIC SIGNAL PROCESSOR

N. J. Berg, M. W. Casseday, A. N. Filipov, and J. M. Pellegrino
Harry Diamond Laboratories
Adelphi, Maryland 20783

Abstract

An acousto-optic architecture for simultaneously obtaining time integration correlation and high-speed power spectrum analysis has been constructed using commercially available TeO_2 modulators and photodiode detector-arrays. The correlator section of the processor uses coherent interferometry to attain maximum bandwidth and dynamic range while achieving a time-bandwidth product of 10^6. Two correlator outputs are achieved in this system configuration. One is optically filtered and magnified 2 : 1 to decrease the spatial frequency to a level where a 25-MHz bandwidth may be sampled by a 62-mm array with elements on 25-μm centers. The other output is magnified by a factor of 10 such that the center 4 μs of information is available for estimation of time-difference-of-arrival to within 10 ns. The Bragg cell spectrum-analyzer section, which also has two outputs, resolves a 25-MHz instantaneous bandwidth to 25 kHz and can determine discrete-frequency reception time to within 15 μs. A microprocessor combines spectrum analysis information with that obtained from the correlator.

I. Introduction

An acousto-optic architecture has been devised to simultaneously obtain time integration correlation and high-speed power spectrum analysis in a single, compact package. As can be seen in figure 1, this processor incorporates two TeO_2

shear-wave modulators in a two-level optical system to obtain two correlator outputs (lower level, figure 1(a)) and two spectrum analyzer outputs (upper level, figure 1(b)). Information from these sources is sent to a controlling microprocessor, which analyzes the received signals and reports results to the system operator. In the present version, the optical system covers a 2 x 3 foot area. This paper discusses considerations involved in the design and construction of such a processor and presents the operating parameters and features of the system. Included are correlation results for a 2-MHz RF chirp input signal and results of multisignal reception by the spectrum analyzer section of the processor. Finally, a parallel combining scheme is proposed to extend the instantaneous bandwidth of systems in which such a processor may be incorporated.

II. Theory Of Operation

The acousto-optic interaction has been studied extensively and reports concerning its use in signal convolvers, correlators, and spectrum analyzers are available.[1-4] Hence, only results pertinent to the operation on this processor will be considered here.

When the incidence angle of the light illuminating the sound wave in an acousto-optic modulator is set to the Bragg angle $\theta_B = \sin^{-1}\left(\lambda/(2\Lambda)\right)$ (where λ is the incident light wavelength and Λ the acoustic wavelength), constructive interference occurs for only a single first-order diffraction. The intensity of the diffracted light I_D, when operating in this Bragg mode, can be shown to be

$$I_D = I_o \sin^2 \left\{ \frac{\pi}{\lambda} \left(M_2 \frac{W}{2\Lambda} P_a \right)^{1/2} \right\} \qquad (1)$$

166

where I_0 is the incident light intensity; W, the width of the acoustic phase fronts; P_a, the acoustic power; and M_2, an acousto-optic figure of merit of the delay line material. For sufficiently small P_a, the diffracted light intensity for well-collimated light may be considered linear with acoustic power.

When a bandpass signal, $A(t)\cos\omega(t + \phi)$, is applied to the modulator, it generates a sound wave, $S(t,z)$, which propagates through the Bragg cell. This wave may be described as

$$S(t, z) = A'(T - z/\upsilon) \cos\omega(t - z/\upsilon + \phi) \qquad (2)$$

where υ is the acoustic propagation velocity, and z is the distance along the Bragg cell. The diffracted light may then be represented by

$$L_D(t, z) = L_0 A''(t - z/v) \cos\left(\omega_\ell t + \omega (t - \frac{z}{\upsilon} + \phi) + \frac{z \sin \theta_B}{\lambda}\right) \qquad (3)$$

where ω_ℓ and L_0 are the incident light frequency and the amplitude, respectively. The diffracted light $L_D(t, z)$ is seen to contain all the signal information between the time t and $t - Z/\upsilon$, where Z is the illuminated length of the Bragg cell, and to exit the cell at the Bragg angle, which may be considered to be proportional to the frequency of the signal for the light and signal frequencies commonly used in these devices. Hence, a spectrum analyzer may be constructed simply by placing a Fourier transform lens behind the modulator to collect and focus the diffracted light onto an array placed at the focal plane of the lens, position along the array corresponding to input signal frequency.

Diffracted light from each of the two modulators (figure 1(a)) may be combined and filtered to remove any undiffracted light to perform correlation. Diffracted light from each cell i (i = 1, 2) is described by

$$L_i(t, x_i) \simeq S_i(t - \frac{x_i}{\upsilon}) \cos\{\omega_\ell t + \omega(t - \frac{x_i}{\upsilon}) + \frac{x_i \sin \theta_D}{\lambda}\} \qquad (4)$$

for $\theta_D = \sin^{-1}((\Lambda - \Lambda_o)/\lambda)$, where Λ_o is the acoustic wavelength at the Bragg-cell design center frequency, ω_o. Beams $L_1(t, x_1)$ and $L_2(t, x_2)$ are combined using a cube beam-splitter, filtered, and so illuminate the time-integrating square-law photodetector arrays A_3 and A_4. The output of these arrays may then be shown to be[5]

$$V(z) \sim \cos(\frac{2}{M}(\omega - \omega_o)\tau) \int_T S_1(t')S_2(t' + \frac{2\tau}{M} - \tau_o) \, dt \qquad (5)$$

where $\tau = z/\upsilon$, $\tau_o = Y/\upsilon$, $t' = t - \tau$, M is the magnification factor of the optical filtering system, and Y, the illuminated length of Bragg cell 2. Equation 5 is thus seen to be the correlation of the bandpass signals $S_1(t)\cos\omega t$ and $S_2(t)\cos\omega t$ offset by the frequency ω_o and in a compressed, shifted time frame. Given that one uses a single laser source and hence forms a coherent optical system, the output is a detected interference pattern of the diffracted light from the two modulators. As such, this correlator is generically similar to the two-beam surface-acoustic-wave (SAW) time integrating correlator previously reported.[6,7]

III. System Design

The size and performance of the processor are affected by both the type of Bragg cell used and the length and diode spacing of the available photodiode arrays which detect the spatial light distributions. If a 50-μs Bragg-cell delay length is used to insure 25-kHz frequency resolution, the physical length (and illuminated aperture) of a $LiNbO_3$ SAW cell would have to be 17.5 cm, while a $Bi_{12}GeO_{20}$ SAW Bragg cell would be 8.7 cm, and a TeO_2 slow-shear bulk-acoustic-wave Bragg cell would be 3.1 cm. Clearly the TeO_2 cell results in the smallest processor as far as the input optics (laser, beam expander, etc.) are concerned. In addition, the greater angular beam-deflection versus frequency of this cell results in much shorter focal length (thus more compact) Fourier-transform lens system to achieve the spot travel required by a given diode-array length for spectrum analysis. The TeO_2 cell offers another advantage in its high diffraction efficiency, which for a single input signal may reach or even exceed 60 percent depending upon the particular cell.

This compactness is achieved with several disadvantages. The shear-wave cell operates maximally with incoming light circularly polarized. As the crystal is optically active, the modulated light is elliptically polarized. Since a large portion of the light exiting each Bragg cell is split off for use in the spectrum analyzer section of the processor, care must be taken to ensure that the light from each cell reaching the correlator arrays is of matched polarization so that optical interference can be observed. This entails appropriate design and custom coatings for beam-splitter and combiner cubes.

Phase distortion in the modulated laser light is also seen to be a problem

in contrast to the virtually distortion-free SAW devices. With Isomet OPT-1 Bragg cells, diffraction performance across the light aperture is good in the direction corresponding to that of sound propagation in the device. Perpendicular to that direction, a variation in diffraction intensity can be observed, which affects the depth of the interference fringes when two beams similarly perturbed are combined. The cause of this phenomenon, although uncertain, may be due to defects or domains in the TeO_2 crystal. Performance under these circumstances may be improved by selective aperturing of the device and/or modulated light which is to be focussed onto the detector array.

A more serious disadvantage is that the spatial-frequency variation versus signal-frequency change at the correlator detector array is greatly increased. From equation 5, the array signal variation with z, the distance along the array, is seen to include a term

$$V(z) \sim \cos\left[\frac{2}{M}(\omega-\omega_o)\frac{z}{\upsilon}\right] \tag{6}$$

For the 617-m/s sound velocity in TeO_2 this yields a spatial frequency of about 3.3×10^4 cycles/m for $M = 1$ and $|\omega -\omega_o| = 2\pi \times 10.3$ MHz. Thus a maximum bandwidth of 20.6 MHz can be sampled by a commercially available detector array with 15-μm diode spacing. For the same array diode spacing, a correlator using $LiNbO_3$ SAW cells would have a usable bandwidth of 114 MHz.

The usable correlation bandwidth with TeO_2 cells can be increased by magnifying the diffracted beams with a spatial filter system. Using a 2 : 1 magnification ratio ($M = 2$), a commercially available 62-mm long, 4096-diode array allows a 25-MHz signal bandwidth with about 3.3 samples per spatial cycle

and displays the full time aperture of the cells. This bandwidth is achieved in commercially available TeO_2 cells with 50-μs delay apertures, providing a performance-matched system.

The second array used for correlation detection is illuminated by only the center section of the diffracted light beams. An aperture stop blocks light from all but the center 4 μs of the Bragg cells, and the spatial extent of this light is magnified by a factor of 10 in the second spatial filter system. The expanded output illuminates a 25.6-mm long, 1024-diode high-dynamic-range detector array that provides high resolution time-difference-of-arrival (TDOA) information. The minimum correlation width expected with 30-MHz bandwidth signals is approximately 67 ns. In the compressed τ space of the correlator, this corresponds to a spatial extent of about 0.2 mm after magnification M = 10. This would be sampled by 8 diodes, allowing TDOA interpolation to within 10 ns.

IV. Spectrum Analysis

The spectrum analyzer section of the processor is illustrated in figure 1(b). Collimated, coherent, circularly polarized laser light (5-mW Helium-Neon) is split using a 50/50 nonpolarizing cube beam-splitter; each beam from this splitter illuminates one of the modulators, incident at the Bragg angle for the cells' center frequency of 45 MHz. The diffracted light from each cell is split into two parts, one of which is sent vertically to another optical level where, after passage through a 720-mm Fourier transform lens, it is focussed onto a high-speed photodiode detector array.

Arrays A_1 and A_2 were chosen for their ultra-fast readout capabilities: each

array can be read out in 15 μs using a combination serial-parallel scheme. The 18.4-mm detector has 1024 elements separated into eight segments; these segments are read out in parallel while the diodes within each segment are read out serially. This high-speed capability is necessary for time-of-reception determination of signal frequency changes. Every 15 μs, an update report is sent to the system controller indicating the arrays' status. One disadvantage of these arrays is the high light intensity necessary to trigger them; the beam-splitter cubes were designed to send 90 percent of the incident light to spectrum analysis processing. Each array covers the full 25 MHz of system processing bandwidth. When the signals received from each of two directional antennas are used as separate inputs to each Bragg cell, direction of arrival information may then be derived via amplitude comparison of these two arrays.

With this configuration, the optical spot size for a single-frequency RF signal is about 60 μm, covering three pixels on the detector. Hence, an individual signal can be resolved to within 25 kHz. As shown in figure 2, signals received simultaneously can be distinguished when they are as little as 50 kHz apart. Signals received sequentially in time, however, can be distinguished with frequency differences as little as 25 kHz. Single signals can be distinguished with this resolution over a dynamic range of approximately 25 dB. This figure is achieved when background electronic-array-noise and signal due to spurious light reflections are subtracted from the signal readings.

V. Time Integrating Correlation

The 10 percent of remaining diffracted light is combined in a beam-splitter/combiner cube and sent to the two time-integrating photodiode detector

arrays. Notice in figure 1(a) that the optical path has been kept as compact as possible. This was done to minimize the walk-off which occurs when interfering beams are combined at greater angles of intersection, corresponding to maximum deviation from the device center frequency. In this configuration, walk-off has been minimized such that the two beams overlap by more than 80 percent, assuring correlation of nearly the full time aperture available.

Figure 3 shows the output of array A_3, which is set to observe the full 50 μs of delay aperture and integrate over a 30-ms time period. The input to each cell consisted of a 2-MHz step-wise chirp, where increasing frequencies are stepped through sequentially. It is an interesting correlation property of these signals that when the system resolution of 25 kHz is finer than the step size Δf, foldover peaks can be observed to either side of the main correlation. The number of these peaks is proportional to Δf. The output of array A_4, which is set to sample the center 4 μs of delay aperture, is shown in figure 4 for the same input signal used for figure 3. The position of this correlation can be easily determined and the information used to obtain TDOA and, hence, direction of arrival.

VI. Bandwidth Enhancement

The acousto-optic signal processor that has been described is limited by practical material considerations, to about 25 MHz instantaneous bandwidth. Figure 5 illustrates a parallel combining scheme for increasing the instantaneous bandwidth of a receiver system employing these processors, without sacrifice of resolution or other processor performance.

In the figure six identical processors are shown, each taking its input

signals from the corresponding IF outputs of two 150-MHz total-instantaneous-bandwidth (input bandwidth) channelized receivers. Each acousto-optic processor output is digitally post-detection processed as a stand-alone system. The outputs from the six post-detection processors are then further analyzed by a system which digitally restores the frequency offset information to each individual output and examines the combined signal. The result is a 150-MHz bandwidth spectrum analyzer of increased time-bandwidth product with 25-kHz frequency resolution and 15-μs time-of-reception resolution, combined with a 150-MHz bandwidth time-integrating correlator able to detect signals and resolve TDOA to better than 10 ns (for maximum bandwidth signals).

VII. Conclusion

An acousto-optic processor that combines the features of high-speed spectrum analysis and time-integrating correlation in a fairly compact optical package has been demonstrated. A new version in more compact form is in the planning stages; this system would be rack-mountable and packaged for RF shielding. Operating parameters will be identical. These processors may be combined for extended bandwidth operation or used as convenient stand-alone operating systems.

References

1). R. Adler, "Interaction Between Light and Sound," IEEE Spectrum, $\underline{4}$, 5, (1967), pp 42-54, and references therein.

2). I. C. Chang, "Acoustooptic Devices and Applications," IEEE Trans. Sonics Ultrason., $\underline{50\text{-}23}$, (1976), p 2.

3). W. T. Rhodes, "Acousto-Optic Signal Processing: Convolution and Correlation," Proc. IEEE, $\underline{69}$, 1, (1981), p. 65.

4). T. M. Turpin, "Spectrum Analysis Using Optical Processing," Proc. IEEE, $\underline{69}$, 1, (1981), p 79.

5). N. J. Berg and J. M. Lee, ed., Acousto-Optic Signal Processing: Theory and Implementation, Marcel Dekker, Inc., New York (1983).

6). M. W. Casseday, N. J. Berg, I. J. Abramovitz, and J. N. Lee, "Wide Band Signal Processing Using the Two-Beam Surface Acoustic Wave Acousto-Optic Time Integrating Correlator," IEEE Trans., $\underline{MTT\text{-}29}$, 5, (1981).

7). N. J. Berg, M. W. Casseday, I. J. Abramovitz, and J. N. Lee, U.S. Patent #4,326,778, 27 April 1982.
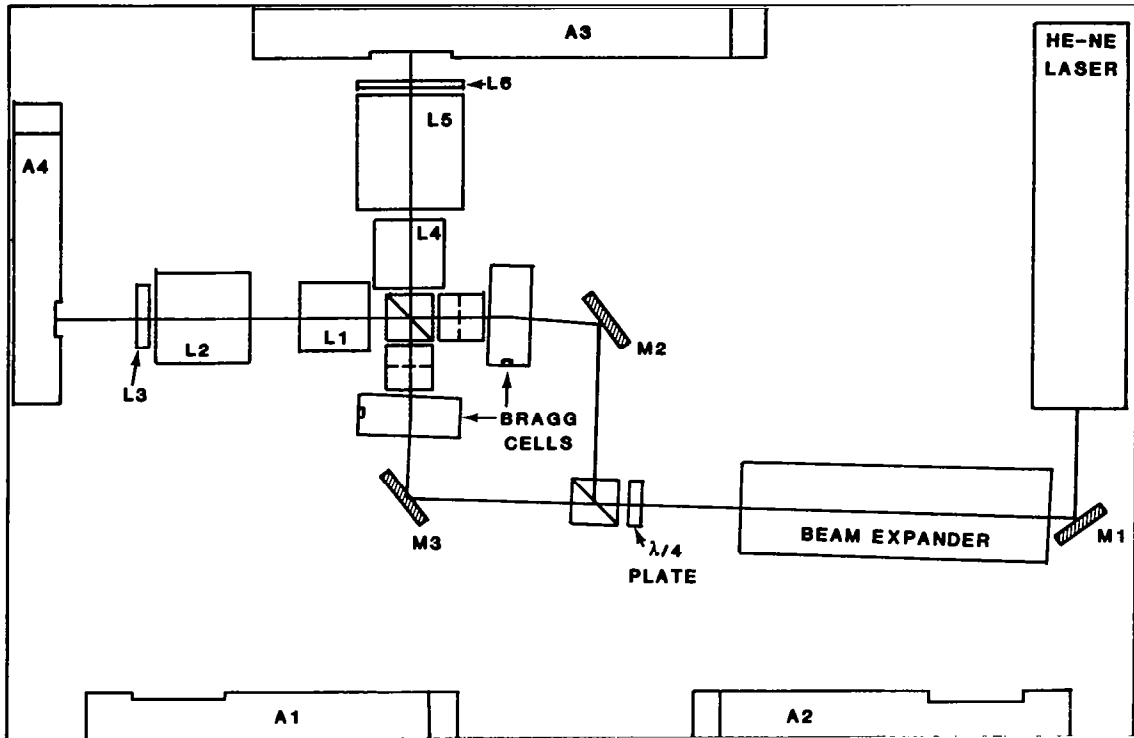
(a) Correlator section (lower optical level)
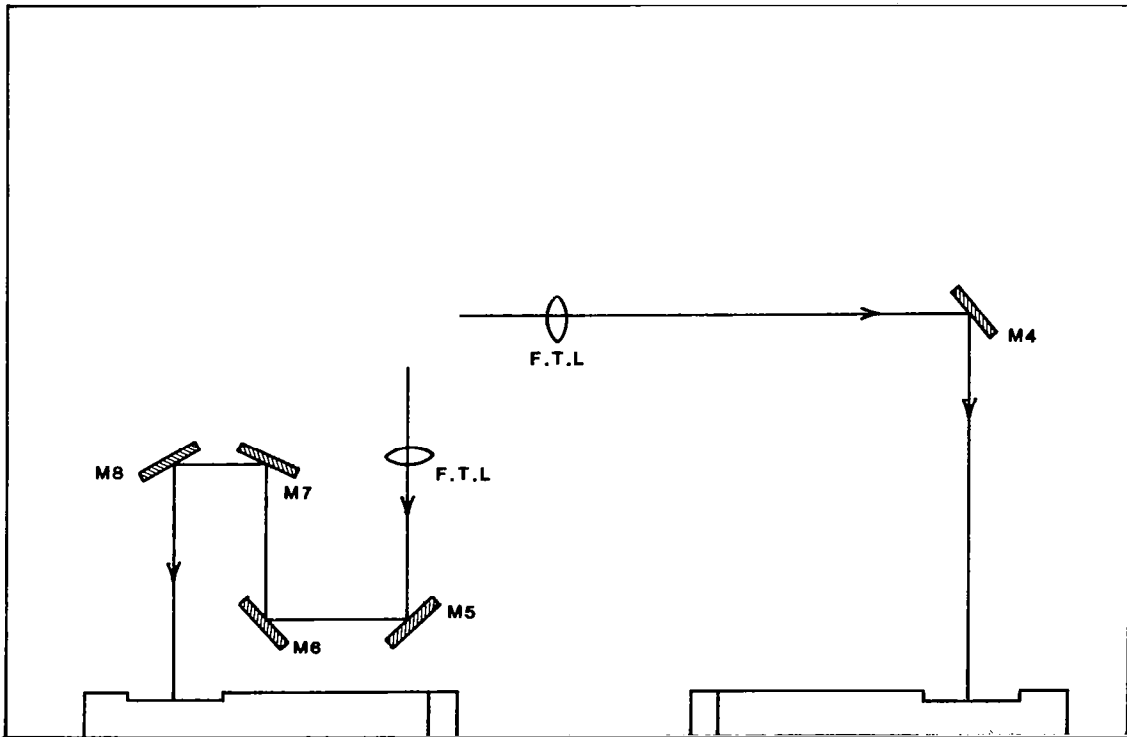
(b) Spectrum analyzer section (upper optical level)

Figure 1.- Schematic of the optical system for multifunction processor.
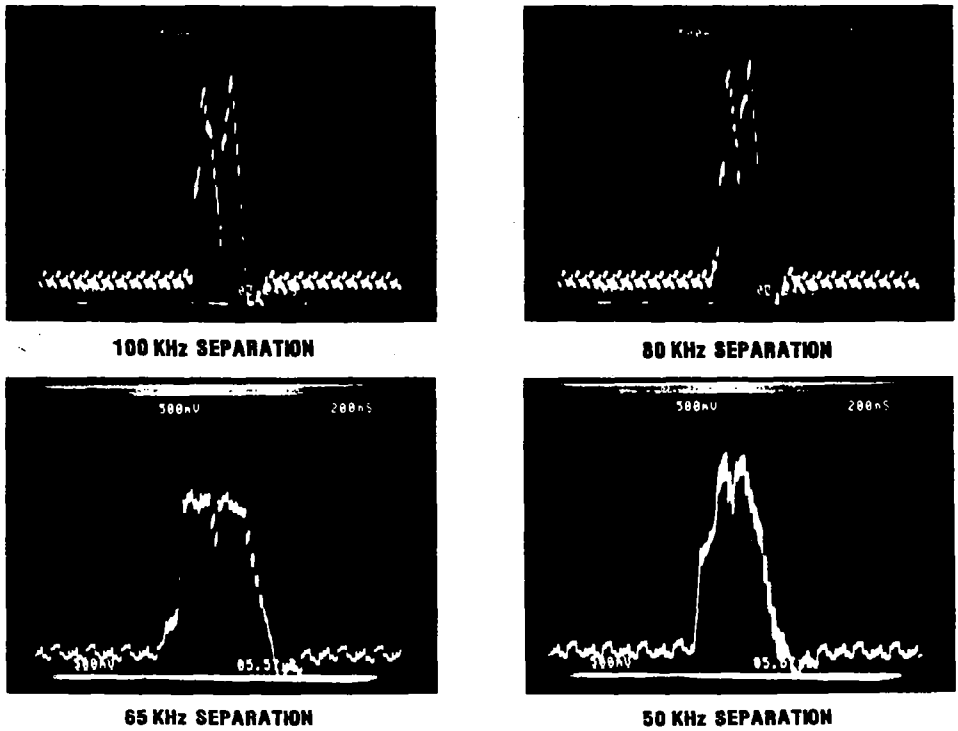
Figure 2.- Output of spectrum analyzer for two simultaneous cw RF input signals with various frequency spacing, Δf.
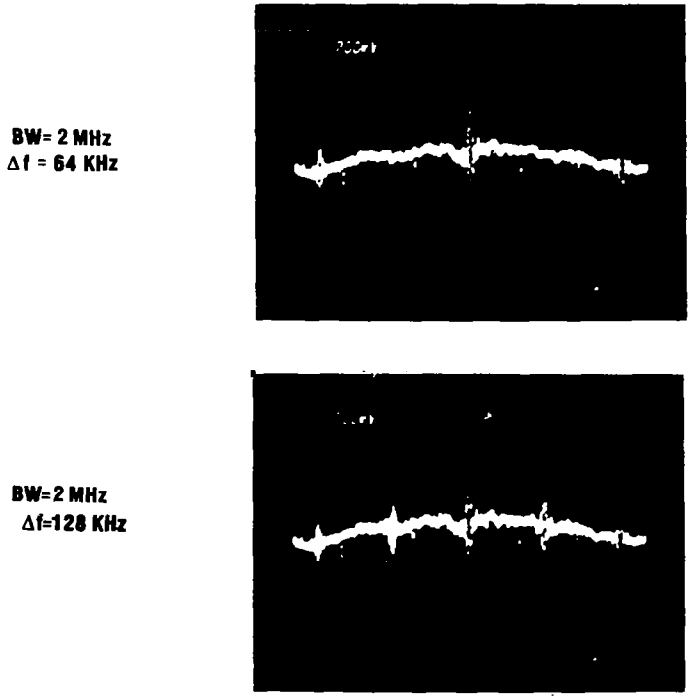
Figure 3.- Correlator output for 2-MHz bandwidth step-wise chirp input to both Bragg cells. Shown are foldover peaks for 64- and 128-kHz frequency spacings.

FULL APERTURE **CENTER**

fc = 40 MHz
BW = 2 MHz
Δf = 64 KHz
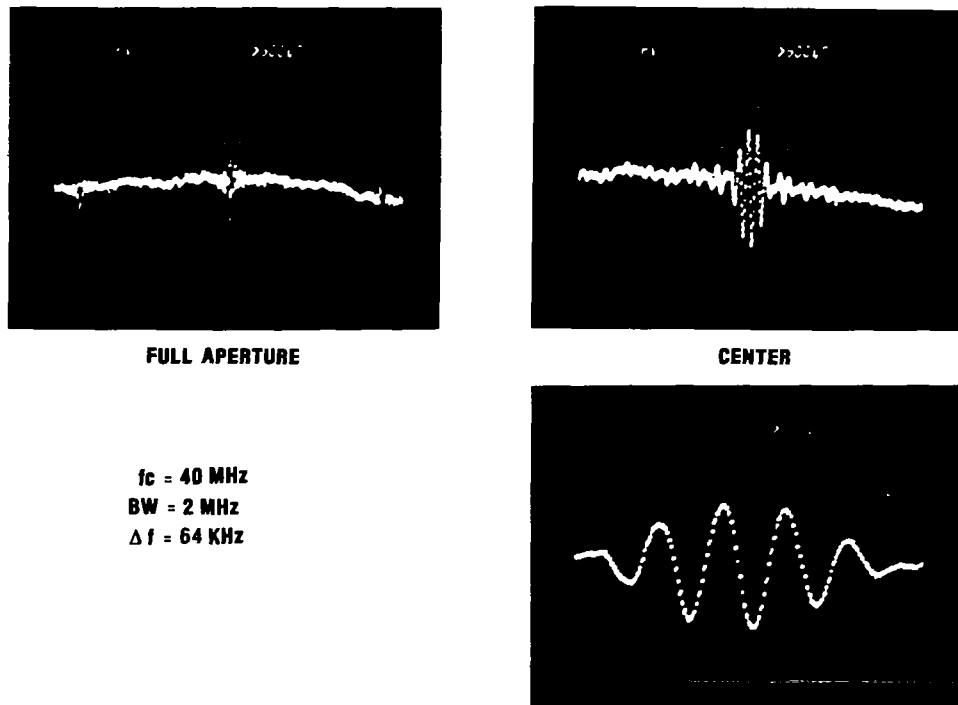
Figure 4.- Output of M = 10 correlator section for same 2-MHz bandwidth
chirp used in figure 3, with Δf = 64 kHz. Shown is full aperture
and center 4 µs of correlation space. Center frequency of
chirp f_c is 40 MHz.
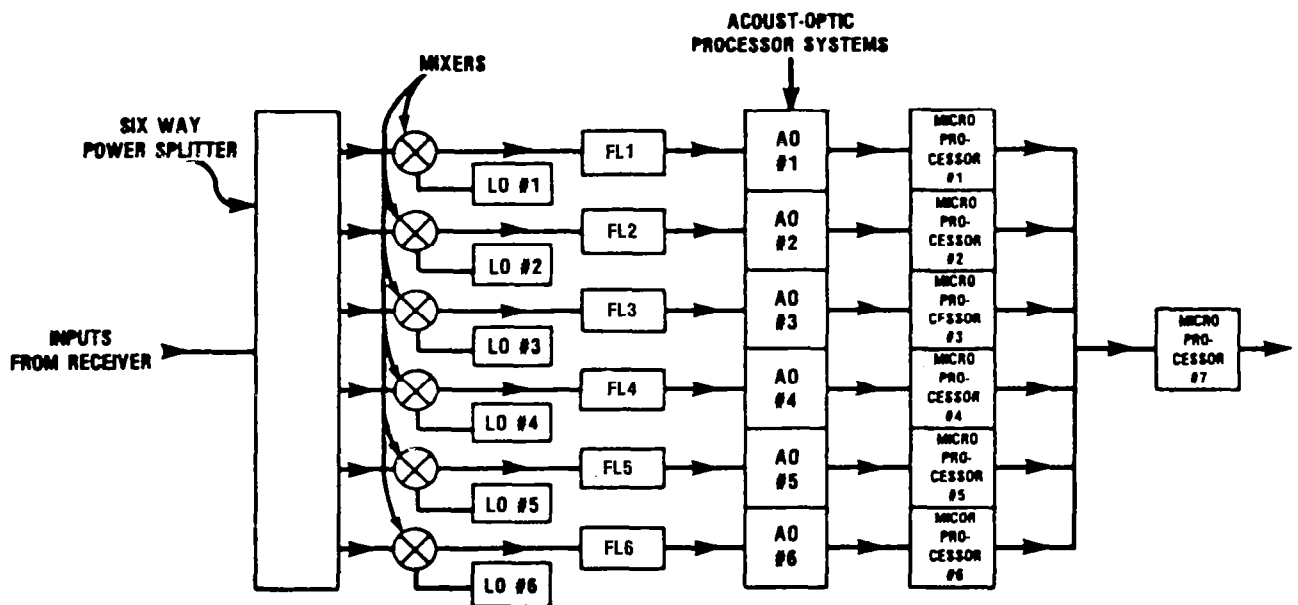
Figure 5.- Parallel combining scheme for processor bandwidth enhancement.

OPTICAL PULSE GENERATOR

USING

LIQUID CRYSTAL LIGHT VALVE

Stuart A. Collins, Jr.
The Ohio State University ElectroScience Laboratory
1320 Kinnear Road
Columbus, Ohio   43212

SUMMARY

This paper deals with numerical optical computing. First various aspects of the program at The Ohio State University are presented. Then a design for an optical pulse generator using a Hughes Liquid crystal light valve and intended for application as an optical clock in a numerical optical computer is considered. The pulse generator is similar in concept to the familiar electronic multivibrator, having a flip-flop and delay units.

INTRODUCTION

This paper concerns the design of an optical pulse generator using a Hughes liquid crystal light valve[1]. The design is presented and a suggested experimental version discussed. The design is quite similar to a conventional electronic multivibrator. In the paper other facets of the general program in numerical optical computing will be outlined.

The pulse generator is intended to augment other optical units in the performance of numerical calculations. We are working on optical adder and storage units, and have demonstrated optical logic gates. All of these are of interest in digital optical computers. If one is interested in a series of sequential computations a clock is also necessary. It is towards this end that the pulse generator was designed.

The pulse generator is one in a series of works in numerical optical computing using optical spatial light modulators conducted by various groups[2-12]. A pulse generator using a master-slave flip-flop has been demonstrated[13], but is fairly complicated. The design presented here has the advantage of simplicity.

In the remainder of the paper some of the aspects of the overall program in numerical optical computing at Ohio State will first be presented. This will be followed by the general approach to the design of the pulse generator. Next a suggested optical layout will be given. Finally a provisional experimental apparatus will be indicated.

BACKGROUND AND PROGRAM

To start, some of the aspects of the present program will be considered. As is known, optical computing has several advantages, including

1. parallel processing
2. high information density
3. computational speed
4. non-interaction of light beams.

We also are considering units using residue arithmetic with the advantages

1. addition, subtraction, multiplication
2. no carries
3. simpler elementary processes
4. error correction.

The general plan of the program has several steps. The first was the development of simple components such as logic gates[4] and flip-flops[2,3]. Along with that is the identification of particular application areas. Special purpose computers such as image processing and cellular automata[14] are possible approaches. Then given a particular application approach the structure and architecture of the computer can be considered.

There are several aspects to the design of computers. They include

1. processing
2. arithmetic
3. logic
4. timing
5. memory
6. architecture
7. input/output
8. instructions
9. codes.

Not all of these are considered simultaneously. The logic, arithmetic, and timing are developed before implementation in a particular architecture.

A good average response time is projected. For typical numbers consider 10 μm image elements, in a square active area 50 mm on a side, each image element having a response time of 10 μsecs; then we have an average response time of 4×10^{-14} secs per image element, a reasonable value. Incorporated with that is the advantage of residue arithmetic, where arithmetic operations being parallel are independent of the size of the numbers.

180

Our program includes work on liquid crystals with the goal of producing improved optical spatial light modulators. The goals of the liquid crystal work in order include

1. speed: 10 µsecs
   with good contrast
2. resolution: 5 µm
3. operation with amorphous
   silicon photoconductor.

The full program includes a many faceted approach, ranging from component design to construction of specific units and studies of design aspects. The various aspects of the program are shown in figure 1. It is distinguished by numerical rather than analog optical computing, the use of residue arithmetic, and an optical spatial light modulator. We have completed one study showing residue arithmetic to be preferred to binary arithmetic[15], mainly because of the response time due to the lack of carries. We are also undertaking further studies on the optical structure of numerical optical computers. In the implementation of particular devices we choose a temporal integrator which combines the operations of an adder, storage unit, and a clock. It is expected that these units will be completed later on this year. We are also working on components. Specifically, as mentioned, the liquid crystal studies are aimed at faster light valves with better contrast and resolution. We are also incorporating fiber optics into optical computer design.

PULSER

We now go on to consider the optical pulser design. As indicated this will be similar in design to a simple electronic multivibrator. We will consider first the electronic version, then schematically indicate an optical implementation. Finally an experimental configuration will be indicated.

The electronic circuit equivalent to the optical pulser is shown in figure 2. There we see two transistors in a bistable configuration. In addition there are delays represented by the RC circuits feeding back from emitter to base. The key items are the bistable unit and the delay elements.

The equivalent optical circuit is shown in figure 3a. This is divided into two parts shown in figures 3b and 3c. The basic bistable flip-flop is shown in figure 3b. There we see two light valves configured so that the output of one serves as the input to the other and vice versa. In actuality the symbol denoting the light valve represents only one image element of that light valve. The prisms marked GT are Glan-Thompson prisms assumed to pass light polarized in the plane of the figure and reflect light perpendicular to it. The light valve AC excitation is set so that with the proper input polarization and the Glan-Thompson prisms acting as analyzers on the output side, a dark input gives a bright output and conversely a bright input gives a dark output. Thus a dark input to the top light valve gives bright input to the bottom light valve which in turn gives the dark input to the top one, providing a consistent situation. If we interchange light and dark then there is another consistent situation, giving the bistable unit.

The delay units are shown in figure 3c, which is a copy of the right hand side of the complete circuit in figure 3a. There we see two identical loops, both having identical operations. In the top one light comes in from the upper left through the Glan-Thompson prism onto the light valve numbered 3. A bright input there causes the light on the output side to go dark after one response time of the light valve. This output is then applied through an analyzer, not shown, to the input of light valve numbered 5. After a second response time the output of that light valve past the Glan-Thompson prism then turns bright.

The essential feature of the delay loop is that if light valve is set up so that the the Glan-Thompson prism is reflecting dark from the top light valve in the flip-flop, then after a delay of two light valve response times bright is transmitted through the Glan-Thompson prism. Both of the delay loops in figure 3c operate identically providing the required delays for both portions of the flip-flop.

The next step is to design an optical configuration with only one light valve rather than the six shown in figure 3a. This design is represented in figure 4. There we see the single light valve in the center with two optical loops, a square one on the bottom and a triangular one on the top.

The square bottom loop is the flip-flop loop. With the single lens, focal length f, positioned a distance 2f from the light valve, a point at one side of the axis on the output side, represented by the dot, is imaged onto the input side on the other side of the axis, as represented by the second dot. The output from that point is then imaged on the first side of the axis onto the input corresponding to the original point.

The delays are provided by the triangular loop. Both spots in the pair are imaged simultaneousely around that loop, one spot corresponding to the top delay loop in figure 3c and the other point to the bottom delay loop. Light from the two spots on the output side of the light valve, labled 1 and 1' in figure 3a, is thus imaged by the lens in the right hand side of the triangle onto the mirror at the top of the loop in figure 4. The lens on the left hand side of the triangle then images the spots back onto the input to the light valve. The corner mirrors in the triangular loop are slightly tipped so that the spots are reimaged on the light valve input to points below the plane of the figure, points 3 and 3' in figure 3a. This also means that light coming off the output side at 3 and 3' will be imaged around the triangular loop below the points at 3 and 3'providing a third pair of spots on the light valve input, those corresponding to 5 and 5' in figure 3a.

The mirrors at the top and to the left of the triangular loop in figure 4 are segmented to return light in the delay loop to the original flip-flop. The two segments are divided by a horizontal line. The segment of the mirror above the line will be tipped in a direction different from the segment below the line. The pairs of spots imaged onto the mirror at the top of the triangle from the first and second times around that loop, points 3 and 3', and 5 and 5', strike the mirror below the dividing line. On the third pass the pair of spots striking the mirror at the top of the triangular loop hit above the dividing line. The top segment of that mirror then directs the

light reflected off it to the bottom segment of the mirror at the left of the loop. That mirror segment is then oriented to direct the light so as to superimpose it on the inputs at 1 and 1', as shown in figure 3a.

The preceding is shown nicely in figure 5, a three-dimensional portrayal of the arrangement of figure 4. We see the light valve in the center of the figure. The spots 1, 1', 3, 3', 5, and 5' are shown on the input side of the light valve. To the bottom is the square loop with its one lens. It images spots 1 and 1' each back onto the other. At the top is the triangular loop with its two lenses and segmented mirrors. Spots 1 and 1' on the light valve output are imaged onto spots 2 and 2' on the top mirror, which are in turn imaged onto spots 3 and 3' below points 1 and 1' on the light valve input. Similarly points 3 and 3' get imaged to spots 5 and 5'. The light from spots 5 and 5' on the light valve output then goes to spots 6 and 6' on the top segment of the top mirror, and from there to the bottom segment of the left-hand mirror and to spots 1 and 1' on the light valve input.

It is noted that although two passes around the delay loop are shown, many more passes around the loop are possible. One merely raises the dividing line between the two segments on the top mirror.

The output can be taken from any one mirror by making it partially transmitting.

An actual experimental arrangement is shown in figure 6, drawn from a photograph of the apparatus. There we see the input to the light valve on the right and other components as indicated in figure 5. The spots on the light valve are roughly three millimeters in diameter.

SUMMARY

To summarize, this paper was divided into two parts. In the first part we considered various aspects of the program in numerical optical computing. This includes system design, apparatus construction, and device studies. The second part of the paper contained a design for an optical pulser using a Hughes liquid crystal light valve. The design is similar to an electronic multivibrator in that it has a flip-flop and a delay to provide switching. The optical design was shown, followed by schematic optical diagram. The design concluded with a three-dimensional optical layout and equipment sketches.

REFERENCES

1.Bleha, W.P.(1978), L.T. Lipton, E. Wiener-Avenear, J. Grinberg, P.G. Reif, D. Casasent, H.B. Brown, and B.V. Markevitch, "Application of the Liquid Crystal Light Valve to Real-Time Optical Data Processing", Opt. Eng. 17, 371 .

2.Sengupta, U.K.(1978), U.H. Gerlach and S.A. Collins, Jr., "Bistable Optical Spatial Device Using Direct Optical Feedback", Opt. Lett. 3, 199.

3.Gerlach, U.H.(1980), U.K. Sengupta, and S.A. Collins Jr., "Single Spatial Light Modulator Bistable Optical Matrix Device Using Optical Feedback",Opt. Eng.19,452.

4.Fatehi, M.T.(1981), K.C. Wasmundt, and S.A. Collins Jr. "Optical Logic Gates using Liquid Crystal Light Valve: Implementation and Application Example", Appl. Opt. 20,2250.

5.Soffer, B.H.(1980),D.Boswell, A.M. Lackner, P.Chavel, A.A. Sawchuk, T.C. Strand,and A.R. Tanguay, Jr., Proc Soc. Photo-Opt. Instrum. Eng. 232,128.

6.Athale, R.A.(1979), and S.H.Lee ,"Development of an Optical Parallel Logic Device and a Half-adder Circuit for Digital Optical Processing", Opt Eng. 18,513.

7.Gallagher, H.J.,(1981),T.K. Gaylord, M.G. Moharam, and C.C. Guest,"Reconstruction of Binary-data-page Thick Holograms for an Arbitrary Oriented Reference Beam,"Appl. Opt.20,300.

8.Tai,A.(1979), I. Cindrich, J.R. Fienup, and C.C. Aleksoff,"Optical Residue Arithmetic Computer with Programmable Computation Modules," Appl. Opt.18,2812.

9.Horrigan,F.A.(1980), and W.W. Stoner, "Residue-based Optical Processor", Optical Information Systems Processing Conference, Proc. Soc. Phoro-Opt. Inst. Eng. 185,19.

10.Psaltis,D.(1979),and D. Casasent,"Optical Residue Arithhmetic: a Correlation Approach," Appl.Opt. 18,163.

11.Warde, C.(1981),A.M. Weiss, A.D. Fisher, and J.I. Thackara,"Optical Information Processing Characteristics of the Microchannel Spatial Light Modulator," Appl. Opt. 20,2066.

12.Cheval.P(1983),R. Forchheimer, B.K. Jenkins, A.A. Sawchuck, T.C. Strand, "Architectures for a Sequential Optical Logic Processor", Proc. 10th International Optical Computinc Conference", Boston Mass., 6-8 April,IEEE Catelog No. 83CH1880-4.

13.Jenkins,B.K.(1982), A.A. Sawchuck, and T.C. Strand, "Sequential Optical Logic Implementation", Jour. Opt. Soc. Am.72,1721.

14.Duff, M.J.B.(1977), and D.M. Watson, "The Cellular Logic Array Image Processor", Comp. Jour. 20, 68.

15.Habiby, S.F.(1982),"A Design Study of a Numerical Optical Temporal Integrator Using Residue Arithmetic," Masters Thesis, The Ohio State University, Columbus, Ohio.

PROGRAM

I. SPECIFICATIONS
- A. NUMERICAL OPTICAL COMPUTING
- B. RESIDUE ARITHMETIC
- C. SPATIAL LIGHT MODULATOR

II. STUDIES
- A. ARITHMETIC
  - RESIDUE VS BINARY
- B. STRUCTURE

III. IMPLEMENTATION
- A. TEMPORAL INTEGRATOR
  1. ADDER
  2. STORAGE
  3. CLOCK
  4. TIME THIS YEAR

IV. COMPONENTS—
LIGHT VALVE DEVELOPMENT
- A. LIQUID CRYSTAL STUDIES
  1. SPEED
  2. RESOLUTION
  3. TIME—ONE YEAR
- B. PHOTOCONDUCTOR—COMBINATION
  1. TIME—TWO YEARS
  FIBER OPTIC DESIGN

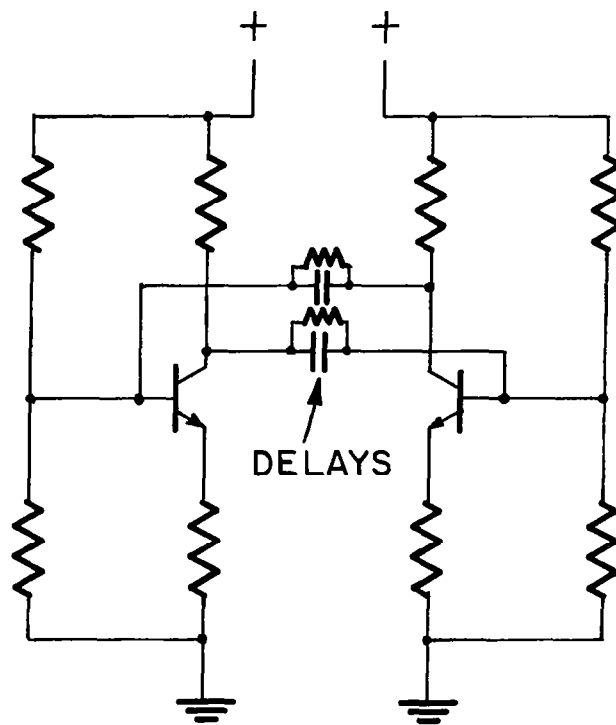Figure 1.- Various aspects of program.

Figure 2.- Electronic circuit equivalent to optical pulser.

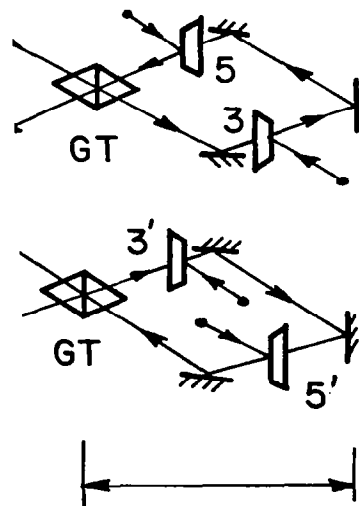(a) Basic configuration.
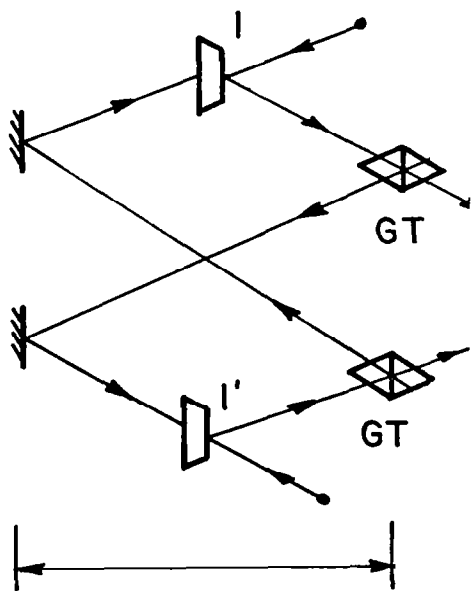
(b) Flip-flop loops.

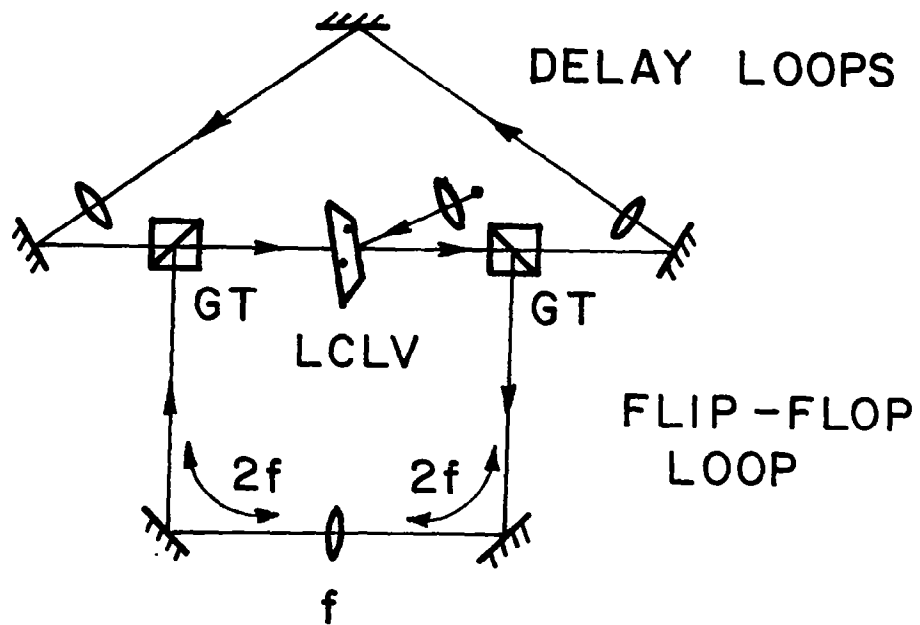(c) Delay loops.
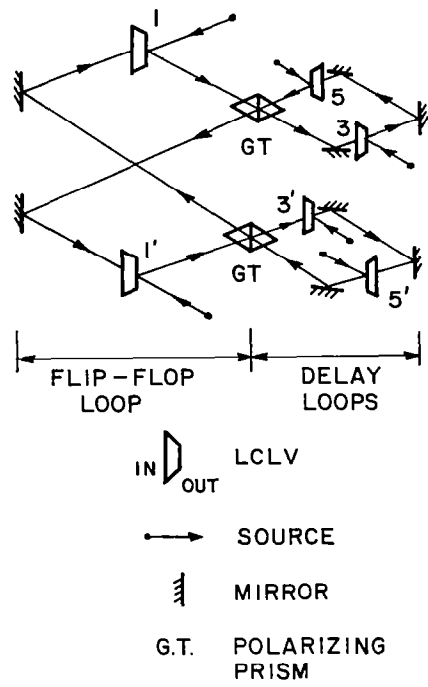
Figure 3.- Equivalent optical circuit.

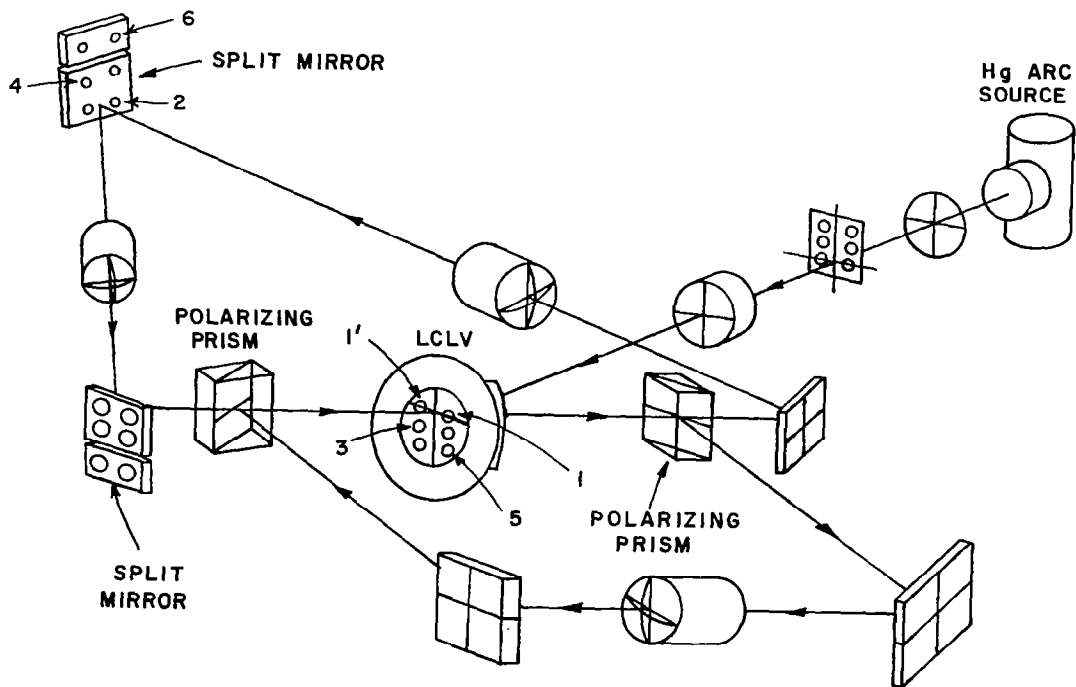Figure 4.- Optical configuration with one light valve.

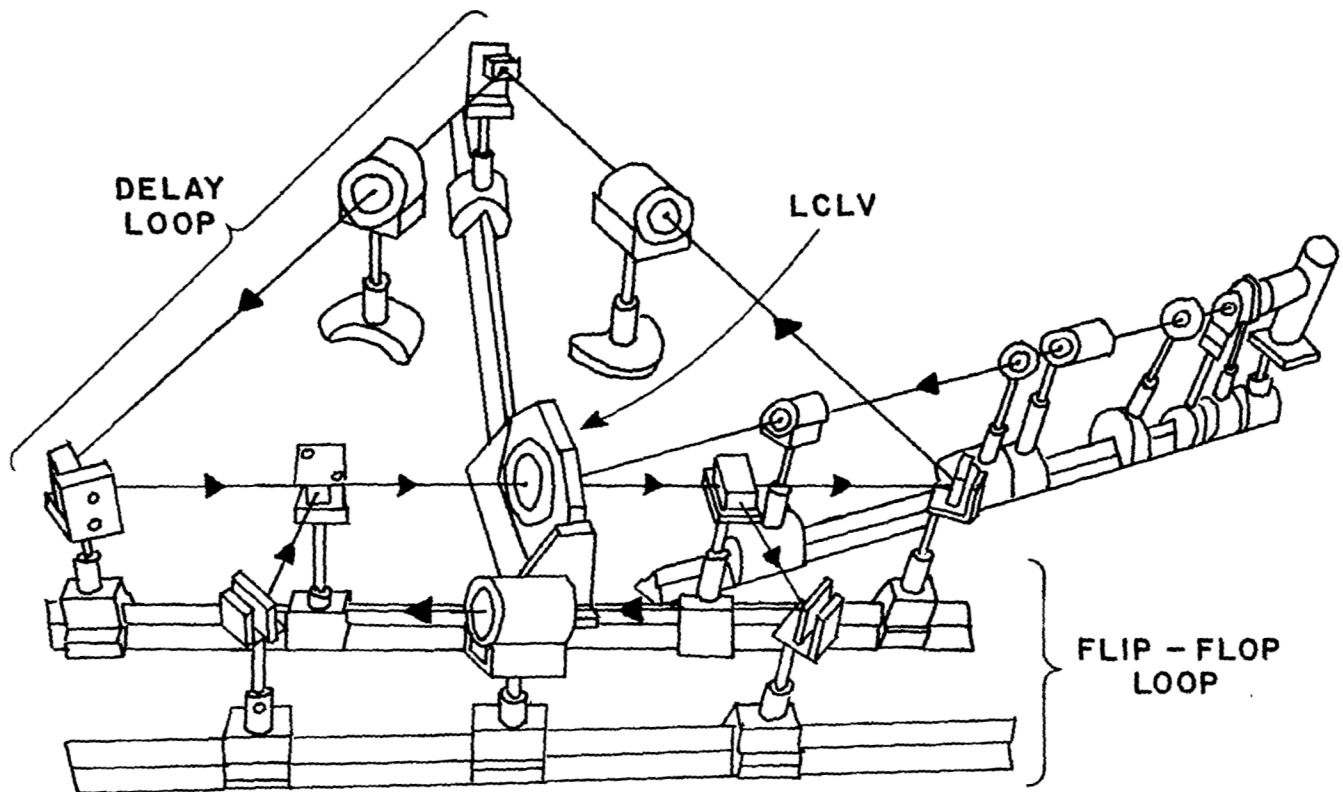Figure 5.- Three-dimensional arrangement of optical configuration.

Figure 6.- Actual experimental arrangement of optical configuration.

PROGRAMMABLE MASKS FOR

OPTICAL INFORMATION PROCESSING

J. H. Goebel, T. Matsumoto, C. Mina, and J. Welch
NASA Ames Research Center
Moffett Field, CA 94035

SUMMARY

Research in progress at NASA Ames Research Center on programmable masks is discussed in this paper. One type is a large area format liquid crystal mask intended for binary optical computation problems. To date, an on-off contrast ratio of >500:1 has been achieved at a switching rate of <1 Hz. With a 32 x 32 format, a ratio of 10^4:1 is desirable. The switching contrast is entirely dependent on the polarized quality; therefore, we believe 10^4:1 in transmission is possible. Larger format masks are under development. An application to Hadamard transform polarized imagery at wavelengths of 1.0 to 2.0 μm, which is competitive with the best monolithic infrared detector arrays, is discussed.

INTRODUCTION

The programmable mask for optical computer applications is currently the missing essential element. To date, matrix-matrix multipliers and systolic array processors have been made, but have been realized with fixed masks (Goodman, Dias, and Woody 1978; Psaltis and Cassasant 1979).

Variable fixed masks have been successfully used for Hadamard transform image encoding in astronomical applications (Singerland 1975, 1976; Davies 1975; and deBatz et al. 1977). Because Hadamard imagery can be performed with repetitive patterns, a truly programmable mask is not essential to realization of the technique.

A nematic liquid crystal cell has been used in a page composer for holographic memories where it acted as the spatial wave polarization modulator (Laburnie, Robert, and Borel 1974). They used a 32 x 32 array format.

Here we report on work in progress, which synthesizes the three preceding concepts,

1)   Programmable masks

2)   Hadamard imagery

3)   Liquid crystal arrays

into a single program. The program is aimed at demonstrating a truly programmable mask. The mask is understandably limited in capability and represents only the first step in our program to develop widely applicable programmable masks.

THE MASK

We have chosen a large scale, binary mask format, suitable for Hadamard transform imagery. The mask consists of a 32 x 32 array of liquid crystal elements, the pixels of which are 1mm x 1mm. It is suitable for transmissive applications. The array was purchased as Model SX402 from Crystalliod Electronics. The reflective backing was removed and the polarizer replaced with a Model NPF-1008H polarizer manufactured by Nitto Electronics Co., Ltd.

The mask consists of two essential elements: the polarizer-analyzer and the liquid crystal array. Each element limits the performance in different manners.

The polarizer-analyzer standard with the display has a contrast ratio of 2:1 which is totally unsatisfactory in this application. We have investigated polarizer properties and found that 1000:1 contrast ratio for crossed polarizers can be achieved over limited wavelength ranges. The polarizer chosen has a ratio in the 1000:1 region near 600 nm. HR8 Polaroid infrared polarizer achieves 1000:1 between 1.2 and 2.0 μm. The liquid crystal is transparent out to 2.5 μm, and thus we expect to be able to achieve the desired performance in the astronomical I and J bandpasses (I = 1.25 μm, J = 1.65 μm). A contrast ratio of 1000:1 is deemed necessary to fully block all pixels, so that when all are off there is no leakage greater than one equivalent pixel, i.e., all the signal is fully modulated for full efficiency. This is required to fully realize the Fellgett multiplex advantage.

The liquid crystal performance is limited by its addressing mode. The Model SX402 is addressed in column and row with no on-pixel storage. This requires the electronics to repetitively address the pixel during the observing period to make the pattern persist. The pattern stabilization time for this array is about 1 second. A 32 x 32 mask requires 1023 patterns for a complete transform cycle, or 1023 sec of dead time. This is a penalty which is application dependent. The astronomical penalty is significant but tolerable, being a 30-50% loss in observing time. Arrays with randomly addressable pixels and storage fet's will be forthcoming, and the 1023 sec dead time will shrink by 100 to 10 sec per cycle. For example, the Casio TV-10 liquid crystal pocket television is suitable for such an application, but was not available at the time when this work was initiated. It has fet storage and much faster response than the display which we are using. Examples of the patterns on the mask are shown in Figure 1. These have been photographed directly from the display when addressed with the row and column drivers. The driver board is also shown.

The exercising and data collection electronics are summarized in Figures 2 and 3. Control is through an HP 9816 computer, which starts the exercise sequence of the mask writing electronics and thereby impresses the sequence of

patterns on the liquid crystal mask. The mask logic control gates the shift register which stores the 1023 bit pattern which is impressed upon the mask and subsequently shifted one bit at a time, 1023 times. The adjustable setup time control allocates the mask rewrite rate. This rate is fast compared with the desired integration time at a setting of the mask, e.g., 17 Hz for 10 sec.

While the exercising electronics is sequencing, the computer is acquiring the detector output through a 12 bit A/D converter and storing the time averaged result in a 1023 array of data points which are subsequently transformed into an image. A flow chart of the entire sequence of exercising/acquiring is is presented in Figure 4.

The Hadamard transform process itself is well studied and discussed in the book by Harwit and Sloane (1977). We have chosen a fast Hadamard transform, the logic of which is given in Figure 5. It is another example of the class of 2-dimensional n^2 computational procedures which can be linearized to n log n steps through a sorting and addition-subtraction algorithm.

REFERENCES

Batz, de, B., Bensammar, S., Delavaud, J., Gay, J., and Journet, A. 1977, Infrared Physics, 17, 305.

Davies, D. W. 1975, J.O.S.A. 65, 707.

Goodman, J. W., Dias, A. R., and Woody, L. M. 1978, Optics Letters 2, 1.

Harwit, M. and Sloane, N. J. A. 1979, Hadamard Transform Optics, Academic Press.

Labrunie, G., Robert, J., and Borel, J. 1974, Applied Optics 13, 1355.

Psaltis, D. and Cassasant, D. 1979, Applied Optics 18, 163.

Slingerland, J. 1975, Rev. Sci. Instrum. 46, 746.

Slingerland, J. 1976, Rev. Sci. Instrum. 47, 1331.
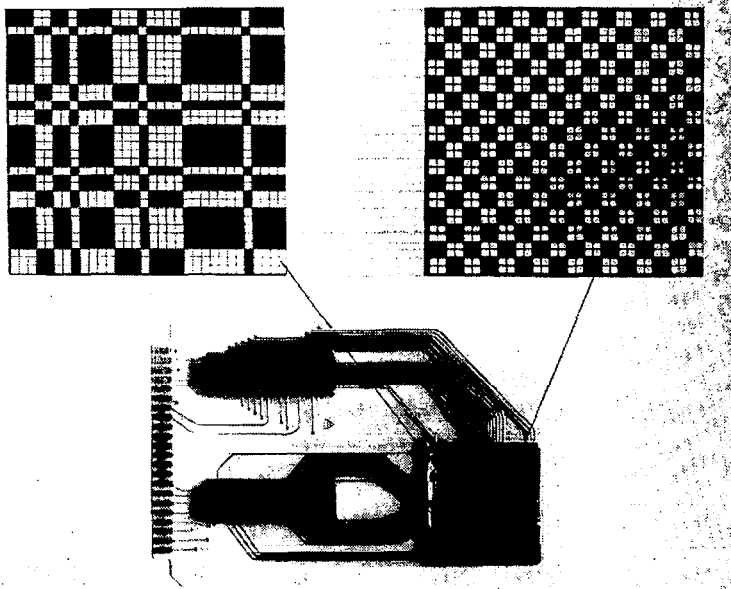
Figure 1.- Liquid crystal programmable mask for optical information processing.
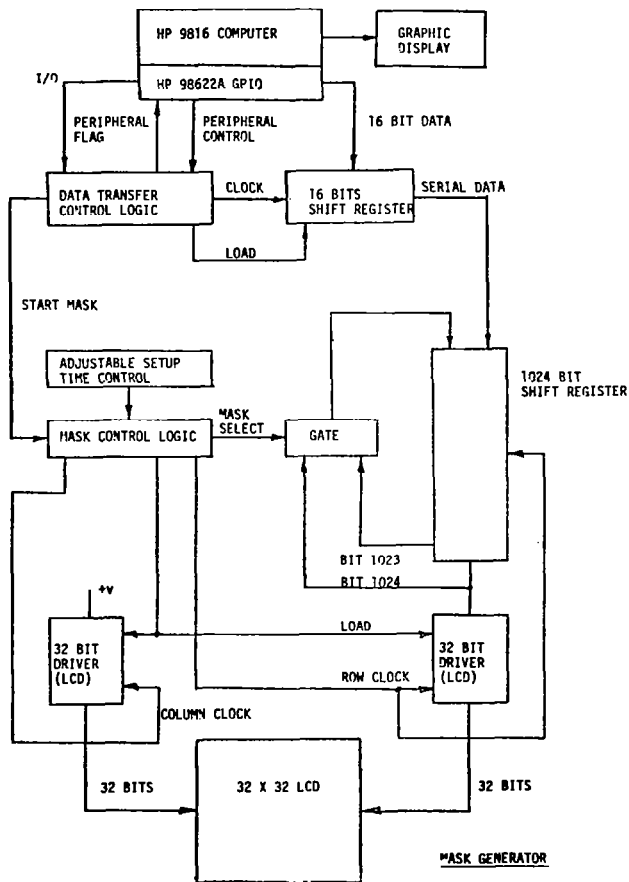
Figure 2.- Exercising and data collection electronics for mask generator.
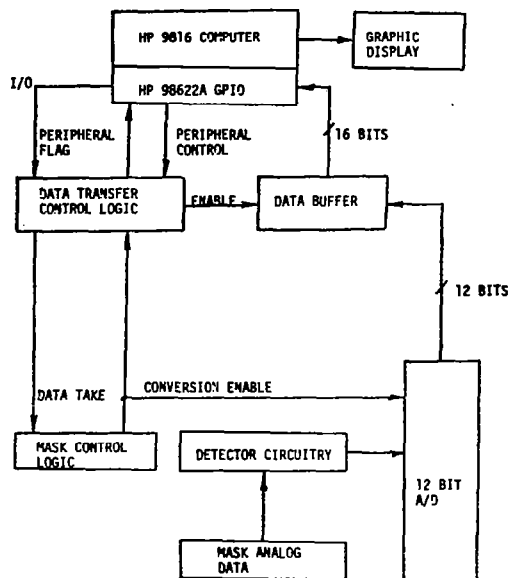
Figure 3.- Exercising and data collection electronics for mask reconstruction.
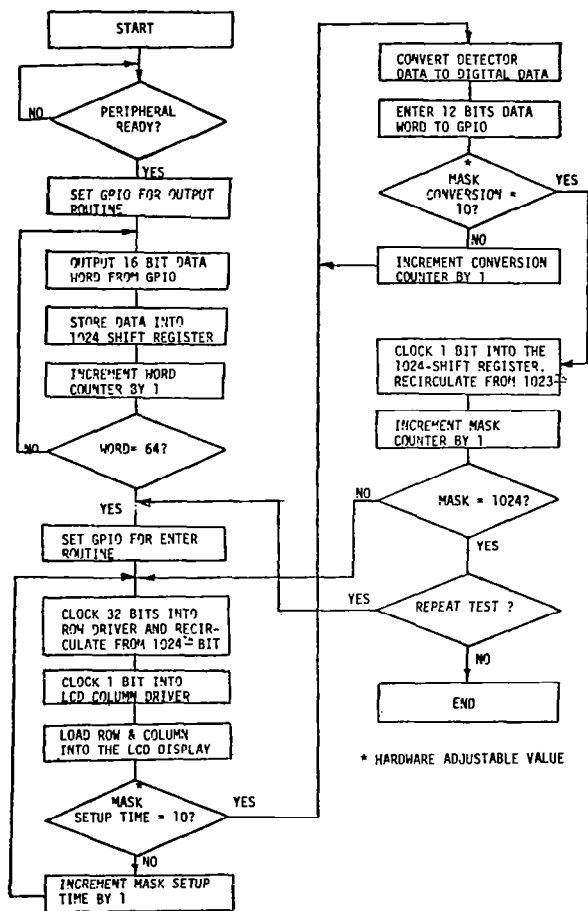
Figure 4.- Flow chart of entire sequence of exercising/acquiring.

```
┌────────────────────────────────────────┐
│   LOAD DETECTOR READINGS INTO ARRAY A   │
└────────────────────────────────────────┘
                    │
                    ▼
┌────────────────────────────────────────┐
│    MAP A INTO C WITH PERMUTATION #1      │
└────────────────────────────────────────┘
                    │
                    ▼
┌────────────────────────────────────────────────┐
│ PERFORM FAST HADAMARD TRANSFORM ON C TO OBTAIN C'│
└────────────────────────────────────────────────┘
                    │
                    ▼
┌────────────────────────────────────────┐
│   MAP C' INTO E WITH PERMUTATION #2      │
└────────────────────────────────────────┘
                    │
                    ▼
┌────────────────────────────────────────┐
│        NORMALIZE E TO OBTAIN F           │
└────────────────────────────────────────┘
                    │
                    ▼
            ┌──────────────┐
            │   STORE F     │
            └──────────────┘
```
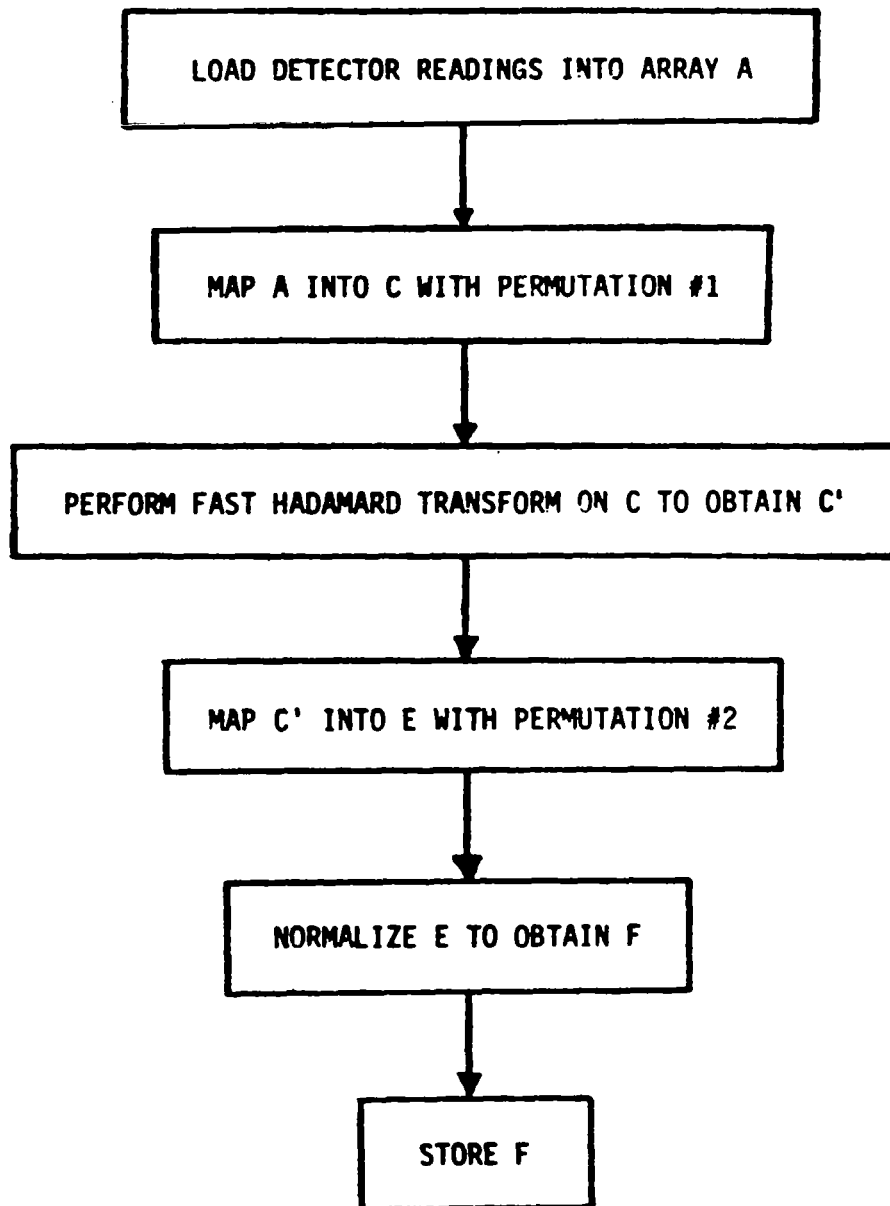
ARRAY F   IS THE FIELD IMAGE MAP
ARRAY A IS THE DETECTOR TIME SEQUENCE
ARRAY C IS THE FHT MA
ARRAY C' IS ARRAY C AFTER THE FHT
ARRAY E IS THE UNNORMALIZED FORM OF F

Figure 5.- Hadamard data processing flow chart.

REAL-TIME SYNTHETIC APERTURE RADAR PROCESSING[*]

Demetri Psaltis, Michael Haney, and Kelvin Wagner
Division of Engineering and Applied Science
California Institute of Technology
Pasadena, California 91125

ABSTRACT

Real-time acousto-optic SAR processors are described and experimentally demonstrated. SAR imaging is performed in one of the architectures by applying the signal to an acousto-optic device and correlating it with chirp signals recorded on an optical transparency by time integration on a CCD detector. In a different implementation, the imaging is performed by interfering the light beams diffracted from two separate acousto-optic devices, one modulated by the radar signal and the second by the reference chirp waveform.

INTRODUCTION

Synthetic aperture radar [1,2] is a powerful technique for the formation of high-resolution images at long wavelengths. The most attractive feature of the technique is the fact that the resolution is not limited by the physical aperture of the receiving antenna but by the bandwidth of the radar and the distance the vehicle carrying the antenna travels while each point of the object being imaged remains illuminated by the radar. Therefore, SAR images of the Earth can be formed with excellent resolution by aircraft or spacecraft that can carry only small antennas. Until recently, the usefullness of this technique has been limited to applications that do not require real-time image formation because of the high computational load associated with forming the focused image from the received radar signals. Typically, the radar returns are recorded on the aircraft or spacecraft carrying the radar, and the images are formed later on the ground by optical or digital computers. The requirements of modern radars and advances in signal processing technologies have raised the possibility of producing SAR images in real-time on board the vehicle carrying the radar. Such capability would enhance significantly the applicability of the SAR imaging method. The advances in the state of the art of digital and optical signal processing technologies that have been accomplished in recent years make it possible to form SAR images in real time. Processing speed, however, is only one of the requirements for a practical SAR processor. Factors such as power consumption, weight, size, cost, and flexibility are also very important. The optical implementation is at a relative disadvantage to a digital implementation with respect to flexibility and accuracy, but low power consumption, size/weight, and cost make the optical implementation the only practical solution in many SAR imaging applications.

We have recently described [3,4] an optical architecture for SAR imaging that is implemented with an acousto-optic device (AOD) as the input transducer and a 2-D CCD detector array on which the SAR image is formed. In this paper the principles of operation of this architecture are reviewed, and experimental demonstration of real-time SAR imaging is presented. A new interferometric architecture is also prsented in which the impulse response of the system is controlled with a second AOD that is modulated by a chirp waveform. The new architecture provides the flexibility of dynamically adapting the parameters of the optical processing to track changes in the radar geometry.

EXPERIMENTAL PROCESSOR

We will present the operation of the processor by describing how it produces a focused image of a point target. A focused SAR image is related to the reflectivity of the area being imaged through a 2-D linear operation. Therefore, the impulse response describes the system completely. The typical side-looking SAR geometry is shown in Fig. 1. An airplane flying at a constant velocity v_a parallel to the ground illuminates an area on the ground through a small antenna mounted on the side of the aircraft. The illuminating radiation is temporally modulated by periodic linear FM pulses. The transmitted waveform is given by the following expression:

$$s(t') = \sum_n \text{rect}\left[\frac{(t'-nT)}{\tau_0}\right] \exp\left[jb_1 (t'-nT)^2\right] \exp(j\omega_0 t') \qquad (1)$$

where t' is time, $1/T$ is the pulse repetition frequency (PRF), τ_0 is the duration of each pulse, b_1 is the chirp rate, and $\omega_0/2\pi$ is the center frequency of the radar. The single-point scatterer on the ground scatters the illuminating field, and part of it is detected by the antenna on the aircraft. For a single-point scatterer the received waveform is a replica of what was transmitted delayed by $2R/c$, where R is the distance from the antenna to the scatterer and c is the speed of light. The term R changes with time as the aircraft flies by the target. From Fig. 1, we find that

$$R(t') = (R_0^2 + x^2)^{\frac{1}{2}} = [R_0^2 + v_a^2 (t' - t_0)^2]^{\frac{1}{2}} \simeq R_0 (1 + v_a^2 (t' - t_0)^2/ 2R_0^2)$$

where R_0 is the distance to the scatter at the time $t' = t_0$ when the vehicle crosses over the scatterer and the assumption has been made that $R_0 \gg x$. Typically, the variation of $R(t')$ during the time the scatterer is illuminated is small enough and it does not affect the time of arrival or the chirping rate of the received pulses. Therefore, each pulse is received with approximately the same delay, $2R_0/c$. This delay is measured by compressing the received pulses, and the image of the scatterer is focused in this manner in the across track (or range) dimension. The variation of R appears as a phase shift on the received waveform. This phase modulation is then used to focus the image in the along tract (or azimuth) direction. With these assumptions and ignoring the effects of the antenna pattern, the received waveform can be written as follows:

$$s(t' - R(t')) \simeq \sum_n rect \left[\frac{(t' - 2R_o/c - nT)}{\tau_o} \right] exp \left[jb_1 (t' - 2R_o/c - nT) \right]$$

$$x \; exp \; (j\omega_o t') \; exp \; [j\omega_o \; v_a^2 \; (nT - t_o)^2/R_o] \tag{2}$$

It is customary to think of this long 1-D signal as a 2-D unfocused image of the ground. We define $\tau = t'-nT$ and $t = nT$, and we write the received signal as a 2-D function as follows:

$$s(\tau,t) = rect \left[\frac{\tau - 2R_o/c}{\tau_o} \right] exp \; [jb_1 \; (\tau - 2R_o/c)^2]$$

$$x \; exp \; [j\omega_o \; v_a^2 \; (t - t_o)^2/R_o] \; exp \; [j\omega_o \tau] \tag{3}$$

The above 2-D function is in general a non-symmetric zone plate whose center $(\tau = 2R_o/c, \; t = t_o)$ is proportional to the position of the point scatterer on the ground. In the optical processor to be described, this signal is focused by spatial integration in the range (τ) direction. The variable t does not represent the continuous time. It is a discrete time variable sampled at the radar PRF. We will refer to it as simply time in the rest of our discussion. In order to characterize and demonstrate the operation of the real-time SAR processor, we have built an apparatus that generates the impulse response signal of Eq.(3). A schematic diagram of the impulse response generator is shown in Fig. 2. The frequency of a 10-MHz oscillator is divided by a factor of 2×10^4 to produce a phase-locked PRF clock at 500 Hz. The same 10-MHz frequency is used to derive a 60-MHz signal, and this signal is then applied to a digitally controlled phase shifter. The phase shifter is addressed by a read-only memory circuit in which a quadratic function is stored. The quadratic function stored in the memory is displayed in Fig. 3. This was obtained through a D/A converter. The memory chip is read-out at the PRF of the radar and consequently the signal following the phase shifter has a slow linear frequency modulation (20 Hz/frame in the experiments presented later) simulating the t variation of the signal in Eq. (3). The PRF clock triggers a circuit that produces a very short pulse (16.6 nseconds), which is in turn mixed with the phase-shifted 60-MHz carrier and applied to a surface acoustic wave device. The dispersive properties of the SAW device cause the impulses to be spread in time to 6 μseconds and in frequency to the range 50 to 70 MHz. The SAW introduces in this manner the τ modulation of the signal in Eq. 3. The output of the SAW is a replica of the signal that is received by a synthetic aperture radar illuminating a scene containing only one point reflector. This signal is displayed by mixing it to the baseband and modulating the intensity (z axis) of an oscilloscope. The horizontal (x) amplifier of the oscilloscope is triggered by the PRF clock, and the vertical axis is deflected by a slow ramp. Fig. 4 shows the 2-D zone plate produced by the system described above. This zone plate is a representation of the unfocused image of a point scatterer.

The signal from the impulse response generator is applied to an AOD. A shear wave TeO_2 device was used in the experiments with a 70-μsec and delay window and a 30-MHz (40-70 MHz) 3 dB bandwidth. The AOD is illuminated by a pulsed laser diode.

The laser pulses are produced at the radar PRF, and they are synchronized to occur when the acoustic signal in the AOD consists of a single chirp generated by the SAW device. The duration of each laser pulse is shorter than the inverse of the bandwidth of the chirp signals and consequently the motion of the travelling acoustic wave does not affect the operation of the processor. A single-mode AlGaAs laser was used in the experiment, at 15 mW peak power and 30 nanoseconds pulse width. The chirped signal forms a phase grating in the AOD with linearly increasing spatial frequency. This is shown in Fig. 5. The light diffracted near the piezoelectric transducer of the AOD in Fig. 5 is diffracted at a larger angle than the light diffracted from the top of the device. Consequently, the diffracted light comes to a focus. The focal plane is located 11.5 cm away from the AOD in the experiment and at this point the diffracted light is well separated from the zero beam and it can be detected. The self focusing of the diffracted light accomplishes the focusing of the SAR image in the range (τ) direction. The optical field at the plane where the diffracted light comes to focus is given by

$$S_1(x,t) = \int S(x'/v,t) \ \exp \left[-jb_1 \ (x'+x)^2 \ /v^2 \right] dx'$$

$$\simeq \text{Sinc} \left[(x-2R_o \ v/c) \ \tau_o b_1 /\pi v^2 \right] \ \exp \left[j\omega_o \ v_a^2 (t-t_o)^2 /cR_o + j\omega_o \tau \right] \tag{4}$$

where x' and x are the spatial coordinates in the plane of the AOD and the detector respectively. The term v is the acoustic velocity. The range-focused signal is phase modulated in t by the azimuth chirp. This phase modulation can only be detected interferometrically. Interferometric detection is accomplished by adding a 60-MHz sinusoid to the radar signal and applying the sum to the AOD. The sinusoid will cause a plane wave to be diffracted in the same direction as the focusing signal beam. The light intensity at plane x is given by

$$I_1(x,t) = \left| S_1(x,t) + \exp(j\omega_o \tau) \right|^2 =$$

$$1 + \text{sinc}^2 \left[(x-2R_o v/c) \ \tau_o b_1 /\pi v^2 \right] + 2 \ \text{sinc} \left[(x-2R_o v/c) \ \tau_o \ b_1 /\pi v^2 \right]$$

$$x \cos \left[\omega_o v_a^2 \ (t-t_o)^2 \ /R_o c \right] \tag{5}$$

The SAR image is focused in the azimuth (t) direction by correlating the time variation of the above function with the function $\cos(\omega_o \ v_a^2 \ t^2 /R_o)$. This is accomplished with a time-integrating optical correlator (as shown by the simple diagram in Fig. 6). A transparency with intensity transmittance $I_2(y) = 1 + \cos(b_2 y^2)$ is illuminated with light whose intensity is temporally modulated by $I_1(x,t)$. The term y is the spatial coordinate perpendicular to x. The light is detected after the transparency on a 2-D detector. For the purpose of this discussion, we can think of the detector as photographic film. If the film travels with velocity v' in the y

direction while it is exposed to light, the detected signal on the film is
$I_3(x,y) = \int I_1(x,t)\, I_2(y+v't)\, dt$. We choose the parameter $b_2 = \omega_o v_a^2/R_o v'^2$, and
the signal accumulated on the detector becomes the autocorrelation of the linear FM
waveform in Eq. (5).

$$I_3(x,y) \simeq 1 + \mathrm{sinc}^2\left[(x-2R_o\, v/c)\, \tau_o\, b_1/\pi v^2\right]$$

$$+\ 2\ \mathrm{sinc}\left[(x-2R_o\, v/c)\, \tau_o\, b_1/\pi v^2\right]\, \mathrm{sinc}\left[(y-t_o v')\, b_2\, Y/\pi\right] \tag{6}$$

where Y is the total distance the moving detector travels.

The first term in Eq. (6) is a constant bias, the second is a signal-dependent
bias term, and the third term is the focused SAR image. The image can be separated
from the bias terms using one of several possible methods. For instance, the bias
alone can be calculated separately on a different detector and then subtracted
from $I_3(x,y)$ to produce an unbiased image. Alternatively, the signal term in Eq. (6)
can be formed on a sufficiently high spatial frequency in either x or y and
separated from the bias terms by electronic filtering.

The detector used in the processor is a 2-D CCD. The photogenerated charge
stored in a CCD can be made to travel along one of the spatial dimensions by
applying pulse waveforms to the device. The charge travels in discrete steps but
this is actually convenient for this system since t is a discrete time variable as
well. The motion of the photogenerated charge is entirely equivalent to the physical
movement of the detector in Fig. 6. Therefore, the CCD performs the correlation in
the azimuth direction by time integration. The appropriate value for the velocity v'
is set by transferring the change pattern on the CCD by one pixel at the radar PRF.

The CCD used in our experiments has 512 pixels in the direction of charge
motion and 320 in the other dimension. The entire SAR processor, shown in Fig. 7, is
constructed by cascading the space-integrating range processor of Fig. 5 and the time-
integrating processor of Fig. 6. A photograph of the experimental setup is shown
in Fig. 8. The mask used as the azimuth reference is shown in Fig. 9. This mask was
generated with a computer-controlled film recorder. Notice that the chirping rate in
the vertical direction is dependent on the horizontal (range) position. This is
necessary for compensation of the range azimuth coupling. (The focal length along
the azimuth direction of the zone plate in Fig. 4 depends on the range of each
target.) A photograph of the focused SAR image produced in real time with the
processor in Fig. 8 from the signal displayed in Fig. 4 is shown in Fig. 10.

The image obtained is that of the single-point scatterer. The dimensions of
this focused spot along the horizontal (range) and vertical (azimuth) directions
determine the resolution of the SAR processor. The width of the spot in the
horizontal direction is expected to be equal to the acoustic velocity divided by the
bandwidth of the chirp (20 MHz) produced by the SAW device [3]. The width of the
spot in Fig. 10 is broader than expected by a factor of 2. We attribute this to
apodization due to the Gaussian shape of the wavefront illuminating the AOD and
possibly abberations in the lenses. The number of pixels that the spot is expected

to occupy in the vertical (azimuth direction) is equal to the total number of pixels of the CCD in the vertical direction (512) divided by 40 (the time-bandwidth product of the azimuth chirp). The measured spot width is approximately equal to what is expected in the azimuth direction. The isometric display of the focused image (shown in Fig. 11) reveals the structure of the bias on which the image is formed. There is a flat plateau due to the collimated reference wave, and for this case of a single-point target, there is an additional ridge along the azimuth direction (the second term in Eq. 3). The sidelobe structure of the focused spot can be observed in the cross-sectional scan (along the azimuth direction), shown in Fig. 12. In Figs. 11 and 12, the compression in the azimuth direction is 80 (2 times more than in Fig. 10). The digital simulation of the autocorrelation of a linear FM waveform with a time-bandwidth product equal to 80 (displayed in Fig. 13) shows that the level and the structure of the optically produced sidelobes are remarkably accurate. The sidelobe level can be reduced further by apodization and/or increasing the pulse compression ratio in the azimuth direction. The value 80 for azimuth pulse compression we used in the experiment is typical for aircraft radars.

ADAPTABLE ARCHITECTURE

In some applications the parameters of the radar such as the velocity and the altitude of the aircraft and the direction in which the antenna is pointed (side looking, forward looking, spotlighting) change dynamically. Consequently, the real-time SAR imager must have the capability of adapting rapidly to such changes in order to continuously produce a well-focused image. The impulse response of the processor described in the previous section is determined in part by the transmittance of the mask used. A real-time spatial light modulator can be used in place of the mask. Since the transmittance of such a device can be changed dynamically, the impulse response of the processor can be adapted to match the radar parameters. An alternate and preferable approach is to use a second AOD in place of the fixed mask. The mask, as we see in Fig. 9, introduces a 2-D spatial light modulation. The modulation along one of the dimensions, however, is simply scaling. Therefore the AOD, which is a 1-D spatial light modulator, can be used to introduce the basic chirp modulation in the y direction. An optical system that images the AOD along the y direction with different magnification for each x position produces a 2-D spatial light distribution, which when detected interferometrically results in a pattern identical to the one shown in Fig. 9. This is shown schematically in Fig. 14. A cylindrical lens L_1 is used to focus the light in the AOD, and L_2 recollimates the diffracted light. The lens L_3 is a cylinder that has focusing power in the vertical direction. Let us assume that the AOD is modulated by a single frequency. The diffracted light in this case is a plane wave, and it will be focused to a horizontal line by the cylindrical lens L_3. The L_3 lens is rotated around a pivot coinciding with the y axis by an angle θ.

The focused line lies in the (x,z) plane, and it is at an angle θ with respect to the x axis. The light propagates as a diverging tilted cylindrical wave after the focal plane of L_3. If we observe interferometrically this light distribution in a plane P_2 perpendicular to the z axis, we will see the pattern shown in Fig. 4. If the interference of the output of the systems in Figs. 5 and 14 is formed on the CCD, the detected signal will be exactly the same as the signal in Eq. 5. It is interesting to note that the tilted cylindrical lens alone is sufficient to produce the desired interference pattern. The AOD, however, provides added flexibility in several respects. The chirping rate and the starting frequency of the azimuth reference can be

dynamically controlled by modulating the AOD with the appropriate temporal waveform. Furthermore, the azimuth correlation can be formed by shifting the signal in the AOD instead of transferring the charges in the CCD. These capabilities are useful for producing multiple looks, i.e., forming independently several images of the same area and adding them to reduce speckle. If the charge pattern in the CCD is travelling during exposure, the focused images are continuously read-out, and therefore it is not possible to add on the detector multiple looks. Finally, the use of the AOD allows us to build the architecture as a cascade of the systems in Figs. 5 and 14, rather than a two-arm interferometer. This is an important consideration when we consider the mechanical stability of the system. The cascaded architecture is shown in Fig. 15. In this architecture, all beams go through the same optics. In order to record a chirp signal on the detector, we must interfere two waves with different degrees of collimation. The second AOD in Fig. 15 is modulated by the sum of a single sinusoid and a chirp signal. The light diffracted by this AOD consists of a plane wave and a diverging spherical wave, and thus the interference of these two diffracted waves after lens L_4 produces fringes with linearly increasing spatial frequency in the y direction, as desired.

REFERENCES

[1] E. N. Leith, Proc. IEEE, 59, 1305 (1971).

[2] I. Cindrich, J. Marks and A. Klooster, Proc. SPIE, 128, 128 (1977).

[3] D. Psaltis and K. Wagner, Optical Engineering, 21, 822 (Sept.-Oct. 1982).

[4] D. Psaltis, K. Wagner and M. Haney, Proc. SPIE, 352, 67 (1982).
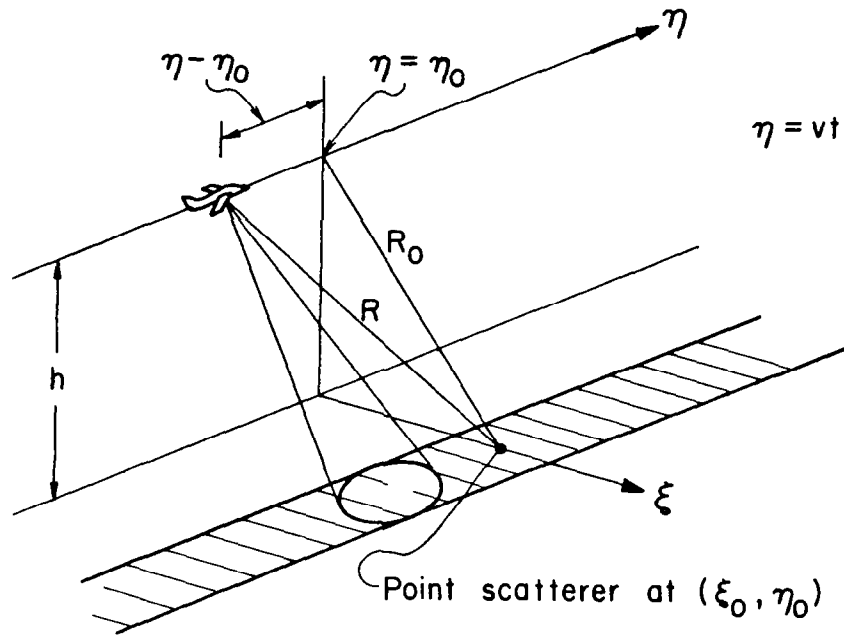
ACKNOWLEDGMENT

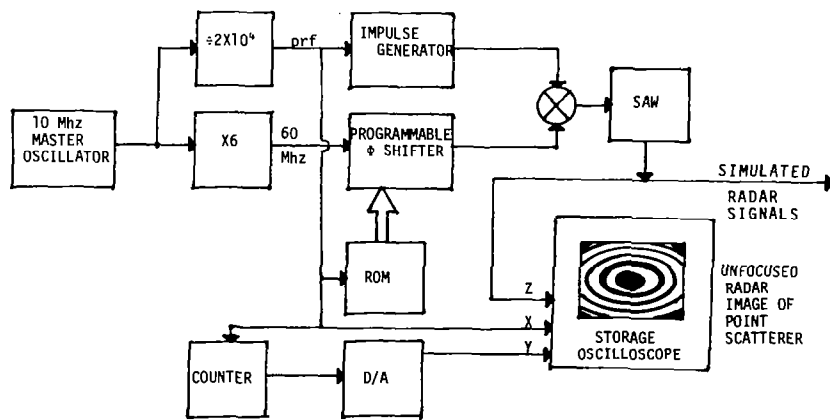Figure 1.- Synthetic aperture radar geometry.

Figure 2.- SAR impulse response simulator.
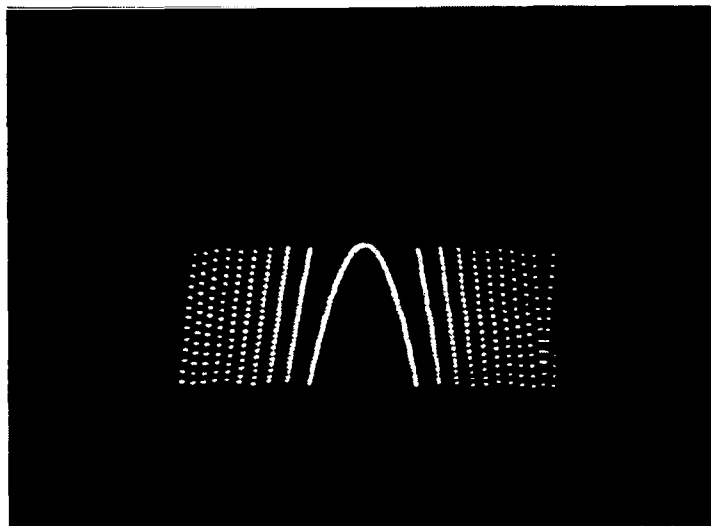
Figure 3.- Quadratic phase modulation simulating
the azimuth phase history.
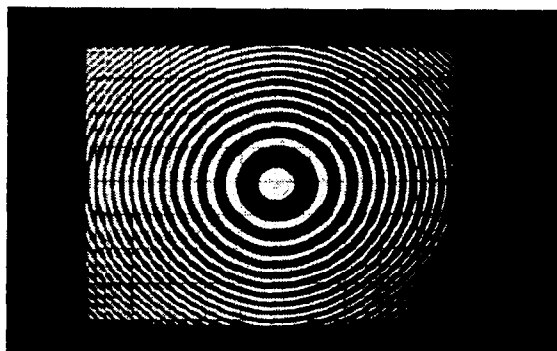
Figure 4.- Simulated SAR impulse
response produced in real time
by the system in figure 2.
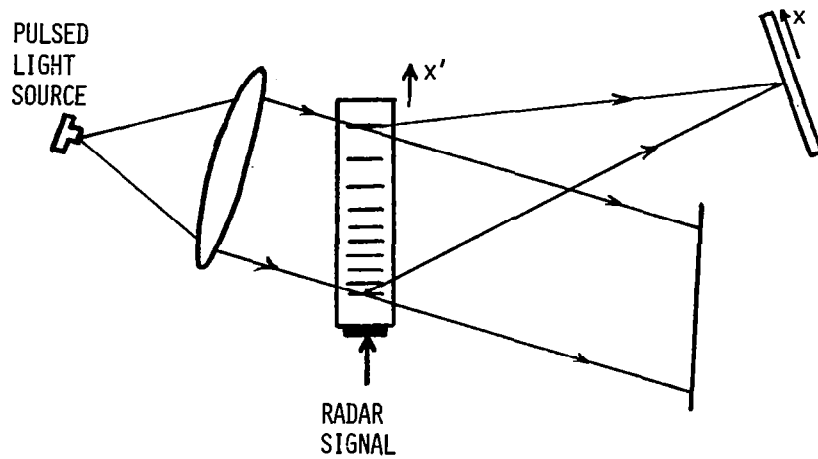
Figure 5.- Acousto-optic processor that performs the
focusing of the SAR image in range.
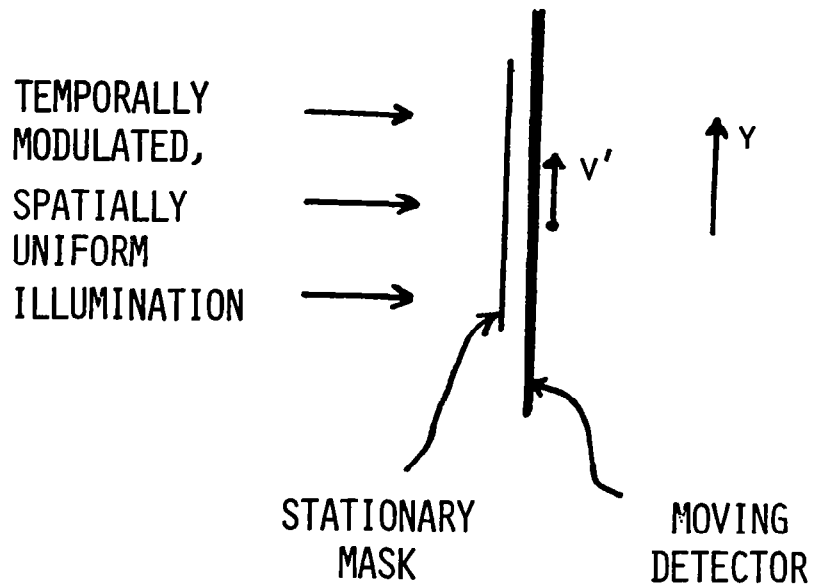
Figure 6.- Time-integrating optical processor that performs
the focusing of the SAR image in azimuth.
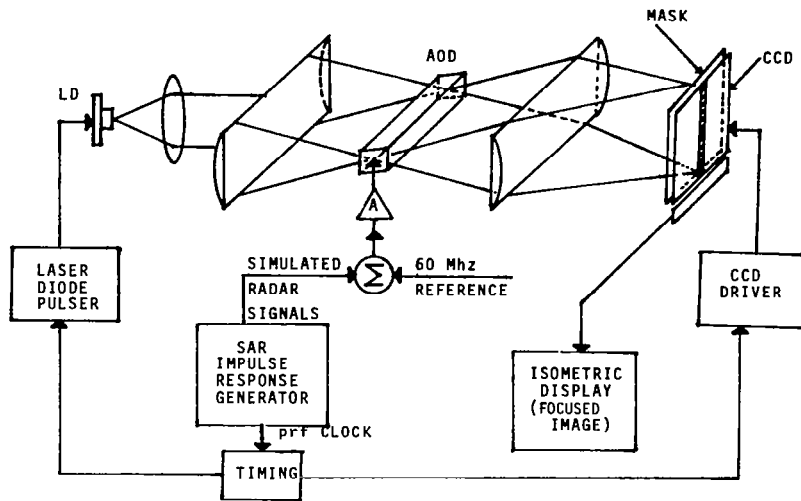
Figure 7.- Schematic diagram of the overall
real-time SAR processor.
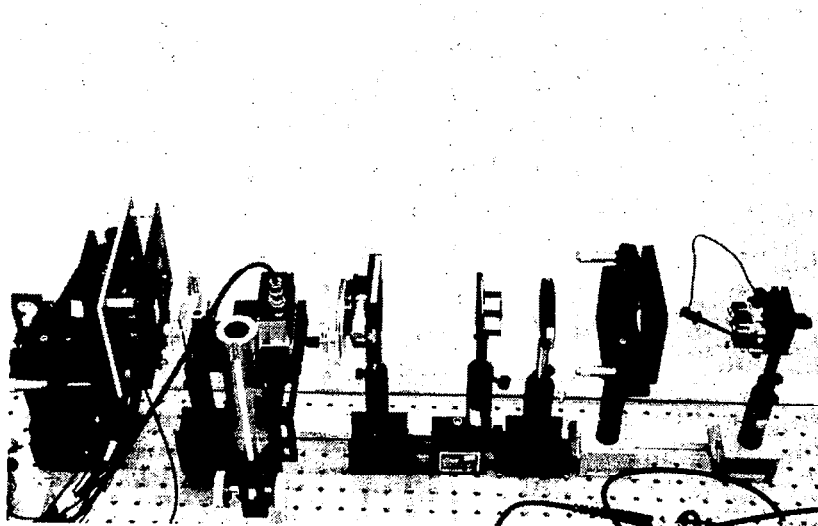
Figure 8.- Experimental SAR processor.
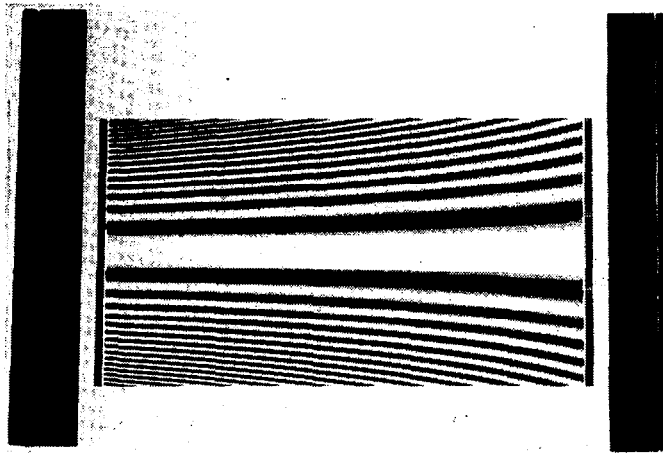
Figure 9.- Computer-generated mask used in
the processor of figure 8.
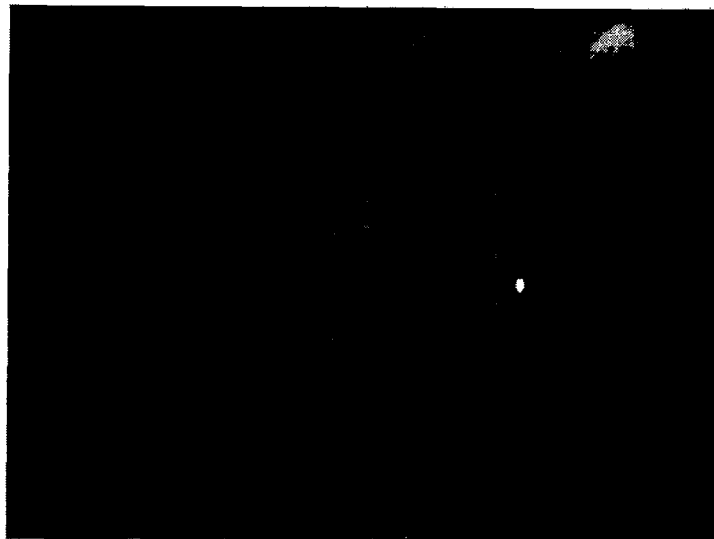
Figure 10.- Focused SAR image of the single-point
scatterer corresponding to the zone plate in
figure 4, produced in real time with the
processor of figure 8.
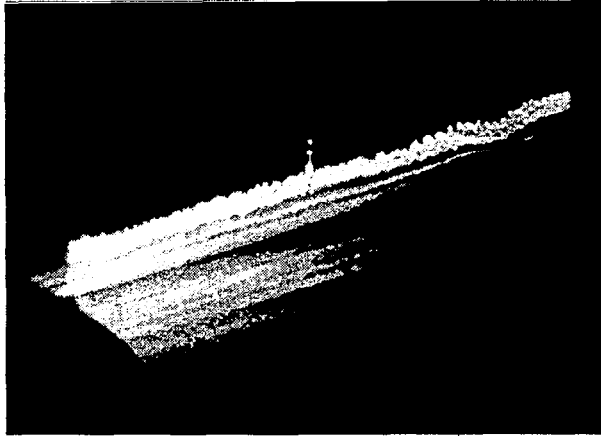
Figure 11.- Isometric display of the
focused point scatterer demon-
strating the bias structure.
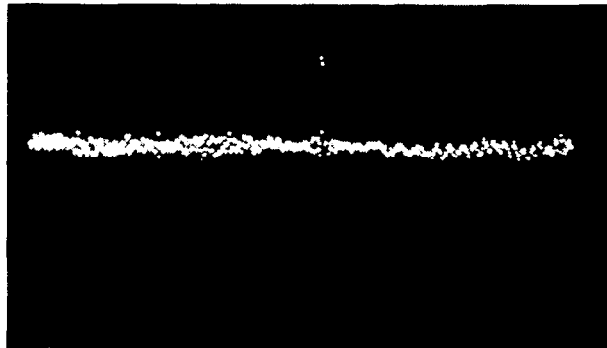
Figure 12.- Cross-sectional scan in
azimuth showing the sidelobe
structure (pulse compression).
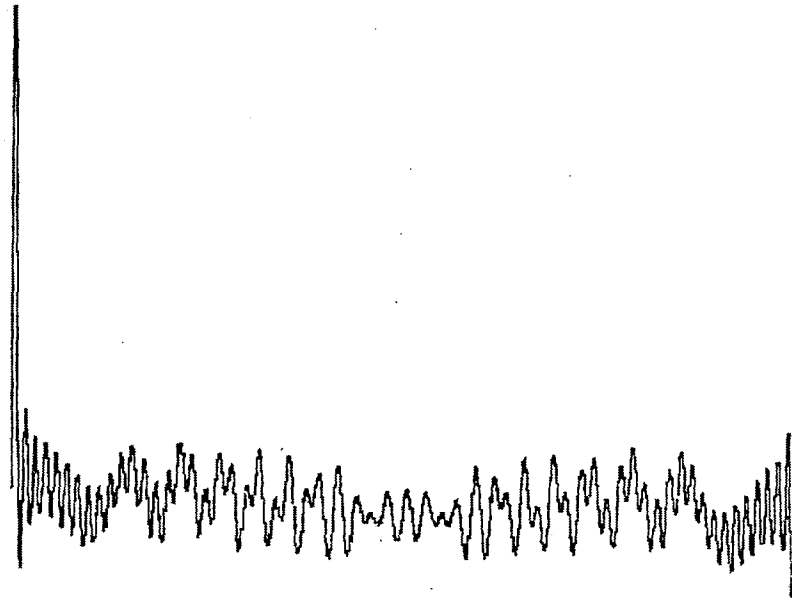
Figure 13.- Digital simulation of the signal
shown in figure 12.

ACOUSTO-OPTIC
DEVICE

TILTED
CYLINDRICAL
LENS

θ

L_1 AZIMUTH L_2 L_3
REFERENCE
SIGNAL
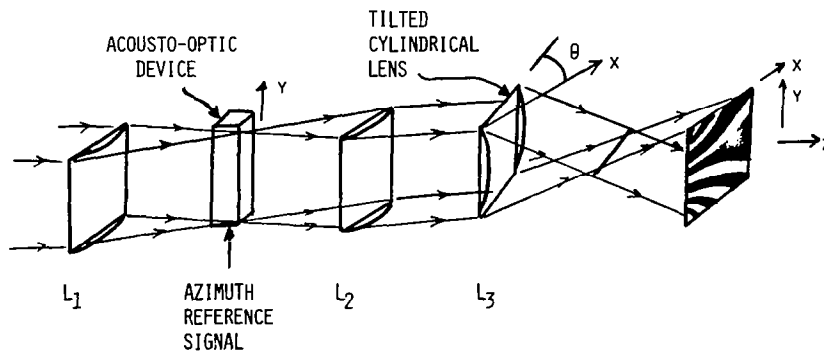
Figure 14.- Acousto-optic system with which the azimuth
reference is interferometrically introduced.

PULSED
LASER
DIODE

ACOUSTO-OPTIC
DEVICES

CCD

RADAR
SIGNAL

REFERENCE
SIGNAL

TOP VIEW

SIDE VIEW
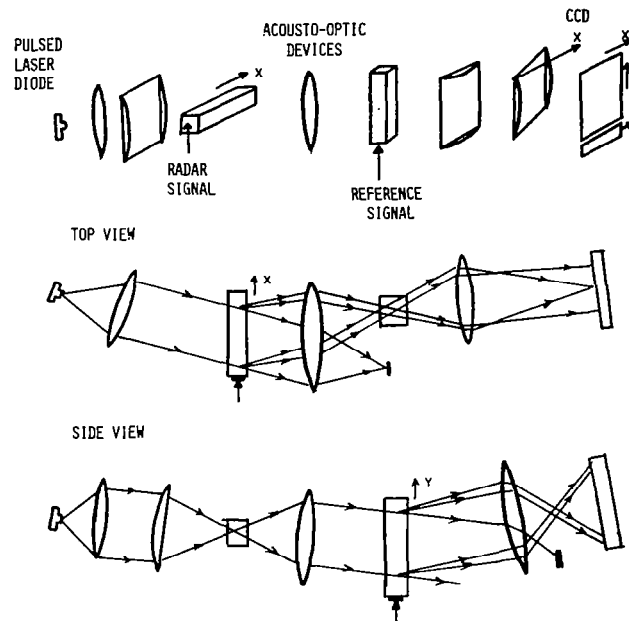
Figure 15.- Optical architecture for SAR
imaging with the azimuth reference
introduced through a second AOD in
place of the mask used in figure 7.

OPTICAL RESIDUE ADDITION AND STORAGE UNITS

USING A HUGHES LIQUID CRYSTAL LIGHT VALVE*

Sarry F. Habiby and Stuart A. Collins, Jr.
The Ohio State University ElectroScience Laboratory
1320 Kinnear Road
Columbus, Ohio   43212

SUMMARY

Optical addition and storage units are described in this paper. These units are implemented using the Hughes Liquid Crystal Light Valve (LCLV) as a spatial light modulator using residue arithmetic for a numerical representation. The main hardware components of the design, besides the light valve, include an array of single-mode optical fibers that provide input information, a polarizing prism in combination with quarter-wave and half-wave retarders for residue arithmetic implementation in the adder, and a holographic lenslet array for spatial stability in the storage unit.

INTRODUCTION

This paper deals with the subject area of numerical optical computing. The optical addition and storage units described in this paper are basic elements that could be used in many devices performing arithmetic operations. The development of such units is essential for the future of the general area of numerical optical computing, where parallel processing and increased speed offer attractive solutions to the problems facing the conventional von Neumann computer architectures of today. In this specific case they are to be used as components of an optical temporal integrator.

The evolution of optical computing in general has progressed from the analog Fourier transform type of optical computing (ref. 1), (ref. 2), (ref. 3) to recent advances in numerical (digital) optical computing (ref. 4), (ref. 5), (ref. 6) in much the same way as electronic computing evolved from the analog to the digital. Residue arithmetic numerical optical computing has also been investigated based on the compatability between the parallel nature of arithmetic operations in residue arithmetic and the parallel processing capability of optics (ref. 7), (ref. 8), (ref. 9), (ref. 10), (ref. 11), and (ref. 12).

In the remainder of this paper the optical addition and storage units are discussed. The next section contains background material on the temporal integrator, the Hughes Liquid Crystal Light Valve, and residue arithmetic. A section describing the basic optical addition operation follows the background material. In this section, an adder formed from a variable diffraction grating produced by interfering light from two single mode fibers in an optical fiber array is first described. After that the method of converting the adder to implement a residue arithmetic representaion using a Glan Thompson polarizing prism is given. The storage unit, which is simply a fedback version of the adder, is described in the subsequent section. The implementation of this unit and provisions for information registration (stability) will be discussed. In the final section, the constructed units will be shown and discussed.

BACKGROUND

This section contains a brief review of the temporal integrator, the Hughes Liquid Crystal Light Valve, and residue arithmetic presented as background material useful in the description of the optical residue addition and storage units.

Temporal Integrator

Figure 1 is a block diagram of a temporal integrator. A temporal integrator maintains a running sum of a string of numbers using an adder and an accumulator. As seen in figure 1, a clocked input and a previously stored value (initially zero) are added. The sum then provides the input to the accumulator. The accumulator is composed of two storage units, two being required for the purpose of decoupled information storage and feedback. The goal of this work is to optically implement this temporal integrator using a residue arithmetic representation of numbers.

Light Valve

A drawing of the Hughes Liquid Crystal Light Valve is shown in figure 2. The central one square inch serves as active area, having a resolution of about 600 lines per inch. The device requires 6 to 10 volts A.C. for operation (ref. 13). This provides an array of 600 x 600 simultaneously and independently accessible image elements. The light valve used in this design has a parallel, rather than a twisted, nematic liquid crystal configuration.

An incident write beam shown at the left in figure 2 strikes a photosensitive CdS film on the input side of the light valve. The CdS film then allows the intensity of this beam to control the field produced across the liquid crystal layer. This in turn effects a change in the tip of the liquid crystal molecules and hence provides a control over their birefringence. This control is available at each image element of the device simultaneously and independently. A polarized read beam incident on the output side of the device,

shown at the right in figure 2, is reflected by a dielectric mirror behind the liquid crystal layer. The intensity of the reflected beam after passing through an analyzer is thus controlled by the the intensity of the light incident on the LCLV input side. The characteristic curve showing the variation of output intensity as a function of input intensity is given in figure 3. Operation between point A for low input intensity and point B for high input intensity is desirable.

The light valve is an essential component in both the addition and storage units mainly as an easily updated bank of variable diffraction gratings in the implementation of both these units. Its role in these units is further described later.

Residue Arithmetic

Residue arithmetic is an alternative scheme for performing addition, subtraction and multiplication. Its advantages are lack of carries and error correction. It also fits in with parallel processing schemes. Residue arithmetic involves a representation of an integer number by a set of residues, which are remainders after division of the integer by a set of bases, one at a time. The representation range (beyond which the residue combinations begin to repeat themselves) is equal to the product of the bases as long as the bases are relatively prime (ref. 14).

Table I shows the residue representation in the bases 2, 3, and 5, giving a unique range of 30. The numbers between 1 and 30 are shown in the left-hand column. Next are columns for bases 2, 3, and 5 containing the residues for those bases. For example, the residue representation of 9 in base 2 is 1, the remainder after dividing 9 by 2. In base 3 it is 0, and in base 5 it is 4. Thus nine is represented by the 3-tuple (1,0,4).

Operations such as addition, subtraction, and multiplication are simply performed so that the sum of the residues gives the residue of the sum and so forth. For example, the addition of 9, represented by (1,0,4), and 3, represented by (1,0,3), is achieved by performing the addition 1+1=0 in base two. 0+0=0 in base three, and 4+3=7 which, after casting out five, gives 2 in base 5. It is evident that the arithmetic operations are performed independently in each base with no need for communication between the bases. The final result is the set of residues (0,0,2) which can be verified in Table I as the residue representation of 12.

Residue arithmetic has been chosen for the numerical representation of numbers to be processed since it is compatible with the parallel processing capability of optical computing. The advantage of residue arithmetic is that arithmetic operations are divided into simple calculations performed in parallel (addition is devoid of carry) independently in each base. Subsequently, this improves the computing speed of the system.

OPTICAL ADDER

In this section the first of the two optical units, the adder, is described. The use of controlled diffraction gratings produced by interfering light from two single mode optical fibers to implement the addition is presented. After that the method of obtaining a residue arithmetic representaion using a Glan Thompson polarizing prism is given.

The principal optical addition operation is shown in figure 4. The numbers to be added are position coded in a linear array as indicated in plane Q. Numerical information is provided through optical fibers with the fiber ends acting as point sources in the input plane.

Twenty-two fibers, representing successive integers, are used to implement base 11 addition. The central two fibers denote zero, and numerical values for input A increase in one direction (positive y direction in figure 4) while numerical values for input B increase in the opposite direction. Light from two illuminated fibers, one in group A and another in group B, passes through a collimating lens to produce interfering plane waves at the input side of the liquid crystal light valve. The interference pattern fringe spacing is a function only of the distance between the illuminated fibers which, in terms of quantized units of fiber separation, is proportional to the sum of the two numbers represented by the corresponding fibers. The distance between a fiber representing the number 4 in group A (four units from the zero in group A) and a fiber representing the number 3 in group B (three units from the zero in group B) is eight units, seven units for the sum of 4 and 3, plus one unit representing the seperation between the two zeroes.

On the output side of the light valve, light incident from another source is reflected by the dielectric mirror and diffracted by the gratings resulting from the incident interference pattern on the light valve input side. The reflected and diffracted light is then focussed in plane P into various diffracted orders of which only the +1 order is retained, as shown at the right of figure 4. The deflected distance from the z axis of the diffracted spot is proportional to the separation of the fibers in the input plane. Thus the addition of two zero inputs gives an output deflection of one unit. The deflected distance past this unit offset is equal to the sum of the two numbers represented by the fibers producing the initial diffraction grating. The range of the adder is limited only by the space-bandwidth product of the light valve.

IMPLEMENTATION OF RESIDUE ARITHMETIC

If the two inputs represent numbers ranging from 0 to b-1 (where b is the residue base size), then the sum can range from 0 to 2(b-1). (The largest designator is (b-1).) The optical unit must, on the other hand, maintain an output spot in the 0 to b-1 range, as is necessary for the residue arithmetic representation. If necessary, the base must be cast out. This is done by using a residue converter based on a polarizing prism, quarter-wave and half-wave plates to distinguish between diffracted spots in the two ranges.

In the residue converter portion of the adder, outputs in the range b to 2(b-1) are treated differently so that they can be moved to the range 0 to (b-1). A half-wave plate is positioned in plane P, the output of the basic addition, now shown at the left in figure 5, in the region where diffracted spots representing sums in the range b to 2(b-1) would appear. The region where diffracted spots in the range 0 to b-1 appear is hence unaffected and light from such spots diverges to the right of plane P and is collimated by the lens located at the left of the Glan Thopmson polarizing prism. Assuming that this light is linearly polarized in the horizontal direction, it is initially passed by the prism. Consequently light diverging from a spot in the range b to 2(b-1) will be vertically polarized due to the half-wave plate in plane P and initially reflected by the Glan Thompson prism.

The beams leaving the prism pass through quarter-wave plates and are reflected by two adjustable mirrors back towards the prism. Travelling through the quarter-wave plates twice, the beam initially transmitted by the prism is reflected by it and vice versa. One of the mirrors is tipped so that the spots from both ranges in plane P are superimposed in the 0 to b-1 range in output plane 0.

This completes the discussion of the adder. Two inputs introduced in a position coded domain (plane Q) via single mode optical fibers are added to provide a sum in plane P and a corrected residue arithmetic sum in plane 0. Information in planes P and 0 is also position coded. In the temporal integrator the output of the adder is the input of the accumulator. The storage units that make up the accumulator are discussed next.

STORAGE UNIT

The storage unit is described in this section. It is simply a fedback version of the adder with provisions for assuring stability. The implementation of this unit and provisions for information registration (stability) will be discussed.

The storage unit is a fedback adder with one input fixed at zero. This is shown in figure 6, where the top portion of the figure has essentially the same configuration as that of the adder. Plane 0, representing the output of the adder, is shown at the left as the input to the storage unit, and planes Q and P are similar to those found in the adder. To the right of plane P a beam splitter provides a flow of information in two directions: output onto the next stage in the temporal integrator and feedback for the implementation of an optical memory. There is no need for the residue conversion unit with the Glan Thompson polarizing prism at that point since casting out the base in this unit is not necessary. One of the inputs is always fixed at zero and hence the maximum sum is b-1.

The feedback loop consists of a set of lenses to provide one-to-one imaging of information from the output side of the light valve back onto the input side as in a conventional bistable configuration (ref. 15). To overcome any positional perturbation a holographic lenslet array is used to provide spatial stable equilibrium. Motion in one direction due to a perturbation is

counteracted by a negative unity magnification (-1) provided by the individual lenses in the lenslet array, thus preserving positional information.

IMPLEMENTED UNITS

The constructed optical addition and storage units will be shown and discussed in this section.

Figure 7 is a drawing of the optically implemented base 11 residue arithmetic adder. A linear array of twenty-two single mode optical fibers provides the input information as shown at the left of the figure. The fibers are held in specially constructed optical fiber couplers incorporating the appropriate coupling lens and are arranged on a metal plate. Light is directed to each coupler via two mirrors, one to direct the light into the individual coupler and the other to select the particular coupler. The fibers are divided into two groups, A and B, corresponding to the two inputs to the adder. Each group has its own selection mirror. The output ends of the fibers are collected in a linear array in a fiber holder consisting of a set of closely spaced grooves. A demagnifying lens (L_m) forms a miniaturized image of that array in plane Q so that the interference from fibers that are furthest apart does not exceed the resolution limit of the light valve.

The components to the right of image plane Q constitute the adder described in a previous section and are labeled CPU in the figure. Note that L_e is an elliptic lens formed from a cylindrical lens and a spherical lens. It images the information (in the form of interference patterns) into slit-shaped patterns on the light valve, allowing many diffraction gratings to be incident on the light valve at the same time. This would correspond to different bases and eventually allow simultaneous implementation of a number of temporal integrators on one device. A detail of this lens operation is given later.

Information is read off the output side of the light valve in similar slit-shaped patterns and a second elliptic lens at the output end is needed for this purpose. The sum information appears at plane P where the aforementioned half-wave plate is shown.

The residue converter is shown at the right of figure 7. Collimated light is incident on the Glan Thompson prism and appropriate quarter-wave plates and mirrors provide a residue arithmetic output in plane 0. A magnifying lens (L_m) at the output end allows a visual check of the operation of the adder.

The elliptic lens discussed in the description of the adder is shown in figure 8. The lens performs an imaging operation in the vertical direction and a Fourier transform in the horizontal direction. Thus light from a pair of point sources on a horizontal line in the input plane is imaged into a slit-shaped interference pattern in the output plane which, in this case, is the plane of the light valve. This allows for introducing information in array form at the input where the y coordinate of a point source (the end of an illuminated fiber) indicates the base and its x coordinate indicates the magnitude of the represented number.

Figure 9 is a drawing of the implemented storage unit. The input to the unit is shown at the top left of the figure. The input takes on the form of an interference pattern resulting from the spot representing the sum obtained in the adder and a fixed point source. An elliptic lens focusses this input to a slit-shaped pattern at the input of the light valve.

The read beam comes in from the lower left in the figure. It is focussed on the output side of the light valve also using an elliptic lens. The reflected and diffracted beam is then fed back to the elliptic lens. The a combination of mirrors and imaging lenses shown in the right half of figure 9. The holographic grating is located in the feedback loop and is shown towards the bottom of figure 9. It is located in plane P which is a position-coded plane, allowing the grating to correct for any spatial perturbation that may exist.

The two mirrors shown at the top of the feedback loop are mounted onto one base to simplify the alignment procedure.

SUMMARY

In this paper we have considered two optical units useful in numerical computing: an adder and a storage unit. They both use a Hughes liquid crystal light valve as the central active element and use the residue arithmetic representation. Both use single mode optical fibers as the means of inputting information. The light valve is employed as an optically controlled diffraction grating. After a brief discussion of residue arithmetic and the light valve, the addition unit was considered. Both the adder and a converter to cast out the residue base were explained. Then the storage unit was discussed. This is a fedback adder with a lenslet array to ensure positional stability. Finally the actual experimental versions of the apparatus were indicated.

REFERENCES

1. Goodman, J.W.,(1968) "Introduction to Fourier Optics," McGraw-Hill Book Company, New York.

2. Preston, K. Jr.(1972), "Coherent Optical Computers," McGraw-Hill, New York.

3. Rhodes, W.T., editor, Digest of Papers of the 1980 International Optical Computing Conference, Proc Soc Photo-Opt. Inst. Eng. IEEE CATALOG No. 80CHI5 48-7.

4. Athale, R.A.(1979), and S.H. Lee, "Development of an Optical Parallel Logic Device and a Half-adder Circuit for Digital Optical Processing," Opt. Eng. 18, 513.

5. Soffer, B.H.(1980), D. Boswell, A.M. Lackner, P. Chavel, A.A. Sawchuk, T.C. Strand, and A.R. Tanguay, Jr., Proc Soc. Photo-Opt. Instrum. Eng. 232, 128.

6. Lee, S., B. Bartholomew, and J. Cederquist, "Two Improved Coherent Optical Feedback Systems for Optical Information Processing," Proc. SPIE 83, 1976.

7. Huang, A.(1979), Y. Tsunoda, J.W. Goodman, and S. Ishihara, "Optical Computation using Residue Arithmetic," Appl. Opt. 18, 149.

8. Huang, A.(1975), "The Implementation of a Residue Arithmetic Unit via Optical and Other Physical Phenomena," International Optical Computing Conference, Digest of Papers, Washington D.C., IEEE Catalog No. 75CH0941-5C, p. 14.

9. Psaltis, D.(1979), and D. Casasent, "Optical Residue Arithhmetic: a Correlation Approach," Appl. Opt. 18, 163.

10. Tai, A.(1979), I. Cindrich, J.R. Fienup, and C.C. Aleksoff,"Optical Residue Arithmetic Computer with Programmable Computation Modules," Appl. Opt.18,2812.

11. Collins, S.A., Jr., J. Ambuel, and E. K. Damon, "Numerical Optical Data Processing," Proceedings of the 1978 International Optical Computing Conference, London, England, September 5-7, 1978, IEEE No. 78CH 1305-2C.

12. Habiby, S.F.(1982),"A Design Study of a Numerical Optical Temporal Integrator Using Residue Arithmetic," Masters Thesis, The Ohio State University, Columbus, Ohio.

13. Bleha, W.P.(1978), L.T. Lipton, E. Wiener-Avenear, J. Grinberg, P.G. Reif, D. Casasent, H.B. Brown, and B.V. Markevitch, "Application of the Liquid Crystal Light Valve to Real-Time Optical Data Processing," Opt. Eng. 17, 371.

14. Szabo, N.S., and R.I. Tanaka, "Residue Arithmetic and its Applications to Computer Technology," Mcgraw-Hill, New York, 1977.

15. Collins, S.A. Jr., U.H. Gerlach, and Z.M. Zackman, SPIE Vol. 185, Optical Processing Systems, 36, 1979.

Table 1.- Residue arithmetic

p=	2	3	5	
z	r_2	r_3	r_5	$z^{-1}\text{Mod}5$
0	0	0	0	-
1	1	1	1	1
2	0	2	2	3
3	1	0	3	2
4	0	1	4	4
5	1	2	0	-
6	0	0	1	1
7	1	1	2	3
8	0	2	3	2
9	1	0	4	4
10	0	1	0	-
11	1	2	1	
12	0	0	2	
13	1	1	3	
14	0	2	4	
15	1	0	0	
16	0	1	1	
17	1	2	2	
⋮	⋮	⋮	⋮	
26	0	2	1	
27	1	0	2	
28	0	1	3	
29	1	2	4	
30	0	0	0	

```
ADD          9     1 Ø 4        AFTER
           + 3     1 Ø 3     CASTING OUT
            12     Ø Ø ②      BASE 5

SUBTRACT     9     1 Ø 4
           - 3     1 Ø 3
             6     Ø Ø 1

MULTIPLY     9     1 Ø 4
             3   X 1 Ø 3
```

ADD ONE   1 IN 2's COLUMN
ADD ZERO   Ø IN 3's COLUMN
ADD FOUR   3's IN 5's COLUMN

```
              1   Ø   3
                  Ø   3
                      3
                      3
PRODUCT = 27:  1   Ø   2
```
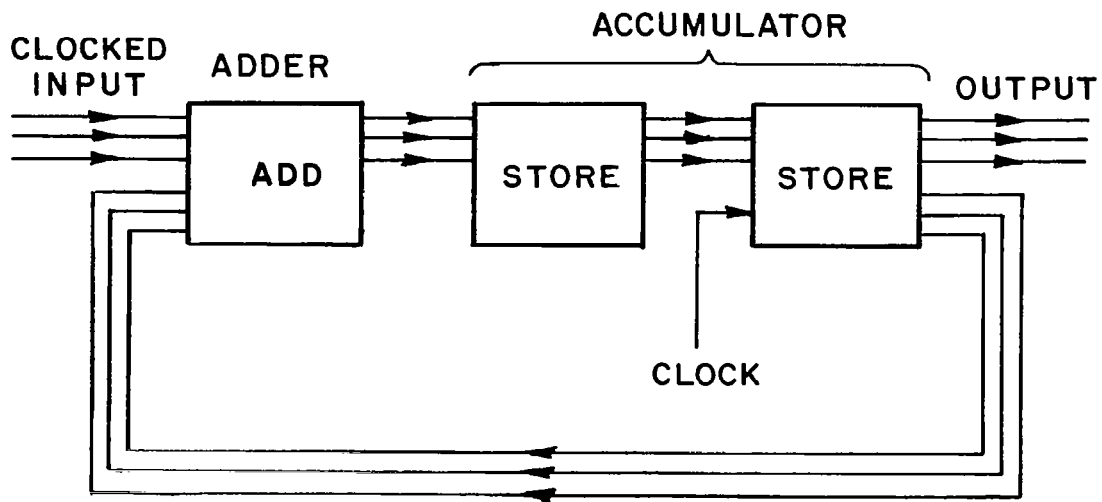
Figure 1.- Block diagram of temporal integrator.
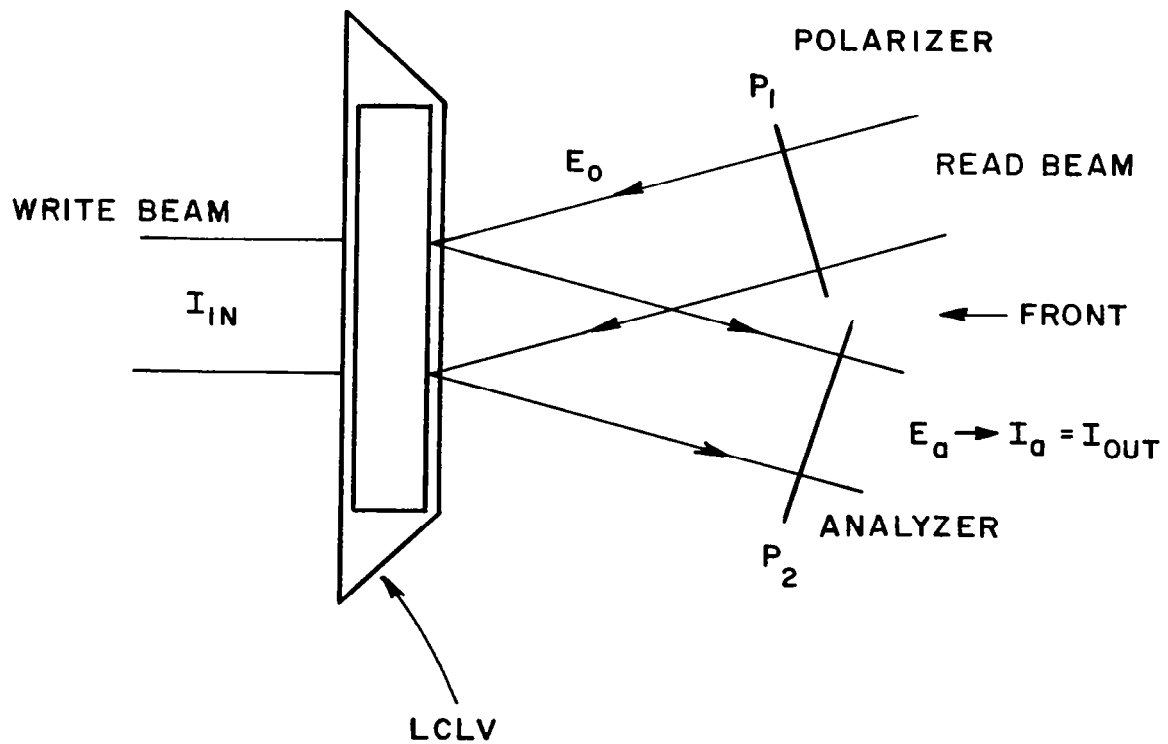
Figure 2.- Hughes Liquid Crystal Light Valve.

Figure 3.- Variation of output intensity as a function of input intensity.
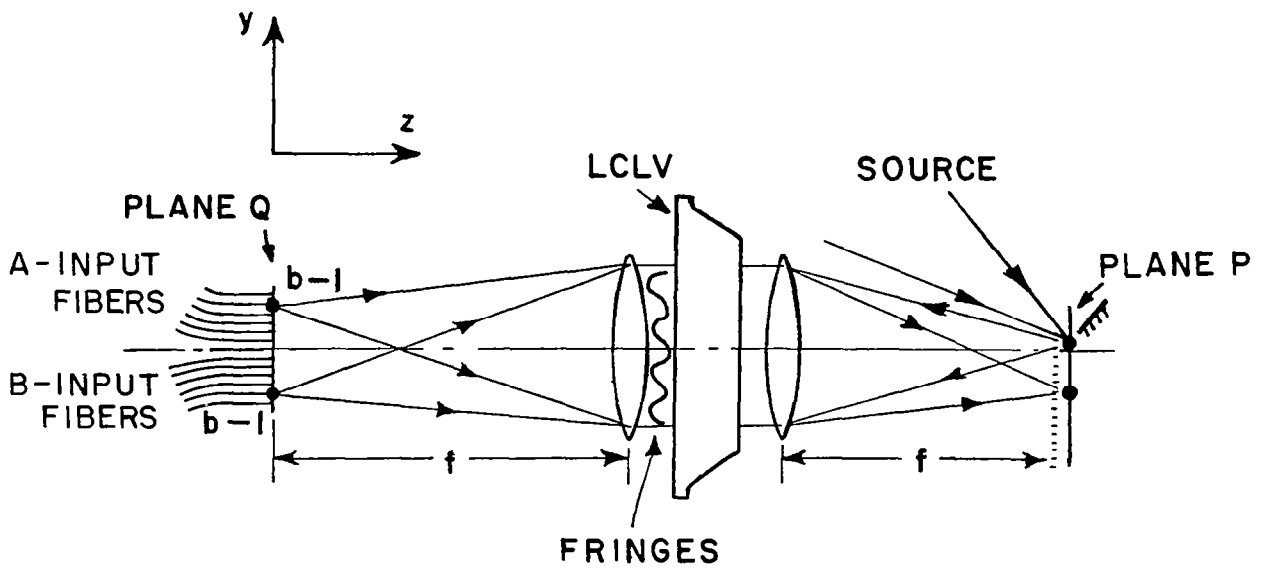
Figure 4.- Principal optical addition operation.

Figure 5.- Residue conversion unit.

FEDBACK LIGHT VALVE

Figure 6.- Optical storage unit.
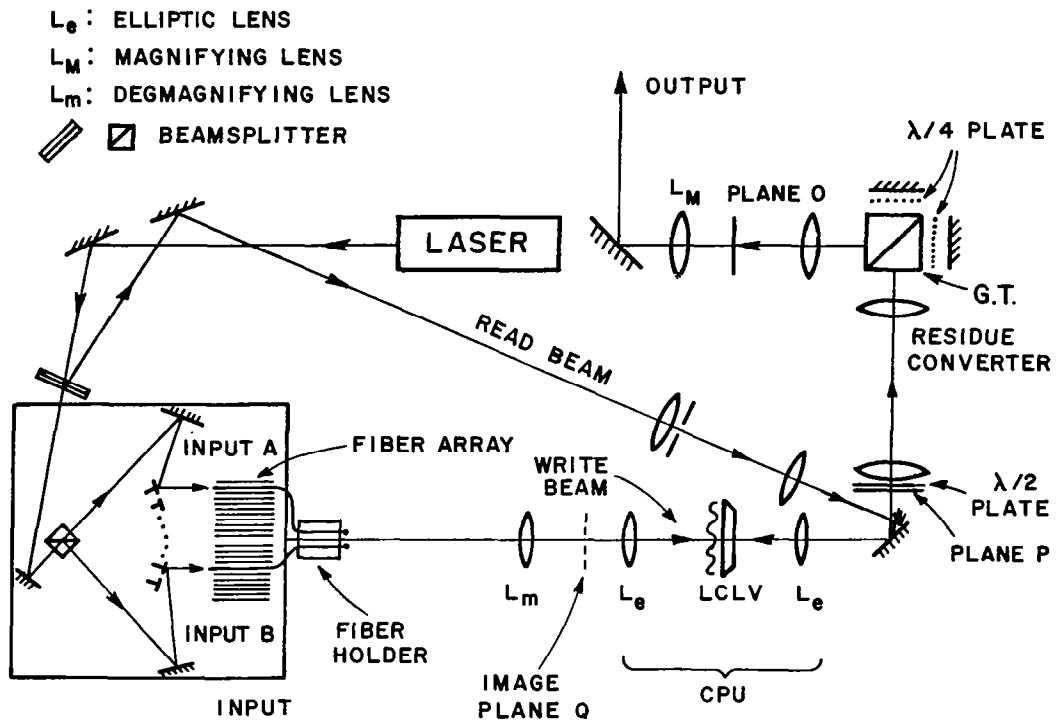
Figure 7.- Optically implemented base 11 residue arithmetic adder.

$$f_x = d$$

$$f_y = \frac{d}{2}$$

Figure 8.- Elliptical lens.

Figure 9.- Implemented storage unit.

INTEGRATED-OPTICAL APPROACHES TO MATRIX MULTIPLICATION*

C. M. Verber and R. P. Kenan
Battelle Columbus Laboratories
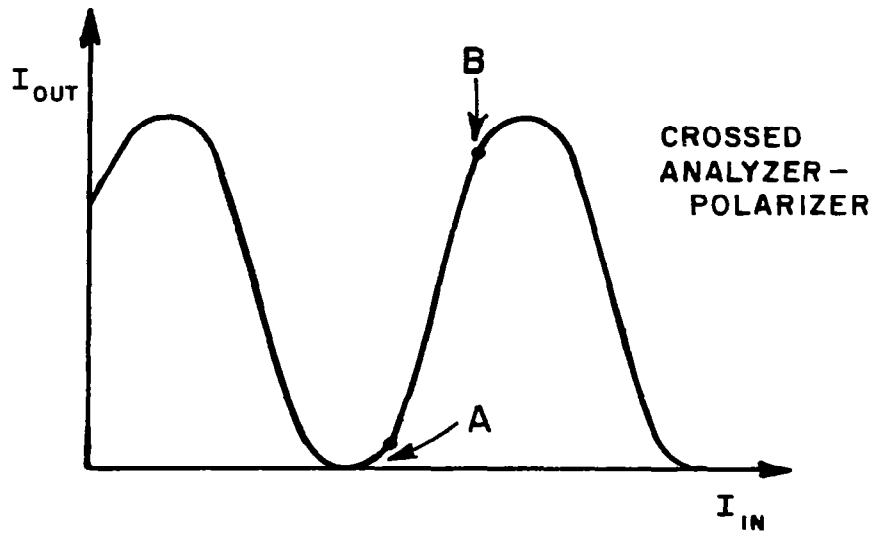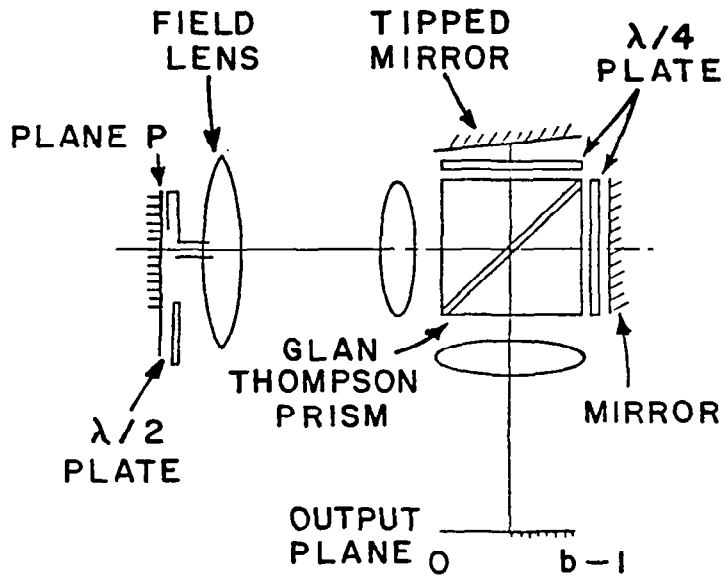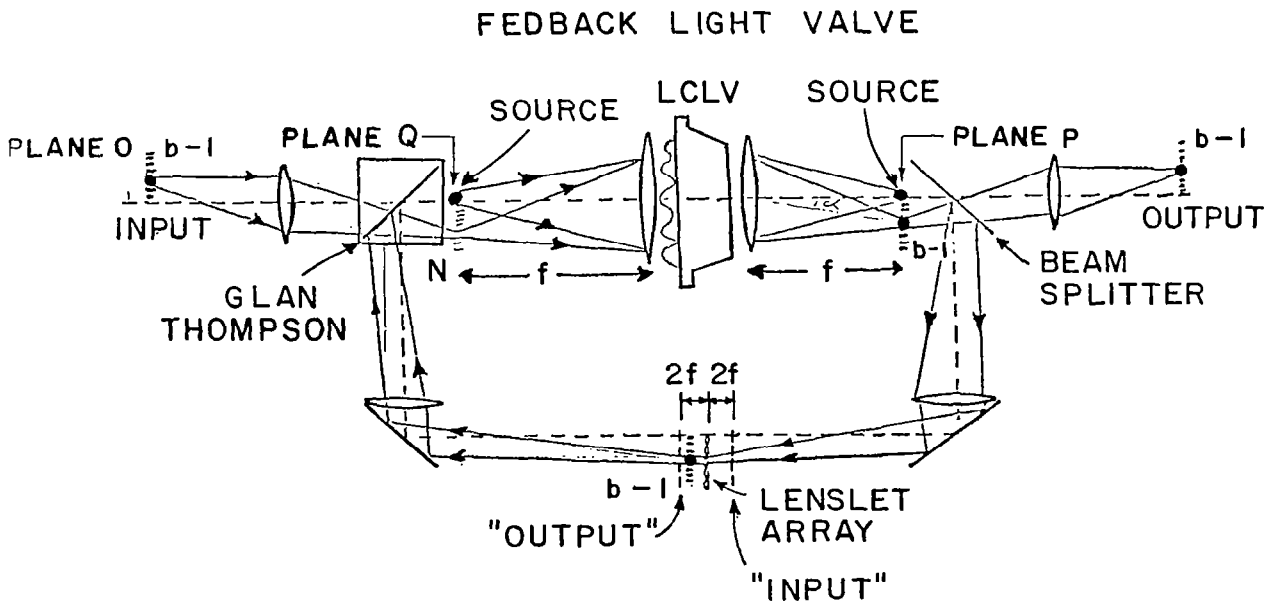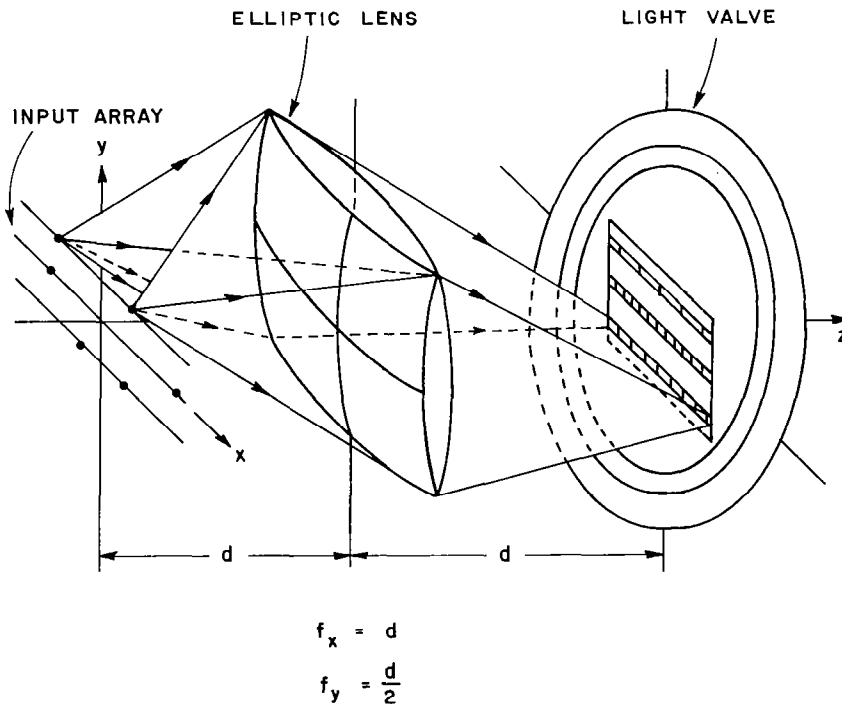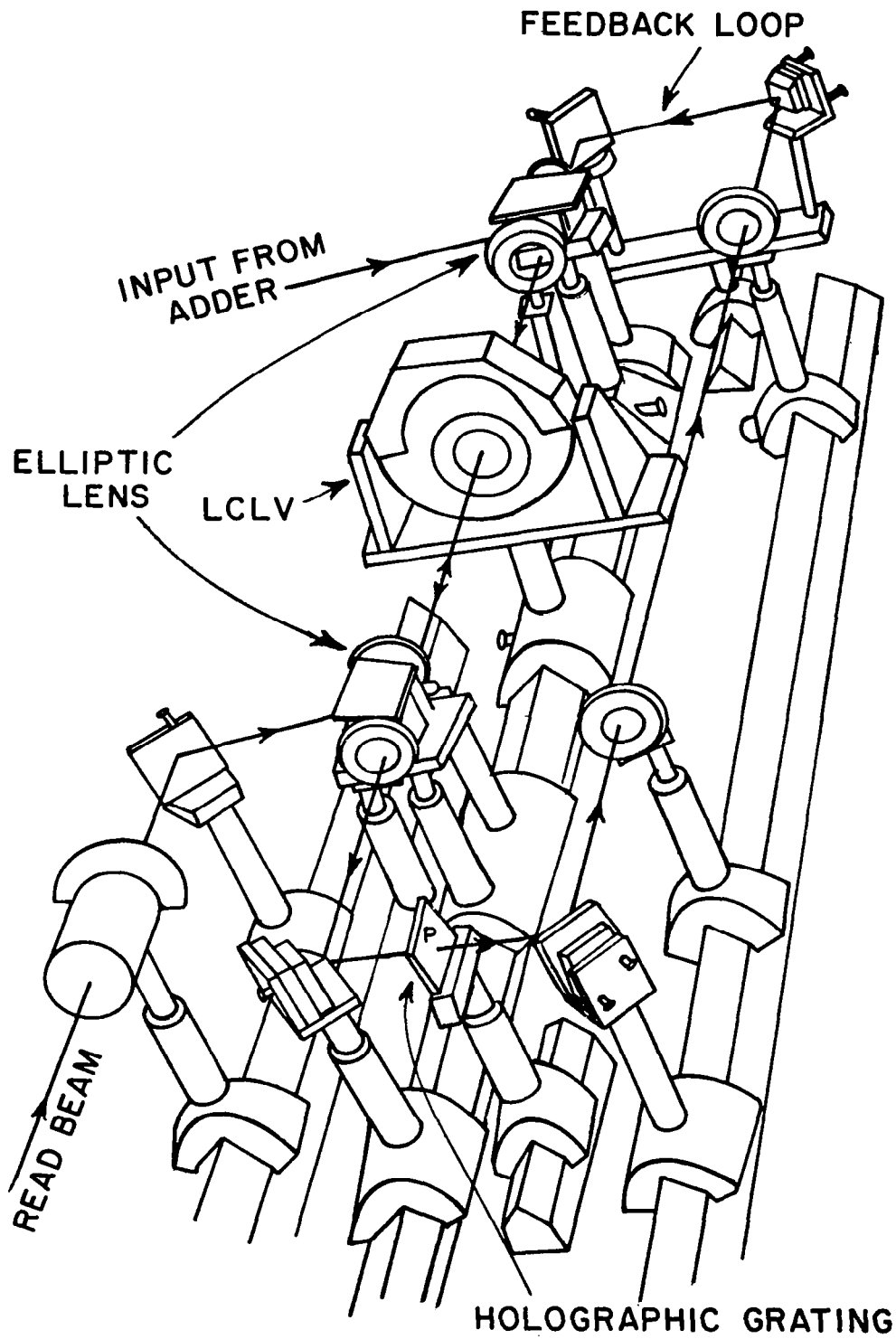Columbus, Ohio 43201

SUMMARY

The solution of matrix equations is essential to carrying out a large variety of control algorithms and to reducing certain types of data such as the output of a multispectral sensor array. Optical techniques and, in particular, integrated-optical circuits (IOC's) can provide compact, low-power devices for performing the matrix multiplications necessary for the solution of these problems. A specific IOC for performing vector-matrix multiplication and several approaches to the design of IOC's for matrix-matrix multiplication will be discussed.

I. INTRODUCTION

There has recently been an increasing amount of interest in the application of optical techniques to the solution of a variety of computational problems. The reasons most commonly cited for this interest are the high processing speeds and the low power consumption which are potential characteristics of optical analog devices, especially if the problem and the algorithm are well chosen. We address here the basic problems of vector-matrix and matrix-matrix multiplication, problems whose solutions open a large variety of signal-processing and control functions to optical implementation. We discuss and compare fully parallel and systolic-type architectures for IOC's for performing these functions. This discussion starts, in the following section, with a review of the basic architecture for systolic processors and the relationship of these criteria to IOC technology.

There are a number of basic integrated-optic components that are available for use in computational devices. In this paper we limit ourselves to planar as opposed to channelized IOCs and rely heavily upon the use of electro-optic gratings whose properties are reviewed in Section III. Following this, we move on to the discussions of matrix multiplication in Section IV. Associated with these analog devices are problems of dynamic range and the nonlinearities that arise from the use of electro-optic gratings. Approaches to the solution of the second of these problems are presented in Section V.

II. SYSTOLIC ARCHITECTURES AND INTEGRATED-OPTICAL CIRCUITS

The approach to computer design known as systolic array architecture was developed by Kung (ref. 1) and others as a method of approaching the problem of VLSI computer design. The basic guidelines are:

---

a. Each datum should be fetched from memory only once
    to avoid the "Von Neuman bottleneck"

b. Each chip should contain only a small number of dif-
    ferent processor subunits, although these subunits
    may be repeated many times on each chip

c. Connections between subunits should be only to
    nearest neighbors to facilitate the rapid flow
    of data and to simplify fabrication

The main disadvantage associated with the use of a systolic architecture in an optical processor is that the progression of the data in discrete steps requires electronic timing circuitry which can place a severe constraint on the ultimate speed of the system. Aside from this problem, we would be hard pressed to compile a better set of design guidelines for integrated-optical circuits than those listed above. We do not yet have available an optically addressable memory for IOCs, although some of Suhara, Nishihara, and Koyama's (ref. 2) surface holograms may be adaptable for this purpose. It is therefore essential that the recourse to memory be minimized since the act of fetching data from a digital store is much slower than the rate at which the IOC is capable of using that data. Second, at this stage in the develop-ment of IOC technology, we have only a small number of operational building blocks available to us. The second guideline is therefore compatible with IOC technology, if only by default. The third guideline is, perhaps, not as important for optical as for electronic systems since it is possible to have optical carriers intersect in either planar or in channel (ref. 3) configurations without causing significant cross talk. Complex interconnection schemes can therefore be implemented without requiring a multilayer structure. However, since the progress of the data through an optical processor is controlled by the speed of light in the device and not by a digital clock, it will be necessary to pay attention to path lengths in high-speed devices to assure that proper synchronism of the data flow is maintained.

There are several obvious advantages to using integrated as opposed to bulk optical techniques for the implementation of high-speed computational algorithms. Perhaps the most important is the fact that a variety of high-speed integrated-optical modulators (ref. 4) and switches (ref. 5) have already been developed and that these require electrical drive signals which are several orders of magnitude less than comparable bulk components. In addition, the integrated systems tend to be more compact than conventional optical systems and lend themselves to mass production by more or less conventional photolithographic techniques. A major shortcoming of the IOC's is that they are not capable of the same flexibility in handling two-dimensional computations as are the bulk devices. A hybrid approach seems to be the obvious solution to this problem.

III. ELECTRO-OPTIC GRATING STRUCTURES

The devices to be described in the following sections rely heavily on the use of electro-optically induced gratings. In this section, we will briefly describe the generation and the operation of these gratings.

The gratings are generated via the electro-optic effect using the fringing field from a set of interdigital surface electrodes. The basic electrode structure is

illustrated in figure 1. The electric field immediately below the electrodes is normal to the waveguide surface, and at the surface in the gap, it is tangential to the waveguide surface. Both of these fields are periodic with periods equal to four line widths (if the line and gap widths are the same). The amplitudes of the index variations induced by the two fields are not, however, equal because they generally invoke different electro-optic coefficients. The net effect of the electrode configuration is to produce a complicated index profile. The fields, to which the refractive index variations are proportional, have been given by Engan (ref. 6) in a Fourier series; for our uses, only the fundamental component is important. The presence of two fields causes the index pattern to be shifted relative to the electrode structure, that is, the maximum of the index modulation does not occur at the centers of the gaps or of the electrode lines, but is displaced somewhat.

The induced gratings can be operated at high efficiency, if desired, using low voltages. A typical result is 95% efficiency at voltages of 4 to 10 volts for grating with electrode lines 2 mm long and a period 8 to 15 μm. The diffraction efficiency of a grating having many fingers appears to follow Kogelnik's (ref. 7) theory in form, but typically does not reach 100% efficiency. The reason for this may be the incomplete overlap of the electric field with the optical field because of the exponential decay of the former with depth into the waveguide. Finally, we mention that the capacitance of the surface electrodes on y-cut $LiNbO_3$ is about 0.5 pF/mm of finger length/finger pair, or 1 pF/finger pair for the 2-mm long fingers.

Electro-optic gratings are capable of performing simple arithmetic (logic) operations on analog (binary) voltage signals. The simplest such operation is performed using the basic element pictured in figure 2. The diffracted light beam has intensity equal to ηI_0, and η is determined by the voltage <u>difference</u> between the two electrodes. For binary (two-level) signals, the result is the exclusive OR (EXOR) logic operation. For analog voltages, the result is a nonlinear function of the voltages, but for small signals it is proportional to $|V_1-V_2|^2$, the square of the voltage difference. The problem of the nonlinearity in the grating response is discussed in Section VII.

To multiply two signals together, we use the "herringbone" structure shown in figure 3. This is essentially two grating-inducing electrode systems using slanted fingers and placed so that the output of the first is the input to the second. In the figure, the gratings have been drawn to share one electrical lead, the ground, but this is not required. The output here is the input intensity multiplied by the product of the efficiencies of the two gratings. Again, because the grating response is nonlinear in the voltages, some arrangement must be used to linearize the device.

IV. MATRIX MULTIPLICATION

It was shown above that the herringbone structure of figure 3 could be used to perform analog multiplication. This concept can be simply extended to compute the scalar product of two vectors as shown in figure 4. Here, the herringbone is segmented; each segment is used to generate the product $A_i B_i$. The products are then summed with the lens to generate the scalar product. We shall now show this structure and some modifications of this structure can be used to perform vector-matrix and matrix-matrix multiplication.

It is possible to compute the product of a matrix and a vector using the segmented herringbone structure along with the engagement architecture shown in figure 5. Voltages representing the vector components and the matrix elements are arranged in the sequence indicated in the figure and synchronously stepped through the engagement region which is simply the segmented herringbone device. The successive products are accumulated on integrating photodetectors as indicated. A schematic of an IOC for accomplishing this is shown in figure 6. A major problem in the practical implementation of this technology is not the fabrication of the IOC, but in the design of a suitable electronic drive circuit which neither unduly limits the speed of the optical device nor overwhelms it with the sheer bulk of the electronic hardware.

A systolic (ref. 1) approach to matrix-matrix multiplication is shown schematically in figure 7. The data flow through the engagement region as indicated; each box in the engagement region is a device that performs a running sum of the products of the respective matrix components which again are flowing synchronously through the device. Note that in order to obtain proper registration of the elements of the two matrices, the components must enter the engagement region in an appropriately skewed array.

A schematic of an integrated-optical circuit for implementing the algorithm of figure 7 is shown in figure 8. In this figure, the herringbone structure has been disassembled. A uniform plane guided wave is incident upon the b_{ij} modulator units where it has the appropriate intensity modulation impressed upon it. This information is then carried by the light through a series of beam splitters which distribute it to the appropriate a_{ij} modulators. Since the optical distribution of information is essentially instantaneous compared to the rate at which the electronic drive circuitry can shift voltages through the system, we must remove the skew from the A matrix element array to maintain proper synchronism. Once again, it would appear that the major challenge in the fabrication of a complete matrix-matrix multiplier using these concepts will be in the design of high-speed, compact electronic drive circuitry.

A fully parallel technique for performing matrix-vector multiplication can also be implemented in a planar integrated-optic configuration using grating modulators. The architecture is based upon that suggested by Goodman et al. (ref. 8) for bulk implementation. The IOC for carrying out the parallel algorithm is shown schematically in figure 9. The herringbone structure is split, and a single N-element integrated-optic spatial light modulator (IOSLM) is used to modulate a uniform guided wave with intensities corresponding to the vector components. This information is distributed by a set of grating beam splitters so that it is incident, at the Bragg angle, upon the groups of grating segments which are excited with voltages corresponding to the matrix elements. The summations required to generate each of the product-vector components are performed by the lenses.

The speed of the fully parallel multiplier is limited only by the signal-to-noise ratio desired at the detectors. There are no electronic clocks or shift registers involved. In addition, the width of the guided optical wave incident upon the device is proportional to N rather than to N2 as in the engagement processor. On the other hand, the engagement device interfaces naturally with digital systems requiring a sequential data flow, and it can be extended to matrix-matrix multiplication. The comparison of the two approaches is summarized in Table I.

V. THE LINEARIZATION PROBLEM

Throughout the preceding sections, we have utilized electro-optic grating arrays as multipliers, and have indicated some of their advantages in this role. Here, we want to discuss a disadvantage of Bragg gratings, namely, their inherent nonlinearity, caused by the dependence of diffraction efficiency on voltage. The preferred approach to resolving this problem is to find an element for multiplication that has a linear voltage response. Other methods are discussed below.

The efficiency of an electro-optic grating can be written, at Bragg incidence, as

$$\eta = \sin^2 (\alpha v)$$

where α is a constant. This nonlinear response means that some method must be found to produce a voltage from the input variable so that an increment in the input variable produces a proportional increment in η. Let x denote the input variable. Then, we need to find a voltage v(x) of the form

$$V(x) = \sin^{-1}[x^{1/2}]/d$$

This can be done with digital electronics, requiring one circuit for each electro-optic grating. Alternatively, some a.c. signal processing could be used, but this becomes more and more complicated as the order of the polynomials increases. The simplest solution will probably be to use an analog electronic circuit to extract the square root of x and adjust the operating voltages so that one remains in the small signal regime. In this case,

$$\eta = (\alpha v)^2 = x$$

This keeps the circuitry simple, although it leads to a loss of signal-to-noise ratio. If noise becomes a problem, as it well may in large-order polynomials, then the full arc sine function must be used.

VI. CONCLUSIONS

In this paper, we have reviewed several kinds of architectures that can be used in an integrated-optical circuit to perform matrix multiplication. All of the devices reviewed utilize electro-optically induced gratings in an electro-optic waveguide. There are, of course, other ways to perform some of these operations, including surface acoustic waves, but the simplicity of fabrication and operation of these grating arrays is very appealing. It should be possible to perform more complex matrix operations such as inversion using integrated-optic techniques. These possibilities are currently under investigation.

REFERENCES

1. Kung, H. T., "Why Systolic Architectures", Computer 15, 37-46 (1982).

2. Suhara, T., Nishihara, H., and Koyama, J., "High-Efficiency Relief-Type Waveguide Hologram", Trans. IECE Japan E61, 167-170 (1978).

3. Kurokawa, T. and Oikawa, S., "Optical Waveguide Intersections Without Light Leak", Appl. Opt. 16, 1033-1037 (1977); Nakajima, H., Horimatsu, T., Seino, M., and Sawaki, I., "Crosstalk Characteristics of Ti-LiNbO$_3$ Intersecting Waveguides and Their Application as TE/TM Mode Splitters", IEEE J. Quantum Electr. QE-18, 771-776 (1982).

4. Thiolouse, P., Carenco, A., and Gugliemli, R., "High-Speed Modulation of an Electrooptic Directional Coupler", IEEE J. Quantum Electr. QE-17, 535-541 (1981); Cross, P.S. and Schmidt. R. V., "A 1 Gbit/s Integrated Optical Modulator", IEEE J. Quantum Electr. QE-15, 1415-1418 (1979).

5. Schmidt, R. V. and Kogelnik, H., "Electro-Optically Switched Coupler with Stepped $\Delta\beta$ Reversal Using Ti-Diffused LiNbO$_3$ Waveguides", Appl. Phys. Lett. 28, 503-506 (1976).

6. Engan, H., "Excitation of Elastic Surface Waves by Spatial Harmonics of Interdigital Transducers", IEEE Transactions on Electron Devices ED-16, 1014-1017 (1969).

7. Kogelnik, H., "Coupled Wave Theory for Thick Hologram Gratings", Bell Syst. Tech. J. 48, 2909-2947 (1969).

8. Goodman, J. W., Dias, A. R., and Woody, L. M., "Fully Parallel High-Speed Incoherent Optical Method for Performing Discrete Fourier Transforms, Optics Letters. 2, 1-3 (1978).

TABLE I.   COMPARISON OF DIRECT AND ENGAGEMENT ARCHITECTURES

	Engagement	Direct
Data Flow	Stepped	Continuous
Electronic Interface	Parallel set of sequential inputs	Fully parallel
Natural Device Geometry	Planar	3-D
Speed	Limited by electronic clock and/or shift register	Limited by detector SNR
Electronic Interface	Complex: N+1 shift registers, 2N D/A converters. All data moves at high speed.	Moderate: Only time dependent values must change
IOC Size	Maximum IOSLM size: N	Maximum IOSLM size: N^2
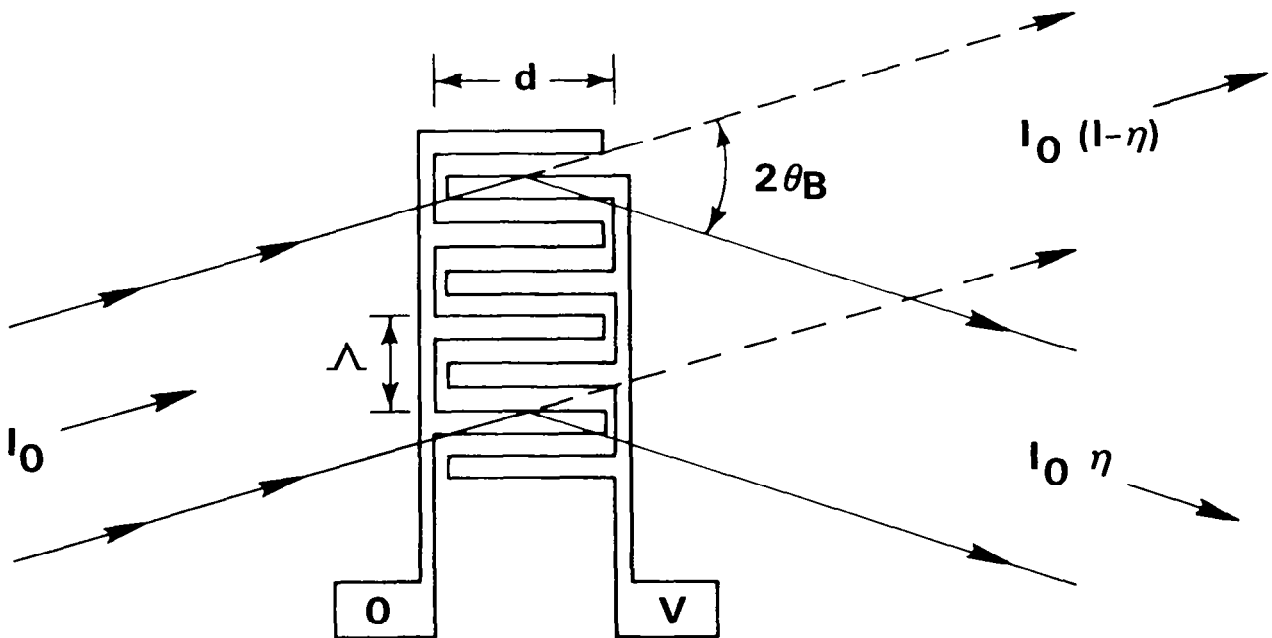
Figure 1.- The basic electrode structure for inducing electro-optic gratings, showing the electrode parameters.
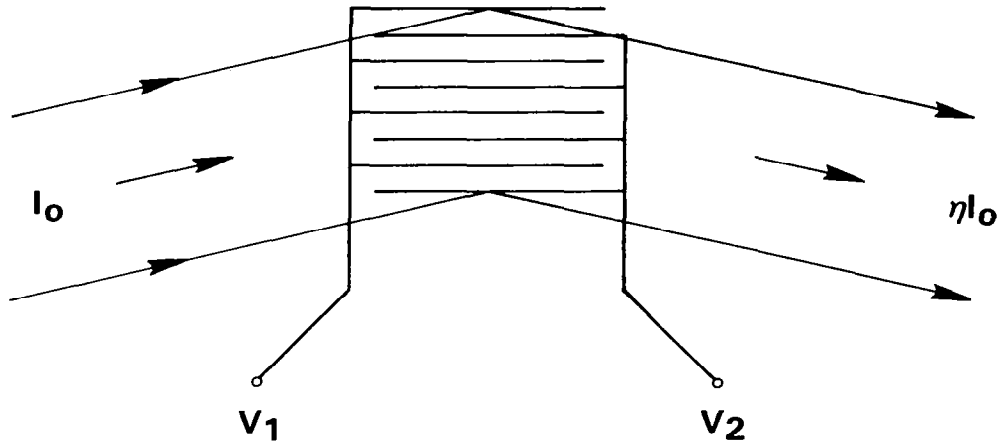
$$\eta = \sin^2 [a(V_1 - V_2)]$$

DIGITAL   Exclusive OR

ANALOG   Subtraction

Figure 2.- Schematic of the use of an induced grating for subtraction (or logical EXOR).
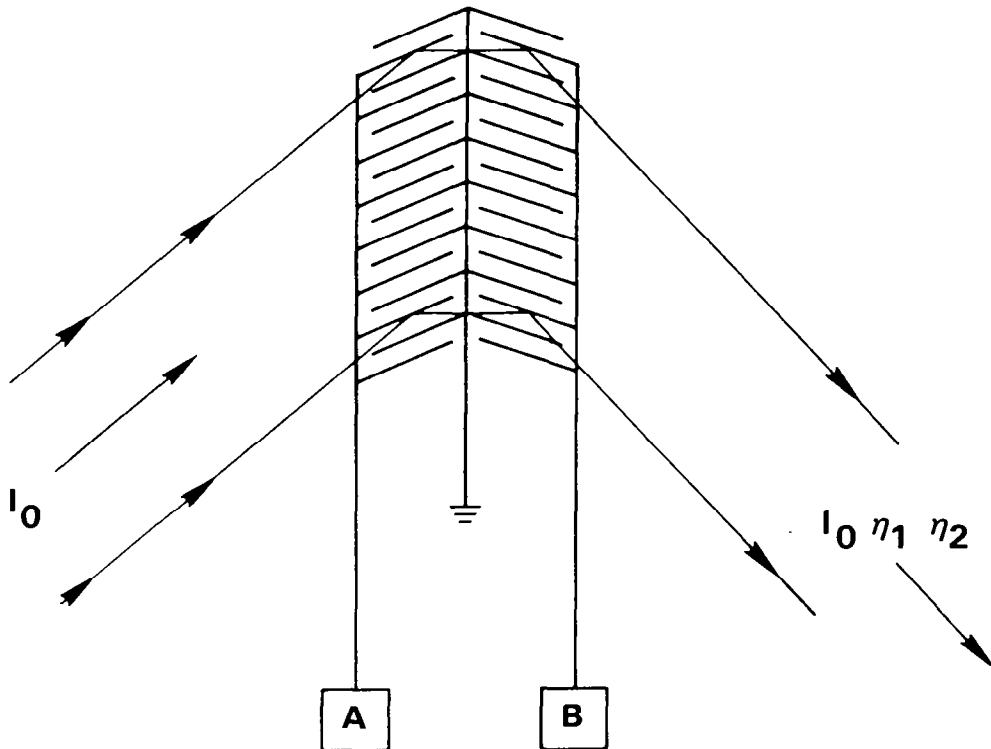
Figure 3.- Schematic of the herringbone electrode structure used for multiplication (or logical AND).

Figure 4.- Schematic of the use of a segmented herringbone to accomplish vector multiplication.
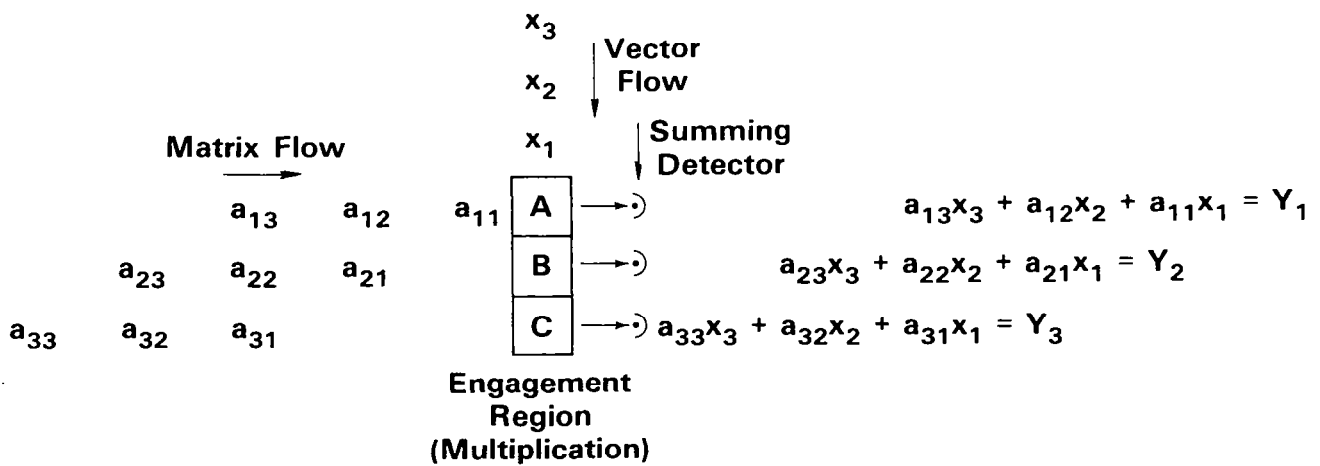
Figure 5.- Illustration of the engagement architecture for vector-matrix multiplication.
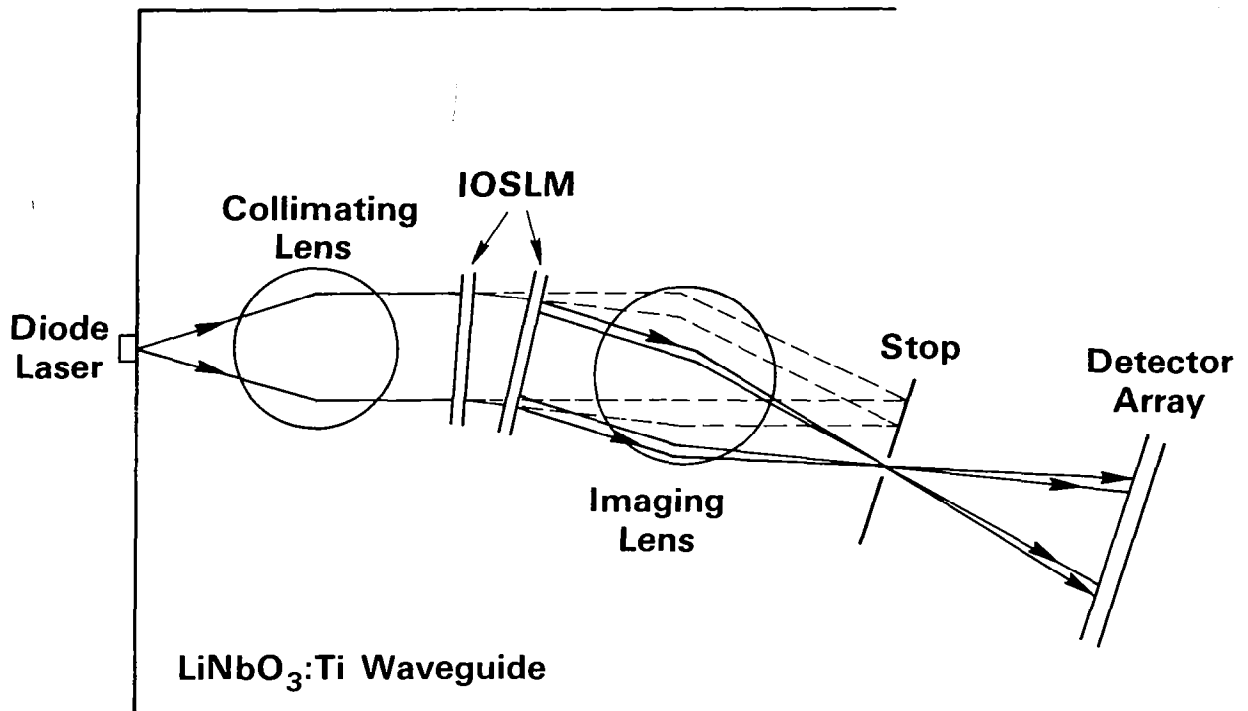
Figure 6.- Integrated-optical realization of the architecture of figure 5.
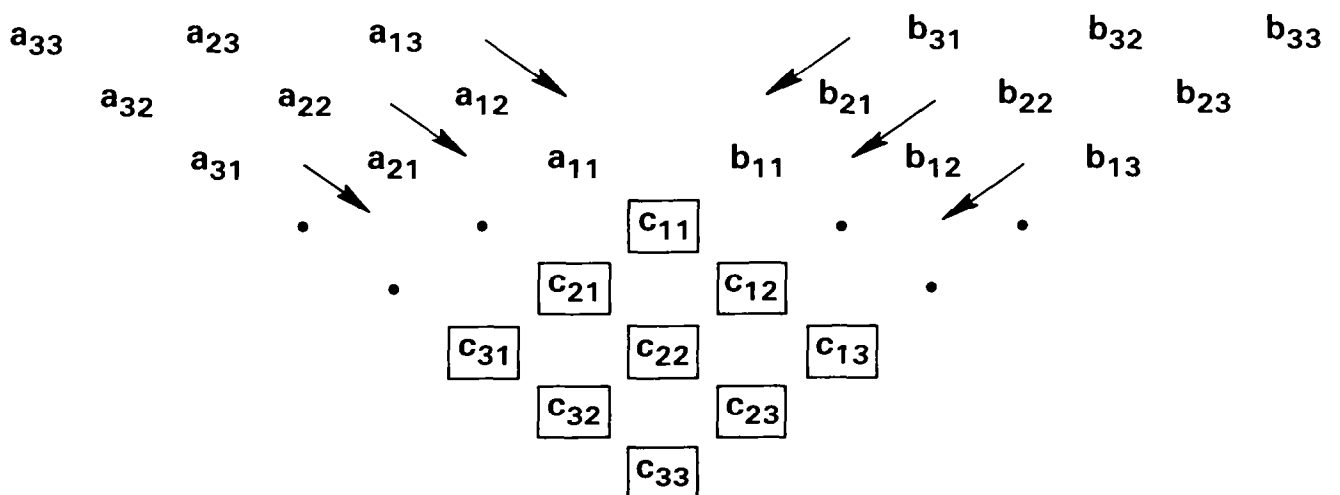
Figure 7.- Illustration of a systolic architecture for matrix-matrix multiplication.

Input Light

b_{33}

b_{23} b_{32}

b_{13} b_{22} b_{31}

a_{33} a_{23} a_{13} • b_{12} b_{21}

a_{32} a_{22} a_{12} • • b_{11}

a_{31} a_{21} a_{11}

Integrating
Detector

Grating
Beam
Splitters

c_{11}

c_{12}

c_{13}

c_{21}

c_{22}

c_{23}

c_{31}

c_{32}

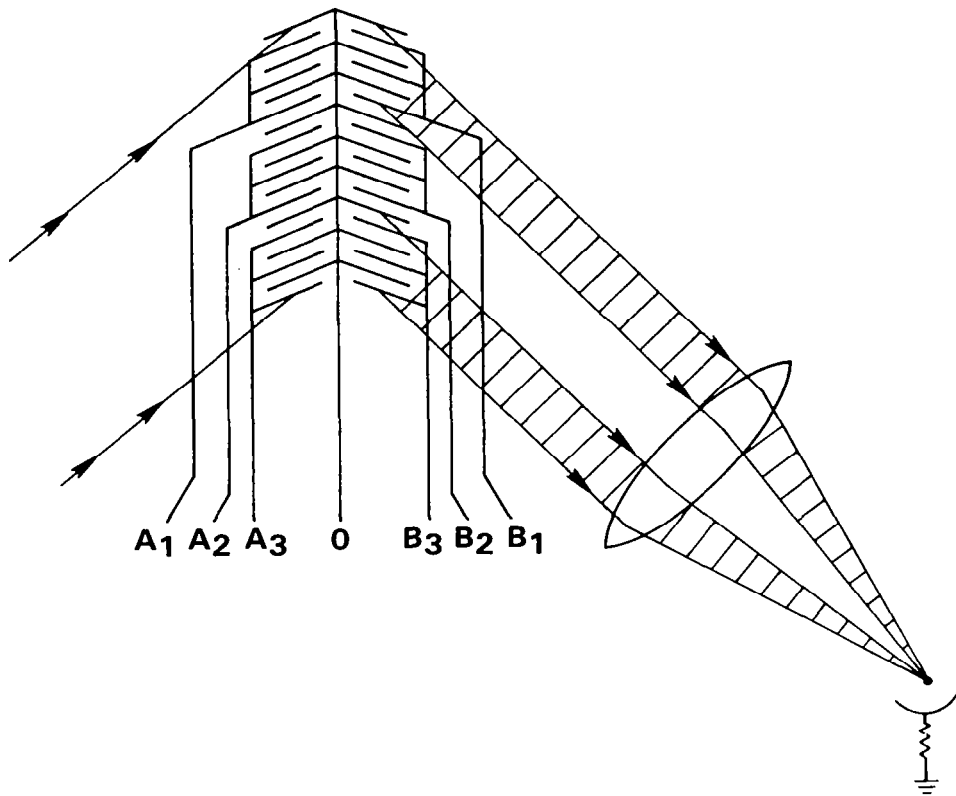c_{33}

Modulator
Unit
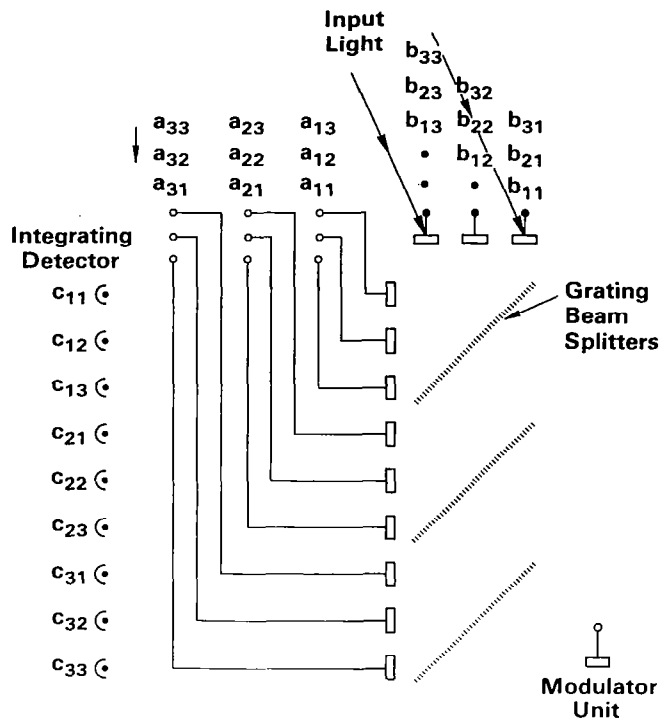
Figure 8.- Schematic layout for an integrated-optical
realization of the architecture of figure 7.

$\eta = 1$

$\eta = 0.5$

$\eta = 0.33$

LiNbO$_3$
Planar
Waveguide

M_{11}
M_{12}
M_{13}
M_{21}
M_{22}
M_{23}
M_{31}
M_{32}
M_{33}

P_1

P_2

P_3

V_3
V_2
V_1

Figure 9.- IOC for direct vector matrix multiplication. The IOSLM in the lower left
is illuminated by a uniform guided wave. This guided wave is modulated in pro-
portion to the vector components as shown. This information is then distributed
via beam splitters to the modulators that carry the matrix information. The
summation is performed optically, and the resultant light is imaged on the
appropriate photodetector.

SYSTOLIC TRIPLE-MATRIX PRODUCT CALCULATIONS

ON PARTITIONED MATRICES

H. J. Caulfield
Innovative Optics, Inc.
Concord, MA   01742

C. M. Verber
Battelle Columbus Laboratories
Columbus, OH   43201

R. L. Stermer
NASA Langley Research Center
Hampton, VA   23665

In order to handle arbitrary-sized matrices with fixed-sized optical matrix processors, it is necessary to expand or contract the problem to fit the processor. Here we examine this preprocessing, show a quite general method, and apply it to the type of triple-matrix product calculation needed for Kalman filtering. Emphasis will be placed on systolic-type processors.

The recent explosion of interest in optical matrix processors (refs. 1-6) needs not be reviewed here except to note that even with spatial light modulators with one-dimensional space-bandwidth products of 1000 or more, we may not be able to handle large matrices. Spatial dimensi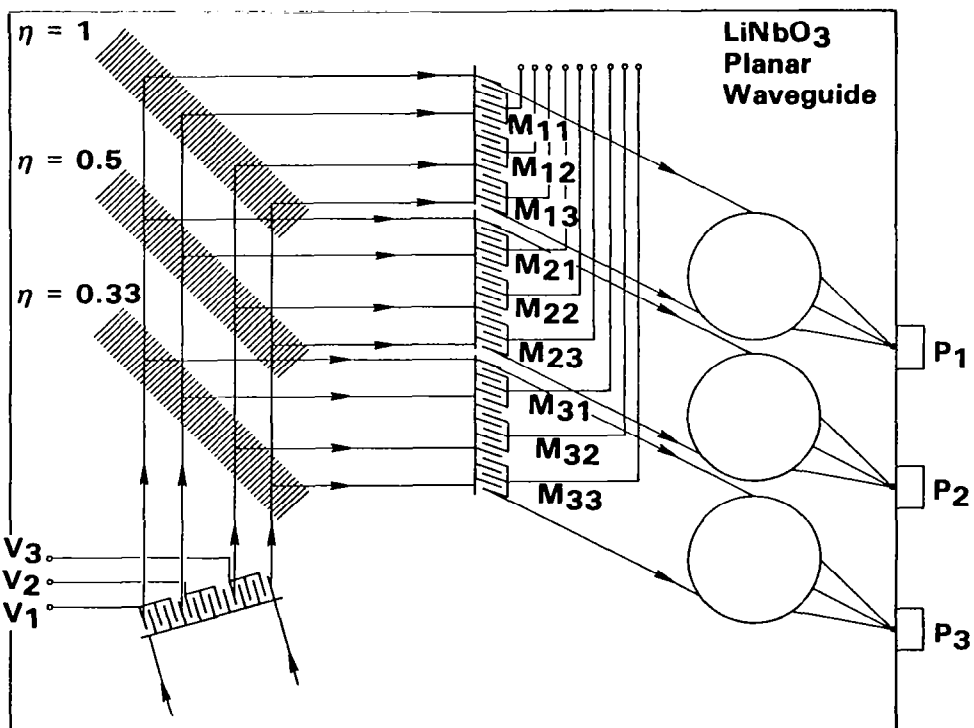onality is used to allow representation of real or complex numbers, to achieve high numerical accuracy through binary representation, and to allow floating-point calculations. As a result, we might find ourselves limited to working with relatively small matrices, say 20×20. Call this processor dimension D. The problem we discuss here is how to match real problems to such a restricted processor. In all that follows, we will illustrate with D = 2 processors.

The first step will be to expand the given matrix so that its dimensions are $mD \times nD$. To do this, we fill out the given matrix with zeros to the right and below. For D = 2 and the given matrices,

$$A = \begin{bmatrix} a_{11} & a_{12} & a_{13} \\ a_{21} & a_{22} & a_{23} \\ a_{31} & a_{32} & a_{33} \end{bmatrix}$$

and

$$B = \begin{bmatrix} b_{11} & b_{12} & b_{13} \\ b_{21} & b_{22} & b_{23} \\ b_{31} & b_{32} & b_{33} \end{bmatrix}$$

We expand to

$$A_E = \begin{bmatrix} a_{11} & a_{12} & a_{13} & 0 \\ a_{21} & a_{22} & a_{23} & 0 \\ a_{31} & a_{32} & a_{33} & 0 \\ 0 & 0 & 0 & 0 \end{bmatrix} = \left[\begin{array}{c|c} A & 0 \\ \hline 0 & 0 \end{array} \right]$$

and

$$B_E = \begin{bmatrix} b_{11} & b_{12} & b_{13} & 0 \\ b_{21} & b_{22} & b_{23} & 0 \\ b_{31} & b_{32} & b_{33} & 0 \\ 0 & 0 & 0 & 0 \end{bmatrix} = \left[\begin{array}{c|c} B & 0 \\ \hline 0 & 0 \end{array} \right]$$

It is easy to show

$$A_E B_E = \left[\begin{array}{c|c} AB & 0 \\ \hline 0 & 0 \end{array} \right]$$

We now partition A_E and B_E into $D \times D$ submatrices. That is

$$A_E = \left[\begin{array}{c|c} A_{11} & A_{12} \\ \hline A_{21} & A_{22} \end{array} \right]$$

and

$$B_E = \left[\begin{array}{c|c} B_{11} & B_{12} \\ \hline B_{21} & B_{22} \end{array} \right]$$

It is well known (ref. 7) that

$$A_E B_E = \left[\begin{array}{cc} A_{11}B_{11} + A_{12}B_{21} & A_{11}B_{12} + A_{12}B_{22} \\ A_{21}B_{11} + A_{22}B_{21} & A_{21}B_{12} + A_{22}B_{22} \end{array} \right]$$

Let us see how we can best order these calculations. Figure 1 shows an optical matrix processor and its supporting electronics. Clearly we need never do more than a $D \times D$ matrix at any time. One memory must store A_E and B_E. The partitioning electronics then selects out of the memory the needed submatrices.

Let A_E and B_E be of dimension $nD \times nD$. If we can afford n^2 parallel $D \times D$ processors, we can use some memory-efficient approach such as the engagement approach shown in figure 2. In many cases, this will be impractical. The other extreme case is that of only one $D \times D$ processor. In that case, we order A_E and B_E submatrices in such a way as to calculate one submatrix at a time of the product matrix so all integration occurs on the D^2 detectors. In our example, we calculate $A_{11}B_{11}$ first and then add to it on the same detectors $A_{12}B_{21}$.

One large and important type of matrix problem is the Kalman filter, a general and powerful estimation technique widely used in many areas such as automatic control (ref. 8). The Kalman filtering process is a recurring, interactive, ordered sequence of matrix inversions, additions, subtractions, and/or multiplications. The most difficult tasks are several triple matrix products of the form ABC. Let us now explore efficient ways of doing $A_E B_E C_E$ products.

In the case in which we can afford n^2 parallel processors, we finish calculating the 1,1 component of $A_E B_E$ just as we need it to multiply the 1,1 component of C_E in the 1,1 multiplier, etc. Thus, except for the time needed for electronic conversions, reformatting, and feedback (see figure 1), the calculation of $A_E B_E C_E$ takes only $3N-1$ single $D \times D$ multiplier clock times to evaluate rather than $2(2N-1)$ if $A_E B_E$ were calculated fully before we begin to calculate $A_E B_E C_E$.

To accomplish the $A_E B_E C_E$ calculation with all integration and memory taking place only at detectors, we need at least $n+1$ $D \times D$ multipliers. The method is easy to understand. First we calculate the 1,1 element of $A_E B_E$ on a single $D \times D$ computer. Then we broadcast it to the n computers that, in parallel, multiply it by the (1,1), (1,2), ..., (1,N) elements of C_E. Then we calculate the 1,2 element of $A_E B_E$, multiply it in parallel with the (2,1), (2,2), ..., (2,N) elements of C_E, and accumulate the sums on the detectors. Because the calculations are likely to be systolic or engagement types, we can (as before) keep all parts of the system busy at all times. That is, the 1,1 component of the 1,2 component of $A_E B_E$ will be available only one clock time after the D,D component of the 1,1 component of $A_E B_E$. Of course the n parallel processors are ready for each element from the single processor as they are calculated. To calculate all n^2 components of $A_E B_E$ takes $n^2 + n-1$ clock times. Only n clock times later, the whole matrix $A_E B_E C_E$ is calculated, so a total of $n^2 + 2n-1$ clock cycles is needed.

These considerations show that an expanding-partitioning-interleaving approach provides an efficient way to use $D \times D$ matrix multipliers to handle arbitrary-sized matrices. The illustration of the triple-matrix products so critical to Kalman filtering shows in some detail how the calculations can be done while using only the $D \times D$ detector arrays for scratch-pad operations (storage of intermediate results).

REFERENCES

1. Goodman, J. W.; Dias, A. R.; and Woody, L. M.: Opt. Lett. 2, 1 (January 1978).

2. Caulfield, H. J.; Dvore, D.; Goodman, J. W.; and Rhodes, W. T.: Appl. Opt. 20, 2263 (July 1981).

3. Casasent, D.; Appl. Opt. 21, 1859 (15 May 1982).

4. Casasent D.; Jackson, J.; and Neuman, C.: Appl. Opt. 22, 115 (1 January 1983).

5. Bocker, R. P.; Caulfield, H. J.; and Bromley, K.: Appl. Opt. 22, 804 (15 March 1983).

6. Athale, R. A. and Collins, W. C.: Appl. Opt. 21, 2089 (15 June 1982).

7. Lancaster, P.: Theory of Matrices. Academic Press, NY, 1969, p. 16 ff.

8. Kalman, R. E.; and Bucy, R. S.: J. Basic Eng. ASME Trans. 83D, 95 (March 1961).

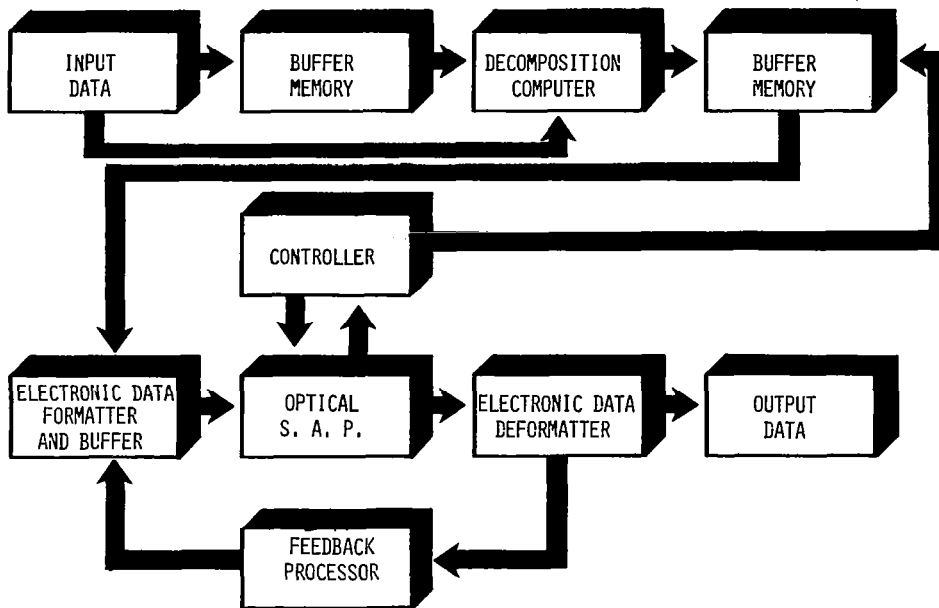Figure 1.- An optical computer will contain more electronics than optics. This figure indicates perfectly some of the functions the electronics must service.
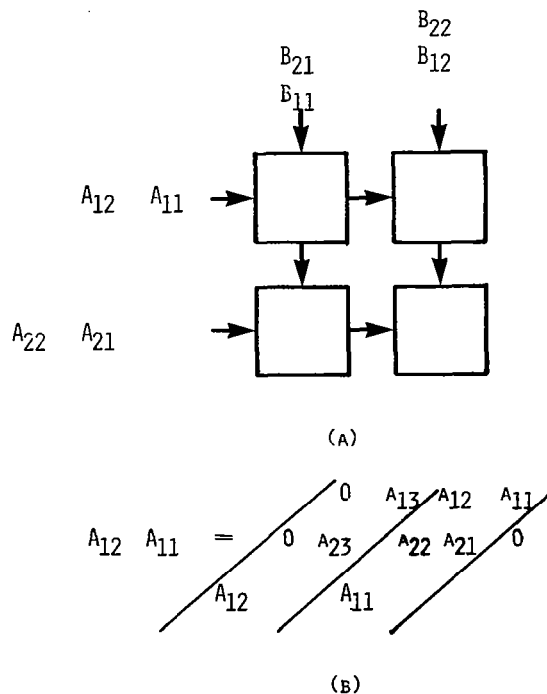

(A)

(B)

Figure 2.- Submatrices can be ordered in the same way as individual components for engagement processing (a). The notation above for the particular case illustrated in the text can be further broken down in terms of individual matrix components (b).

INTEGRATED OPTICAL SIGNAL PROCESSING WITH MAGNETOSTATIC WAVES

A. D. Fisher and John N. Lee
Naval Research Laboratory
Washington, D.C. 20375

ABSTRACT

Magneto-optical devices based on Bragg diffraction of light by magnetostatic waves (MSW's) offer the potential of large time-bandwidth optical signal processing at microwave frequencies of 1 to 20 GHz and higher. A thin-film integrated-optical configuration, with the interacting MSW and guided-optical wave both propagating in a common ferrite layer, is necessary to avoid shape-factor demagnetization effects. The underlying theory of the MSW-optical interaction is outlined, including the development of expressions for optical diffraction efficiency as a function of MSW power and other relevant parameters. Bragg diffraction of guided-optical waves by transversely-propagating magnetostatic waves and collinear TE↔TM mode conversion induced by MSW's have been demonstrated in yttrium iron garnet (YIG) thin films. Diffraction levels as large as 4% (7 mm interaction length) and a modulation dynamic range of ~30 dB have been observed. Potential signal processing applications are mentioned, including: spectrum analyzers, convolvers/correlators, deflectors, nonreciprocal optical isolators, and tunable narrowband optical filters. Advantages of these MSW-based devices over the analogous acousto-optical devices include: much greater operating frequencies, tunability of the MSW dispersion relation by varying either the rf frequency or the applied bias magnetic field, simple broad-band MSW transducer structures (e.g., a single stripline), and the potential for very high diffraction efficiencies.

INTRODUCTION

Optical techniques are being increasingly utilized to meet the ever-growing data rate requirements of signal processing and communications applications. A key element has been acousto-optic modulators,[1,2] which employ Bragg diffraction of light by acoustic waves to achieve large time-bandwidth (TBW) signal-processing products. Unfortunately, acoustic waves cannot be efficiently excited at frequencies beyond a few GHz due to material acoustic attenuation,[1] whereas a growing number of applications require operation up to 20 GHz and beyond. Other alternatives, such as direct modulation of semiconductor lasers and traveling-wave electro-optic modulators have not achieved these operating frequencies or been successfully configured into transverse, large TBW geometries. A new class of magneto-optic devices,[3,4] however, based on Bragg diffraction of light by magnetostatic waves (MSW), offers the potential of large time-bandwidth product modulation directly at signal frequencies of up to 20 GHz and beyond.

Interactions between optical beams and magnetostatic and magnetoelastic waves were first observed over a decade ago,[5-11] using bulk ferrite samples in the form of bars, rods, or slabs. Optical modulation by microwave signals in excess of 20 GHz had been reported in some of those early experiments,[7] However, no optical signal processing applications followed, because those bulk geometries suffer from large spatial variations in the MSW dispersion relation which are caused by internal magnetic field nonuniformities due to shape-factor demagnetization.[12]

A thin-film geometry, however, has a uniform internal field[12-14] which has spurred the development of high quality epitaxial yttrium iron garnet, $Y_3Fe_5O_{12}$ (YIG), thin films on gadolinium gallium garnet (GGG) substrates for bubble memory devices and electronic MSW delay-line filters.[15,16] The magneto-optic and IR transparency properties of these thin films have also been exploited to build integrated optical low-frequency modulators[17,18] and nonreciprocal isolators[19,20] utilizing optical Faraday rotation induced by an external magnetic field. These facts suggest the configuration illustrated in Fig. 1, in which an MSW is employed to diffract a guided-optical beam propagating in the same YIG thin film. The traveling refractive index grating, which is magneto-optically induced by the MSW, couples a diffracted optical beam into the polarization orthogonal to the input polarization.

Diffraction of a guided optical wave by an MSW is analogous to optical diffraction by a surface acoustic wave (SAW) and has the potential to significantly enhance a wide variety of integrated-optical applications which had previously been implemented with SAW's. These include: spectrum analyzers, convolvers/correlators, tunable narrowband optical filters, deflectors, and switches. Potential advantages of MSW optical devices, aside from operating at frequencies up to 20 GHz and beyond, include: very simple wide-band transducer structures (e.g., a single stripline), tunability of the MSW wavevector and group velocity at a fixed RF frequency by varying an external applied magnetic field, and the potential for very high diffraction efficiencies.

THEORY OF MSW GUIDED-OPTICAL WAVE INTERACTION

An MSW is a microwave electromagnetic wave which propagates in a ferrite biased by an external magnetic field. As such, the MSW is described by Maxwell's equations with a permeability tensor $\bar{\bar{\mu}}$ which can be derived[14] from the gyromagnetic equation of motion $\partial \bar{M}/\partial t = \gamma(\bar{H} \times \bar{M})$ and the relations $\bar{m} = \bar{\bar{\chi}}\bar{h}$ and $\bar{\bar{\mu}} = \mu_0(\bar{\bar{I}} + \bar{\bar{\chi}})$. Here $\bar{M} = \bar{M}_0 + \bar{m}$ is the intrinsic magnetization of the ferrite with $\bar{m}$ and $\bar{M}_0$ as RF and DC components, respectively. $\bar{H} = \bar{H}_0 + \bar{h}$ is the magnetic field in the ferrite expressed as the sum of an RF component, $\bar{h}$, and an applied DC field, $\bar{H}_0$. The saturation magnetization of YIG is $4\pi|\bar{M}| = 1750$ Gauss and its gyromagnetic ratio, γ, is 2.8 MHz/Oe.

Solving Maxwell's equations with the thin-film boundary conditions results in solutions for the RF fields and for the dispersion relation, i.e., the MSW wave vector magnitude $k_m \equiv |\bar{k}_m|$ as a function of the microwave frequency, Ω. Four types of solutions are found[13,16,21] depending on the direction of the magnetic bias field relative to $\bar{k}_m$ and the thin-film surface normal $\hat{n}$, as illustrated in the lower section of Fig. 1. There are two dielectric waveguide-like waves called forward volume waves (FVW) and backward volume waves (BVW, with negative group velocity), and two types of magnetostatic surface waves (MSSW). The MSSW decay in intensity away from the YIG surfaces and are distinguished by the parameter $s = \pm 1$, where $\bar{k}_m$ is in the direction $s(\bar{H}_0 \times \hat{n})$. The MSW is usually excited by a single stripline antenna, which can either be deposited directly on the YIG as in Fig. 1 or be a microstrip circuit on a grounded alumina substrate contacted to the YIG.[3,4] The MSW field solutions generally correspond to a traveling circular or elliptical precession of $\bar{M}$ about the bias field direction $\bar{H}_0$. Most practical applications are characterized by an MSW wavelength much shorter than that of the RF field external to the ferrite, i.e., $2\pi/k_m \ll \Omega/c$. The RF exciting fields thus appear uniform to the MSW, which then obeys Maxwell's equations in the quasistatic limit ($\dot{D}=0$); hence the name magnetostatic wave. The dispersion relations reveal that k_m ranges from zero to infinity as the rf frequency Ω varies over the bounded range $\gamma[H_0(H_0+4\pi M)]^{1/2} < \Omega < \gamma(H_0+4\pi M)$ for MSSW and

$\gamma H_O < \Omega < \gamma[H_O(H_O+4\pi M)]^{1/2}$ for FVW and BVW. For example, with $H_O=4\pi M$ (1750 Gauss for YIG) the FVW and BVW limits are 4.90-6.93 GHz and the MSSW limits are 6.93-9.80 GHz.

As a specific example, with $\bar{H}_O$ applied along $\hat{z}$ in Fig. 1, the s=+1 MSSW is excited and the RF $\bar{h}$ field in the YIG thin film can be written as[22] $\bar{h} = h_x\,\hat{x} + h_y\,\hat{y} + h_z\,\hat{z}$, where

$$h_x = H_t\,\frac{a_1 a_2}{a_2-a_1}\left(\frac{e^{-k_m x}}{a_1} - \frac{e^{k_m y}}{a_2}\right)e^{-i(\Omega t - k_m sy)} \qquad (1a)$$

$$h_y = ish_x \qquad (1b)$$

and

$$h_z = 0 \qquad (1c)$$

Here $a_1 = 2 + \gamma 4\pi M/(s\Omega + \gamma H_O)$, $a_2 = \gamma 4\pi M/(s\Omega - \gamma H_O)$, and $0 < x < d$ corresponds to the YIG layer. Since very thin YIG films ($d < 15$ μm) are generally employed, $k_m d \ll 1$ is a valid approximation and Eq.(1a) becomes

$$h_x = H_t\,\exp(-i(\Omega t - k_m sy)) \qquad (1d)$$

According to Eq. (1b), $\bar{h}$ is a circular precession about $\bar{H}_O$. H_t is directly proportional to the rf power and defines the precession angle θ_h of the magnetic field, i.e., $\sin\theta_h = H_t/H \simeq H_t/H_O$. Figure 2a shows part of the dispersion relation for this MSSW. The corresponding propagation delay ($\tau_g = (y/2\pi)\partial k_m/\partial\Omega$) and the radiation resistance R_m of the stripline antenna employed to excite the MSW are shown as a function of frequency in Fig. 2b. MSW delays greater than 500 nsec/cm can be obtained. With wide striplines, e.g., $b > 0.1$mm, the radiation impedance, $Z_m = R_m + iX_m$, often restricts the effective MSW bandwidth.[21,22] Curves similar to Fig. 2b, in conjunction with the measured level and delay of the power coupled out from the MSW (e.g., at another transducer placed at B in Fig. 1) are useful for experimentally tuning k_m of the MSW.

The optical refractive index changes due to the magneto-optic effect in a ferrite are a function of the magnetization vector $\bar{M}$. Using $\bar{m} = \bar{\bar{\chi}}\bar{h}$ with $\bar{h}$ given by Eqs. (1), $\bar{M}$ can be written as $\bar{M} = M_O\hat{z} + m_y\hat{y} + m_x\hat{x}$, and the real part of the RF components are:

$$m'_x = M_t\cos(\Omega t - k_m sy) \qquad (2a)$$

$$m'_y = M_t\,\sin(\Omega t - k_m sy) \qquad (2b)$$

and

$$M_t = -\frac{\gamma M}{s\Omega - \gamma H}\,H_t = M\sin\theta_m \qquad (2c)$$

Here θ_m is the precession angle of $\vec{M}$. The corresponding <u>optical</u> permittivity tensor $\bar{\bar{\varepsilon}}$ has terms which are linear and quadratic in M:[11,23]

$$\bar{\bar{\varepsilon}}(t)= \varepsilon_0 \begin{pmatrix} \varepsilon & ifM_0 & -ifm'_y \\ -ifM_0 & \varepsilon & ifm'_x \\ ifm'_y & -ifm'_x & \varepsilon \end{pmatrix} + \frac{\varepsilon_0}{M^2} \begin{pmatrix} g_{12}M_0^2 & 0 & g_{44}M_0 m'_x \\ 0 & g_{12}M_0^2 & g_{44}M_0 m'_y \\ g_{44}M_0 m'_x & g_{44}M_0 m'_y & g_{11}M_0^2 \end{pmatrix} \quad (3)$$

In these expressions, an isotropic ferrite is assumed and second order RF terms in m'_x, m'_y are neglected. The linear coefficient f can be expressed in terms of the material Faraday rotation ϕ_F; i.e., $f \simeq 2\sqrt{\varepsilon}\,\phi_F/k_0 M$, where $k_0\sqrt{\varepsilon} = k_{opt}$ is the optical wavenumber $(k_0=\omega/c)$. For YIG, $\phi_F \simeq 280^\circ/\text{cm}$ at 1.15 μm[18]. In the approximate calculations which follow, the quadratic magneto-optic coefficients, g_{ij}, are assumed to be small enough that the second term in Eq.(3) can be neglected.

In general, the component of the RF magnetization $\bar{m}$ along the direction of optical propagation results in a traveling refractive index grating which can diffract between orthogonally polarized optical modes. For example, the ε_{13} and ε_{31} optical permittivity elements in Eq. (3) will induce coupling between the TE and TM waveguide modes of an optical wave with a component of travel $(\bar{k}_{opt})$ along the $\pm \hat{y}$ direction in Fig. 1. Since $\bar{\bar{M}}$ is in approximately circular precession about the bias field direction $\bar{H}_0$, there is very little RF magnetization $\bar{m}$ along $\bar{H}_0$. Hence, essentially no diffraction is expected when the direction of optical propagation is along $\bar{H}_0$; any diffraction is of second order in $\bar{m}$ and very weak, arising from quadratic g_{44} terms in ε or any ellipticity of the $\bar{\bar{M}}$ precession. Examination of the bias field directions in Fig. 1 reveals that a FVW or BVW is preferable for transverse diffraction with $\bar{k}_{opt}$ along $\pm \hat{z}$ in Fig 1, which is perpendicular to the direction of MSW propagation, $\bar{k}_m$. An MSSW is better suited for a collinear geometry with $\bar{k}_{opt}$ along $\pm \hat{y}$ in Fig. 1, which is co/contradirectional with $\bar{k}_m$.

A simple expression for the growth of diffracted mode intensity I_d with interaction length L is obtained for the special case of collinear interaction; using coupled mode theory:[24]

$$\frac{I_d}{I_o} = \frac{4\kappa^2}{4\kappa^2+\Delta\beta^2} \; \sin^2\left[\frac{1}{2} L \sqrt{4\kappa^2+\Delta\beta^2}\right] \tag{4a}$$

where

$$\kappa = \frac{|\varepsilon_{31}| \, k_o \sqrt{\varepsilon}}{2\varepsilon_o\varepsilon} \simeq s\phi_F \frac{\gamma H_o}{s\Omega-\gamma H_o} \sqrt{\frac{2 \, k_m c P_M}{Z_o\Omega}} \left|\frac{s\Omega-\gamma H_o}{s\Omega-\gamma H_o-4\pi M\gamma}\right| \tag{4b}$$

and $\Delta\beta=\beta_E-\beta_M-k_m$ with β_E and β_M are the wavenumbers of the coupled optical modes. Here P_m is the MSW power density (w/m^2) in the YIG; $Z_o = 377$ ohms; and diffraction between orthogonal polarization of the same m-number optical waveguide modes, which are far from cutoff, is assumed.

Similar expressions describe the general case of transverse diffraction at an arbitrary Bragg angle.[25] In order for efficient coupling to occur, $\bar{k}_m$ must result in phase matching between the coupled modes, i.e. $\bar{k}_m = \bar{\beta}_E - \bar{\beta}_m$, which corresponds to satisfaction of the Bragg condition. This is termed "anisotropic Bragg diffraction,"[26] because the magnitudes of the incident and diffracted wavevectors differ, i.e., $\beta_E \neq \beta_M$. As Fig. 3 illustrates, the behavior of the incident and diffracted angles is significantly different from the more familiar isotropic case. An input Bragg angle of $\theta_i=0$ occurs when $k_m = \sqrt{2k_o\sqrt{\varepsilon}}(\beta_E-\beta_M) \equiv k_{mo}$ with TM→TE conversion; and $\theta_i=0$ does not occur for TE→TM conversion. Instead of the isotropic case of deflection about the axis perpendicular to $\bar{k}_m$, the diffracted optical beam undergoes negligible deflection when $k_m<k_{mo}$. When desirable, large deflections can be obtained by operating with $k_m>k_{mo}$. In one-dimensional transverse spatial modulator applications, e.g. Fig. 1, the MSW-diffracted beam is easily separated from the input zero-order beam by virtue of its orthogonal polarization.

In analogy with acousto-optic interactions, the diffracted optical wavefront is amplitude modulated by the driving signal level as well as frequency shifted. The optical frequency of the diffracted beam is $\omega_d = \omega + \Omega$ when $\bar{k}_d = \bar{k}_i + \bar{k}_m$ holds or $\omega_d = \omega - \Omega$ for $\bar{k}_d = \bar{k}_i - \bar{k}_m$. For small κ the phase matching bandwidth to the first null is determined by the interaction length L; i.e., $\Delta k_m = \pm 2\pi/L$. The phase matching envelope of Eq. (4a) is sketched on the right side of Fig. 2a for conversion between the TE and TM modes for $m = 5$.

With increasing RF power the coupling coefficient κ becomes limited by MSW saturation, which occurs when the precession angle θ_m reaches a few degrees. For example $\theta_m = 2^\circ$ corresponds to a maximum coupling coefficient of 17 m^{-1} in Eq. (4b), or an interaction length of $\pi/2\kappa = 9.2$ cm for 100% conversion. Over a practical interaction length of a few cm, the maximum conversion is approximately $(\kappa L)^2$, e.g. 12% for $L = 2$ cm.

Ferrite material properties impact the performance of these MSW guided-optical devices in a variety of ways. The dependence of diffraction efficiency on ϕ_F, γ, and M is evident in Eqs. (4). The Faraday rotation ϕ_F of YIG can be significantly increased by doping it with various impurities such as Pb or Bi (e.g., $BiY_2Fe_5O_{12}$ has

$\phi_F = 20600°/cm$ at 295°K and $\lambda=0.633$ μm,[27] which decreases with increasing wavelength to $\phi_F = 2600°/cm$ at 1.15 μm[28]). The optical attenuation α in the thin film will adversely affect diffraction efficiency if it exceeds about 1 cm^{-1}. YIG has a transparency window for λ between 1.1 μm and 5 μm, where a < 1 cm^{-1} can be obtained for low-order guided-optical modes (e.g., m < 6). Absorption of the magnetostatic wave can be serious if the ferrite film is not of sufficient quality as indicated by the ferromagnetic resonance linewidth, ΔH. The MSW absorption is approximately 76.4ΔH dB per μsec of propagation delay[14] and epitaxial YIG films with ΔH < 0.3 Oe (for Ω < 10 GHz) can be obtained.[14]

EXPERIMENTAL DEMONSTRATIONS

Bragg diffraction of guided-optical waves by magnetostatic waves has been demonstrated[3,4] in both the transverse one-dimensional modulator configuration of Fig. 1 and a collinear geometry. Both $TE_m \rightarrow TM_m$ and $TM_m \rightarrow TE_m$ conversion were observed for optical modes in the range of m = 1 through 5 at the 1.15 μm HeNe laser wavelength. Light diffraction levels as high as 4% were obtained, with a 7mm interaction length and an MSW approaching saturation. Below saturation, the linear dynamic range was ~ 30 dB and the diffraction efficiency was ~ 5%/RF-watt (over 1 cm, with an RF-to-MSW insertion loss of ~ 15 dB). With impedance matching networks and Bi doped YIG, diffraction efficiencies approaching 100% over one cm for only 10 mW of RF power may be achievable. So far, diffraction has been demonstrated over a frequency range of 1 to 6.5 GHz, (which was the full range of the microwave oscillator employed).

Figure 4 shows the angular deflection produced by anisotropic Bragg diffraction in the transverse geometry of Fig. 1. A FVW magnetostatic wave was employed, with the magnetic field H_0 applied approximately normal to the YIG film plane. The upper trace of Fig. 5 was made by scanning a pinhole photodetector across a weak mode-converted beam, caused by DC Faraday rotation induced by a small component of H_0 applied along the direction of optical propagation. By chopping the RF feed to the MSW and using a lock-in amplifier, the profile of the MSW-diffracted beam was simultaneously displayed on the lower trace. Initial positive results have also been obtained from a time-integrating correlator configuration, in which the signal modulating the MSW was correlated with information placed on the input beam by an acousto-optic modulator.

Figure 5 depicts the diffracted beam intensity for collinear $TM_5 \rightarrow TE_5$ mode conversion as a function of the RF frequency Ω, with fixed H_0. The sinc sidelobe structure predicted by Eq. (4a) is evident. The peak to first null width is about 15 MHz. This agrees with the theoretical width predicted by the dispersion relation for $\Delta k_m = 2\pi/L = 898$ m^{-1} (L = 7 mm).

APPLICATIONS

Bragg diffraction of guided-optical waves by magnetostatic waves provides a basis for constructing a variety of enhanced integrated optical signal processing devices. Applications of the transverse diffraction geometry include: optical point modulators operating at 20 GHz or higher, one-dimensional spatial light modulators, spectrum analyzers, convolvers/correlators, deflectors, and switches. The codirectional geometry is potentially useful for narrowband tunable optical filters, convolvers/correlators, magnetometers, and nonreciprocal optical isolators.

Some integrated optical applications of the transverse geometry, which are currently under investigation, are illustrated by Fig. 6. In the spectrum analyzer application the light from a laser diode is collimated by the lens L_1 and amplitude

254

modulated by the MSW signal $f_2(t-y/v_g)$, where v_g is the MSW group velocity. The second lens is positioned with d_2 equal to one focal length f, so that it produces the Fourier transform of $f_2(y)$ at the detector, which then images an intensity proportional to the square of the magnitude of the Fourier transform of $f_2(y)$ (f_1=constant and there is no g(y) spatial filter in Fig. 6). Luneburg or geodesic lenses[1] are being considered for implementing the two YIG thin-film integrated-optical lenses.

In the time-integrating correlator application, the laser diode is modulated by $f_1(t)$. The collimated beam following lens L_1 is then modulated by $f_2(t-y/v_g)$ and imaged onto the detector array (with $1/d_1 + 1/d_2 = 1/f$). In a suitably designed system[1], the detector elements, which integrate their incident intensity for a time T, produce a signal term in O(y) proportional to the correlation

$$\int_0^T f_1(t)f_2(t-y/v_g)dt \tag{5}$$

A space-integrating convolver or correlator can be implemented by modulating the collimated beam by the product of the MSW signal $f_2(t-y/v_g)$ and the spatial filter g(y). Potential means for implementing g(y) include: overlays deposited on the YIG film, an array of meander-line Faraday magneto-optical modulators,[18] or another MSW propagating in the opposite direction. Lens L_2, with $d_2 = f$, performs a spatial integration onto the central detector element, which, in a suitably designed system,[1] produces a signal in $O_0(t)$ proportional to the convolution

$$\int_0^L g(y)f_2(t-y/Vg)dy \tag{6}$$

Convolution and correlation can also be performed in a collinear configuration by employing double diffraction from two counterpropagating MSW signals (e.g., one MSW converts TE_0 to TM_1 and the other TM_1 to TE_2). The collinear geometry can also function as a tunable narrowband optical filter[1] by exploiting the variation of $\beta_{TE}-\beta_{TM}$ with optical wavelength in conjunction with the strong dependence of mode conversion on phase mismatch, $\Delta\beta$, as seen in Eq. (4a). The optical center frequency is proportional to the MSW wavevector magnitude k_m and can be tuned by varying either the RF frequency or the magnetic bias field. Another potential application of the collinear configuration is as a sensitive magnetometer by utilizing the dependence of k_m, and hence phase mismatch $\Delta\beta$, on the external bias field. A field resolution of better than 10^{-4} Oe may be possible.[25] An optical isolator can be constructed by exploiting the nonreciprocal nature of mode conversion induced by Faraday rotation.[19,20]

MSW integrated optical devices can directly process signals with center frequencies of 20 GHz or higher. Their bandwidth, however, is significantly less, being limited by, first, the Bragg phase-matching condition, secondly , the passband of the MSW exciting antenna, and finally, the intrinsic MSW limits for a given bias field H_0. The Bragg-limited bandwidth can be broadened by employing multiple or phased-array transducer structures similar to those used for SAW acousto-optic modulators.[1,2] The passband of the MSW antenna radiation impedance can be increased by using impedance matching networks, thin stripline antennas, and thick YIG films.[22] It may be possible to broaden the intrinsic MSW limits by employing properly designed H

field gradients. For example, an increase of $H\hat{x}$ along $-\hat{z}$, from H_1 to H_2 in Fig. 6, may be able to alleviate both the MSW and Bragg limitations. The MSW dispersion relation, frequency limits, and radiation impedance all shift to higher frequency with increasing H, which causes signal components at higher frequency to be launched further down the stripline where H is larger. The position of the MSW traversal of the collimated beam in Fig. 6 thus shifts to the right, but k_m can be held near its optimal Bragg value by using the shift of the MSW dispersion relation with field to counteract the increase in frequency. Using such techniques as multiple YIG-film layers, ground planes, and H field gradients, purely electronic MSW signal processing devices with a 1 GHz bandwidth and a time-bandwidth product of 230 have been reported.[15,16]

CONCLUSIONS

The MSW guided-optical interactions discussed here are expected to lead to a variety of high-performance integrated optical signal processing devices. These MSW-optical devices are currently in an early stage of development, with their basic feasibility having been demonstrated. Unlike high-frequency acousto-optical signal processors, an MSW-based optical system can operate directly at frequencies up to 20 GHz and beyond, and hence does not require signal-frequency downshifting with the attendant complexity of local oscillators, filters, and multiplexers. MSW transducers are also generally much more compact, reliable, and easier to fabricate than SAW transducers; and MSW-optical devices show promise of requiring less drive power, since diffraction efficiencies approaching 10^4 %/watt/cm may be realizable. These MSW-based optical devices not only improve upon SAW integrated optical devices, but also offer new capabilties such as nonreciprocal optical isolation, extension of the Bragg bandwidth by applying a spatial gradient in the applied magnetic field, or scanning a single ~ 1 GHz bandwidth device over a >20 GHz band by adjusting the applied magnetic field.

REFERENCES

1. N. J. Berg and John N. Lee, <u>Acousto-Optic Signal Processing Theory and Implementation</u> (Marcel Dekker Inc., New York, 1983).

2. C. S. Tsai, "Guided-wave acoustooptic Bragg modulators for wide-band integrated optic communications and signal processing", IEEE Trans on Circuits and Systems, CAS-26, 1076 (1979).

3. A. D. Fisher, John N. Lee, E. S. Gaynor and A. B. Tveten, "Optical guided-wave interactions with magnetostatic waves at microwave frequencies", Appl. Phys. Lett. 41, 779 (1982).

4. A. D. Fisher, John N. Lee, E. S. Gaynor and A. B. Tveten, Diffraction of guided-optical waves in magnetostatic wave delay lines", Proc. 1982 IEEE Ultrasonics Symp., 541 (1982).

5. L. K. Anderson, "Observation of optical interaction with ferrimagnetic resonance", Appl. Phys. Lett. 1, 44 (1962).

6. J. F. Dillon and J. P. Remeika, "Visual observations of magnetostatic modes", Applied Phys. Lett. 2., 38 (1963).

7. J. T. Hanlon and J. F. Dillon, "Microwave modulation of light in ferromagnetic resonance", J. Appl. Phys. 36, 1269 (1965).

8. R. W. Dixon, "Photoelastic properties of selected materials and their relevance for applications to acoustic light modulators and scanners", J. Appl. Phys. 38, 5149 (1967).

9. J. H. Collins and D. A. Wilson, "Optical probing of magnetostatic modes in YIG delay lines", Appl. Phys. Lett. 12, 331 (1968).

10. A. W. Smith, "Diffraction of light by magnetoelastic waves", IEEE Trans. Sonics and Ultrasonics SU-15, 161 (1968).

11. H. L. Hu and F. R. Morganthaler, "Strong infrared-light scattering from coherent spin waves in YIG", Appl. Phys. Lett. 18, 307 (1971).

12. B. A. Auld, "Magnetostatic and magnetoelastic wave propagation in solids", <u>Applied Solid State Science</u>, Vol. 2, p. 2 (Academic Press, New York, 1981).

13. R. W. Damon and J. R. Eshbach, "Magnetostatic modes of a ferromagnet slab", J. Phys. Chem. Solids. 19, 308 (1961).

14. C. Vittoria and N. D. Wilsey, "Magnetostatic wave propagation losses in an anisotropic insulator", J. Appl. Phys. 45, 414 (1974).

15. J. D. Adam, T. W. O'Keeffe, and Michael R. Daniel, "Magnetostatic wave devices for microwave signal processing", Proc. SPIE 241, 96 (1980).

16. J. M. Owens, L. Carter, C. V. Smith and J. H. Collins, "Magnetostatic waves, microwave SAW?", Proc. 1980 IEEE Ultrasonics Symp., 512 (1980).

17. S. F. Sauter, M. M. Hanson, and D. L. Fleming, "Multifunction integrated-optic device using magnetically alterable phase gratings", Appl. Phys. Lett. 30, 11 (1977).

18. P. K. Tien, R. S. Martin, R. Wolfe, R. C. LeCraw, and S. L. Blank, "Switching and modulation of light in magneto-optic waveguides of garnet films", Appl. Phys. Lett. 21, 394 (1972).

19. S. T. Kirsch, W. A. Biolsi, S. L. Blank, P. K. Tien, R. J. Martin, P. M. Bridenbaugh, and P. Grabbe, "Semileaky thin film optical isolator", J. Appl. Phys. 52 3190 (1981).

20. A. Shibukawa and M. Kobayashi, "Optical TE-TM mode conversion in double epitaxial garnet waveguides", Appl. Opt. 20, 2444 (1981).

21. P. R. Emtage, "Interactions of magnetostatic waves with a current", J. Appl. Phys. 49, 4475, (1978).

22. A. K. Ganguly and D. C. Webb, "Microstrip excitation of magnetostatic surface waves", IEEE Trans. Microwave Th. and Tech. MTT-23, 998 (1975).

23. L. D. Landau and E. M. Lifshitz, Electrodynamics of Continuous Media (Addison-Wesley, Reading, Mass, 1960).

24. A. Yariv, "Coupled mode theory for guided-wave optics", IEEE J. Quan. Elec. QE-9, 919 (1973).

25. A. D. Fisher, E. S. Gaynor, and John N. Lee, "Magnetostatic wave devices for integrated-optical signal processing", Proc. 1983 IEEE Ultrasonics Symp., (1983).

26. R. W. Dixon, "Acoustic diffraction of light in anisotropic crystals", IEEE J. Quan. Elec. QE-3, 85 (1967).

27. P. Hansen, K. Witter, and W. Tolksdorf, "Magnetic and magneto-optic properties of lead- and bismuth- substituted yttrium iron garnet films", Phys. Rev. B., 27, 6608 (1983).

28. D. E. Lacklison, G. B. Scott, H. I. Ralph, and J. L. Page, "Garnets with high magnetooptic figures of merit in the visible region", IEEE Trans. on Magnetics MAG-9, 457 (1973).
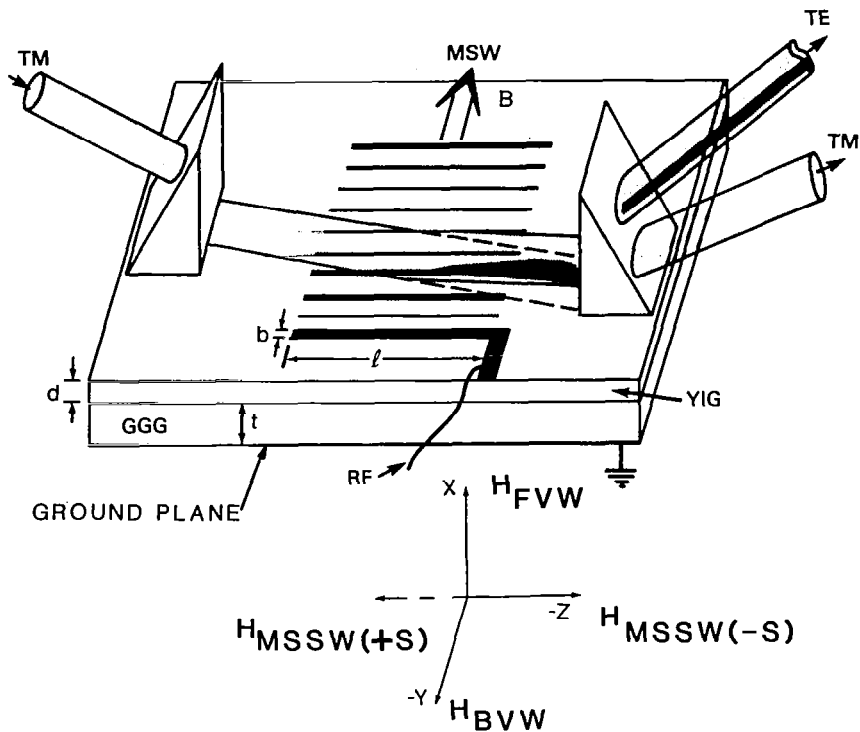
Figure 1.- Bragg diffraction of guided-optical wave by MSW. d = 11.7 μm; t = 0.635 mm; ℓ = 15 mm; and H_o = 0.5(4πM) = 875 Oe.
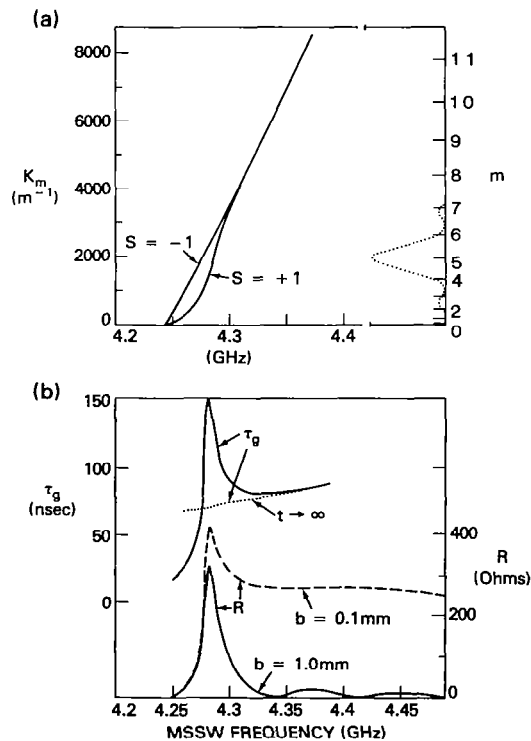

Figure 2.- Theoretical MSSW behavior versus frequency. (a) Dispersion relation for s = ± 1. Dotted curve is phase matching envelope for m = 6. (b) Radiation resistance (R = R_m ℓ/2) and group delay versus frequency. t→∞ corresponds to no metallic ground plane. R is shown for two values of stripline width, b.
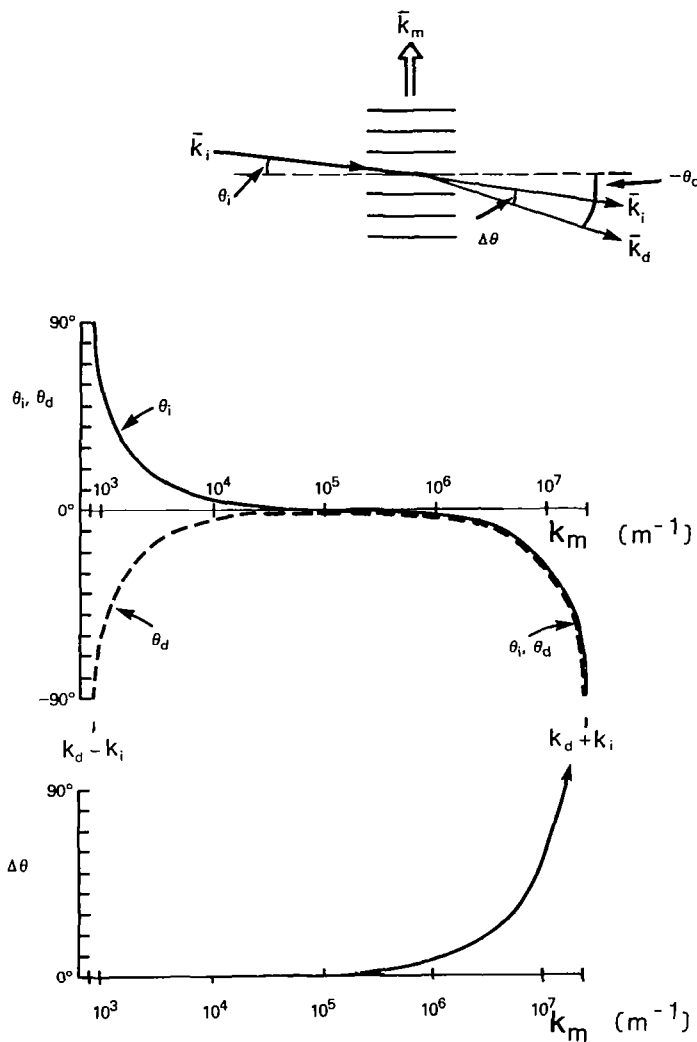
Figure 3.- Diffraction angles versus MSW wave vector $\bar{k}_m$ for anisotropic Bragg diffraction.
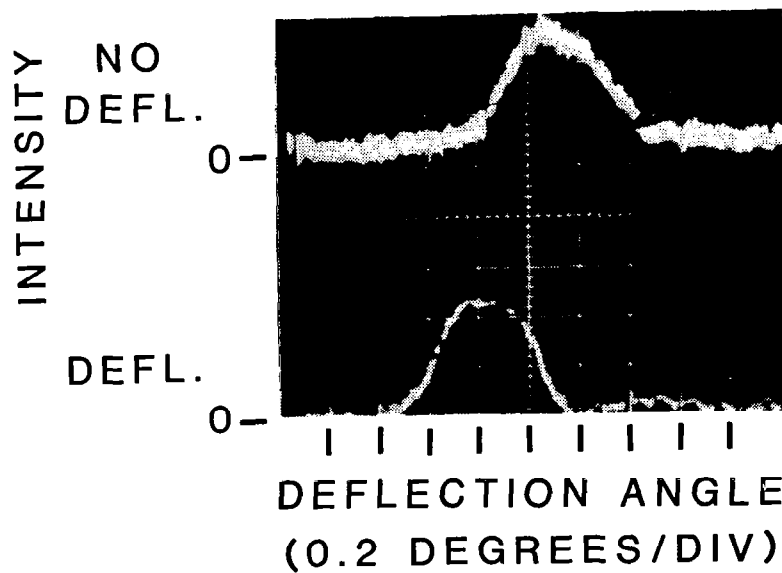

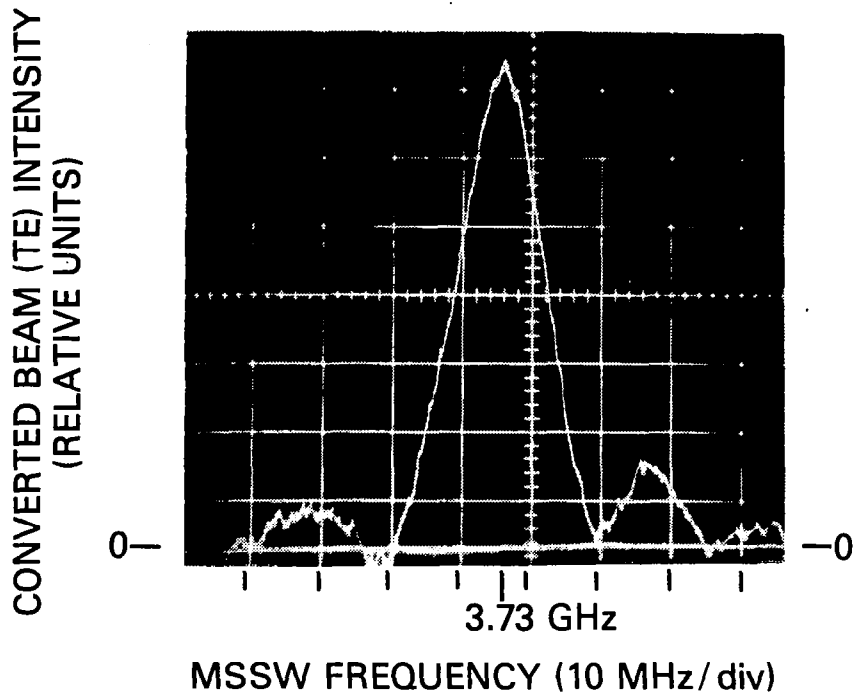Figure 4.- Beam deflection in transverse Bragg diffraction geometry $(\theta_i = 0.5)$.

Figure 5.- Diffraction intensity as function of MSSW frequency for co-directional TM →TE$_4$ coupling. H$_o$=660 Oe; geometrical dimensions same as in Figure 1.
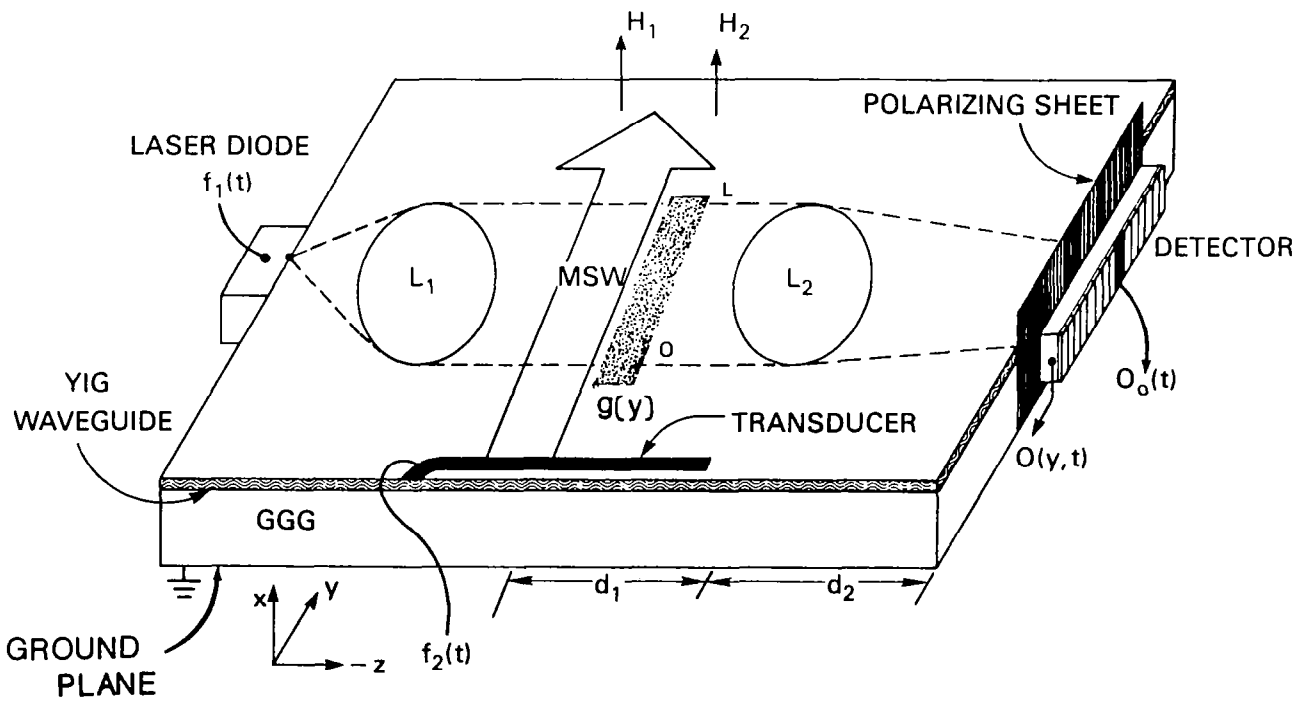

Figure 6.- An integrated-optical configuration for signal processing with magnetostatic waves.

Gregory Adamovsky
John Carroll University
Physics Department
Cleveland, OH 44118

Byong H. Ahn
USA NV & EOL
Night Vision & Electro-Optics Lab.
Laser Div., Bldg. 357
Ft. Belvoir, VA 22060

Edmund Altonji
ITT Corporation
390 Washington Avenue
Nutley, NJ 07110

David Armitage
Lockheed Research Lab.
3251 Hanover Street
Dept. 52-54, Bldg. 202
Palo Alto, CA 24306

R. A. Athale
NRL
Code 6530
Washington, DC 20375
(202) 767-5630

T. E. Batchman
University of Virginia
2535 Kimbrough Cir.
Charlottesville, VA 22901

Robert Baumbick
NASA Lewis Research Center
MS 100-1
21000 Brookpark Road
Cleveland, OH 44135

Harry Benz
NASA Langley Research Center
MS 473
Hampton, VA 23665
(804) 865-3535

Norman J. Berg
Harry Diamond Labs.
2800 Powder Mill Road
Adelphi, MD 20783
(202) 394-2520

Tom Bicknell
JPL
4800 Oak Grove Dr.
Pasadena, CA 91103
FTS 792-2523

Joe C. Bradley
Westinghouse
19 Hillside Ave.
Towson, MD 21204
(301) 765-7508

Jean Breedlove
The Aerospace Corp.
P.O. Box 92957, M4-934
Los Angeles, CA 90009
(213) 648-5034

Alfred J. Burford
USA/FSTC
220 7th St. N.E.
Charlottesville, VA 22901
296-5171, 5676

James J. Burk
University of Arizona
Optical Sciences Ctr.
Tucson, AZ 85721
(602) 621-1021

Charles E. Byvik
NASA Langley Research Center
MS 160
Hampton, VA 23665
(804) 865-3127

Richard F. Carson
University of Virginia
Dept. of Electrical Engineering
C Wing, Thornton Hall
Charlottesville, VA 22901

Lt. Col. Robert W. Carter, Jr.
AFOSR
AFOSR/NE
Bolling AFB, DC 20332
(202) 767-4931

Steven Cartwright
University of Dayton Research Inst.
300 College Park
Dayton, OH 45469
(513) 229-3724

H. J. Caulfield
Innovative Optics, Inc.
P.O. Box 1275
Concord, MA 01342
(612) 663-9500

Gordon Chin
NASA Goddard Space Flight Center
Code 693.0
Greenbelt, MD 20771
(301) 344-5333

Ivan O. Clark
NASA Langley Research Division
MS 470
Hampton, VA 23665
(804) 865-3777

Robert C. Clausen
Honeywell
Corporate Technology Center
10701 Lyndale Ave., So.
Bloomington, MN 55337
(612) 887-4099

Stuart A. Collins, Jr.
Ohio State University
ElectroScience Lab.
1320 Kinnear Rd.
Columbus, OH 43212
(614) 422-5045

Antonio R. Dias
ERIM
P.O. Box 8618
Ann Arbor, MI 48107
(313) 994-1200, Ext. 523

Uzi Efron
Hughes
3011 Malibu Canyon Rd.
Malibu, CA 90265

Sverre T. Eng
Jet Propulsion Lab.
4800 Oak Grove Dr.
M.S. 198-226
Pasadena, CA 91109

Harry Erwin
NASA Johnson Space Center
308 Oak
Friendswood, TX 77546
(713) 483-3660

Joseph W. Fikes
International Laser Systems
3404 N. Orange Blossom Trail
Orlando, FL 32804
(305) 295-4010

Arthur Fisher
NRL
Code 6537, NRL
Washington, DC 20375
(202) 767-5630

David Flannery
USAF – Avionis Lab.
AFWAL/AADO-2
Wright Patterson AFB, OH 45433

Archibald L. Fripp
NASA Langley Research Center
MS 470
Hampton, VA 23665
(804) 865-3777

Charles Garvin
Harry Diamond Labs.
2800 Powder Mill Road
Adelphi, MD 20783
(202) 394-2520

John Goebel
NASA Ames Research Center
MS 244-7
Moffett Field, CA 94035
FTS 448-6525

William R. Graver
Riverside Research Inst.
1701 N. Ft. Myer Dr.
Arlington, VA 22209

David Greenfeld
Harry Diamond Labs.
2800 Powder Mill Road
Adelphi, MD 20783
(202) 394-2520

Sarry F. Habiby
Ohio State University
2565 Riverside Dr., 4J
Columbus, OH 43221
(614) 486-8075

Lorna J. Harrison
Harry Diamond Labs.
2800 Powder Mill Road
Adelphi, MD 20783
(202) 394-2520

Paul J. Hayes
NASA Langley Research Center
MS 470
Hampton, VA 23665
(804) 865-3777

Darrel Hopper
FTD/TQTA
Wright Patterson AFB, OH 45433
(513) 257-6716

Larry J. Hornbeck
Texas Instruments
Rt. 1, Box 162
Van Alstyne, TX 75095
(214) 995-2260

Phil Howerton
University of Virginia
Dept. of Electrical Engineering
Thornton Hall
Charlottesville, VA 22903

Fred Huck
NASA Langley Research Center
MS 473
Hampton, VA 23665
(804) 865-3535

Lynn Hutcheson
Honeywell
10701 Lyndale Ave., S.
Bloomington, MN 55343
(612) 887-4052

Scott Israel
Lockheed Electronics
1501 U.S. Highway 22
Plainfield, NJ 07061
(201) 757-1600, Ext. 2420

Daniel J. Jobson
NASA Langley Research Center
MS 473
Hampton, VA 23665
(804) 865-3535

Alan R. Johnston
Jet Propulsion Laboratory
4800 Oak Grove Drive
Mail Stop 198/231
Pasadena, CA 91109
(213) 354-4054

David R. Johnson
NASA Langley Research Center
MS 235
Hampton, VA 23665
(804) 865-3907

Steve Katzberg
NASA Langley Research Center
MS 473
Hampton, VA 23665
(804) 865-3535

Ronald L. Kirk
The Holotronics Corp.
424 North Main Street
Findlay, OH 45840
(419) 422-4270

John Krawczak
Sperry DSD
Box 3525
St. Paul, MN 55165
(612) 456-4205

James L. Lafuse
DOD
9321 Farewell Rd.
Columbia, MD 21045
(301) 859-6440

Sing H. Lee
University of California at
San Diego
Elect. Engr. & Computer Sci. Dept.
La Jolla, CA 92093

Carl J. Magee
NASA Langley Research Center
MS 499
Hampton, VA 23665
(804) 865-3418

John A. Neff
DARPA/DSO
1400 Wilson Blvd.
Arlington, VA 22209
(202) 694-5800

Charles P. Neuman
Dept. of Electrical & Computer
Engineering
Carnegie-Mellon University
Pittsburgh, PA 15213
(412) 578-2460

Charles Nichols
NASA Langley Research Center
MS 470
Hampton, VA 23665
(804) 865-3777

Steve Park
NASA Langley Research Center
MS 125A
Hampton, VA 23665
(804) 865-2070

Melvin Pedinoff
Hughes Research Labs.
3011 Malibu Canyon Rd.
Malibu, CA 90265

John M. Pellegrino
Harry Diamond Labs.
2800 Powder Mill Road
Adelphi, MD 20783
(202) 394-2520

Benjamin J. Pernick
Grumman Aerospace
M.S. A-08/35
Bethpage, NY 11714
(516) 575-2231

Nasser Peyghambarian
University of Arizona
Optical Sciences Center
Tucson, AZ 85721
(602) 621-4903

Ting-Chung Poon
Virginia Polytechnic Institute &
State University
Dept. of Electrical Engineering
Blacksburg, VA 24061

Demetri Psaltis
Cal Tech
Pasadena, CA 91125
(213) 356-4856

Michael C. Reichenbach
Lockheed Elec. Co.
1501 U.S. Highway 22
Plainfield, NJ 07061

Thomas C. Robbins
Dept. of Defense
9800 Savage Rd.
Attn: R533
Ft. Meade, MD 20755
(301) 859-6440

Jeffrey B. Sampsell
Texas Instruments
13500 N. Central Exp.
M/S 105
Dallas, TX 75265
(214) 995-4592

Richard Samms
Information & Control Systems, Inc.
28 Research Drive
Hampton, VA 23666

Jag J. Singh
NASA Langley Research Center
MS 235
Hampton, VA 23665
(804) 865-3907

Eugene Skurnick
ITT – Avionics
390 Washington Ave.
Nutley, NJ 07110
(201) 284-3360

Martin Sokoloski
NASA Headquarters
RTC-6
Washington, DC 20546

Robert L. Stermer
NASA Langley Research Center
MS 470
Hampton, VA 23665
(804) 865-3777

USA/FSTC
220 7th St., N.E.
Charlottesville, VA 22901
296-5171

Poohsan N. Tamura
Honeywell CTC
10701 Lyndale Ave., South
Bloomington, MN 55420
(612) 887-4557

Armand R. Tanguay, Jr.
University of Southern California
523 Seaver Science Center
University Park MC-0483
Los Angeles, CA 90089-0483
(213) 743-6152

Thomas H. Thornton
Jet Propulsion Labs.
M.S. 198-226
4800 Oak Grove Drive
Pasadena, CA 91109
454-3560

Chen S. Tsai
University of California, Irvine
Dept. of Electrical Engineering
Irvine, CA 92717
(714) 856-5144

Anthony VanderLugt
Harris Corp.
P.O. Box 37
Melbourne, FL 32902
(305) 727-4742

Carl M. Verber
Battelle Columbus Labs.
505 King Ave.
Columbus, OH 43201
(614) 42405710

Gilbert H. Walker
NASA Langley Research Center
M.S. 160
Hampton, VA 23665
(804) 865-3781, 3127

Cardinal Warde
MIT
Room 13-3134
Cambridge, MA 02139

Martin F. Wehling
USAF
AFATL/DLMI
Eglin AFB, FL 32542
(904) 882-5252, 2838

George P. West
The Holotronics Corp.
424 N. Main Street
Findlay, OH 45840
(419) 422-4270

R. Gale Wilson
NASA Langley Research Center
MS 473
Hampton, VA 23665
(804) 865-3535

Francis T. S. Yu
Penn State University
Electrical Engineering Dept.
University Park, PA 16802
(814) 234-8929 (Home)
       863-2989 (Office)

John M. Zavada
U.S. Army Research Office
P.O. Box 12211
Research Triangle Park, NC 27713
(919) 549-0641

1. Report No. NASA CP-2302	2. Government Accession No.	3. Recipient's Catalog No.
4. Title and Subtitle OPTICAL INFORMATION PROCESSING FOR AEROSPACE APPLICATIONS II		5. Report Date March 1984
		6. Performing Organization Code 506-54-13-20
7. Author(s) Robert L. Stermer, Compiler		8. Performing Organization Report No. L-15754
		10. Work Unit No.
9. Performing Organization Name and Address NASA Langley Research Center Hampton, VA 23665		11. Contract or Grant No.
		13. Type of Report and Period Covered Conference Publication
12. Sponsoring Agency Name and Address National Aeronautics and Space Administration Washington, DC 20546		14. Sponsoring Agency Code

15. Supplementary Notes

16. Abstract
The proceedings of the Optical Information Processing Conference II held on August 30-31, 1983, in Hampton, Virginia, are presented. The state of systems architecture design to perform matrix operations were presented. Detailed component and device papers review the state of optical circuit technology. Optical information processing techniques offer significant potential for meeting projected information processing requirements in projected aerospace systems.

17. Key Words (Suggested by Author(s)) Integrated optics Optical computers Optical components Optical devices	18. Distribution Statement Unclassified - Unlimited Subject Category 74

19. Security Classif. (of this report) Unclassified	20. Security Classif. (of this page) Unclassified	21. No. of Pages 274	22. Price A12